Vertical Integration of Optical Waveguides in the AlGaAs/GaAs Semiconductors

by

Zhongfa Liao

A thesis submitted in conformity with the requirements
for the degree of Doctor of Philosophy

The Edward S. Rogers Sr. Department of Electrical & Computer Engineering
University of Toronto

Vertical Integration of Optical Waveguides in the AlGaAs/GaAs Semiconductors

Zhongfa Liao

Doctor of Philosophy

The Edward S. Rogers Sr. Department of Electrical & Computer Engineering
University of Toronto

2018

Abstract

The rapidly growing Internet services put a higher bandwidth requirement on datacenters. A low-power and low-cost photonic integrated circuit (PIC), using wavelength division multiplexing (WDM), holds the promise to further scale the density, reach, and bandwidth needed for next-generation datacenter networks. Multi-guide vertical-integration (MGVI) scheme improves device yields, saves substantial fabrication costs and offers many other advantages. The $Al_xGa_{1-x}As$ semiconductors provide optical gain and allow for the monolithic integration of different active and passive components. In this thesis, we demonstrate the vertical integration of optical waveguides via the MGVI scheme in the $Al_xGa_{1-x}As$ semiconductors.

First, we begin by developing wet chemical etching techniques and demonstrate sacrificial etching of $Al_xGa_{1-x}As$ layers with a low aluminum content against layers with a high aluminum content. We also demonstrate sacrificial etching of $Al_{0.7}Ga_{0.3}As$ layers against $Al_xGa_{1-x}As$ layers with $x < 0.5$ in hydrofluoric acid (HF) solutions, and fabricate suspended waveguides. Second, we develop inductively-coupled plasma reactive ion etching (ICP-RIE) recipes which enable highly precise and anisotropic etching. We fabricate 800-nm wide and 3.2-μm deep straight $Al_xGa_{1-x}As$ waveguides and measure a propagation loss of 6.7 dB/cm for the fundamental TE mode at a wavelength of 850 nm. Third, we fabricate a vertically integrated spot-size converter

(SSC), which allows for an efficient coupling in the two-guide-layer wafer. We measure an insertion loss of 0.4 dB between two waveguide layers at the wavelength of 850 nm. The total insertion loss including fiber-waveguide interfaces is -3 dB (-1.5 dB after correction for 28% Fresnel reflection at uncoated facets). We design an arrayed waveguide grating (AWG) for WDM, one key application of the MGVI scheme in $Al_xGa_{1-x}As$, in the two-guide-wafer and discuss our preliminary experiments. Finally, we design a three-guide-layer wafer which integrates a waveguide photodiode (WGPD) and simulate a responsivity of 0.66 A/W using Crosslight® SimuPICS3D tools.

Acknowledgments

First and foremost, I would like to thank my supervisor, Prof. J. Stewart Aitchison, for his ongoing support and mentorship over the past four years, and for making my studies at the University of Toronto possible. This work required the constant attention and dedication of my supervisor to ensure all the tools, equipment, and materials were provided to push the work forward. In addition to the supervision on technical matters pertaining to this thesis, I must also thank my supervisor for cultivating an environment where I could develop interpersonal skills and for frequently encouraging me to explore new avenues of personal development. I am deeply indebted to him.

I would like to thank Profs. Li Qian and Amr Helmy for many inspiring discussions during my graduate studies. I would like to thank the staff and technicians at the Toronto Nanofabrication Center (TNFC), Dr. Alexander Tsukernik, Dr. Edward Huaping Xu, Dr. Henry Lee, Yimin Zhou and Harlan Kuntz for their continuous support, patience, and cooperation during the projects in the thesis. I would like to extend my gratitude to the staff and technicians at the Quantum Nanofabrication Center (QNC) at the University of Waterloo for the access to their cleanroom facilities. I would like to thank Dr. Nathan Nelson-Fitzpatrick, Rodello Salandanan, Matt Scott and Brian Goddard for their support. Much of the work was done with their help at QNC.

I would like to thank my colleagues and friends, who have contributed substantially both academically and morally to my growth during my Ph.D. I would like to thank Dr. Arnab Dewanjee, Dr. Xiao Sun and Dr. Pisek Kultavewuti for many academic discussions. I would like to thank Xiaofeng Xu, Dr. Fei Ye, Dr. Feihu Xu, Dr. Zhiyuan Tang, Dr. Dongpeng Kang, among many others, for numerous discussions on professional and personal affairs. I would like to especially thank Yiwei Zhang and Jianfeng Qiu for their continuous moral support, which is beyond words, during the last six years of our acquaintance.

Above all, I would like to thank my parents for raising me, creating an environment for me to freely pursue my personal development and putting their faith in me. I am indebted to them for their love.

Table of Contents

List of Tables

List of Figures

List of Publications

Publications relevant to the thesis

Z. Liao, M. Alam and J. S. Aitchison, "Experimental demonstration of vertically integrated AlGaAs/GaAs waveguides," in 2016 IEEE Photonics Conference (IPC), Waikoloa, HI, 2016.

P. Kultavewuti, Z. Liao and J. S. Aitchison, "2D high-contrast AlGaAs waveguides for nonlinear applications," in 2016 IEEE Photonics Conference (IPC), Waikoloa, HI, 2016.

Z. Liao and J. S. Aitchison, "Precision etching for multi-level AlGaAs," Optical Material Express, vol. 7, no. 3, pp. 895-903, 2017.

Z. Liao, S. J. Wagner, M. Z. Alam, V. Tolstikhin and J. S. Aitchison, "Vertically integrated spot-size converter in AlGaAs-GaAs," Optics Letters, vol. 42, no. 20, pp. 4167-4170, 2017.

Z. Liao and J. S. Aitchison, "Monolithic integration of waveguide photodiodes (WGPD) with vertically integrated AlGaAs waveguides," in 2017 IEEE Photonics Conference (IPC), Orlando, FL, 2017.

Publications not included in the thesis

James C. H. Poon, Zhongfa Liao, Takaya Suzuki, Miranda M. Carleton, John P. Soleas, J. Stewart Aitchison, Golnaz Karoubi, Alison P. McGuigan and Thomas K. Waddell, "Design of biomimetic substrates for long-term maintenance of alveolar epithelial cells," Biomater. Sci., 6, 292-303, 2018.

Chapter 1
Introduction

1 Introduction

This chapter introduces datacenter communications trends, optical interconnects for intra-datacenter communications and different integration schemes for III-V semiconductor photonic circuits, especially the multi-guide vertical-integration (MGVI) scheme.

1.1 Data center communications

1.1.1 Data centers

The exploding popularity of Internet services and the trend toward "cloud" computing have resulted in a dramatic increase of datacenter bandwidth requirement. Such Internet services include video/audio streaming services, cloud storage for consumers and businesses as well as internet of things (IoT) services. Most of these applications are running in datacenters that are transparent to end users. Datacenter computing and content streaming are becoming more and more popular and rapidly growing.

A datacenter is a massively parallel super computing infrastructure, which consists of clusters with thousands of servers networked together. Figure 1.1 shows a schematic of a typical datacenter cluster, with servers arranged into racks of 20-40 machines each. Servers within the same rack are connected through a top of rack (TOR) switch. Rack switches are connected to cluster switches which provide connectivity between racks and form the cluster-fabrics for warehouse-scale computing.

At the center of the Internet style of computing is a cloud of geographically distributed datacenters connected by a large-capacity network. As far as a user is concerned, the datacenter network appears as a single computer or storage device. Internet-style computing offers many benefits. Scalability is the first one. All user data resides in the network and are accessible anywhere in the world as long as there is a network connection. Internet-style computing also provides a platform for easy data sharing and collaboration. Since end users need not be concerned with maintaining their own computing equipment, there is operational expense and capital reduction. Without a good reliable and scalable network infrastructure, none of the above benefits can happen.

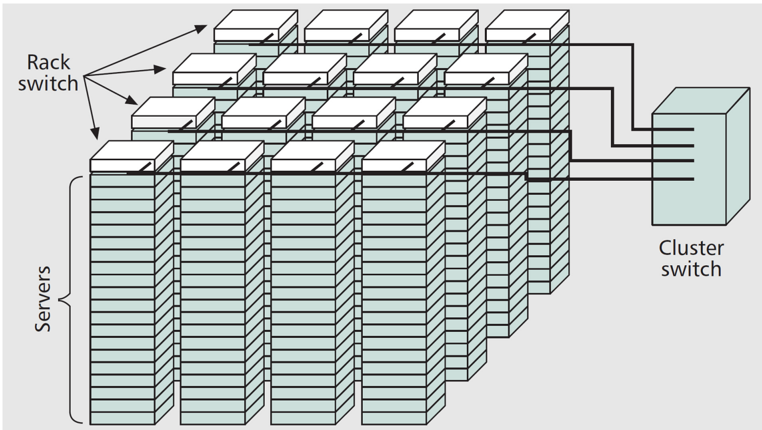

Figure 1.1 Typical view of a cluster inside a warehouse-scale datacenter. Figure is from [1].

1.1.2 Data center trends

The ever-growing need for cloud resources has driven up the number of hyperscale datacenters and the traffic within them. The number of workloads and computing instances are mainly driven by datacenter virtualization and cloud computing growth. Among the various Internet services provided to consumers, video streaming and social networking are the main driving forces, which are also the two fastest growing applications. Within enterprise/business segment, compute and collaboration are the two main contributors. Cisco® publishes Cisco® Global Cloud Index (GCI) whitepaper every year as an ongoing effort to forecast the growth of global data center and cloud-based IP (Internet protocol) traffic. The following is a snapshot of the current status and trends. Annual global data center IP traffic will reach 20.6 Zettabytes [ZB] (1.7 ZB per month) by the end of 2021, up from 6.8 ZB per year (568 Exabytes [EB] per month) in 2016 [1]. Global data center IP traffic will grow 3-fold over the next 5 years. Overall, data center IP traffic will grow at a compound annual growth rate (CAGR) of 25 percent from 2016 to 2021 [1].

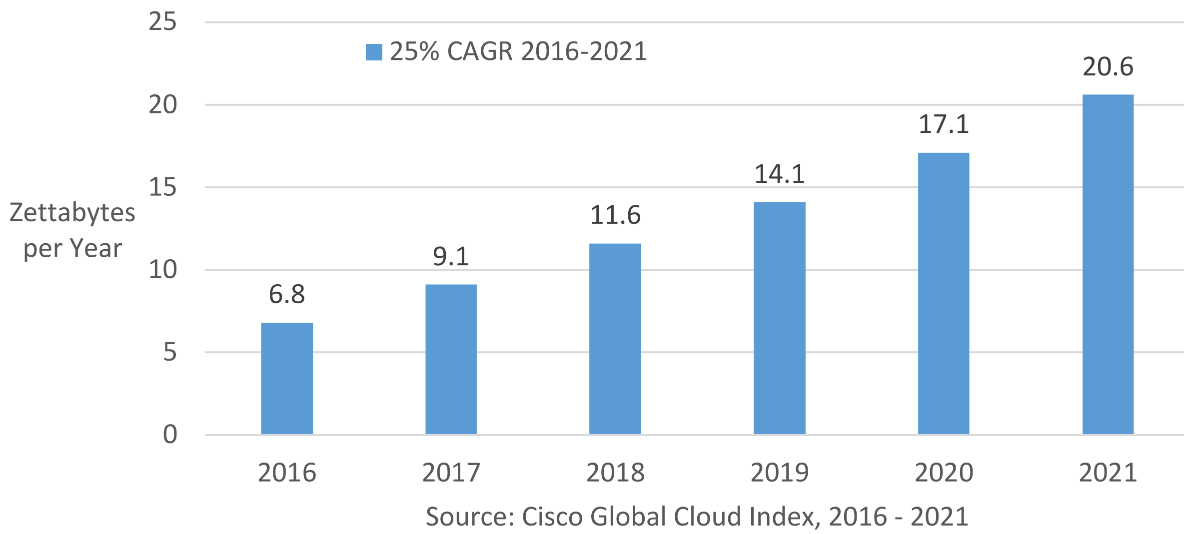

Figure 1.2 Global data center traffic growth [1].

By 2021, installed data center storage capacity will grow to 2.6 ZB, up from 663 EB in 2016, nearly a 4-fold growth [1]. Storage utilization varies by type of storage and generally ranges from 30 to 70 percent, especially given that deployments of additional capacity are growing quickly. Globally, the data stored in data centers will grow 4.6-fold by 2021 to reach 1.3 ZB by 2021, up from 286 EB in 2016 [1].

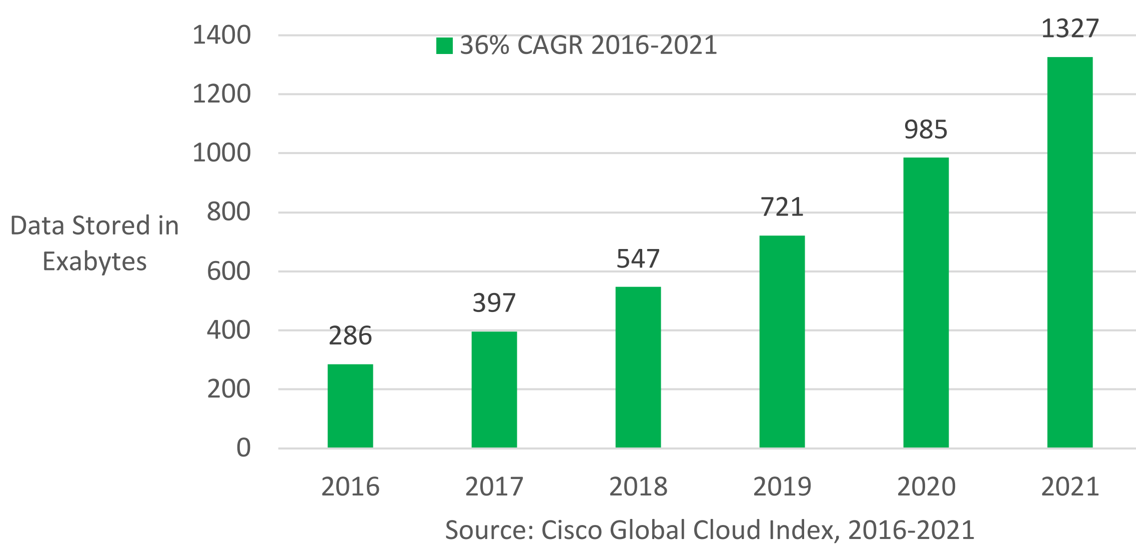

Figure 1.3 Actual data stored in data centers [1].

The global data center IP traffic can be sorted by its destinations. The definitions are as follows:

- Data center to user: Traffic that flows from the data center to end users through the Internet or IP wide-area-networks (WANs)
- Data center to data center: Traffic that flows from data center to data center
- Within data center: Traffic that remains within the data center, excludes traffic within the rack

The portion of traffic residing within the data center will decline slightly over the forecast period, accounting for 75.4 percent of data center traffic in 2016 and 71.5 percent by 2021 [1]. It is still the main contribution to global data center IP traffic. Traffic between data centers is growing faster than either traffic to end users or traffic within the data center, and by 2021, traffic between data centers will account for almost 14 percent of total data center traffic, up from 10 percent at the end of 2016 [1]. The high growth of this segment is due to the increasing prevalence of content distribution networks, the proliferation of cloud services and the need to shuttle data between clouds, and the growing volume of data that needs to be replicated across data centers. Overall, traffic within the data center and traffic between data centers will represent 85 percent of total data center by 2021, and traffic exiting the data center to the Internet or WANs will be only 15 percent of traffic associated with data centers.

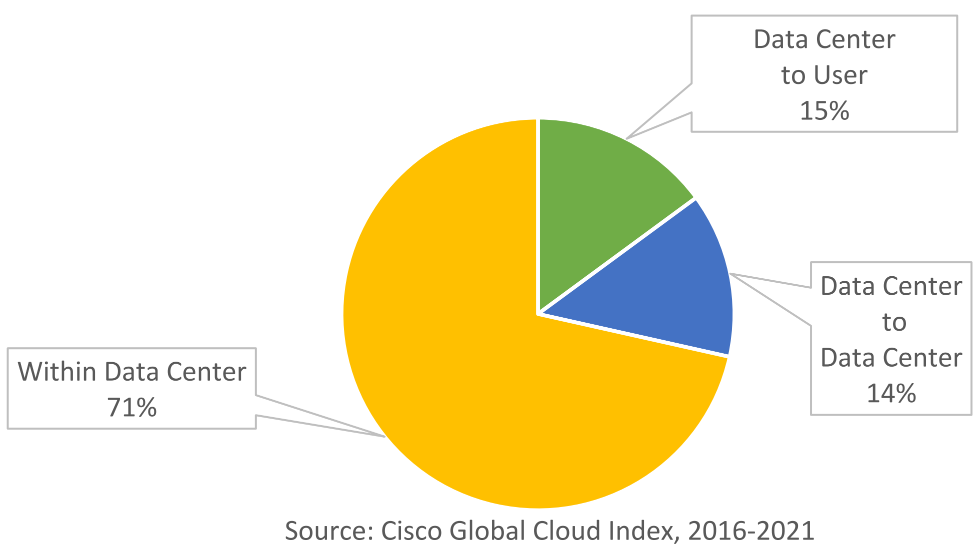

Figure 1.4 Global data center traffic by destination in 2021 [1].

1.1.3 Optical interconnects in intra-datacenter network

A datacenter can consist of either one building or multiple buildings, as shown in Figure 1.5. Fiber optic technologies play critical roles in datacenter operations. Optical interconnections, with reach between 10 m to 2 km, are of paramount importance for intra-datacenter connectivity in a warehouse-scale computer. Within the same building, vertical cavity surface emitting laser (VCSEL)-based low-power and low-cost short reach (SR) multi-mode optics are already playing an important role. Long reach (LR) optics, at 1310 nm wavelength and based on higher-power single-mode distributed feedback (DFB) lasers, are now being used for inter-building interconnections.

Given the huge optical interconnect bandwidth needed, interconnect bandwidth must scale from 10 Gbps through 40 Gbps to 100 Gbps. In addition to bandwidth growth, the power, cost, and space density must scale at the same time to satisfy the needs of mega-datacenter computing. To further scale the density and reach a higher data rate, a photonic integration circuit (PIC) using wavelength-division multiplexing (WDM) is inevitable [2, 3].

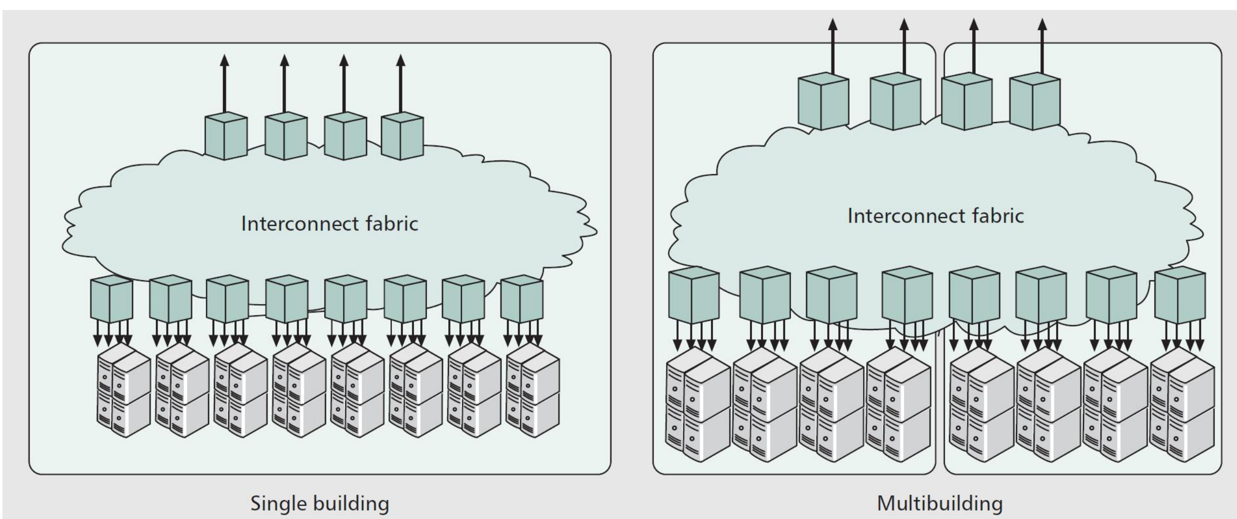

Figure 1.5 Hierarchies of intra-datacenter cluster-switching interconnect fabrics. Figure is from [1].

WDM has been widely adopted in WANs. Since fiber is scarce between remote datacenters, spectral efficiency is important. This makes WDM a natural fit for WAN interconnection. Traditionally, the intra-datacenter environment was fiber rich and spectral efficiency was never an important concern. However, as bandwidth and datacenter size grow, the cost of fiber, together with the expense of termination and management, has become a significant portion of overall link cost. In addition, increasingly large fiber bundles can present problems for mechanical clearances and air flow, making equipment more susceptible to thermal and cooling issues.

Figure 1.6 is a simplified presentation of 100Gb/s link cost, as a function of distance, using three different optical interconnect technologies: (1) VCSEL SR transceiver, (2) edge-emitting DFB LR transceiver, and (3) integrated WDM transceiver with 10 wavelengths [3]. The starting point at 10m is the combined cost of optical transceivers and fiber terminations. Longer links become more expensive since longer fiber cables cost more. At various reaches, the slope ($/meter) of the WDM links is ten times lower than the slope for single-mode fiber and twenty times lower than the slope for multi-mode fiber. This is a result of (1) the relatively lower cost of single-mode fiber to multi-mode fiber and (2) the bundling of wavelengths within a single-mode fiber, such that only one fiber is needed for transmitting the same amount of bandwidth. When the cost of WDM and an uncolored DFB transceiver is the same for an identical amount of bandwidth, integrated WDM technology can result in drastic reduction of link cost. From the per-link capital expenditure perspective, even if the WDM transceiver costs 1.5 times that of an uncolored DFB LR for the same amount of bandwidth, there is still a clear advantage to using WDM at reaches beyond 800 meters.

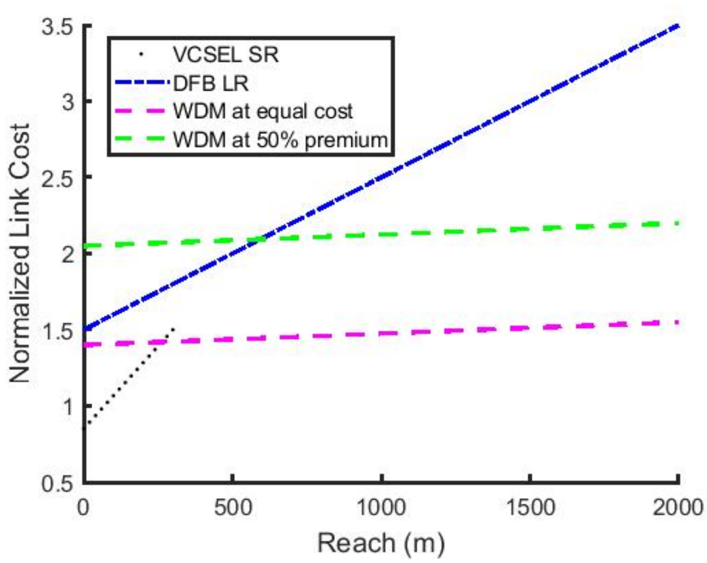

Figure 1.6 Normalized 100G link cost using SR, DFB LR and WDM [3].

The greatest challenge with the application of WDM in datacom is scaling the technology in size, power, and cost simultaneously. It is difficult to meet datacom requirements with discretely packaged single-wavelength WDM transceivers. Photonic integrated circuits (PICs) could meet datacom power, space, and cost requirements of datacom, and significantly improve the landscape of next-generation datacenter interconnections [4]. Monolithic integration aims at lowering costs by taking advantage of streamlined planar circuit processing at wafer scale.

With WDM, the true potential of the vast bandwidth available with single-mode optical fibers is fully exploited. A low-power and low-cost photonic integration circuit (PIC), using wavelength division multiplexing (WDM), holds the promise to further scale the density, reach, and data rates needed for next-generation datacenter networks, and to enable new network architectures and applications.

1.2 Integration schemes in III-V PICs

The development of photonic integrated circuits (PICs) has been advancing rapidly over the last two decades. The main goals of bringing optical systems onto an integrated platform are to miniaturize optical components for better space efficiency and to lower cost. Integrating several optical components onto a single chip via modern microfabrication technology can eliminate many production costs. Monolithically integrated optical components are defined by lithography and thus aligned lithographically with high precision, which improves device lifetime and reliability. Photonic integrated circuits have been implemented using dielectric materials such as silica glass and lithium niobate. Silicon has also been exploited in the last decade for creating several integrated devices. However, the primary limitation of using such materials is that they do not emit light. For active PICs, in which optical gain is required, such as those requiring lasers, detectors or semiconductor-optical-amplifiers (SOAs), it is most desirable to choose an integration platform that naturally provides gain, such as one based on a III-V semiconductor. Furthermore, it is desirable for these platforms to enable the monolithic integration of different active and passive components with a minimal compromise in the performance of the individual components.

One of the biggest challenges facing monolithic photonic integration is the requirement of different bandgap energies for different functional components. PICs require three basic optical functions: 1) light generation and amplification; 2) light guiding and coupling; and 3) light detection. For example, active regions of high-performance light generation and amplification components such as lasers and amplifiers usually consist of strained quantum wells whose transition energies lie at the photon energy in order to achieve high optical gain. Similarly, light guiding and coupling components need materials with a bandgap larger than the photon energy to minimize propagation losses. Finally, light detection components require undoped materials with a bandgap smaller than the photon energy to ensure efficient optical absorption. To maintain the high performance of the discrete components in an integration platform, efficient optical power transfer between these different optical functions must be also realized.

Currently, PICs are based on many different integration schemes, including etch-and-regrowth [5, 6], quantum-well intermixing (QWI) [7, 8], selective-area growth [9] and hybrid material integration [10]. In the etch-and-regrowth scheme, epitaxial layers are sequentially grown in different regions of the wafer to optimize different functions. Although regrowth provides freedom to optimize each required function, integration of different components suffers from high reflectivity at the etched-and-regrown region and unetched region [11]. Device characteristics are strongly affected by the regrowth interface which is subject to possible contamination during wafer processing between the regrowth steps [12, 13]. Etch-and-regrowth is the most flexible approach, however, it is also the most expensive one due to the high cost and low yield of multiple epitaxy steps.

Quantum well intermixing (QWI) involves intentionally introducing defects which in turn allow inter diffusion between the atoms in the quantum wells (QWs) and the atoms in the barriers of a quantum well structure [7, 14]. There are many ways to introduce these defects, including impurity induced disordering [7], impurity-free selective layer disordering [15], sputtered SiO_2 disordering process [16, 17], ion implantation induced intermixing [18-20] and laser induced intermixing [21]. The inter diffusion alters the compositional the profile of the QW, which changes the quantum confinement potential, which subsequently blueshifts the bandgap and lowers the refractive index of the QW structure. Light generation and amplification components are fabricated in the non-intermixed regions, and low-loss light guiding components are realized in the intermixed regions. The integrated optical functions must share a similar material structure since growth occurs in only a single step. It is difficult to optimize the light guiding material for special device functions such as polarization-insensitive waveguides [22] and waveguides with high coupling efficiencies to single-mode optical fibers [23]. This compromises device performance.

In the selective-area growth (SAG) scheme, the substrate is patterned with dielectric masks. By changing the width of the mask openings, the local material growth rate can be changed [9, 24]. Therefore, the thickness and the transition energy of the quantum wells can be varied within a certain range. As in etch-and-regrowth, device characteristics can be affected by the surface conditions, since growth is performed on a substrate that is subject to possible contamination. As in QWI, all integrated optical functions must share a similar epitaxial structure, since growth occurs in only a single step, leading to compromises in integrated device performance.

Hybrid-material integration involves heterogeneously integrating active III-V semiconductor components with passive components on a different substrate, i.e. silicon waveguides [10]. Several bonding techniques are being used: molecular bonding [25], metal bonding [26] and adhesive bonding [27]. The main disadvantage of hybrid material integration is that it suffers from complicated fabrication processes. Hybrid integration of compound semiconductors and silicon can potentially be free of multiple epitaxy steps; however, it requires wafer bonding to provide an active layer, which can be costly. In addition, mixing multiple types of active devices on the chip requires either a compromise in performance of each device when using the same bonded active layer.

1.3 Multi-guide vertical-integration

The aforementioned integration methods have drawbacks that limit the integration complexity and incur high fabrication costs. One alternative is regrowth-free vertical integration, in which functional waveguides composed of different yet compatible III-V semiconductor materials are vertically stacked in one epitaxial growth run and coupled to each other by means of lateral tapers defined in a process of fabrication [28-34]. In this scheme, the wafer is grown in a single epitaxial growth run. Multiple waveguide levels are stacked on top of each other. Epitaxial layers within each level are optimized for a specific function. The top-most level has a waveguide core with the lowest band gap energy of the entire structure and hosts optically active devices such as lasers and photodetectors. A second active level with the next lowest band gap energy can be placed directly below to host devices such as modulators or pre-amplifiers. Passive devices, such as filters and splitters, and routing waveguides can be located on one or more passive levels. The bottommost level typically has a large waveguide core that forms part of a spot-size converter (SSC), or mode expander for coupling to and from optical fibers. To move light between two levels, waveguides on the upper level are tapered laterally in a fashion that allows low-loss adiabatic power transfer.

1.3.1 MGVI in indium phosphide (InP)

This integration scheme, known by the names of single-mode vertical integration [28], asymmetric twin-waveguide (ATG) technology [29], multi-guide vertical-integration (MGVI) [30], or taper-assisted vertical integration (TAVI) [35], has been proven a versatile PIC platform in the InP material system.

In essence, MGVI is a generalization of the asymmetric twin-guide scheme [23, 29, 31, 36], but allows for more comprehensive photonic integration. The first papers on the twin-guide scheme appeared in the field of AlGaAs-based lasers [37, 38]. Later this concept was applied in the InP-based integration [39]. In the original twin-guide scheme, the modal propagation constants of the two guides have to be equal in order for the beating and power exchange to be effective. The coupling length critically depends on the thickness and composition of the intermediate layers. Stringent tolerance in the coupling length results in unpredictable behavior in lasers. As a result, the original twin-guide scheme had very limited applications.

A variation of the idea has been developed: the asymmetric twin-waveguide scheme (ATG) [23, 29, 31, 36]. In this vertical integration technique, two separate waveguide layers are used, which are now intentionally different, such that there is no phase matching. The propagation constant of the mode in the upper, active waveguide should be larger than that of the mode in the lower, passive waveguide. In that case, the mode entering through the lower waveguide can evolve in to the mode of the upper waveguide in a lateral adiabatic taper placed in the upper layer. Therefore, no mode conversion takes place. The main advantage of the ATG scheme is that different waveguide levels can be separately optimized to some extent for different functions, which lays out the foundation for this scheme’s popularity. Waveguide photodiodes [23], lasers [31, 36, 40], splitters and multiplexers [41] have been successfully demonstrated in this platform.

Single-mode vertical integration is the use of quantum wells on top of a passive waveguide layer [28, 42, 43]. The quantum wells do not form a separate waveguide level whereas the quantum wells along with the passive waveguide layer collectively support one single mode, thus the name single-mode vertical integration. In the active region, the evanescent tail of the guided mode overlaps with the QWs and provides the required absorption or gain for the device. In the passive region, the QW layers are etched away leaving only the passive waveguide layer.

Multi-guide vertical integration (MGVI) generalizes the above integration schemes in to multiple waveguide levels [30]. It has been proven a versatile PIC platform in the InP material system. Two-guide [32], three-guide [33], and even four-guide [34] vertical integration PICs have been successfully developed and commercialized in InP.

1.3.2 Advantages of MGVI

The MGVI scheme has several advantages over other photonic integration methods. By far, the key advantage of MGVI is that only a single epitaxial growth step is required throughout the fabrication process run. This saves substantial cost in several ways: 1) expensive epitaxial regrowth processes are not necessary, 2) device yield from a single wafer is higher because imperfections and nonuniformity from regrowth are eliminated, and 3) wafer growth and lithography are decoupled and can be performed at separate facilities. Another advantage is that it allows for decoupling of device development and circuit development, which is akin to how modern microelectronic devices are developed. Generic building block designs can be developed for each optical function and be separately verified. Complete circuits are then assembled into the PIC layout from these building blocks with only minor adjustments to optimize performance.

1.4 Comparison of component solutions

Presently, data center interconnects are dominated by 10 Gbps optical links based on VCSELs emitting at 850 nm and MMFs. VCSELs are small and cheap – already in 850 nm and potentially in 1310 nm windows. The same is true for surface-illuminated photodetectors (SIPDs). Projected increases in data traffic will require upgrading the links to 40 Gbps and then 100 Gbps and the physical size of the data center interconnects require links up to 2 km [44]. The upgrade path to 100 Gbps using VCSELs is to use multiple lanes over parallel optics. While VCSELs are relatively inexpensive, the reach distance of such links is limited to less than 150 meters due to the modal dispersion in MMFs. The use of MMFs in parallel optics drives up the cost. VCSELs and SIPDs are not multiplexable in any way except with space-division multiplexing (SDM).

Proposals of using higher bit rate with fewer lanes reduce cabling cost but would further limit the reach distance. The other option for 100 Gbps links is to use WDM over single mode fibers (SMFs) in the 1.31/1.55 μm windows. DFB lasers can be modulated in directly or externally, with the external modulation offering certain advantages in terms of laser count and advanced modulation format feasibility. DFB lasers and waveguide photodetectors (WGPDs) are multiplexable in any conceivable way: space, wavelength, polarization, and also suitable for advance modulation formats like quadrature phase-shift keying (QPSK) or pulse-amplitude modulation (PAM). However, working in the 1.31/1.55 μm windows requires lasers built in InP/InGaAsP material systems, which is again more costly and expensive to process. Poor temperature stability of InP lasers forces the use of active cooling, which drives up cost. Currently, most transceivers are constructed with discrete components and assembly cost is an issue.

GaAs is much less costly than InP and less expensive to process [31-33]. GaAs, which has long been used for microelectronics industry, has been largely overlooked for use in PICs over the last two decades because of its emission wavelength of 850 nm. The wavelength of 850 nm is not suitable for the long distance optical links which has long been the focus of the optical communication industry. However, as optical links are deployed on shorter length scales for datacenter communications, the 850 nm wavelength is no longer a restriction [45]. Cost-wise, the advantages of GaAs are related to the fact it is a more robust material to process and therefore more commonly used in low-cost production, e.g. of wireless communication ICs. Furthermore, 6” GaAs wafers are a commodity now while commercial supply of InP wafers is still limited to 4” (which remain quite expensive) with the bulk of InP photonics processed on 3” or 2” wafers. Finally, PIC footprint size scales down with a reduction of operating wavelength and increase of index contrast between materials it is made from. Overall, a combination of less expensive base material/processing, bigger wafers, and smaller dies amounts to a sizable cost reduction, easily of an order of magnitude. From the interface performance standpoint, whereas shorter wavelength range of 0.85μm in GaAs PICs instead of 1.31 μm in InP PICs naturally results in a higher laser turn-on voltage and lower detector quantum efficiency, using wider bandgap material has some advantages. On the transmitter side, weaker Auger recombination and inter-valence band absorption in 0.85 μm GaAs lasers result in higher temperature stability. In addition, wider bandgap materials feature stronger exciton absorption peaks and sharper absorption edges, thereby improving the characteristics of electro-absorption modulators (EAMs). On the receiver side, one little understood advantage of GaAs PICs is that they are built on a substrate that is opaque for any wavelength generated by GaAs transmitter, whereas in InP receiver PICs, their substrate is transparent for any wavelength generated by InP transmitter. This difference results in a higher tolerance of GaAs WDM receiver PICs to optical crosstalk associated with stray light leaked into the substrate.

1.5 Novelty of work

In this thesis, I demonstrate the viability of the multi-guide vertical-integration (MGVI) scheme in the $Al_xGa_{1-x}As$ semiconductors for datacenter applications. I have solved technical challenges in device fabrication, wet chemical etch techniques, dry etch techniques and fabrication processes, for the fabrication of MGVI devices. I achieve the highest order of magnitude difference in etch rates, to my knowledge, for the dry etch recipes. With the etch techniques and fabrication processes, I am able to control etch depths very precisely and create highly anisotropic waveguide sidewalls, without the use of etch stop layers. I report on the design, fabrication and characterization of the first, to my knowledge, vertically integrated spot-size converter (SSC) in $Al_xGa_{1-x}As$ operating in the 850 nm spectral range. I achieve a very high conversion efficiency for the SSC. It marks a major step towards building the MGVI platform in $Al_xGa_{1-x}As$ as a versatile and cost-efficient PIC technology for applications in data center interconnects. Potential applications of the vertical integration approach include non-invasive biosensing and quantum optics, which are detailed in Section 8.2. The new SSC design in a three-guide-layer chip features a total length of 350 μm, making it one of the shortest SSCs of its kind. The vertical integration of waveguide photodiodes (WGPDs) demonstrates the viability to build passive and active devices onto a single chip in the $Al_xGa_{1-x}As$ semiconductors. The thesis demonstrates the viability of MGVI scheme in the $Al_xGa_{1-x}As$ semiconductors in the 850 nm spectral range.

1.6 Scope and outline of thesis

I design two different wafers. The first one is a two-guide-layer chip hosting one high-confinement waveguide layer on the top and one large-dimension waveguide layer on the bottom. The second wafer structure is a three-guide-layer chip with an additional third waveguide layer on the top of the wafer for waveguide photodiode integration. Using the first wafer, I investigate wet chemical etch techniques as a possible means of fabricating AlGaAs-GaAs photonic devices. I use wet chemical etching techniques with the HF family to fabricate suspended waveguides. Using the first wafer, I analyze dry etching techniques using inductively-coupled plasma reactive ion etching (ICP-RIE) and develop dry etch recipes with various characteristics, which serve as the main fabrication technique for the devices presented in this thesis. I design, fabricate and test a spot-size converter (SSC) on the first wafer. In addition, I design and show preliminary fabrication results of an arrayed waveguide gratings (AWGs) in the first wafer. I design and integrate waveguide photodiodes (WGPDs) on the second wafer, making it a three-guide-layer chip. The outline of the thesis is as follows.

Chapter 2 discusses models for index of refraction (RI) of $Al_xGa_{1-x}As$ materials and models for changes in RI when dopants and free carriers are present in these materials. Chapter 3 investigates wet chemical etch techniques as a possible means of fabricating $Al_xGa_{1-x}As$ devices in the two-guide-layer wafer and the fabrication of suspended waveguides in HF solutions. Selectivity and suitability of this approach is discussed. Chapter 3 also presents fabrication and measurement results of suspended waveguides in a different wafer structure. Chapter 4 presents the development of dry etch techniques using ICP-RIE that prove to be successful in fabricating the devices presented in this thesis. The emphases have been etch rate and etch depth precision, surface and sidewall roughness, selectivity between wafer and photoresist, and reproducibility of the recipes. Chapter 5 gives the design, fabrication and test results of the SSC in the two-guide-layer wafer. A very high coupling efficiency is achieved. Chapter 6 discusses the design and preliminary fabrication results of an AWG in the two-guide-layer wafer. Chapter 7 presents the three-guide-layer chip. It features a much-improved design of large-dimension bottom waveguide, improved design of SSCs with shorter coupling length and a WGPD for light detection. Chapter 8 provides a summary and outlines future directions of the thesis.

Chapter 2
Aluminum gallium arsenide

2 Aluminum gallium arsenide

This chapter introduces different models for calculating the index of refraction and bandgap energy of $Al_xGa_{1-x}As$ materials. The change in the index of refraction due to dopants and free carriers is also studied.

2.1 Index of refraction

The $Al_xGa_{1-x}As$ semiconductors are important materials for the fabrication of optoelectronic devices. To design and fabricate multiple-quantum-well (MQW) lasers, detectors and modulators, the index of refraction, n, has to be precisely known as a function of wavelength, λ, and aluminum concentration, x.

There are many semi-empirical models in the literature, which were developed to fit experimental data [46-49]. Stern calculated the refractive indices of GaAs near the bandgap from the absorption coefficient using the Kramers-Kronig dispersion relations where he assumed high-energy peaks could be expressed by delta functions [50]. Afromowitz calculated the room temperature refractive index of $Al_xGa_{1-x}As$ at energies below the direct band edge based on the single-effective-oscillator model, which approximated the imaginary part ϵ_2 with a delta function [51]. Adachi carried out extensive work in developing semiempirical models for calculating the refractive indices of III-V semiconductors, including $Al_xGa_{1-x}As$ [52-54]. Adachi's model is most useful around the band gap energies. Jenkins [55], Lin [56, 57], and Kokubo [58] extended Adachi's model. Based on Adachi's model, Deri derived models that achieved better consistency among the data reported by different groups by employing a common reference for the composition x in terms of the direct gap E_0 [59]. Gehrsitz determined the refractive indices of $Al_xGa_{1-x}As$ epitaxial layers with compositions in the range ($0.176 < x < 1$) accurately below the band gap wavelengths to $\lambda = 3$ µm [60]. Gehrsitz's model is most useful for near-IR wavelengths.

In this thesis, Gehrsitz's model is used to calculate refractive indices of $Al_xGa_{1-x}As$ for wavelengths below the bandgap energy while Deri's model is used to calculate refractive indices of $Al_xGa_{1-x}As$ for wavelengths around and above the bandgap energy. It was found that these two models agreed with refractive index libraries in RSoft® CAD tools and Lumerical® tools.

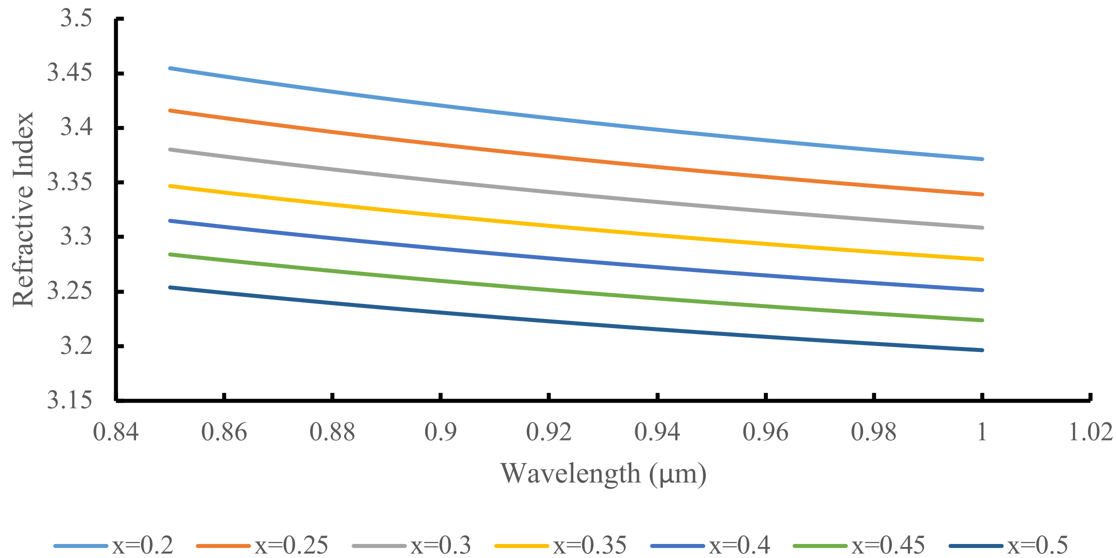

Figure 2.1 Gehrsitz's model for refractive indices of $Al_xGa_{1-x}As$, for x = 0.2, 0.25, 0.3, 0.35, 0.4, 0.45 and 0.5, in the spectral range of between 850 nm and 1000 nm [60].

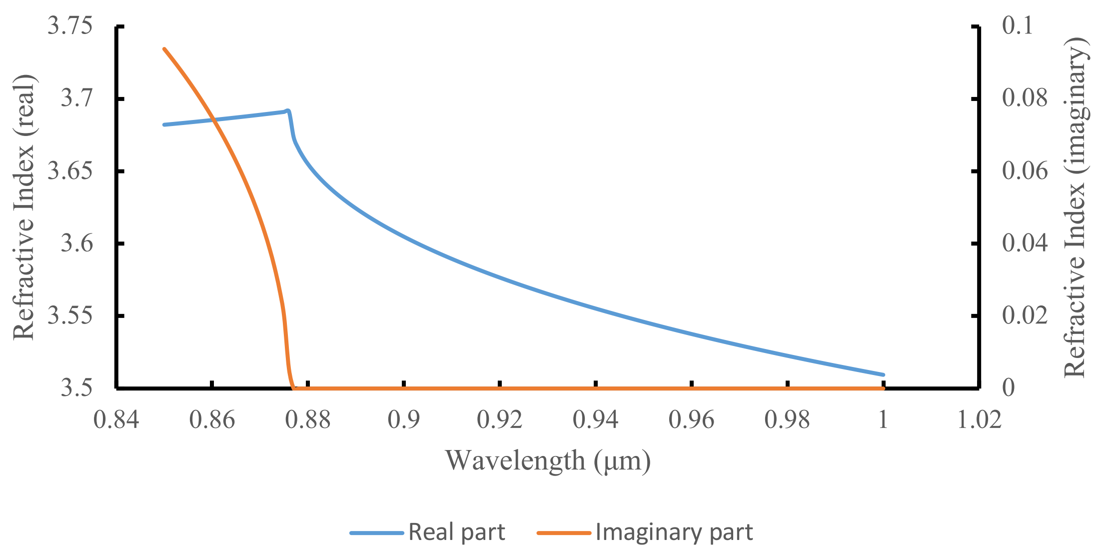

Figure 2.2 Deri's model for refractive indices, both real part and imaginary part, of GaAs in the spectral range of between 850 nm and 1000 nm [59].

2.2 Carrier induced changes

Carrier induced change of refractive index, Δn, of InP, $Al_xGa_{1-x}As$, and $In_xGa_{1-x}As$ have been investigated by multiple authors and the key contributions relevant to this work are summarized here. Band filling (Burstein-Moss effect), band-gap shrinkage and free-carrier absorption (plasma effect) effects were included. Carrier concentrations between 10^{16} cm^{-3} and 10^{19} cm^{-3} and photon energies between 0.8 eV (λ = 1550 nm) and 2.0 eV (λ = 620 nm) were considered. The models that were used in this thesis were mainly based on two references where the validity of the models had been demonstrated through experimental data in the literature. The results of the changes in refractive index, Δn, give a guidance on determining whether the carrier induced changes should be included in the optical simulation of the devices in this thesis.

Free carrier induced refractive index change was traditionally treated by the classical Drude theory [61], where plasma effect by using a simple harmonic oscillator model was considered. Drude theory ignores the effects from ionized impurities and other carrier-related effects around the bandgap. This theory is only valid at a very low doping concentration and a low optical frequency. The results are not applicable at the frequencies used in practical integrated-optics. The lack of experimental Δn data due to free carriers in the literature turned researchers to the Kramers-Kronig theory. Absorption data due to free carriers are available in the literature and can be used to verify calculation models. Once the formulation of carrier-induced absorption spectrum is derived, one can use Kramers-Kronig dispersion relations to predict the change of the refractive index.

A few papers appeared in the literature in 1990s including Huang's [62] and Bennett's [63]. Huang's paper looked at free carrier effects for *n*-type $Al_xGa_{1-x}As$. Bennett's paper looked at III-V semiconductors when there was current injection, *n*-type doping and *p*-type doping. Bennett's paper is more useful for estimating the intrinsic region of the photodetector as well as *n*- and *p*-contacts. First, starting with Bennett's paper, a model is reproduced to match the results given in the relevant reference papers using InP as a reference material. Second, the reproduced model is used to predict the change of refractive index of $Al_xGa_{1-x}As$ and $In_xGa_{1-x}As$ for MQW *p-i-n* photodetectors.

2.2.1 Theory and results

2.2.1.1 Band filling effect

A decrease in absorption for photon energies slightly above the nominal bandgap was observed when they are doped. This effect is most pronounced in semiconductors with small effective masses and band gaps. The effect, known as Burstein-Moss effect, can be explained by band filling effect [64, 65]. In the case of *n*-type semiconductors, the density of states in the conduction band is sufficiently low and a small number of electrons can fill the band to an appreciable depth. With the lowest energy states filled in the conduction band, electron from the valence band requires greater energy than nominal bandgap to be optically excited to the conduction band. Due to larger effective masses, *p*-type semiconductors have higher density of states. This effect is smaller for a given carrier concentration. Because band filling is a result of the presence of free carriers, injection should be equivalent to doping, except that injection will result in band filling effects from both electrons and holes.

If parabolic bands are assumed, optical absorption, $\alpha_0(E)$, near the band gap in a direct bandgap semiconductor is given by:

$$\alpha_0(E) = \frac{C}{E}\sqrt{E - E_g}\ (E > E_g)$$

…………………………………….. (Equation 2.1)

$$\alpha_0(E) = 0\ \left(E < E_g\right)$$

…………………………………….. (Equation 2.2)

where E is photon energy, E_g and C are bandgap energy and a constant, respectively, which are material-specific. The above equations can be written to explicitly take care of heavy and light holes:

$$\alpha_0(E) = \frac{C_{hh}}{E}\sqrt{E - E_g} + \frac{C_{lh}}{E}\sqrt{E - E_g}\ (E > E_g)$$

…………………………………….. (Equation 2.3)

$$\alpha_0(E) = 0 \; (E < E_g)$$

…………………………………. (Equation 2.4)

C_{hh} and C_{lh} are obtained from the parameter C for heavy holes (hh) and light holes (lh), respectively. The reduced effective masses of the electron-hole pairs are given as follows.

$$\mu_{ehh} = \left(\frac{1}{m_e} + \frac{1}{m_{hh}}\right)^{-1}$$

…………………………………. (Equation 2.5)

$$\mu_{elh} = \left(\frac{1}{m_e} + \frac{1}{m_{lh}}\right)^{-1}$$

…………………………………. (Equation 2.6)

$$C_{hh} = C\left(\frac{\mu_{ehh}^{3/2}}{\mu_{ehh}^{3/2} + \mu_{elh}^{3/2}}\right)$$

…………………………………. (Equation 2.7)

$$C_{lh} = C\left(\frac{\mu_{elh}^{3/2}}{\mu_{ehh}^{3/2} + \mu_{elh}^{3/2}}\right)$$

…………………………………. (Equation 2.8)

In the case of band filling, there is a finite probability that a state in the conduction band will be occupied by an electron and/or a state in the valence band will be empty of electron. If we denote an energy in the valence band by E_a and an energy in the conduction band by E_b, then the absorption is

$$\alpha(N, P, E) = \alpha_0(E)[f_v(E_a) - f_c(E_b)]$$

…………………………………. (Equation 2.9)

In the above equation, the *f(x)* is the Fermi-Dirac function. The change in absorption coefficient is

$$\Delta\alpha(N,P,E) = \alpha(N,P,E) - \alpha_0(E)$$

………………………………….. (Equation 2.10)

The change of refractive index is calculated through the Kramers-Kronig relation:

$$\Delta n(N,P,E) = \frac{2c\bar{h}}{e^2}\int_0^\infty \frac{\Delta\alpha(N,P,E')}{E'^2 - E^2}dE'$$

………………………………….. (Equation 2.11)

Table 2.1 Values of semiconductor parameters (T = 300 K).

	InP	GaAs	$In_{0.2}Ga_{0.8}As$
E_g (eV)	1.3507	1.424	0.8137
C ($cm^{-1}s^{-1/2}$)	3.0464×10^{12}	2.4580×10^{12}	1.1350×10^{12}
C_{hh} ($cm^{-1}s^{-1/2}$)	1.9246×10^{12}	1.6317×10^{12}	7.5797×10^{11}
C_{lh} ($cm^{-1}s^{-1/2}$)	1.1218×10^{12}	8.2637×10^{11}	3.7705×10^{11}
ϵ_s	12.4	12.9	13.23
n	3.52	3.6	3.63
m_e (m_0)	0.075	0.0630	0.0545
m_{hh} (m_0)	0.56	0.5100	0.4900
m_{lh} (m_0)	0.12	0.0820	0.0708
m_{dh} (m_0)	0.6	0.5317	0.5078
μ_{ehh} (m_0)	0.066	0.0561	0.0491
μ_{elh} (m_0)	0.046	0.0356	0.0308
N_C (cm^{-3})	5.1442×10^{17}	3.9604×10^{17}	3.1883×10^{17}
N_V (cm^{-3})	1.1537×10^{19}	9.7100×10^{18}	9.0624×10^{18}
χ_{cr} (cm^{-3})	1.2902×10^{17}	6.7919×10^{16}	4.0780×10^{16}

Material-specific parameters are based on [66]. There exists some discrepancy compared to the data that were used in Bennett's paper [63]. In [63], only some of the simulation parameters are provided. In order to interpolate aluminum/indium concentration in $Al_xGa_{1-x}As/In_xGa_{1-x}As$, analytical expressions are used to estimate the above parameters based on [66]. For the parameter *C*, there exists a discrepancy for InP's *C* parameter (about 25% smaller compared to

[63]). $C = 3.05\times10^{12}$ is used in part of our calculation instead of 4.40×10^{12} used in the reference paper. The discrepancy manifests itself in the calculated $\Delta\alpha$ value which carries a factor of 0.75 compared to the value provided by Bennett. All the other parameters are in good agreement with those reported in [63]. The following figures compare our InP calculation with the reference paper.

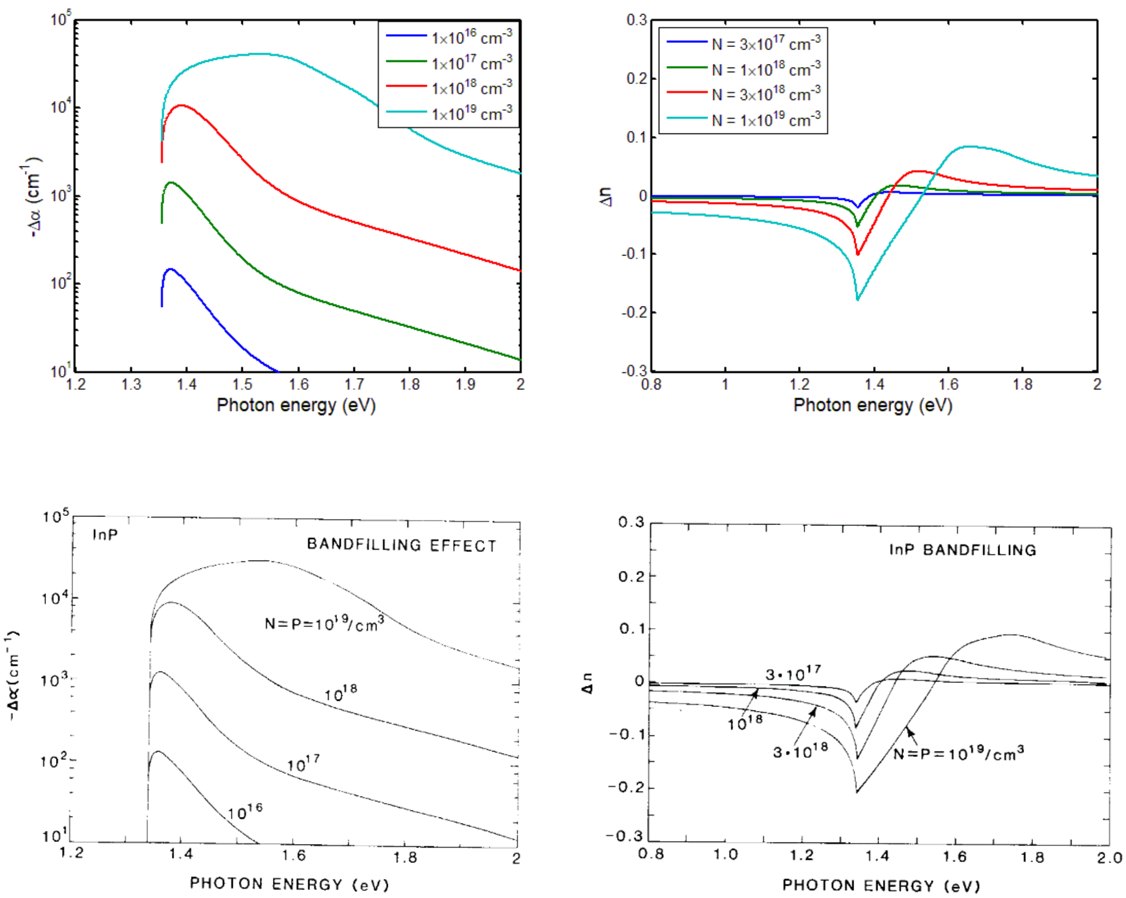

Figure 2.3 (Left panel) comparison of changes in absorption coefficient due to electron-hole injection and the resultant band filling in InP; (right panel) comparison of changes in refractive index due to band filling in InP. Bottom figures are from [63].

As can been seen, the model has been successfully reproduced. It will be later applied to $Al_xGa_{1-x}As$ and $In_xGa_{1-x}As$ to calculate the change in their refractive indices due to the presence of free carriers, *n*-doping and *p*-doping in the materials.

2.2.1.2 Bandgap shrinkage

The basic mechanism is that injected electrons will occupy states at the bottom of the conduction band [63]. If the concentration is large enough, the electron wavefunctions will overlap, forming a gas of interacting particles. The electrons will repel one another by Coulomb forces. In addition, electrons with the same spin will avoid one another for statistical reasons. The net result is a screening of electrons and a decrease in their energies, lowering the energy of the conduction band edge. A similar effect of holes increases the energy of valence band edge. Shrinkage effects are determined by free carrier density, and are independent of impurity concentration.

$$\Delta E_g(\chi) = \frac{\kappa}{\epsilon_s}(1 - \frac{\chi}{\chi_{cr}})^{1/3}, \chi > \chi_{cr}$$

…………………………………….. (Equation 2.12)

$$\Delta E_g(\chi) = 0, \chi < \chi_{cr}$$

…………………………………….. (Equation 2.13)

Where κ is a fitting parameter and χ_{cr} is critical concentration of free carriers. χ_{cr} is about 1.4 times the Mott critical density [67]

$$\chi_{cr} = 1.6 \times 10^{24} (\frac{m_e}{1.4\epsilon_s})^3$$

…………………………………….. (Equation 2.14)

In the above equation, we used m_e instead of m_{hh} or m_{lh} because bandgap shrinkage effects start at a much lower concentration for electrons than holes. The above equation predicts $\chi_{cr} = 7\times10^{16}$ cm^{-3} for *n*-type GaAs, which is in good agreement with 5×10^{16} cm^{-3} [68]. Therefore, this formula is applied to InP and $In_{0.2}Ga_{0.8}As$ without further verification. The values for the fitting parameter κ are 0.11, 0.125, and 0.14 for *p*-GaAs, *n*-GaAs and carrier injected electron-hole plasmas in GaAs. Finally, the band-gap-shrinkage-induced absorption change is

$$\Delta\alpha(\chi, E) = \frac{C}{E}\sqrt{E - E_g - \Delta E_g(\chi)} - \frac{C}{E}\sqrt{E - E_g}$$

………………………………….. (Equation 2.15)

The above equation predicts that Δα will always be positive, largest near the bandgap and rapidly decrease for higher energy. With Δα results, Δn is calculated through Kramers-Kronig theory.

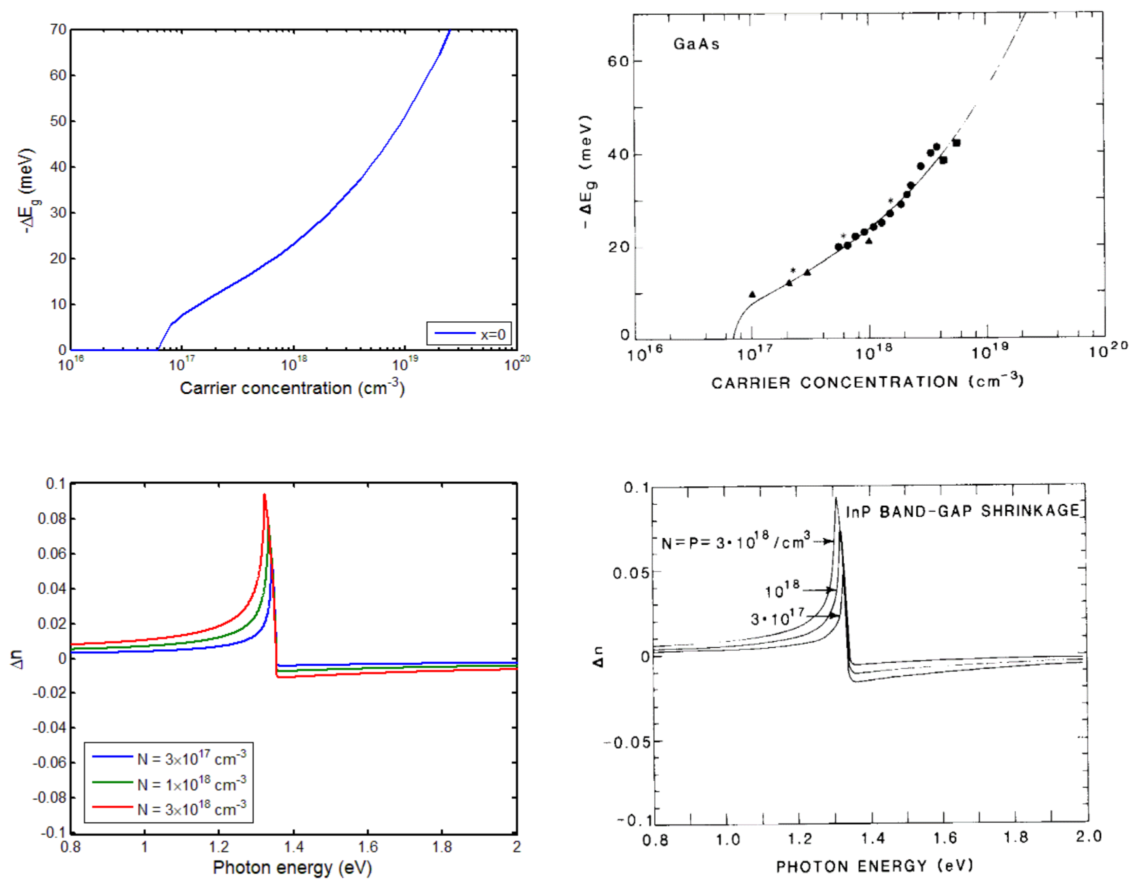

Figure 2.4 (Top) Comparison of bandgap shrinkage effects in GaAs with κ = 0.14 and χ_{cr} = 7×10^{16} in the reproduced model and the data given by [68]; (bottom) comparison of changes in refractive index of InP due to electron-hole injection and the resultant bandgap shrinkage. Right figures are from [63].

The calculated Δn is the same as [63] because $C = 4.40\times10^{12}$ is used. This confirms that the discrepancy in Figure 2.3 indeed results from different input data. However, it was found that the material-specific parameters provided by [66] gave more precise estimate for $Al_xGa_{1-x}As$ and $In_xGa_{1-x}As$. This source is going to be used for $Al_xGa_{1-x}As$ and $In_xGa_{1-x}As$ materials that are relevant to the projects throughout the thesis. In conclusion, the model is successfully reproduced and will be later applied to $Al_xGa_{1-x}As$ and $In_xGa_{1-x}As$.

2.2.1.3 Free-carrier absorption

Thus far, we have considered changes due to the interband absorption due to band filling and bandgap shrinkage. In addition, a free carrier can absorb a photon and move to a higher energy state within a band. In the Drude model, this is intraband free carrier absorption, also known as plasma effect. According to [69], the corresponding change is

$$\Delta n = \frac{-6.9 \times 10^{-22}}{nE^2}\left\{\frac{N}{m_e} + P\left(\frac{m_{hh}^{1/2} + m_{lh}^{1/2}}{m_{hh}^{3/2} + m_{lh}^{3/2}}\right)\right\}$$

…………………………………… (Equation 2.16)

The sign of Δn is always negative, hence it will add to bandfilling for energies below the bandgap. Because the E^2 dependence in the denominator, the plasma effect increases as the photon energy decreases. On the other hand, both the band filling and bandgap shrinkage are the largest around the bandgap.

2.2.1.4 Collective effects

So far, three effects, including band filling, bandgap shrinkage and free-carrier absorption, were assumed to be independent. However, the first two effects actually interplay a lot. Therefore, in calculating the combination of effects, band filling was based on the band gaps that had been obtained by considering bandgap shrinkage. The results agree well with reference [63].

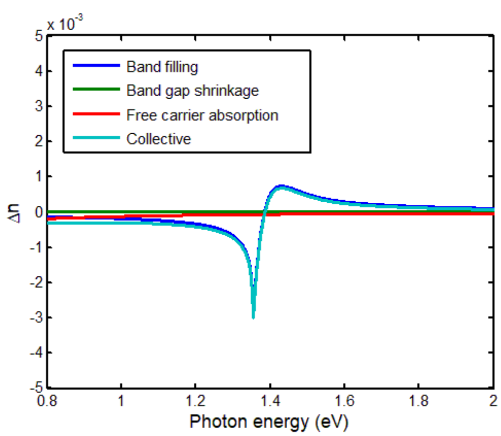

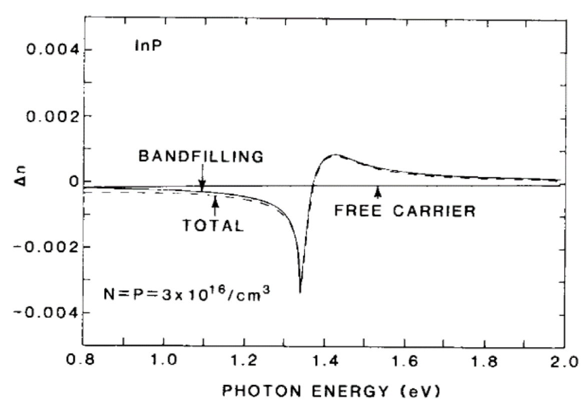

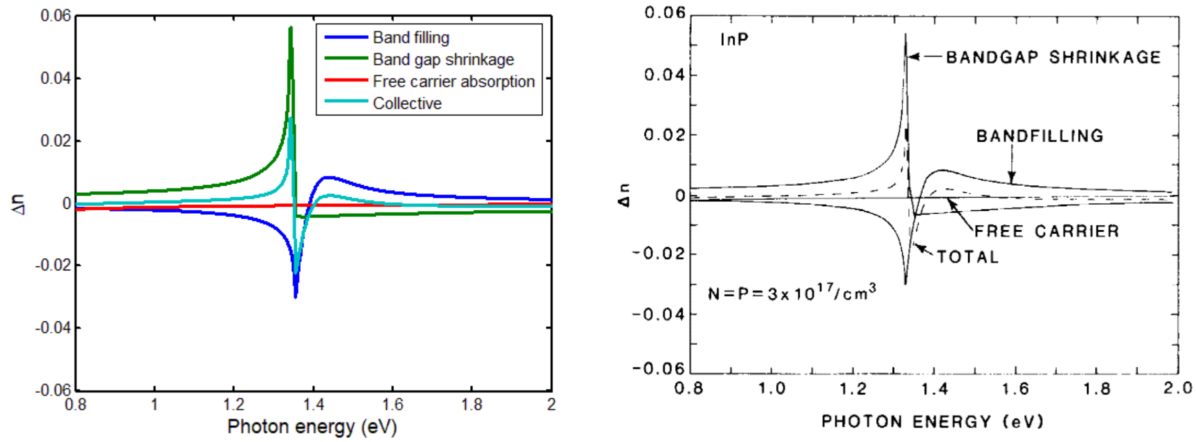

Figure 2.5 Calculated changes of refractive index from band filling, bandgap shrinkage and free-carrier absorption for different carrier concentrations. (Top) N = P = 3×10^{16} cm^{-3}; (bottom) N = P = 3×10^{17} cm^{-3}. Right figures are from [63].

In Figure 2.5 (top), the concentration is lower than the critical carrier density. Therefore, the bandgap shrinkage effect is zero throughout the photon energy range. The dominant effect is band filling effect. In Figure 2.5 (bottom) where the carrier density is larger than χ_{cr}, the bandgap shrinkage effect comes into play and dominates over the other two effects. Near the bandgap, the total index change can be as high as 0.02.

2.2.2 Application of the models

In the last section, we focus on carrier injection effects where charge neutrality is assumed, indicating N = P. If we are going to look at doping induced effects, we are going to use N only, i.e. N = 1×10^{18} cm^{-3}, and leave P at unintentional doping level, which is usually at 5×10^{15} cm^{-3}. The opposite holds for *p*-type semiconductors, i.e. P = 3×10^{18} cm^{-3} and N = 1×10^{15} cm^{-3}.

We use $Al_{0.2}Ga_{0.8}As$ for *n*-contact layer and GaAs and $In_{0.2}Ga_{0.8}As$ for MQW layers, we need to know the carrier induced effects in order to calculate the absorption coefficient change (imaginary part) and (real part) refractive index change. Table 2.2 lists material-specific constants that are relevant to the calculation. These material-specific constants are taken from [66].

Table 2.2 Values of semiconductor parameters (T = 300 K).

	$Al_{0.2}Ga_{0.8}As$	GaAs	$In_{0.2}Ga_{0.8}As$
E_g (eV)	1.6734	1.424	0.8137
C ($cm^{-1}s^{-1/2}$)	4.0936×10^{12}	2.4580×10^{12}	1.1350×10^{12}
C_{hh} ($cm^{-1}s^{-1/2}$)	2.7437×10^{12}	1.6317×10^{12}	7.5797×10^{11}
C_{lh} ($cm^{-1}s^{-1/2}$)	1.3499×10^{12}	8.2637×10^{11}	3.7705×10^{11}
ϵ_s	12.332	12.9	13.23
n	3.5117	3.6	3.63
m_e (m_0)	0.0796	0.0630	0.0545
m_{hh} (m_0)	0.5600	0.5100	0.4900
m_{lh} (m_0)	0.0956	0.0820	0.0708
m_{dh} (m_0)	0.5860	0.5317	0.5078
μ_{ehh} (m_0)	0.0697	0.0561	0.0491
μ_{elh} (m_0)	0.0434	0.0356	0.0308
N_C (cm^{-3})	5.6247×10^{17}	3.9604×10^{17}	3.1883×10^{17}
N_V (cm^{-3})	1.1236×10^{19}	9.7100×10^{18}	9.0624×10^{18}
χ_{cr} (cm^{-3})	1.5681×10^{17}	6.7919×10^{16}	4.0780×10^{16}

2.2.2.1 $Al_{0.2}Ga_{0.8}As$ as *n*-contact

We study the change in refractive index at various doping levels for the martial $Al_{0.2}Ga_{0.8}As$. N will be varied and P is kept at unintentional doping level, which is usually at 5×10^{15} cm^{-3}. In order to see the effects that different carrier concentrations have on the material, we choose four different doping levels for *n*-doped $Al_{0.2}Ga_{0.8}As$: N = 1×10^{17} cm^{-3}, 5×10^{17} cm^{-3}, 1×10^{18} cm^{-3}, and

5×10^{18} cm^{-3}. A spectral range between 1.2 eV (1033 nm) and 1.5 eV (827 nm), which is roughly the same as the wavelength range of the projects in this thesis, was considered.

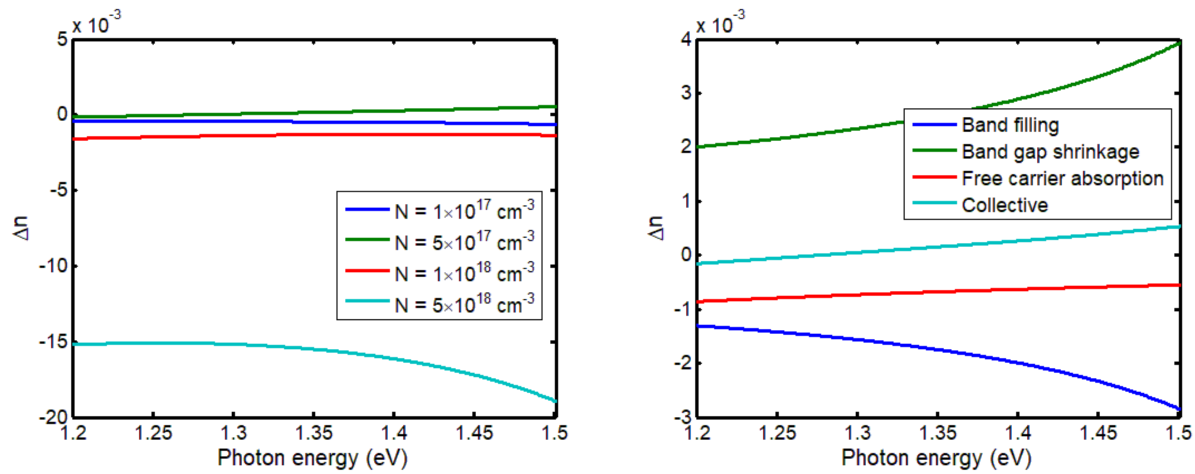

Figure 2.6 (Left chart) Calculated collective change of refractive index of *n*-doped $Al_{0.2}Ga_{0.8}As$ for N = 1×10^{17} cm^{-3}, 5×10^{17} cm^{-3}, 1×10^{18} cm^{-3}, and 5×10^{18} cm^{-3}. (Right chart) Breakdown of the collective effect in to constituent effects at a doping level of 5×10^{17} cm^{-3}.

As can be seen from the left chart of Figure 2.6, at doping concentration below N = 5×10^{17} cm^{-3}, the doping induced refractive index change for photon energies between 1.2 eV (1033 nm) and 1.5 eV (827 nm) is negligible. As can been seen from the right chart of Figure 2.6, overall, the change in refractive index resultant from any of the three constituent effects at a doping level of N = 5×10^{17} cm^{-3} is smaller than 4×10^{-3}. The collective effect is small enough to be ignored. In Chapter 7 when we design waveguide photodiode (WGPD), we choose a doping level of N = 5×10^{17} cm^{-3} for the $Al_{0.2}Ga_{0.8}As$ *n*-contact. The change in the imaginary part of the refractive index is irrelevant because the spectral range of between 1.2 eV (1033 nm) and 1.5 eV (827 nm) is never above the band gap energy of $Al_{0.2}Ga_{0.8}As$.

2.2.2.2 GaAs in the absorption region

Assuming charge neutrality in the active region, we have N = P, which has been assumed when reproducing the model for InP. Again, in order to see the effects that different carrier concentrations have on the material, we choose four different doping levels for *n*-doped GaAs: N = 1×10^{17} cm^{-3}, 5×10^{17} cm^{-3}, 1×10^{18} cm^{-3}, and 5×10^{18} cm^{-3}. A spectral range between 1.2 eV (1033 nm) and 1.5 eV (827 nm), which is relevant to the projects in this thesis, was considered.

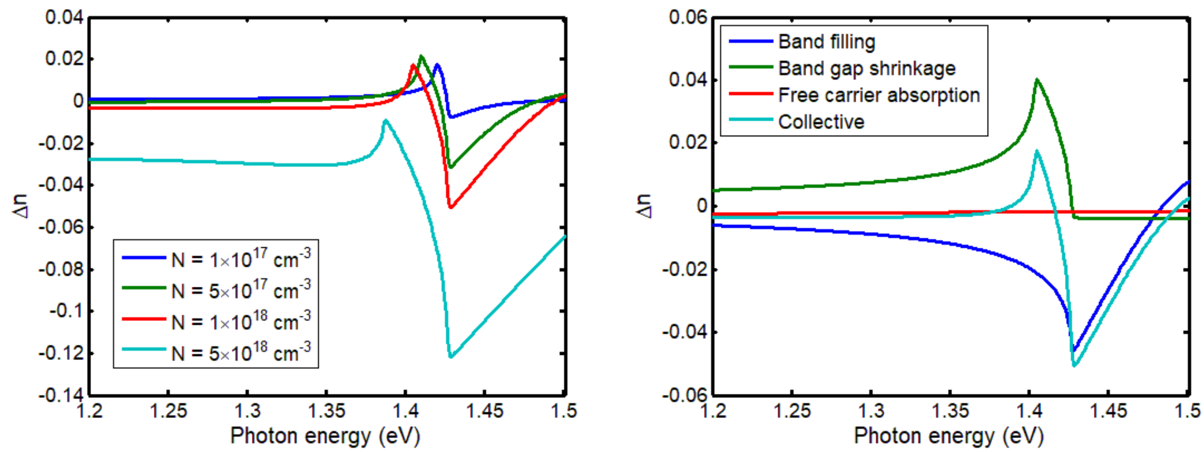

Figure 2.7 (Left chart) Calculated collective change of refractive index of GaAs for N = P = 1×10^{17} cm^{-3}, 5×10^{17} cm^{-3}, 1×10^{18} cm^{-3}, and 5×10^{18} cm^{-3}. (Right chart) Breakdown of the collective effect in to constituent effects at a carrier concentration of 1×10^{18} cm^{-3}.

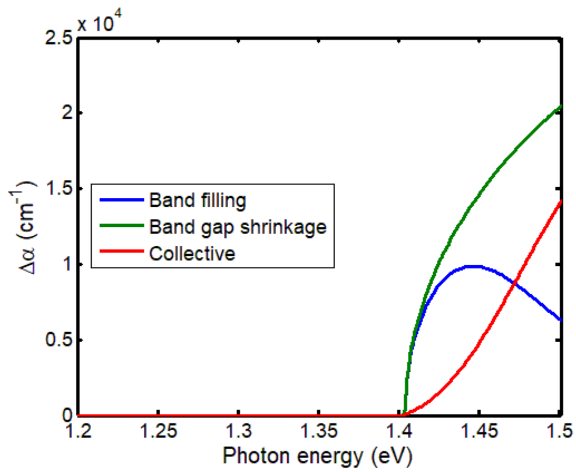

Figure 2.8 Breakdown of the collective change of absorption coefficient of GaAs in to constituent effects at a carrier concentration 1×10^{18} cm^{-3}. The sign of the Δα due to band filling has been flipped for a better appearance of the plot.

2.2.2.3 $In_{0.2}Ga_{0.8}As$ in the absorption region

Simulation the change of refractive index of $In_{0.2}Ga_{0.8}As$ is similarly done. Because the thickness of the $In_{0.2}Ga_{0.8}As$ used as the well material in multiple-quantum-well (MQW) structure is only, the change in the refractive index would have limited effects. In addition, the calculation of the change in the absorption coefficient is more relevant for bulk materials than for quantum well structures.

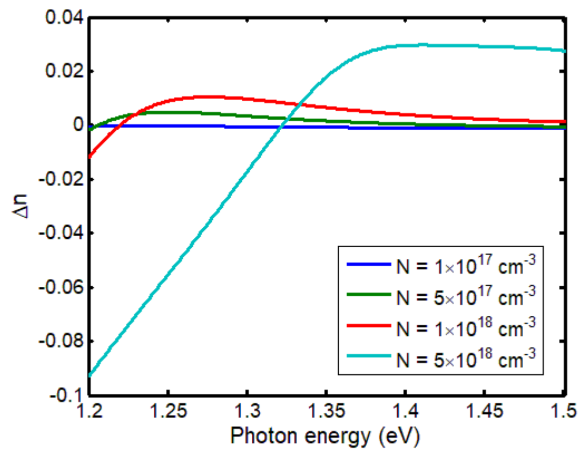

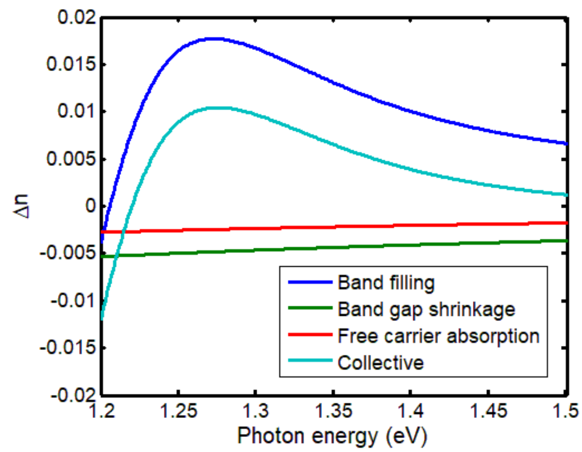

Figure 2.9 (Left chart) Calculated collective change of refractive index of $In_{0.2}Ga_{0.8}As$ for N = P = 1×10^{17} cm^{-3}, 5×10^{17} cm^{-3}, 1×10^{18} cm^{-3}, and 5×10^{18} cm^{-3}. (Right chart) Breakdown of the collective effect in to constituent effects at a carrier concentration of 1×10^{18} cm^{-3}.

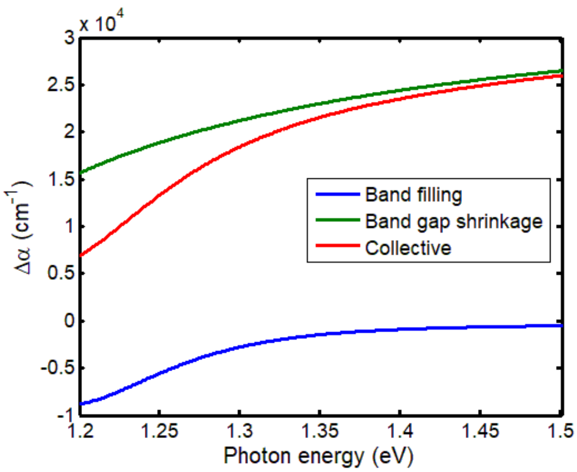

Figure 2.10 Breakdown of the collective change of absorption coefficient of GaAs in to constituent effects at a carrier concentration 1×10^{18} cm^{-3}.

2.2.2.4 $Al_{0.3}Ga_{0.7}As$ and GaAs as *p*-contact

We study the change in refractive index at various doping levels for the martial $Al_{0.3}Ga_{0.7}As$. P will be varied and N is kept at unintentional doping level, which is usually at 5×10^{15} cm^{-3}. In order to see the effects that different carrier concentrations have on the material, we choose four different doping levels for *p*-doped $Al_{0.3}Ga_{0.7}As$: N = 1×10^{17} cm^{-3}, 5×10^{17} cm^{-3}, 1×10^{18} cm^{-3}, and 5×10^{18} cm^{-3}.

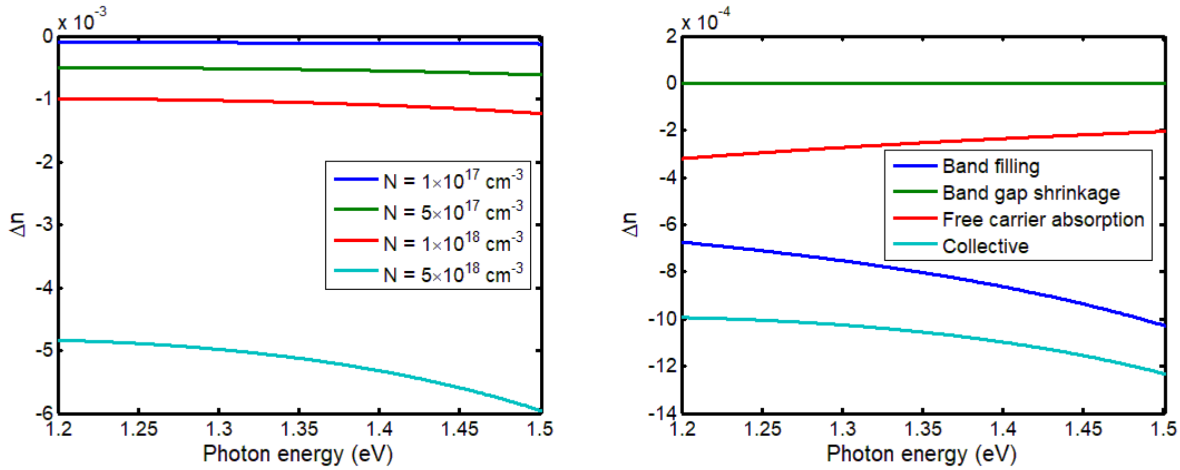

Figure 2.11 (Left chart) Calculated collective change of refractive index of *p*-doped $Al_{0.3}Ga_{0.7}As$ for P = $1{\times}10^{17}$ cm^{-3}, $5{\times}10^{17}$ cm^{-3}, $1{\times}10^{18}$ cm^{-3}, and $5{\times}10^{18}$ cm^{-3}. (Right chart) Breakdown of the collective effect in to constituent effects at a doping level of $1{\times}10^{18}$ cm^{-3}.

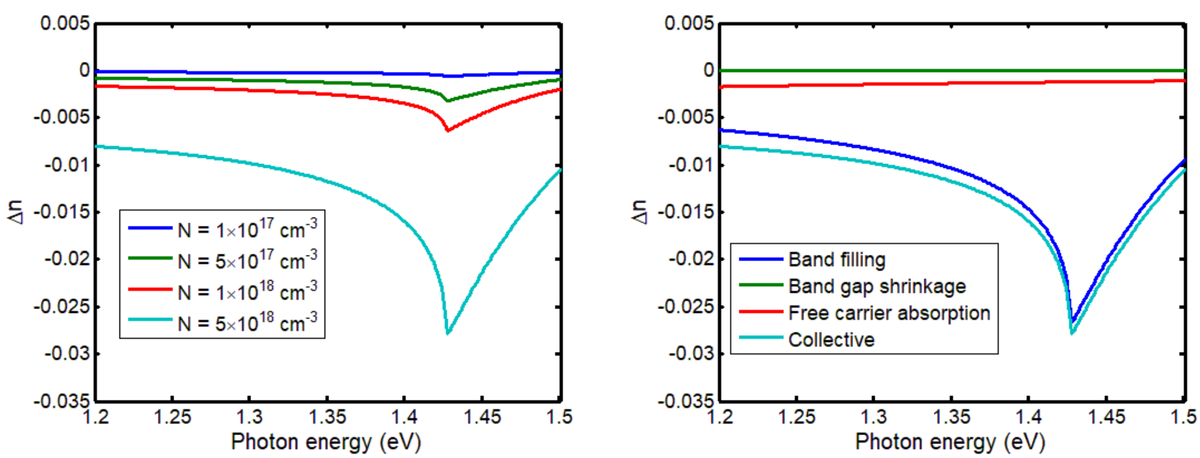

Figure 2.12 (Left chart) Calculated collective change of refractive index of *p*-doped GaAs for P = $1{\times}10^{17}$ cm^{-3}, $5{\times}10^{17}$ cm^{-3}, $1{\times}10^{18}$ cm^{-3}, and $5{\times}10^{18}$ cm^{-3}. (Right chart) Breakdown of the collective effect in to constituent effects at a doping level of $5{\times}10^{18}$ cm^{-3}.

As can be seen from the left chart of Figure 2.11, at doping concentration below P = $1{\times}10^{18}$ cm^{-3}, the doping induced refractive index change for photon energies between 1.2 eV (1033 nm) and 1.5 eV (827 nm) is negligible. As can been seen from the right chart of Figure 2.11, overall, the change in refractive index resultant from any of the three constituent effects at a doping level of P = $1{\times}10^{18}$ cm^{-3} is smaller than $1{\times}10^{-3}$. The collective effect is small enough to be ignored. In Chapter 7 when we design waveguide photodiodes (WGPDs), we choose a doping level of P =

1×10^{18} cm^{-3} for the $Al_{0.3}Ga_{0.7}As$ *p*-contact. The change in the imaginary part of the refractive index is irrelevant because the spectral range of between 1.2 eV (1033 nm) and 1.5 eV (827 nm) is never above the band gap energy of $Al_{0.3}Ga_{0.7}As$.

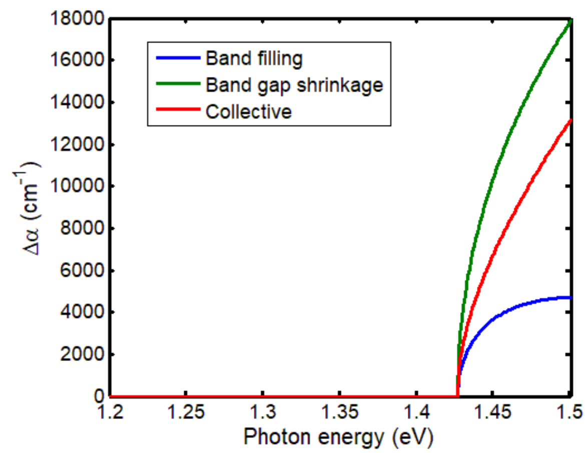

Figure 2.13 Breakdown of the collective change of absorption coefficient of p-doped GaAs in to constituent effects at a doping level of 5×10^{18} cm^{-3}. The sign of the $\Delta\alpha$ due to band filling has been flipped for a better appearance of the plot.

2.3 $Al_xGa_{1-x}As$ wafers

The $Al_xGa_{1-x}As$ wafers used in the projects described in this dissertation were grown using metal-organic chemical vapor deposition (MOCVD).

2.3.1 Two-guide-layer $Al_xGa_{1-x}As$ chip

The two-guide-layer $Al_xGa_{1-x}As$ chip was used for the development of wet chemical etch recipes (Chapter 3), the development of inductively coupled plasma reactive ion etching (ICP-RIE) dry etch recipes (Chapter 4), the design and fabrication of a spot-size converter (Chapter 5) and the design and fabrication of an arrayed waveguide grating (AWG) (Chapter 6).

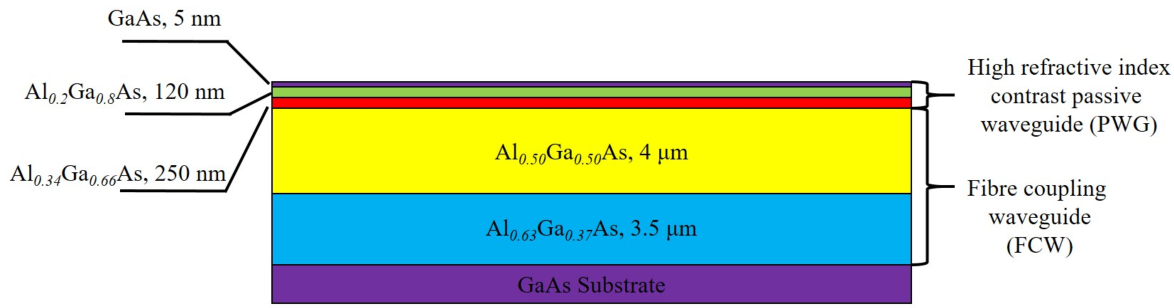

Figure 2.14 Wafer description of the two-guide-layer $Al_xGa_{1-x}As$ chip. The intended functionality is shown along with the material composition and thickness of each layer.

The wafer used in the experiments consists of five layers of $Al_xGa_{1-x}As$ with different aluminum concentrations and is shown in Figure 2.14. They are 5 nm of GaAs, 120 nm of $Al_{0.2}Ga_{0.8}As$, 250 nm of $Al_{0.34}Ga_{0.66}As$, 4 µm of $Al_{0.5}Ga_{0.5}As$, and 3.5 µm of $Al_{0.63}Ga_{0.37}As$ from top to bottom and are grown on an n-type (100) GaAs substrate. The first three layers on the top are suitable for implementing high refractive index contrast waveguides for on-chip signal processing. The two bottom layers were designed as a large-dimension waveguide for efficient end-fire coupling to single-mode fibers.

2.3.2 Three-guide-layer $Al_xGa_{1-x}As$ chip

The three-guide-layer $Al_xGa_{1-x}As$ chips consist of sixteen epitaxial layers, which are shown in Figure 2.15. Starting from the *n*-type GaAs substrate, the four bottom layers are for implementing fiber coupling waveguide with large cross-sectional waveguide dimension to facilitate end-fire coupling to single mode fibers. The next three layers are suitable for implementing high refractive index contrast waveguides for on-chip signal processing. The nine layers on the top are used for designing waveguide photodiodes. A compressively strained layer of 10 nm $In_{0.2}Ga_{0.8}As$ layer is used as the well material for the quantum well based waveguide photodiode. The doping profile in the waveguide photodiode (WGPD) layers is as follows. The *n*-contact layer, $Al_{0.2}Ga_{0.8}As$, is silicon *n*-doped to 5×10^{17} cm^{-3}. The absorption layers, which include the 20 nm $Al_{0.2}Ga_{0.8}As$ to GaAs grading layer, 40 nm GaAs, 10 nm $In_{0.2}Ga_{0.8}As$ well layer and 340 nm GaAs are undoped. The 25 nm GaAs to $Al_{0.3}Ga_{0.7}As$ grading layer, 500 nm $Al_{0.3}Ga_{0.7}As$ upper cladding layer and 25 nm $Al_{0.3}Ga_{0.7}As$ to GaAs grading layer are carbon *p*-doped to 1×10^{18} cm^{-3}. The 100 nm GaAs *p*-contact layer is carbon *p*-doped to 5×10^{18} cm^{-3}.

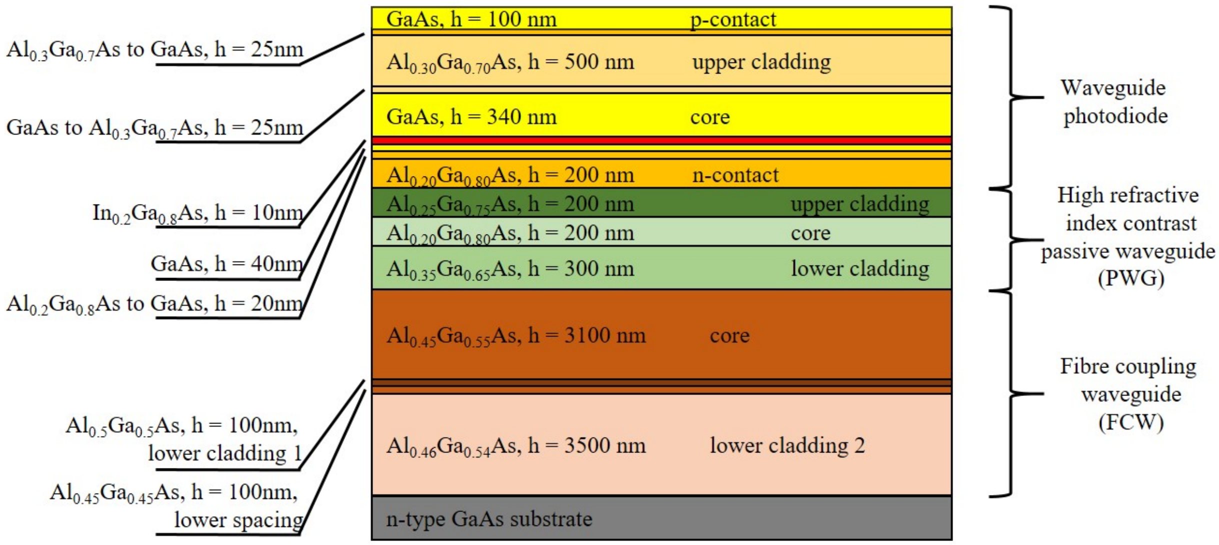

Figure 2.15 Wafer description of the three-guide-layer $Al_xGa_{1-x}As$ chip. The intended functionality is also shown along with the material composition and thickness of each layer.

2.4 Conclusion

In this chapter, the refractive indices of $Al_xGa_{1-x}As$ materials were studied. Using Gehrsitz's model, we calculated the refractive index of the $Al_xGa_{1-x}As$ materials for photon energies below the band gap energy. Using Deri's model, we calculated the refractive index of the GaAs material for photon energies below and around the band gap energy. The change of the refractive index of $Al_xGa_{1-x}As$ and $In_xGa_{1-x}As$ was also studied. These models were utilized in the design of the two wafer structures used in this thesis. The details of the design methodology will be outlined in Chapters 5 and 7.

Chapter 3
Wet etch techniques for AlGaAs devices

3 Wet etch techniques for AlGaAs devices

This chapter discusses wet chemical etch techniques for fabricating waveguide structures in $Al_xGa_{1-x}As$ semiconductors. We analyze wet etching techniques using our first wafer, a two-guide-layer wafer, and demonstrate successful sacrificial etching of $Al_xGa_{1-x}As$ layers with a low aluminum content on $Al_xGa_{1-x}As$ layers with a high aluminum content. Selectivity of 15:1 and 40:1 for citric acid, or succinic acid wet etchants have been obtained. These wet etchants provide a means of achieving precise etch depths. In addition, this chapter demonstrates sacrificial etching $Al_{0.7}Ga_{0.3}As$ layers against $Al_xGa_{1-x}As$ layers with $x < 0.5$ on a different wafer structure in HF solutions, and fabricate suspended waveguides for potential monolithic and vertical integration of nonlinear optical components

3.1 Wet chemical etch techniques

Since many III–V devices require the exposure of buried layers for metal contact formation and/or the formation of mesa structures for electrical isolation from adjacent devices on the same wafer, etching will always be a critical fabrication step. “Wet” (liquid-phase) etches are the simplest to implement since they require only simple benchtop glassware (or plasticware if HF is involved). The key issues to be considered in selecting a particular etch process for any application are rate, uniformity, selectivity, critical dimension control, feature profile and surface damage that can degrade electronic properties and, therefore, device performance.

The most favorable characteristic of wet etches is their ability to cause virtually no surface electronic damage [70, 71]. The least desirable wet etch characteristic for many applications is the unavoidable tendency to undercut etch masks. This is observed whether there are nearly equal vertical and lateral etch rates (isotropic etching) or etch rates that depend on the specific exposed crystal planes of the semiconductor (crystallographic etching). Precise control of critical dimensions is made more difficult by the frequently strong dependence of wet etch rates on temperature, solution agitation and crystallographic alignment of the mask.

3.2 Surface cleaning

The surface cleaning of GaAs and other semiconductors involves two different aspects. The first is the removal of contaminants, such as organic compounds and metal ions. The second is the removal of the native oxide to expose the bare semiconductor for subsequent processing such as metal contact deposition. The existence of native oxide is detrimental to the fabrication of $Al_xGa_{1-x}As$ devices as it is subject to a very different etching process compared to $Al_xGa_{1-x}As$ epitaxial layers.

3.2.1 Regular organic contaminants

When the surface is not heavily contaminated by organics, a 10-min boil in acetone, a 5-min boil in methanol and a DI water rinse can be sufficient. Sonication using ultrasound can also be used as an alternative to enhance cleaning efficiency. In this thesis, acetone, IPA and DI water are used in combination of heating and sonication when necessary to remove regular organic contaminants.

3.2.2 Metal ion contaminants

For removal of metal ion contaminants, rinsing with chemicals that can form complexes with a wide variety of metal ions can be quite effective. Ammonium hydroxide solutions are an excellent choice for this. NH_4OH is formed by dissolving NH_3 in water: $NH_3+H_2O \leftrightarrow NH_4OH$. The ammonium ion is in equilibrium with ammonia (NH_3) in solution and ammonia is known to form soluble metal complexes, $M(NH_3)_{y+x}$, with many transition metals. This is highly desirable since transition metals can degrade electronic properties.

3.2.3 Native oxides

Two additional advantages of NH_4OH solutions are their ability to remove the native oxide of GaAs and their saponification capability. $Al_xGa_{1-x}As$ oxidizes when it is exposed to air. The rate at which it oxidizes increases as the aluminum content in $Al_xGa_{1-x}As$ increases. Manual handling of wafers brings possible contact with fats. Saponification is the process of hydrolyzing a fat (a fatty acid ester) with OH^- to form glycerol and a fatty acid salt (soap), both of which are highly soluble. In this thesis, one part of 30% NH_4OH is mixed with ten parts of DI water to clean metal ion contaminants, native oxides and fats. Heating and sonication are used depending on the surface conditions of samples.

3.3 Basics of wet etch

3.3.1 Profiles and rates

Three aspects are important: etch profile, etch rate and surface roughness. The most important consideration in selecting a wet etch recipe is the profile of the etched features. This is primarily controlled by whether the etch process is reaction-rate limited, or diffusion controlled. Assuming an adequate supply of oxidizer, whether the rate of the dissolution process will be limited by the supply of acid, or base (diffusion controlled) or by the activation energy of the dissolution reaction (reaction-rate limited) will be determined by the relative magnitudes of their respective terms. Any reaction has the potential to be either reaction-rate limited or diffusion controlled. It is merely a question of which effect dominates. If an activation energy for an etch process is less than 5 kcal/mol, it will probably be diffusion controlled, while a value greater than 10 kcal/mol probably means reaction-rate control.

Etch rate is another very important parameter. Excessively fast rates will cause poor surface quality. Therefore, the supply of acid or base etchants needs to be carefully controlled. Dissolution of the oxide is controlled by solution pH. H_2O_2 is generally used as an oxidizer. Oxidation rate is generally controlled by the strength of the oxidizer so increasing the H_2O_2 fraction increases the etch rate. However, surfaces tend to roughen with etchants that contain >15% H_2O_2 or with pH values equals 7.5 or higher. At higher pHs, there is less efficient oxide removal so the thickening oxide can crack and float away in small segments, this exposes the underlying surface for further oxidation. This cracking and flaking is inherently a non-uniform process and results in surface roughness. Therefore, the supply of oxidizer needs to be carefully controlled.

3.3.2 Diffusion controlled etch process

An etch process that is diffusion controlled is highly sensitive to the degree of agitation so controlled stirring or rotation is important to achieve consistent and predictable results. Slow rotation (<100 rpm) permits very uniform thinning of a wafer. Fast rotation in a centrifuge can decrease lateral undercutting. In practical terms, “rotation” often consists of manually swirling the sample holder in solution, which may not be very reproducible. Stirring at a reproducible rate with a magnetic stirrer or an over-head propeller design can produce more predictable results.

The classic profile of a diffusion-controlled reaction is shown in Figure 3.1 (left). Lateral undercut proceeds at a rate comparable to the vertical etch rate in the field region away from the mask. However, a shallow trench or downward bulge forms near the edge of the mask and slopes back away from the edge. As the etch proceeds in time, the mask-edge region appears more and more like the field region more remote from the mask edge and the downward bulge becomes less prominent with time Figure 3.1 (right).

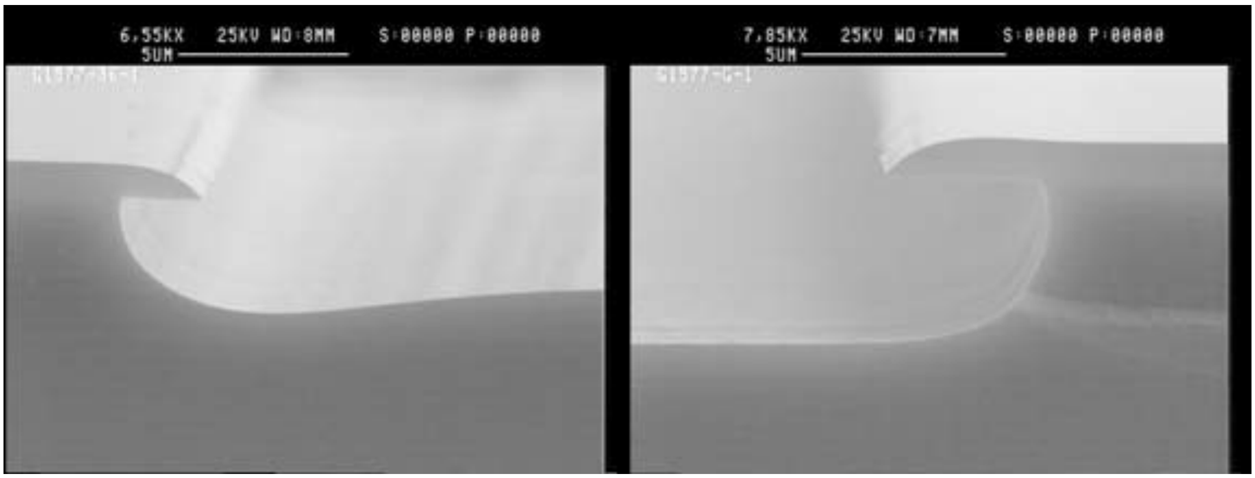

Figure 3.1 Diffusion-controlled etch profiles: (left) classic profile; (right) profile with flatter bulge. Figures are from [72].

3.3.3 Reaction-rate limited etch process

An etch process that is reaction-rate limited displays a pronounced dependence on temperature and are relatively insensitive to agitation. One important feature of reaction-rate limited etch process is differences in the etch rates of different crystal faces, which have different activation energies for their oxidation. $Al_xGa_{1-x}As$ has a cubic zinc sulphide or zinc blende structure, with two interpenetrating face-centered cubic (fcc) lattices. A wide range of profiles are possible [73].

3.4 Acidic selective wet etch

GaAs is not soluble in non-oxidizing acids from pH 1 to 7, so an oxidizer such as H_2O_2 is combined with the acid to produce an effective etchant. Examples of non-oxidizing acids include HCl, H_2SO_4, H_3PO_4 and organic acids such as citric and succinic acids. The listed ratios in Table 3.1 are volume ratios and refer to volumes of concentrated acids and bases as purchased (i.e.

undiluted), 30% H_2O_2, 50% by weight citric acid in water or 20% by weight succinic acid in water. When specific pHs are listed, NH_4OH is generally used to adjust the pH.

The primary determining factors of selectivity include the relative amounts of oxidant and acid, the degree of dilution at a fixed acid/oxidant ratio and the pH. Often the rates for both materials may increase as a process parameter is adjusted, but one will increase much faster.

In many inorganic acid/H_2O_2 solutions where the anion doesn't preferentially form complexes with Ga or Al, rates for AlGaAs are somewhat faster than for GaAs, with the rates increasing roughly linearly with Al mole fraction. For example, at pH 1 GaAs may etch at 0.3 µm/min while $Al_{0.5}Ga_{0.5}As$ etches at 0.65 µm/min. This difference may be enough to give isotropic profiles for AlGaAs under conditions that produce crystallographic etching of GaAs.

The citric/ H_2O_2 etchants start with a stock citric acid solution that is composed of 1 g of citric acid in 1 ml DI water. This should be mixed at least one day early to insure all the citric acid dissolves since the dissolution is an endothermic reaction and the solution cools noticeably as the citric acid dissolves. The desired volume ratio of this solution is mixed with 30% H_2O_2 at least 15 min before etching to allow the solution to return to room temperature before use (this combination heats upon mixing). For citric/H_2O_2 ratios greater than 1, the rate is reaction-rate limited and crystallographic etching occurs. At lower citric/peroxide ratios, bubble formation on the surface can be a problem [74-76].

If one plans to use compositional selectivity for etch-stop purposes, the greater retardation that can be obtained by relatively small changes in Al content can increase the process window in terms of the overetch time for etching the entire wafer to a uniform depth. While overetching in solution, it is always important to remember that lateral etching is proceeding at a rate comparable to vertical etching, so significant differences in device dimension can occur for different overetch times.

Table 3.1 summarizes relevant literature papers on selective wet etch recipes of $Al_xGa_{1-x}As$/GaAs. Some comments that are relevant to the fabrication requirements of $Al_xGa_{1-x}As$ devices are added for each recipe.

Table 3.1 Acid wet etch.

Etchants	Etch rate (µm/min)	T (°C)	Comments
Citric acid/H_2O_2 [77]	0.6	24	no mask attack
10 citric acid/1 H_2O_2 [74]	2	18	Etch rate 95:1 GaAs:$Al_{0.3}Ga_{0.7}As$
Citric acid/H_2O_2 [76]	0.15–0.4	27–100	Etch rate > 80:1 GaAs:$Al_{0.28}Ga_{0.72}As$
4 citric acid/1 H_2O_2 [70]	0.36	20	Etch rate > 155:1 GaAs:$Al_xGa_{1-x}As$
Citric acid/H_2O_2 [75]	0.006–0.040	r.t.	116:1 GaAs:$Al_{0.3}Ga_{0.7}As$
4 citric/1H_2O_2/1 H_2O [76]	0.35	0–27	1:1 GaAs:$Al_{0.28}Ga_{0.72}As$
15 succinic/1 H_2O_2 [78, 79]	0.15	r.t.	$Al_xGa_{1-x}As$ as f(succinic:H_2O_2, x, pH, T)
HCl/4 H_2O_2/40 H_2O [80]	0.22	r.t.	Isotropic
HF [81]	0.1	80	< 1:10 GaAs:$Al_xGa_{1-x}As$ for $x \geq 0.4$

Pre-cleaning in 10:1–20:1 H_2O/NH_4OH improves etching reproducibility. Ratios are volume ratios using concentrated acid sources unless otherwise indicated. Citric = 1 g citric acid/1 g H_2O (50 wt% solution); H_2O_2 = 30 wt% solution; Succinic = 1 g succinic acid/5 g H_2O; H_2O_2 = 30 wt% solution; NH_4OH adjusts pH; r.t. = room temperature, i.e. from 19–25 °C.

3.4.1 Etching of GaAs against $Al_{0.2}Ga_{0.8}As$

According to [82], etching experiments were performed in a 500-ml glass beaker at room temperature using citric acid-based etchants. First, anhydrous citric acid crystals were dissolved in H_2O. Second, a pH of the citric acid solution was adjusted by the addition of NH_4OH. The pH was controlled precisely within a range of ± 0.05. Finally, this mixture was mixed with H_2O_2 at a given volume ratio. The amount of material removed during etching was determined by masking a portion of the substrate surface with resist from etchants and measuring the resultant step height. The sample was etched for a set time with no stirring. Etching was stopped by rinsing in H_2O for approximately 1 min. The photoresist mask was then removed in acetone and blown dry with N_2. The height of the etched step was measured using a profilometer that has a minimum resolution of 1 nm.

No measurable etching was detected for NH_4OH/H_2O_2 at pH of 6.5. The etch rate of GaAs and $Al_{0.15}Ga_{0.85}As$ as a function of the concentration of citric acid for the citric acid-based etchants with citric acid/H_2O_2 ratio of 100 and pH of 6.5 is shown in Figure 3.2 on the left. The selectivities of GaAs/$Al_{0.15}Ga_{0.85}As$ and GaAs/$Al_{0.3}Ga_{0.7}As$ are shown in Figure 3.2 on the right. The selectivity decreases with the increasing citric acid/H_2O_2 ratio. For a 1 wt% citric acid/H_2O_2 solution, the selectivities of GaAs/$Al_{0.15}Ga_{0.85}As$ and GaAs/$Al_{0.3}Ga_{0.7}As$ are over 80 and 120, respectively.

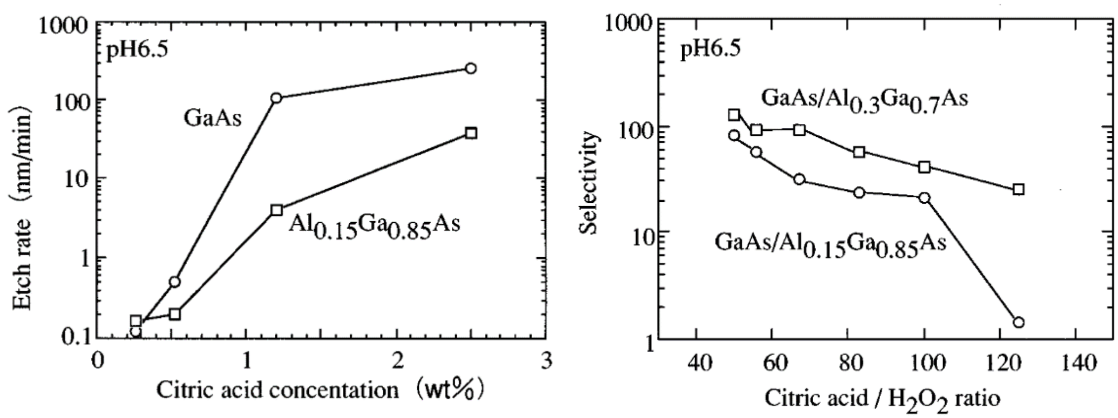

Figure 3.2 (Left) GaAs and $Al_{0.15}Ga_{0.85}As$ etch rate as a function of citric acid concentration using a solution with citric acid/H_2O_2 of 100 and a pH of 6.5. (Right) Etch selectivity of GaAs/$Al_{0.15}Ga_{0.85}As$ and GaAs/$Al_{0.3}Ga_{0.7}As$ etch rate as a function of citric acid/H_2O_2 ratio at a pH of 6.5. Figures are from [82].

Based on the discussion, 1 wt% citric acid/H_2O_2 solution at a ratio of 50:1 can achieve etching of GaAs/$Al_{0.2}Ga_{0.8}As$ with a selectivity of 100. However, the GaAs layer in the two-guide-layer $Al_xGa_{1-x}As$ chips is only 5 nm, which is for preventing the wafer from oxidizing. With such a thin thickness, there is no need to selectively etch GaAs with respect to $Al_{0.2}Ga_{0.8}As$. The 5 nm GaAs layer can be etched along with $Al_{0.2}Ga_{0.8}As$ to simplify the fabrication process.

3.4.2 Etching of $Al_{0.2}Ga_{0.8}As$ against $Al_{0.34}Ga_{0.66}As$

According to [70], using a 4:1 solution of citric acid/H_2O_2 at 20 °C, selectivities of 155, 260, and 1450 have been obtained for GaAs on $Al_xGa_{1-x}As$ with $x = 0.3$, 0.45 and 1.0, respectively. The sample used in [70] were grown by MBE on undoped (100) GaAs substrates. Epitaxial $Al_xGa_{1-x}As$ structures of various mole fractions ($0 < x < 0.45$) consist of a 300 Å undoped GaAs cap layer, a 5000 Å $Al_xGa_{1-x}As$ layer and a 3000 Å GaAs buffer layer. Samples were patterned with AZ5214 photoresist. Citric acid monodydrate was mixed 1:1 with DI water by weight to make citric acid. Citric acid/H_2O_2 solution was prepared by adding 30% H_2O_2 to the citric acid in the desired proportion just before etching.

It is observed that the highest selectivity for the $Al_{0.3}Ga_{0.7}As$ is obtained at a solution ration, r, of between 3 and 4, shown in Figure 3.3 on the left. The etch mechanism of GaAs in citric acid/H_2O_2 was reported to be: with $r < 2$, the etch process is diffusion controlled; with $r > 2$, the etch process is reaction-rate limited. Therefore, for practical applications, it is desirable to use solutions with $r > 2$.

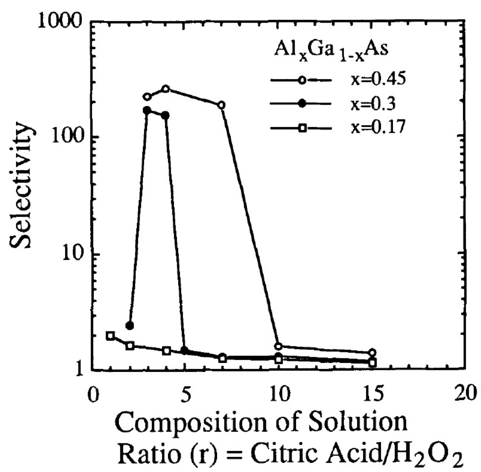

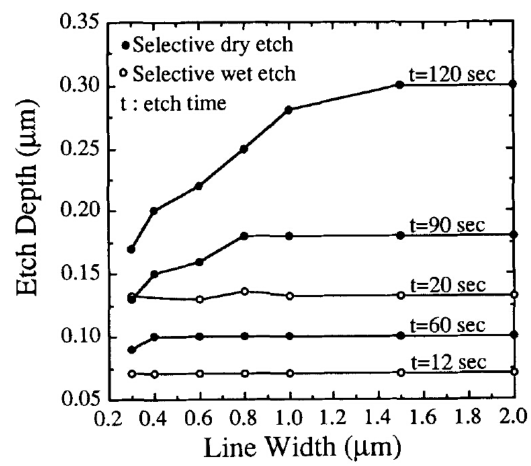

Figure 3.3 (Left) Selectivity as a function of composition of solution. The ratio *r* is of citric acid to H_2O_2. (Right) Etch depth vs line width using 4:1 citric acid/H_2O_2 solution. Figures are from [70].

It was reported that that a remarkable etching uniformity was achieved for different etch depths from 0.07 μm to 0.13 μm and for different electron-beam defined lines widths ranging from 0.3 to 2 μm [70]. Based on the above discussion, citric acid/H_2O_2 solution at a ratio of 4:1 can achieve etching of $Al_{0.2}Ga_{0.8}As$ /$Al_{0.34}Ga_{0.66}As$ with a selectivity of about 15.

3.4.2.1 Experimental results

In this section, an overview of the wet etch developments carried out in this thesis will be given. First, we cleave out a sample with a desirable area from a brand-new wafer. Second, the sample should go through regular organic contaminant cleaning, which includes sonication in acetone for two minutes, sonication in IPA for two minutes and DI water rinse for about one minute. In situations where sonication is inappropriate, i.e. when there are fine nanostructures on the sample already, we can soak the sample in acetone at 50 °C (< 55°C boiling point to avoid hazards) for two minutes and IPA at 60°C (< 83°C boiling point) for two minutes and then rinse the sample in DI water. Organic contaminants can be effectively removed at an elevated temperature in acetone and IPA. Finally, the sample is dried using a nitrogen gun.

The next task is to remove metal ion contaminants and native oxide. First, the sample is soaked in room temperature 30 wt% ammonium hydroxide/DI water at a 1:10 volume ratio for about 30 seconds. Depending on the age of the sample, this time can vary and go up to one minute. An additional advantage of using ammonia is the ability of saponification (ability to hydrolyze fats). Second, the sample is rinsed in DI water for one minute. Finally, the sample is dried using a nitrogen gun. Because native oxides will regrow again right after cleaning, the deposition of photo-resists, or electron beam lithography resists should follow immediately (best within 10 mins if the sample is to go through epitaxial regrowth according to the literature).

After going through cleaning steps, the sample is ready for electron beam lithography (EBL). Negative tone EBL resists ma-N2405 and ma-N2410 are used. So far, the negative tone resist ma-N 2405 is the best choice for EBL. It has the following advantages: 1) high resolution, 2) good thermal stability, 3) high dry/wet etch resistance, 4) easy to remove and 5) insensitive to white light.

Table 3.2 Organic contaminants removal.

Step 1	Sonication or heated soak at 50 °C in acetone for two minutes
Step 2	Sonication or heated soak at 50 °C in IPA for two minutes
Step 3	Rinse in DI water for one minute
Step 4	N_2 dry up

Table 3.3 Metal ion contaminants removal.

Step 1	Soak in RT 30 wt% NH_4OH/DI water at a 1:10 volume ratio for about 30 seconds
Step 3	Rinse in DI water for one minute
Step 4	N_2 dry up

Table 3.4 EBL resist deposition and EBL using ma-N 2405 (ma-N 2410).

Step 1	Spin coating speed 4000 rpm, 60 seconds, acceleration 584 rpm, resulting 500 nm (1200 nm for ma-N 2410) thickness
Step 2	Post deposition bake 90 °C, 2.5 mins (4 mins for ma-N 2410)
Step 3	EBL writing dose 225 $\mu C/cm^2$ (175 $\mu C/cm^2$ for ma-N 2410), 100 kV, current 5 nA
Step 4	Develop in ma–D 525, (10.5 mins for ma-N 2410)
Step 5	DI water rinse, 5 mins
Step 6	N_2 dry up

The developed ma-N2405 photoresist samples are shown in the following figures. The thicknesses of ma-N2405 and ma-N2410 are about 500 nm and 1000 nm, respectively. The waveguide widths are generally slightly smaller than the designed values.

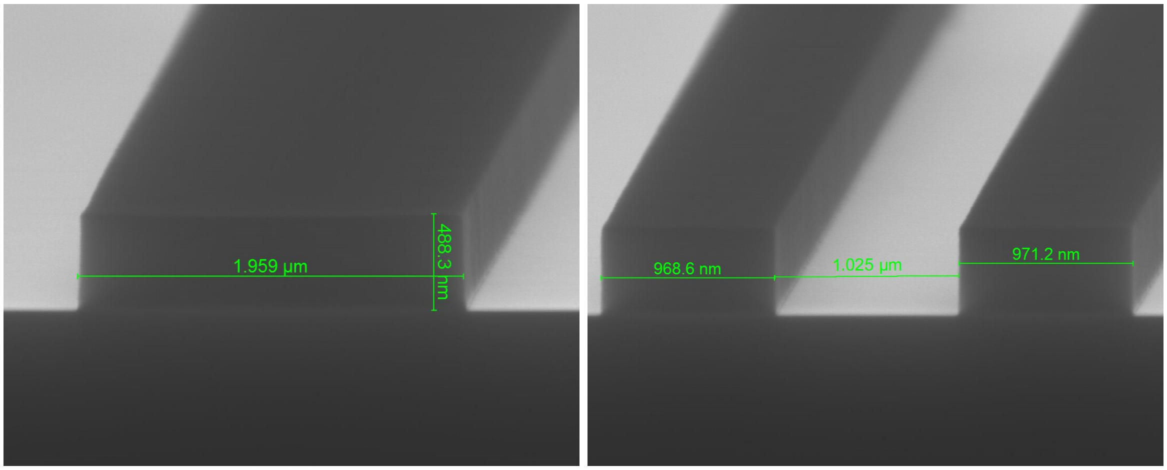

Figure 3.4 Samples of developed photoresist ma-N2405. (Left) waveguide pattern width 2 µm, (right) waveguide pattern width 1 µm.

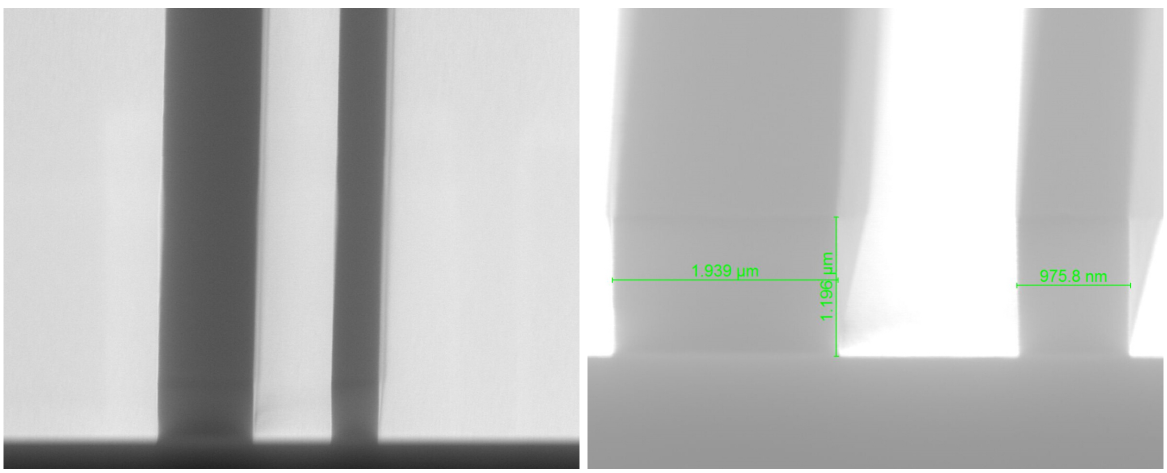

Figure 3.5 Samples of developed photoresist ma-N2410. (Left) waveguide pattern width 2 µm, (right) waveguide pattern width 1 µm.

The sample is ready for wet chemical etch. The mixture is 50 wt% monohydrate citric acid with 30 vl% H_2O_2 mixed at 4:1 volume ratio. The etch protocol is shown in Table 3.5. In Step 2 of Table 3.5, RT 30 wt% NH_4OH/DI water is used to wash away any residual etchant from Step 1.

Table 3.5 Selective etching $Al_{0.2}Ga_{0.8}As$ over $Al_{0.34}Ga_{0.66}As$ in 4:1 citric acid/H_2O_2 solution.

Step 1	50 wt% monohydrate citric acid/30 vl% H_2O_2 at 4:1, for a certain time
Step 2	Soak in RT 30 wt% NH_4OH/DI water at a 1:10 volume ratio for about 30 seconds
Step 5	DI water rinse, for one minute
Step 6	N_2 dry up

Scanning electron microscope images of the etched samples are shown in Figure 3.6. The etch depth of the sample as a function of time is shown in Figure 3.7. The etch rates for GaAs, $Al_{0.20}Ga_{0.80}As$ and $Al_{0.34}Ga_{0.66}As$ are about 360 nm/min, 180 nm/min and 1.8 nm/min [70]. The etch rate for $Al_{0.20}Ga_{0.80}As$ has been confirmed using data shown in Figure 3.7. It should take about 40-41 seconds to etch through the 120 nm $Al_{0.20}Ga_{0.80}As$ layer. The etch rate for $Al_{0.34}Ga_{0.66}As$ has also been confirmed. After the first 40 seconds, which is supposed to be enough to etch through the 120 nm $Al_{0.20}Ga_{0.80}As$, the increase of etch depth was only about 6 nm for another 30 seconds, meaning an etch rate of 12 nm/min. Therefore, the selectivity between $Al_{0.20}Ga_{0.80}As$ and $Al_{0.34}Ga_{0.66}As$ is about 15.

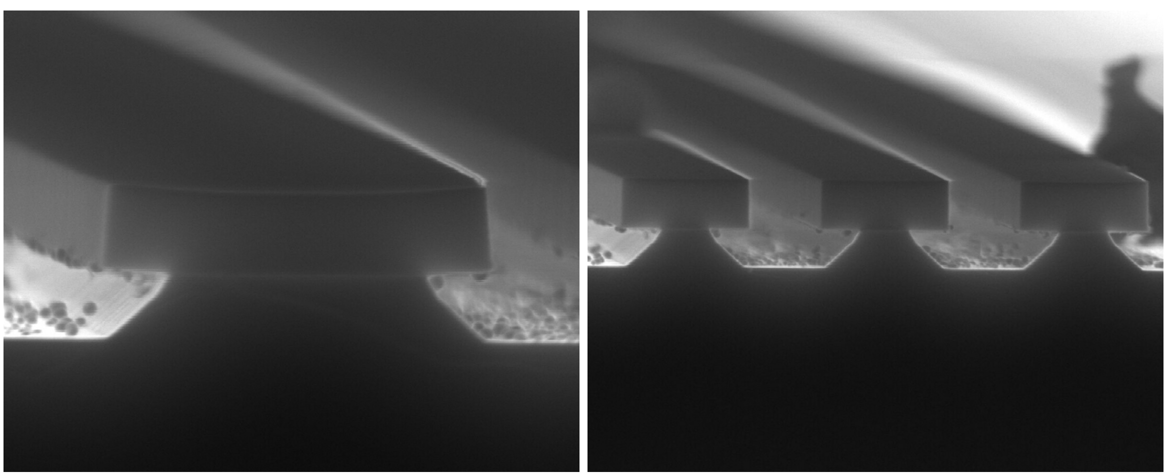

Figure 3.6 Samples etched in citric acid/H_2O_2. Photoresist still remains on the etched nanostructures.

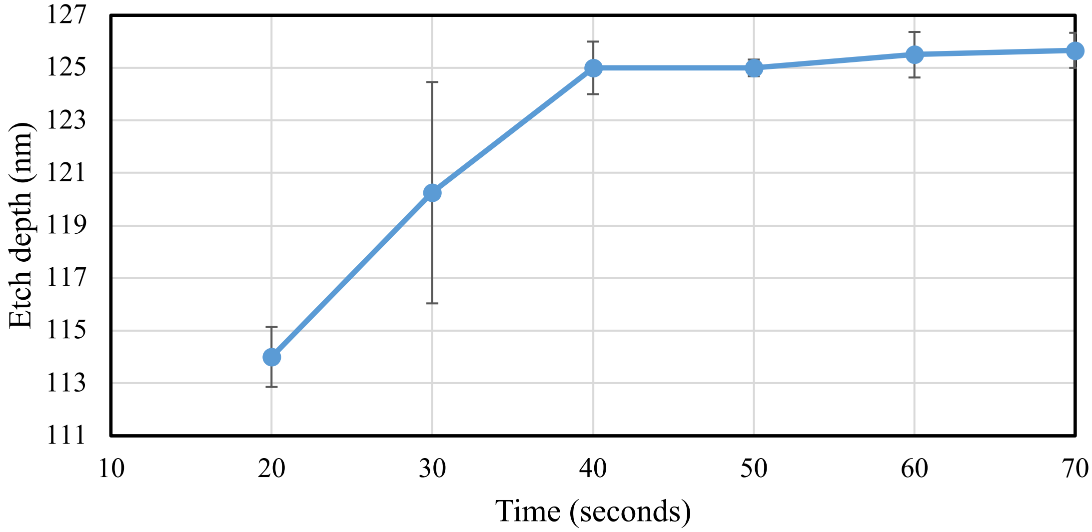

Figure 3.7 Etch depth of the sample as a function of time in citric acid/H_2O_2 solution. Etch depths were measured at multiple points (number of points ≥ 3) of a sample using scanning electron microscope (SEM). Error bars representing one standard error are shown.

3.4.3 Etching of $Al_{0.34}Ga_{0.66}As$ against $Al_{0.5}Ga_{0.5}As$

According to [78], it was found that $Al_xGa_{1-x}As$ ($x < 0.4$) may be selectively etched with respect to $Al_yGa_{1-y}As$ ($y \geq 0.5$), with a selectivity higher than 150. Extended surface exposure to air was found to affect the etch rates, most interestingly for $Al_{0.4}Ga_{0.6}As$. Several $Al_xGa_{1-x}As$ samples were grown in a Varian Gen II molecular beam epitaxy machine and used to determine the etch rates. In all $Al_xGa_{1-x}As$ samples with higher mole fractions ($x > 0.5$), 100 Å GaAs caps were grown to prevent the samples from oxidizing. All etch-rate data were obtained from etching under constant stirring with a magnetic bar. In all cases, the etched surface exhibited featureless morphology. Of course, since the etching solution studied here is primarily intended for selective etching, and etch stop layers naturally provide flat templates. For the $Al_xGa_{1-x}As$ system, an etching solution consisting of 20 g of succinic acid, 100 ml of water, and 6.7 ml of hydrogen peroxide was selected. Enough ammonium hydroxide was then added to raise the pH of the solution to 4.2. Figure 3.8 shows the dependence of the etch rate on the aluminum mole fraction. The etch rate remains fairly constant between mole fractions of 0 and 0.4, and falls more than one hundredfold from $Al_{0.4}Ga_{0.6}As$ to $Al_{0.5}Ga_{0.5}As$. Consequently, $Al_xGa_{1-x}As$ ($x < 0.4$) may be etched over $Al_yGa_{1-y}As$ ($y \geq 0.5$), with a selectivity better than 150. In effect, the succinic acid/hydrogen peroxide system performs a function opposite to that of hydrofluoric acid, which etches higher-mole-fraction $Al_xGa_{1-x}As$ faster. For the higher mole fractions, it was necessary to leave the samples in the etching solution for up to 2 h. Separate experiments were conducted to verify that the lifetime of the solution was more than 2 h. Once the etch rates were determined, a multilayer structure was grown to demonstrate selective etching. A layer of $Al_{0.4}Ga_{0.6}As$ was selectively etched over an $Al_{0.6}Ga_{0.4}As$ etch-stop. The $Al_{0.4}Ga_{0.6}As$ layer used in these experiments was not capped with GaAs, and we found that the etch rate for such uncapped samples depends on the length of exposure to air. As shown in Figure 3.8, the etch rate dropped by a factor of about 75 after exposure to air for one day. Exposure to air for an hour, however, did not affect the etch rate significantly. Presumably, the formation of a thick native oxide layer, coupled with the relative inability of succinic acid to dissolve it, reduces the etch rate to very low values, at least for the first 2 h. For mole fractions of 0.3 or less, long-term exposure to air did not affect the etching rate significantly. For mole fractions higher than 0.4, the etch rate for the fresh surface was already too small to be of much practical interest, except as an etch-stop layer. The sharp drop in the $Al_{0.4}Ga_{0.6}As$ etch rate upon exposure to air may in fact find applications. It may be possible to preferentially recess $Al_{0.2}Ga_{0.8}As$ with respect to $Al_{0.4}Ga_{0.6}As$ by using an etching solution kept at room temperature. Figure 3.8 also depicts the etch rates for the long-term air-exposed $Al_{0.4}Ga_{0.6}As$ samples etched in succinic acid-hydrogen peroxide solutions which were heated to 65 °C. In this heated solution, the etch rate of $Al_{0.6}Ga_{0.4}As$ is more than 30 times slower than that of $Al_{0.4}Ga_{0.6}As$. Therefore, $Al_{0.4}Ga_{0.6}As$ may be recessed with respect to $Al_{0.6}Ga_{0.4}As$ either by etching fresh material at room temperature or by raising the solution temperature to 65°C for an air-exposed surface.

The conclusion is selective etching of $Al_{0.34}Ga_{0.66}As$ over $Al_{0.5}Ga_{0.5}As$ can be as high as 150.

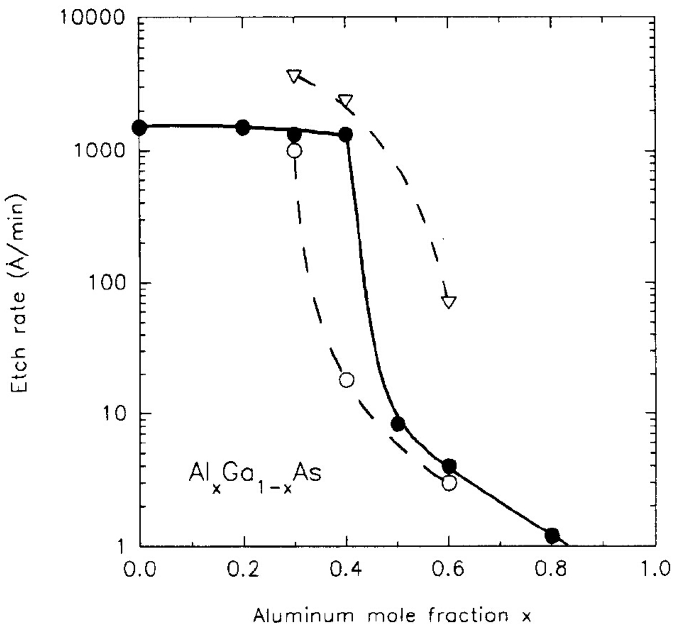

Figure 3.8 Etch rates of $Al_xGa_{1-x}As$ as a function of the aluminum mole fraction *x* for fresh samples etched at room temperature (filled circles), air-exposed samples etched at room temperature (open circles), and air-exposed samples etched at 65 °C (open triangles). Figure is from [78].

3.4.3.1 Experimental results

The sample preparation steps are similar as in Section 3.4.2.1. The mixture for the chemical etch is succinic acid (made of 20 grams crystalline succinic with 100 ml DI water), and 6.7 ml of 30 vl% H_2O_2. The etch protocol is shown in Table 3.6. In step 2, RT 30 wt% NH_4OH/DI water is used to wash away any residual etchant from step 1.

Table 3.6 Selective etching $Al_{0.34}Ga_{0.66}As$ over $Al_{0.5}Ga_{0.5}As$ in 15:1 succinic acid/H_2O_2.

Step 1	Succinic acid/H_2O_2 mixed at 15:1 volume ratio, etch for a certain time
Step 2	Soak in RT 30 wt% NH_4OH/DI water at a 1:10 volume ratio for about 30 seconds
Step 3	DI water rinse, for one minute
Step 4	N_2 dry up

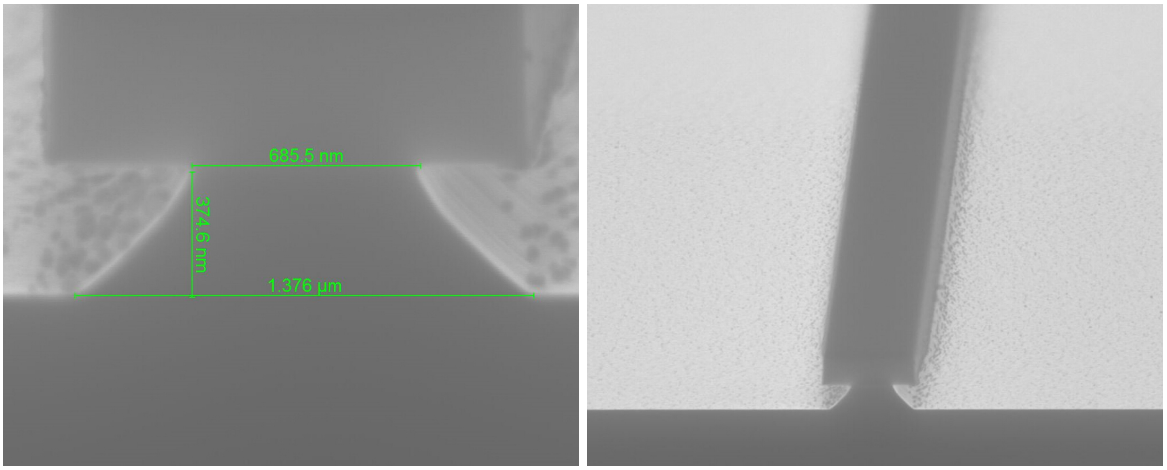

Figure 3.9 Samples etched in succinic acid/H_2O_2. Photoresist still remains on the etched nanostructures.

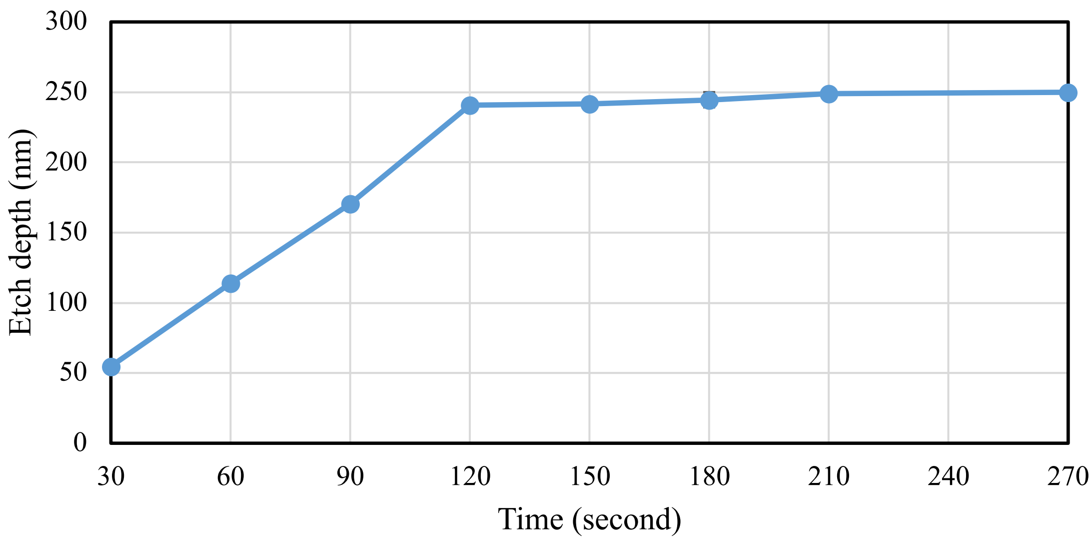

Figure 3.10 Etch depth of the sample as a function of time in succinic acid/H_2O_2 solution. The first two layers (the 5 nm GaAs and 120 nm $Al_{0.20}Ga_{0.80}As$) of the samples used here were etched by citric acid first.

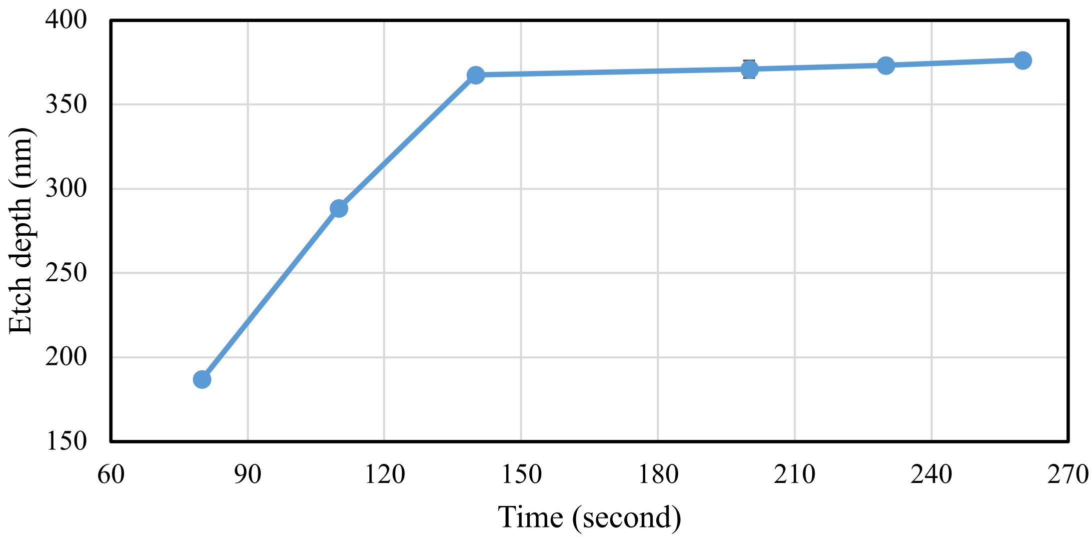

Figure 3.11 Etch depth of the sample as a function of time in succinic acid/H_2O_2 solution.

The etch rate for $Al_{0.34}Ga_{0.66}As$ is about 160 nm/min and the etch rate for $Al_{0.50}Ga_{0.50}As$ is about 4 nm/s. The measured selectivity is about 40. Etch depths were measured at multiple points (number of points ≥ 3) of a sample using scanning electron microscope (SEM). Error bars representing one standard error are shown in Figure 3.10 and Figure 3.11.

3.5 Fabrication of suspended waveguides using HF

This work was done in collaboration with Pisek Kultavewuti. My main contribution to the work is the fabrication of the waveguides.

3.5.1 Hydrofluoric acid family of etchants

The hydrofluoric acid family of etchants require the addition of an oxidizer to etch GaAs. However, HF without oxidizers can selectively etch $Al_xGa_{1-x}As$ with an Al mole fraction $x > 0.5$. As early as 1978, it was noted by Konagai et al. that thick $Al_{0.7}Ga_{0.3}As$ films exhibited rapid isotropic etching when immersed in an HF solution, while pure GaAs and $Al_{0.5}Ga_{0.5}As$ remained unaffected by the etchant [83]. Further investigations by Yablonivitch et al. revealed that HF in varying concentrations is an effective isotropic etchant for $Al_xGa_{1-x}As$ when the aluminum mole fraction is greater than $x = 0.5$, while exhibiting a precipitous decrease in etch rate for mole fractions below $x = 0.4$, with a remarkable etch selectivity greater than 10^7 [84]. This etch system was initially of interest in solar cell production as a cost-effective method for fully releasing large-area (> 1 cm^2) single crystal heterojunction multilayers from GaAs substrates. Now it is generally of particular importance for intrinsically large area, thus expensive devices like high efficiency III-V solar cells [85] and the integration of high quality optoelectronic III-V structures on silicon large scale integrated circuits [86, 87]. Etch rates of $Al_xGa_{1-x}As$ in different HF concentrations have been analyzed in detail in [88]. The results are reproduced and shown in Figure 3.12. In order to fabrication a highly confining suspended waveguide, we are interested in etching the $Al_{0.7}Ga_{0.3}As$ lower cladding, while retaining the $Al_{0.3}Ga_{0.7}As$ and $Al_{0.2}Ga_{0.8}As$ layers of the waveguide core, the wafer structure of which is shown in Table 3.7. As can be seen from Figure 3.12, in 10% HF, the etch rate of $Al_{0.7}Ga_{0.3}As$ is about 0.4 μm/min while that of $Al_{0.3}Ga_{0.7}As$ is only 3×10^{-5} μm/min, providing a selectivity of 10^4. Etching of $Al_xGa_{1-x}As$ for micromachining has been reported using HF concentrations of 10% or less [89, 90]. It has been suggested that higher HF concentrations may result in excessive generation of H_2 bubbles as an etch product, which can prevent further etching or even crack the supporting film [84]. Therefore, we chose 10% HF as the etchant for suspended waveguide fabrication.

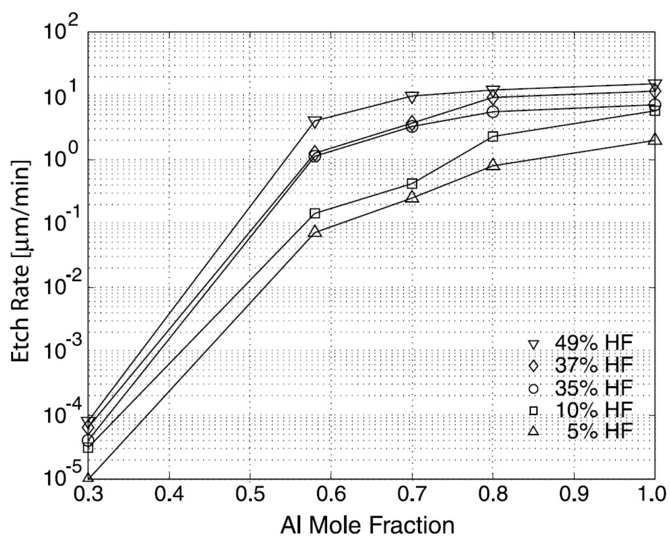

Figure 3.12 Lateral etch rate of $Al_xGa_{1-x}As$ versus Al mole fraction at different HF concentrations. Figure is from [88].

Adding H_2O_2 to HF allows GaAs to be etched as well, and the selectivity depends on the acid/oxidant ratio. Compared to the hydrofluoric acid family, many etchants that have been developed for sacrificial GaAs etching, such as ammonium hydroxide [91], citric acid [74, 75], or succinic acid [79] combined with hydrogen peroxide, provide only moderate selectivity to

$Al_xGa_{1-x}As$ films, on the order of 100:1 for GaAs:$Al_{0.3}Ga_{0.7}As$. Despite the potential advantages of the hydrofluoric acid family for sacrificial GaAs etching, when researchers want to selectively etch GaAs versus $Al_xGa_{1-x}As$, a less dangerous etchant is always preferred. These less dangerous etchants have been talked about in Section 3.4.

3.5.2 Suspended waveguides for nonlinear optics

The III-V semiconductor $Al_xGa_{1-x}As$ has been shown to be an ideal nonlinear material due to a combination of large second and third order nonlinear coefficients while allowing for operation in a wavelength region with low two-photon absorption. More recently, $Al_xGa_{1-x}As$ has been proposed as a candidate material for integrated quantum photonics [92], where it offers low-loss optical waveguides and electro-optic modulators. Integrated waveguides in GaAs/$Al_xGa_{1-x}As$ have been shown to be an excellent platform for a range of nonlinear optical effects. In particular, nonlinear waveguides efficiently perform wavelength conversion [93-95], the generation of supercontinuum light sources [96, 97] and the production of correlated photon pairs [98-101].

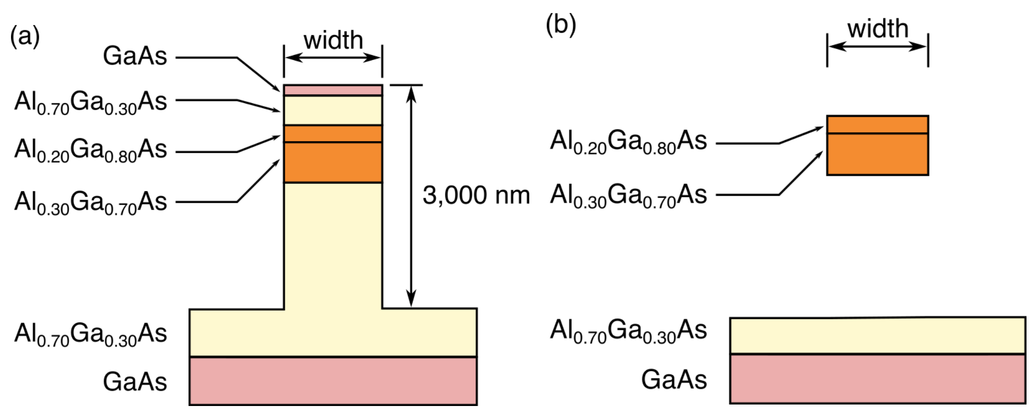

Figure 3.13 (a) Cross-section of a deep etched $Al_xGa_{1-x}As$ nonlinear waveguide, and (b) a cross-section of a suspended waveguide fabricated with dry and wet etchings.

The efficiency of a third-order nonlinear optical interaction depends on the mode confinement and the dispersion of the waveguide [102], which is enhanced in a high index contrast waveguide [94, 103]. A typical $Al_xGa_{1-x}As$ nonlinear waveguide consists of a deep etched structure as shown in Figure 3.13(a). In this structure only the horizontal axis experiences a high index contrast, while the index contrast in the vertical direction is much smaller [93, 94, 104, 105].

As a consequence, only the dispersion properties of the transverse electric (TE) mode, whose major electric field is horizontally oriented, can be controlled by the waveguide geometry. Only the TE mode can be engineered to have a zero dispersion in the 1500 nm telecommunications window [106]. On the other hand, the dispersion behavior of the transverse magnetic (TM) mode remains close to that of the bulk material. As a consequence, the waveguide has a considerable polarization mode dispersion that can limit the efficient generation of photonic polarization-entangled states in terms of the entanglement level and the state production bandwidth [107]. An independent control over the dispersion properties of both the TE and TM modes is necessary in order to optimize the nonlinear interaction for the two fundamental modes. Hence, a nonlinear $Al_xGa_{1-x}As$ waveguide with a high index contrast in two dimensions is needed. This can be achieved with an AlGaAs-on-insulator (AlGaAsOI) approach [10, 108]; however, the technique involves wafer bonding, and limits the potential for vertical integration.

In this work, we fabricate and characterize 2D high index contrast $Al_xGa_{1-x}As$ waveguides made from a multi-layer $Al_xGa_{1-x}As$ wafer that could potentially find applications in monolithic and vertical integration of passive and active devices. We report on the design, fabrication and testing of a symmetrical, suspended $Al_xGa_{1-x}As$ waveguide fabricated using a combination of wet and dry etching techniques; the cross-section of such waveguides is depicted in Figure 3.13(b). Such a waveguide allows for the independent control of the dispersions for the TE and TM modes, reduces substrate leakage loss, and opens up the possibility of opto-mechanical effects based in $Al_xGa_{1-x}As$ structure.

3.5.3 Fabrication and measurement results

The sample was prepared from a multi-layer $Al_xGa_{1-x}As$ structure, which was grown via metal-organic chemical vapor deposition (MOCVD) technique on a GaAs substrate. The details of the wafer structure are shown in Table 3.7 and schematically in Figure 3.13. First, we cleaved a sample with an area of about 2×2 cm^2, removed the 10 nm GaAs cap (layer no. 5) in a 50w.t.% citric acid:H_2O_2 at 4:1 volume ratio for two minutes (the recipe was described in Section 3.4.2), and removed the upper cladding (layer no. 4) in a 10% 1.5-molarity hydrofluoric (HF) acid in H_2O for two minutes [88]. The HF solution only removed the $Al_xGa_{1-x}As$ layer with x = 70% aluminum concentration from the wafer and left the core material (layer n. 2 and layer n. 3 in Table 3.7) intact. We proceed to fabricate deep etched $Al_xGa_{1-x}As$ waveguides using a combination of electron beam lithography (EBL) and ICP-RIE dry etching techniques in which we achieved an etch depth of 2000 nm [109]. The etch depth of 2000 nm was deep enough to expose the $Al_{0.7}Ga_{0.3}As$ layer (layer n. 1 in Table 3.7) for the subsequent HF etch. More details of the dry etch techniques are presented in Chapter 4. We then deposited a layer of PMMA onto the whole sample, and removed it only in the areas designed for suspended waveguides. The sample was then dipped in to the same HF solution for 70 seconds to dissolve the lower cladding. Finally, the end facets of the sample were cleaved to form coupling facets.

Table 3.7 Details of the multi-layer $Al_xGa_{1-x}As$ wafer used to fabricate suspended $Al_xGa_{1-x}As$ waveguides, listed from bottom to top. The term *x* and *n* are the aluminum molar fraction and refractive index, calculated at the wavelength of 1550 nm and at 300 K based on [60].

layer no.	Function	thickness [nm]	x	n
5	GaAs cap	10	0	3.3753
4	AlGaAs cladding	200	0.70	3.0232
3	AlGaAs core	200	0.20	3.2662
2	AlGaAs core	500	0.30	3.2150
1	AlGaAs cladding	4000	0.70	3.0232
0	GaAs substrate		0	3.3753

Figure 3.14(a) shows a scanning electron microscope (SEM) image of the suspended waveguide and the associated bridge structures used to support the structure. An overview of the chip is shown schematically in Figure 3.14(b). The area outside the wet etched area (purple box in Figure 3.14(b)) is protected from the HF solution and the waveguides have a typical deep etched structure. The full-cladding waveguides are necessary to support the ends of the waveguide and for coupling to the suspended section. A transition region between the two waveguide structures exists at the interface between the wet etched and non-wet etched regions and is highlighted with a blue box in Figure 3.14(a). Since the transition region is formed by wet etching, which is challenging to control, the number of the transition region should be kept as low as possible. To facilitate input and output end-fire coupling via the full-cladding waveguide, two transitions are required. Another important component is the bridge that provides a mechanical support of the

suspended waveguide. Since the bridge is in contact with the suspended waveguide, it can perturb the propagation along the waveguide and induce additional loss. The simplest bridge structure is one where the main waveguide and the bridge cross each other without any change in shape around the crossing location. Intuitively, the narrower the width of the bridge, the less insertion loss of the crossing. The structure of the bridge crossing was further optimized to reduce the insertion loss, the optimization method of which is detailed in [110]. Using the particle swarm optimizer in Lumerical® FDTD [111], an average transmission of 98% per crossing was obtained in the wavelength range between 1500 nm and 1600 nm, for waveguide widths between 700 nm and 1000 nm.

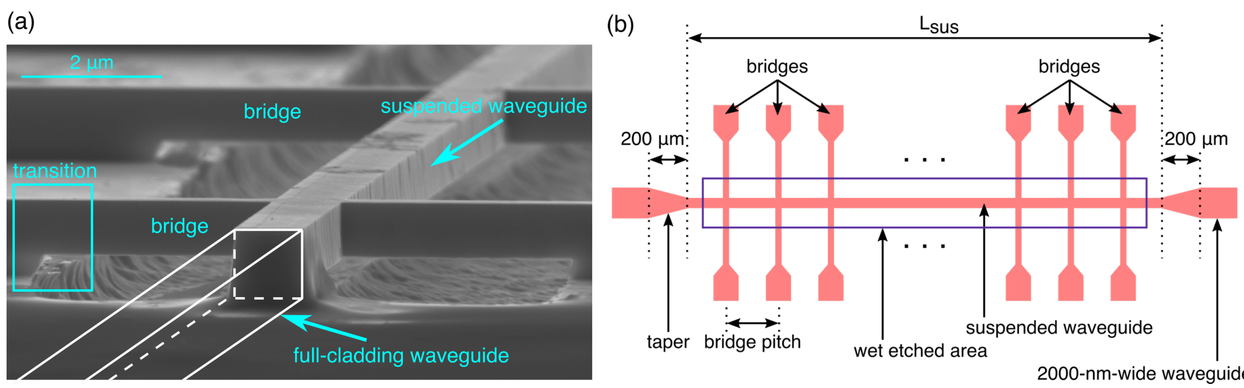

Figure 3.14 (a) A micrograph of a suspended waveguide device. (b) A top-view schematic of the structure of the suspended waveguide.

The resultant devices in this sample are (1) 2-mm-long full-cladding waveguides, (2) suspended waveguides that are 100 to 500 microns long and without a bridge, (3) suspended waveguides for the same lengths but with one simple bridge, (4) 2-mm-long suspended waveguides with 4, 9, and 19 optimized bridges that are evenly distributed, and (5) 2000-nm-wide full-cladding waveguides whose lengths span from the sample input facet to the output facet. The width of the waveguides in groups (1), (2), (3) and (4) varied from 600 nm to 1300 nm with an increment of 50 nm. The ends of these waveguides were tapered to 2000-nm-wide full-cladding waveguides that extended to the edge of the sample for power coupling. This set of devices allowed us to extract the propagation loss of the suspended waveguides that was in addition to the corresponding full-cladding waveguides and the insertion loss of the bridge. The simple bridges were constructed with various main waveguide widths but a fixed bridge width of 500 nm.

We characterized the propagation losses of the waveguides using the Fabry-Perot (FP) measurement technique; the experimental setup is shown in Figure 3.15. A tunable, continuous-wave (cw) laser source (TLS) operating in the telecommunication band was coupled into the waveguide using a 40x microscope objective. A combination of fiber polarization controller (FPC), half-wave plates (H), and polarization beam splitter (PBS) were used to adjust the optical power and the linear polarization state of light to selectively excite solely the TE or TM mode. As the wavelength of the continuous-wave (cw) tunable laser source (TLS) is swept with in a 5 nm bandwidth centering at 1550 nm, the input and output powers are recorded at the two power meters (PMs).

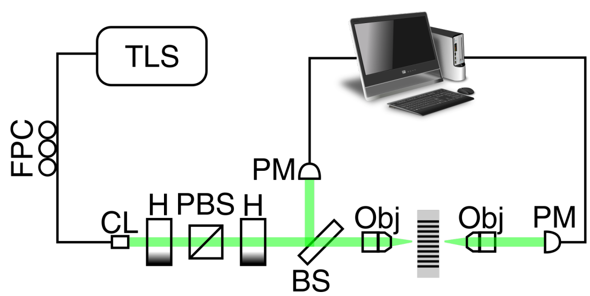

Figure 3.15 A Fabry-Perot transmission measurement setup; including a tunable laser source (TLS), a fiber polarization controller (FPC), a collimating lens (CL), half-wave plates (H), a polarization beam splitter (PBS), a beam sample (BS), power meters (PM), and objective lenses (Obj).

3.5.4 Results and Discussion

The losses of a 2 μm-wide, standard waveguide were measured to be 10±1 and 16±1 dB/cm for the TE and TM polarizations respectively. The propagation loss of other narrower full-cladding waveguides is plotted with green diamonds in Figure 3.16 for both the TE (left) and TM (right) modes. The error bars for these measurements were ±1 dB, including the uncertainty in estimating facet reflectivity and detected power fluctuations. For waveguide widths larger than 900 nm, the TE mode has an average propagation loss of 11 dB/cm. The loss then rises abruptly when the waveguide width narrows. This is due to a larger electric field at the side wall and hence a larger scattering loss due to surface roughness. In addition, the TE mode suffers from substrate leakage since it is squeezed laterally by the waveguide sidewall. The average propagation loss for the TM mode is about 25 dB/cm. It is generally higher than that of the TE mode in the full-cladding waveguides because its electric field component is vertically-orientated, experiences less index contrast, and therefore leaks more to the substrate. Note that the full-cladding waveguides that are narrower than 850 nm are too lossy to characterize using the FP method.

The propagation loss of the suspended waveguides was measured for devices with 500-µm-long suspended section. The total insertion loss was measured and the contributions due to the input and output waveguide connections were subtracted. An estimate for the transition loss between the suspended and non-suspended waveguides were obtained from a 3D-FDTD simulation: as T = 0.95 (TE) and T = 0.90 (TM). For the waveguides wider than 950 nm, the propagation loss for the TE mode for different widths has a large degree of scatter which could be attributed to the nonideality in the fabrication process. Nonetheless, given a flat trend of the loss observed in the full-cladding waveguides, the average of the measured loss can be estimated for the suspended waveguides. For the TE mode of these waveguides, the average propagation loss is 25±1 dB/cm. For waveguides narrower than 950 nm, the propagation loss increases as the width decreases as expected. On the other hand, the average propagation loss of the TM mode in the suspended waveguide is 34±1 dB/cm.

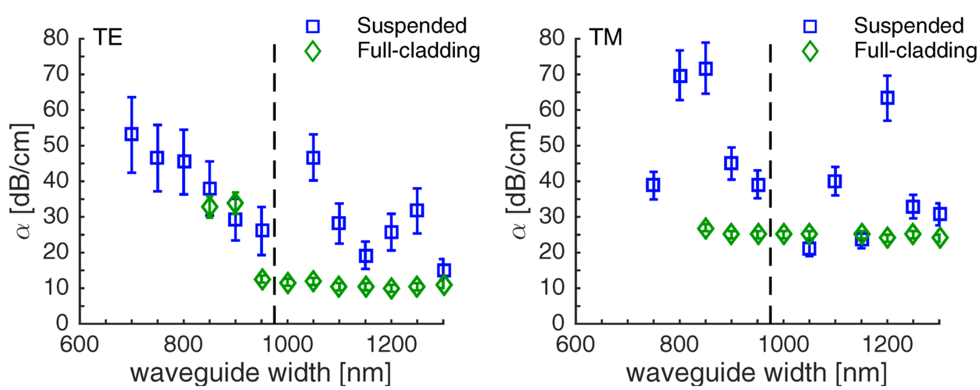

Figure 3.16 The propagation loss of the TE (left) and TM (right) modes in several full-cladding and suspended waveguides.

The propagation losses of these waveguides are high, which could be attributed to the sidewall roughness formed at the dry etching step. We note that deep etched waveguides with very low propagation loss has been demonstrated [104]. Hence, we project that it is possible to reduce the propagation loss of the suspended waveguide much further by starting with a low-loss dry etching procedure and optimized wet etching. In summary, we fabricated suspended $Al_xGa_{1-x}As$ waveguides that could improve optical nonlinear effects due to a higher 2D high index contrast. The demonstration of suspended waveguides structures could find potential applications in the monolithic and vertical integration of passive and active devices. The propagation losses of such waveguides are measured to be 25±1 dB/cm and 34±1 dB/cm for the TE and TM mode, respectively, which are still high but could be further reduce by optimizing both the dry and wet etching steps. Results are published in [110].

3.6 Conclusion

In this chapter, we discussed wet chemical etch recipes based on our two-guide-layer $Al_xGa_{1-x}As$ chips. The $Al_{0.20}Ga_{0.80}As$ layer can be etched with a selectivity of 15 with respect to $Al_{0.34}Ga_{0.66}As$ layer. The $Al_{0.34}Ga_{0.66}As$ layer can be etched with a selectivity of 40 with respect to $Al_{0.50}Ga_{0.50}As$ layer. The etched surface is very smooth. As expected, the wet etch recipes produce undercut and slanted sidewalls, which is undesirable for fabrication of $Al_xGa_{1-x}As$ devices. Because the etch proceeds laterally and creates more undercut after the vertical etch has been almost stopped, etch time need to be precisely controlled to fabricate $Al_xGa_{1-x}As$ devices to certain dimensions. However, wet chemical etch recipes are known to have minimal adverse effects on the electronic properties of the devices. This is good for a lot of applications such as lasers and detectors fabrication.

In addition, we reported on the design, fabrication and testing of a symmetrical, suspended $Al_xGa_{1-x}As$ waveguide fabricated using a combination of wet etching techniques using HF and dry etching techniques, which is the topic of Chapter 5. The suspended $Al_xGa_{1-x}As$ waveguide allows for the independent control of the dispersions for the TE and TM modes, reduces substrate leakage loss, and opens up the possibility of opto-mechanical effects based in $Al_xGa_{1-x}As$ structure.

Chapter 4
Dry etch techniques for AlGaAs devices

4 Dry etch techniques for AlGaAs devices

This chapter introduces the procedures of developing dry etch recipes for fabricating highly anisotropic waveguides.

4.1 Inductively-coupled plasma (ICP) RIE

Dry etch techniques are essential for the precise fabrication of optoelectronic devices, which requires accurate control of etch rate, selectivity, structural profile, and surface morphology while minimizing device damage. The widely used high-density plasma etch systems for GaAs are electron cyclotron resonance (ECR) and inductively coupled plasma (ICP) systems. These systems have resulted in improved etch characteristics as compared to conventional reactive ion etching (RIE). This is attributed to plasma densities that are 2 to 4 orders of magnitude higher than RIE, thus improving the III-V bond breaking efficiency, sputter and desorption of etch products formed on the surface. Additionally, since ion energy and ion density can be more effectively decoupled, plasma-induced damage is more readily controlled. In general, ICP sources are more attractive than ECR sources, due to their less complicated design, better process control and easy scaling up for production [112]. In an ICP etcher, the ion energy incident on the wafer can be effectively decoupled from the plasma generation by independently applying rf power to the wafer chuck, allowing for the possibility of low etch-induced damage at high etch rates.

There have been tremendous efforts in analyzing etching characteristics in various gas mixtures, such as $Cl_2/BCl_3/Ar$ [113, 114], Cl_2/BCl_3 [115, 116], Cl_2/N_2 [117-120], $Cl_2/Ar/O_2$ [121, 122], BCl_3/N_2 [123-126], $BCl_3/Ne/Ar$ [127, 128], $SiCl_4/Cl_2/Ar$ [129, 130], and $SiCl_4/O_2/N_2$ [131]. Among these gas mixtures, Cl_2 and BCl_3 are the main gases that provide strong chemical etching characteristics while Ar, N_2, O_2, and Ne provide a mechanism of balancing chemical etching with physical sputtering. Cl_2 dissociates easily and possesses the strongest chemical reactivity. Isotropic waveguide sidewalls are usually created if only Cl_2 is used. BCl_3 is less reactive compared to Cl_2. It is mainly used to remove native oxide, scavenge water vapor, improve sidewall passivation, reduce residue formation and suppress post etch corrosion for GaAs microwave device fabrication. The combination of Cl_2 and BCl_3 is the most popular candidate for etching GaAs devices. There is a trend of using BCl_3/Cl_2 in combination with N_2 because N_2 is known to passivate waveguide sidewalls more efficiently and is easier to control waveguide verticality.

In terms of applications, ICP-RIE recipes are used in fabricating optical waveguides [113, 122, 129, 130, 132], photonic crystals [114, 119, 123, 124], via holes [115, 116, 128], nanowires [118] and so on. The feature sizes that are involved in the fabrication of optical waveguides, photonic crystals and nanowires are usually between tens of nanometers to a couple of microns. The etch rates for such structures are in the range of 100 nm/min to a couple of μm/min. During the fabrication of high quality optical devices, a lot of practical issues need to be considered, including chamber conditioning [129], uniformity [125], mask stripping [133], surface morphology [134]. In comparison, the fabrication of via holes often involves feature sizes in the range of a couple of hundred micrometers. The etching characteristics are usually not applicable to the fabrication of optical waveguides.

4.2 Optical waveguide fabrication challenges

Selective etching of GaAs over AlGaAs or InGaP is possible in some gas compositions, i.e. $BCl_3/SF_6/N_2/He$ [125, 132, 135, 136]. Selectivity of GaAs over $Al_xGa_{1-x}As$ ($x = 0.2$) > 200:1 has been reported [132, 135]. While selective etching of GaAs over AlGaAs provides a means to fabricating high quality optical waveguides, it is not always necessary and sometimes can be prohibitively complex or impossible depending on the wafer design. Alternatively, optical emission spectroscopy, when available, can be utilized to stop an epitaxy layer [126]. In Chapter 3, we explored wet etch techniques which relied on selectivity between $Al_xGa_{1-x}As$ with different aluminum concentrations (different x values). However, for ICP-RIE techniques, in order to provide selectivity, etch stop layers are usually inserted between $Al_xGa_{1-x}As$ layers. This is problematic for wavelength around 850 nm, because the workable etch stop layers have lower bandgap energies and induce unacceptable absorption losses in the devices [137]. Without etch stop layers, the inability to achieve accurate etch depth control can render devices useless.

In the MGVI scheme, multiple waveguide levels are stacked on top of each other with each level hosting a different type of device. Because of the variety of functionalities, the dimensions of the devices can vary significantly. Etch depths between 100 nm and 3 μm need to be precisely achieved in multiple etching steps in a single chip. Fabrication of the chips need to on highly precise and anisotropic etching using recipes that do not reply on etch stop layers. In this chapter, we present ICP-RIE fabrication techniques for MGVI $Al_xGa_{1-x}As$ based PICs. Two dry etch recipes have been developed with almost two orders of magnitude difference in etch rates. The first one used BCl_3 and achieved an etch rate of 0.25 nm/s while the second one used Cl_2/N_2 gases and achieved an etch rate of more than 20 nm/s. We fabricated simple $Al_xGa_{1-x}As$ nanowaveguides of 800 nm width using these recipes and measured a propagation loss of 6.7 dB/cm at the wavelength of 850 nm. While previous attempts at building MGVI chips were mainly made in the InGaAsP material system, the recipes described in this chapter represent an important step forward in demonstrating the feasibility of making MGVI chips in the $Al_xGa_{1-x}As$ material system

4.2.1 Wafer structure

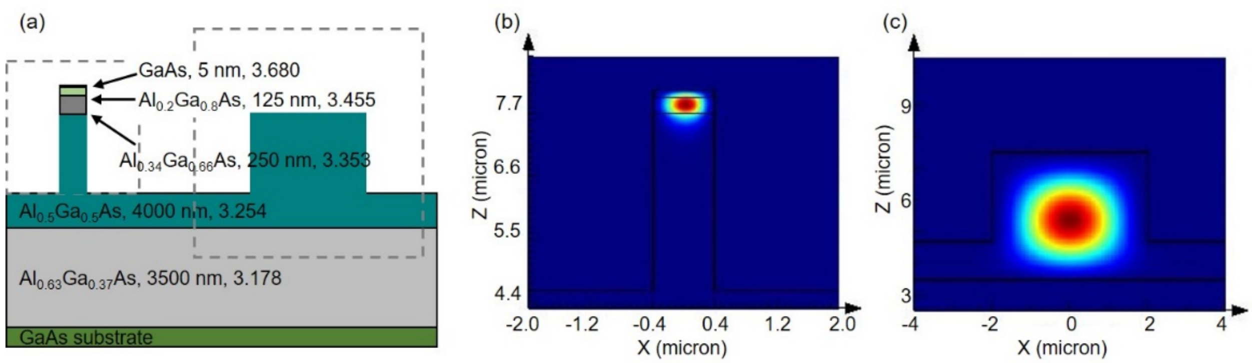

Figure 4.1 a) Wafer schematic showing layer thicknesses and refractive indices. b) TE mode profile for an 800 nm wide waveguide in the high confinement upper layer. c) TE mode profile for a 4 µm wide waveguide in the lower layer. Figures are from [109].

The wafer used in the experiment consists of five $Al_xGa_{1-x}As$ layers with different aluminum concentrations. They are a 5 nm GaAs, a 120 nm $Al_{0.2}Ga_{0.8}As$, a 250 nm $Al_{0.34}Ga_{0.66}As$, a 4 µm $Al_{0.5}Ga_{0.5}As$ and a 3.5 µm $Al_{0.63}Ga_{0.37}As$ from top to bottom and are grown on an *n*-type (100) GaAs substrate. The first three layers on the top are suitable for implementing high refractive index contrast waveguides for on-chip signal processing. The two bottom layers are good for making large-dimension waveguides that facilitate end-fire coupling. Schematic of the wafer structure is shown in Figure 4.1(a). Modal fields were simulated using Lumerical® MODE solutions. The electric field intensities of TE modes of high confinement waveguide and large waveguide are shown in Figure 4.1(b) and (c), respectively.

4.2.2 Sample preparation

Test samples were prepared using the following process steps. Firstly, a large sample was soaked in acetone for 10 mins and then in IPA for 10 mins. Secondly, the sample was soaked in 30% NH_4OH:DI water = 1:10 for 30 seconds and then rinsed with running DI water for 30 seconds. Lastly, either ma-N2400 series photoresist, or HSQ was spin coated on to the sample. Simple waveguides with various widths were exposed using e-beam lithography (EBL). The resultant samples were masked with 500 nm ma-N2405, 1000 nm ma-N2410 or 600 nm HSQ. The samples prepared using HSQ were hard-baked at 250 °C for 60 mins to improve hardness. We cleaved the large sample into smaller pieces with an area about 25 mm^2. Etching was carried out in Oxford Instruments Plasmalab system 100 with ICP 380 which can handle 4" diameter wafers and has a 380 mm diameter ICP source. Substrate DC bias is independently controlled by an RF generator at 13.56 MHz. The inductively coupled plasma source is a 380 mm diameter coil powered by a 1.7-2.1 MHz generator that can deliver up to 5 kW. Oxford Instruments Plasmalab system 100 with ICP 380 etch sources produce a high density of reactive species at low pressure. All samples were etched for 4 mins unless otherwise noted. The two baseline recipes for fast and slow etch are listed in Table 4.1.

Table 4.1 Baseline recipes for fast and slow etch recipes. Table is from [109].

	Pressure (mTorr)	rf power (W)	ICP power (W)	Gas flow (sccm)	Temperature (°C)
Slow etch recipe	5	200	600	50 BCl_3	10
Fast etch recipe	5	50	600	20 Cl_2/5 N_2	20

4.3 Slow etch recipe with BCl_3

In order to fabricate the highly confining waveguides on the upper layer very precise control of the etch depth is required. To achieve this, we developed the following BCl_3 etch process. It is known that BCl_3 scavenges aluminum oxides and eliminates lag times [138]. This is crucial in achieving a precise shallow etch because a fast etch recipe with unpredictable lag times inevitably diminishes the accuracy of the etch depth. It has also been reported that BCl_3 achieved equi-rate etching for $Al_xGa_{1-x}As$ of different aluminum concentrations [139]. These two factors are important since the slow etch recipe was used in etching the top layers which were prone to native oxides and encompassed several $Al_xGa_{1-x}As$ layers. We kept the chamber pressure constant at 5 mTorr in the experiment but varied other parameters, including rf power, ICP power, gas flow rate and temperature. Samples with 500/1000 nm ma-N2405/2410 were used. Etch depths were obtained from at least four locations on the small sample, which had an area of about 25 mm^2. Etch rates were calculated as the averaged depths divided by etch times. The same etch depth measurement and etch rate calculation methods were followed throughout this Chapter.

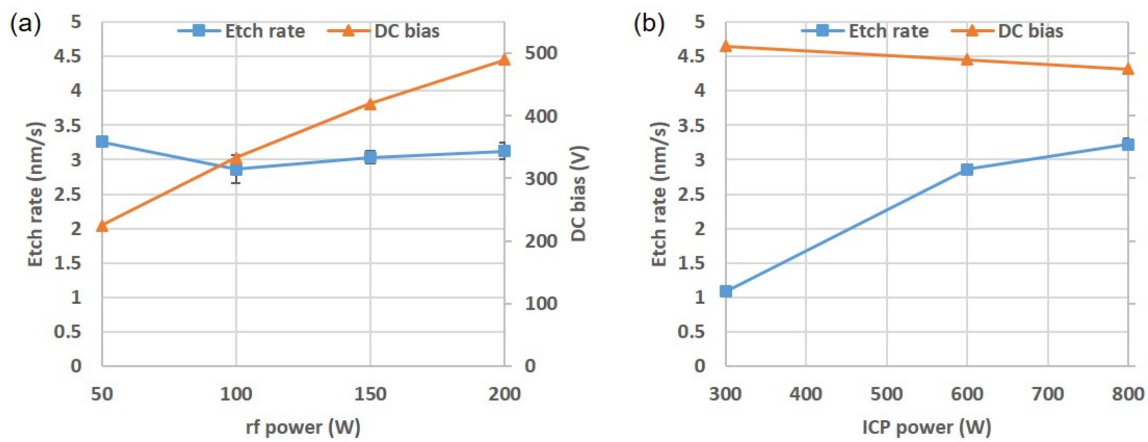

Figure 4.2 Etch rate and DC bias voltage as a function of (a) rf power at 600 W ICP and (b) ICP power at 200 W rf, respectively, at 5 mTorr, 50 sccm BCl_3 and 10 °C. Samples were etched for 2 mins. Photoresist ma-N2410 was the mask. Figures are from [109].

The etch rate showed little change when the rf power was varied from 50 to 200 W. This can be understood as the dominant etch mechanism was chemical etching. Increasing the rf power basically increased ion energy and physical sputtering, which remained insignificant under the conditions explored. When the ICP power was varied from 300 to 800 W, the etch rate increased significantly due to increased ion density and flux. We recorded the DC bias voltage of the sample chuck. For samples etched using recipes from Figure 4.2, sidewalls were found to be overcut when the DC bias was higher than 400 V. A close examination revealed that the overcut emerged because of photoresist reflow which then covered the sidewalls as etching proceeded. As a result, the widths of the waveguides were larger at the bottom of the structure. On the other hand, samples showed undercut sidewalls when DC bias voltage was about 200 V. This could be attributed to no resist reflow and insufficient ion energy for ion assisted chemical etching. Overall, an rf power of 100 W seemed to strike a balance. Samples etched using recipes from Figure 4.2(a) are shown in Figure 4.3.

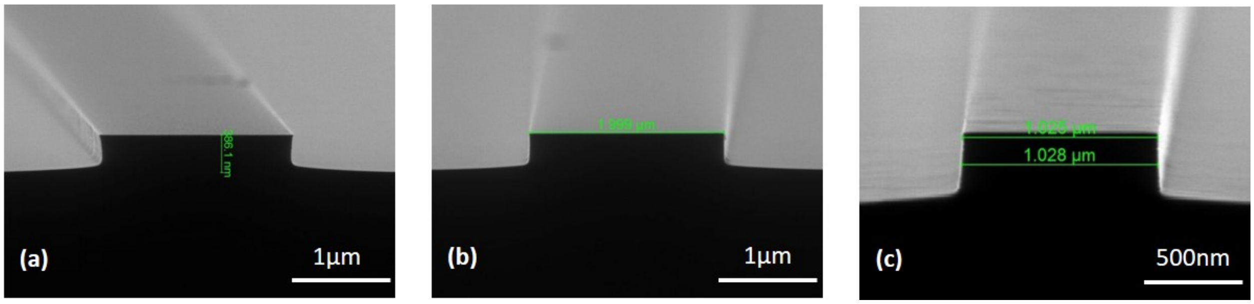

Figure 4.3 Scanning electron micrographs of samples etched using rf power (a) 50 W, (b) 100 W and (c) 200W at 5 mTorr, 600 W ICP, 50 sccm BCl_3 and 10 °C. Figures are from [109].

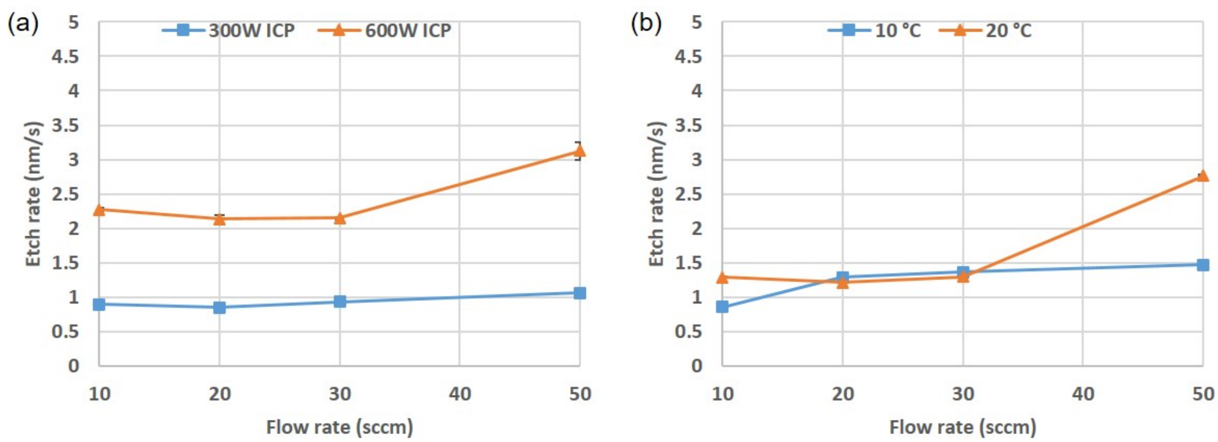

Figure 4.4 Etch rate as a function of BCl_3 flow rate. (a) Two ICP power levels were examined at 5 mTorr, 200 W rf and 10 °C. 512 V and 500 V bias voltages were recorded for both ICP power levels. (b) Two temperatures were examined at 5 mTorr, 100 W rf and 300 W ICP. 350 V bias voltage was recorded for both temperatures. Figures are from [109].

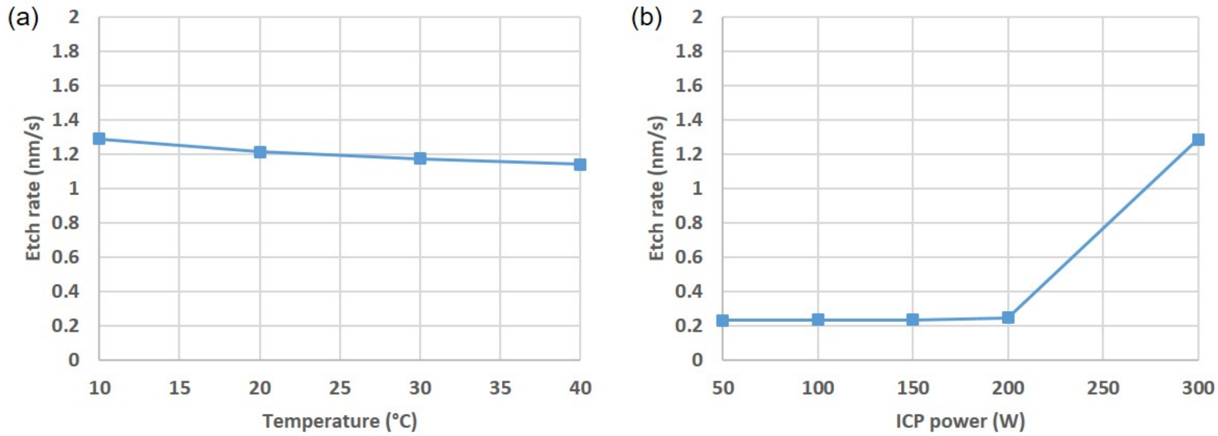

Figure 4.5 (a) Etch rate as a function of temperature at 5 mTorr, 100 W rf, 300 W ICP and 20 sccm BCl_3. 350 V bias voltage was recorded. (b) Etch rate as a function of ICP power at 5 mTorr, 100 W rf, 10 sccm BCl_3 and 20 °C. 300 V bias voltage was recorded between 50 W and 200 W. 350 V bias voltage was recorded at 300 W ICP. Figures are from [109].

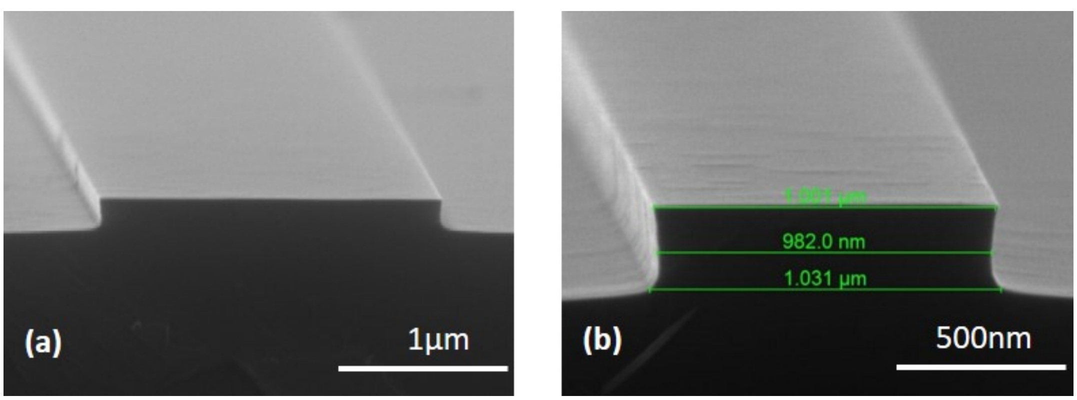

Figure 4.6 SEMs of samples etched using (a) 10sccm and (b) 20sccm BCl_3 at 5 mTorr, 100 W rf, 300 W ICP and 10 °C. Figures are from [109].

The change of etch rate as a function of gas flow rate was also examined. As shown in Figure 4.4(a), the gas flow rate didn't noticeably influence the etch rate at an ICP power level of 300 W. A similar trend was reported by [140] and therefore running excessive gas was discouraged. At an ICP power level of 600 W, the etch rate was about 50% higher at a BCl_3 flow rate of 50 sccm owing to an increased ion concentration coupled with a higher ion flux at the elevated ICP power. Overall, the etch rate was reduced by about half when the ICP power was changed from 600 W to 300 W, indicating a diffusion-limited etch: higher ICP power induced a higher ion flux which carried away etch byproducts faster and resulted in higher etch rates. The photoresists ma-N2405 and ma-N2410 were used for the 300 W and 600 W ICP power, respectively. Due to strong physical sputtering, overcut sidewalls resembling Figure 4.3(c) were observed in both cases. Therefore, we decreased the rf power to 100 W and set the 300 W ICP power as a 'new' baseline. As shown in Figure 4.4(b), etch rate was almost invariant at 10, 20 and 30 sccm BCl_3 at 10 °C and 20 °C. Figure 4.6 shows samples that were etched using 10 and 20 sccm BCl_3 at 10 °C.

To further confirm temperature dependence of etch rate, we varied temperature up to 40 °C. A decline in etch rate can be seen in Figure 4.5(a). This trend could be explained as follows. It's known that ions traversing the ion sheath region would assume the substrate temperature long before they reach the substrate. A higher temperature resulted in stronger scattering thus fewer ions reached the substrate. While the elevated temperate didn't increase the chemical reactivity, it led to weaker desorption of byproducts and thus a lower etch rate. Lowering the ICP power would decrease etch rate and give reasonably low etch rates. As shown in Figure 4.5(b), etch rate as low as 2.5 Å/s could be obtained and resultant DC bias was reasonably low. Selectivity of ma-N 2400 series photoresist was larger than 2:1. The rapid drop of etch rate when ICP power was reduced to 200 W could be attributed to a combination of reduced ion flux, which reduced desorption, and insufficient reactive ions, which limited reaction with the substrate. Further exploration was not carried out. Samples etched under these temperatures and ICP power had almost the same profile as shown in Figure 4.6.

4.4 Fast etch recipe with Cl_2/N_2

The large coupling waveguide in the lower layer requires a much deeper etch. To facilitate the fabrication of vertically integrated waveguides, we developed the following fast etch process based on a combination of Cl_2/N_2. Compared to Ar, N_2 is preferred for balancing chemical activity and physical sputtering [112, 117]. N_2 can also passivate sidewalls and gives more flexibility to control the sidewall profile. In addition, a two-compound composition makes it easier to vary the interplay between chemical etching and physical sputtering. Samples with 600 nm HSQ were used in the following experiments.

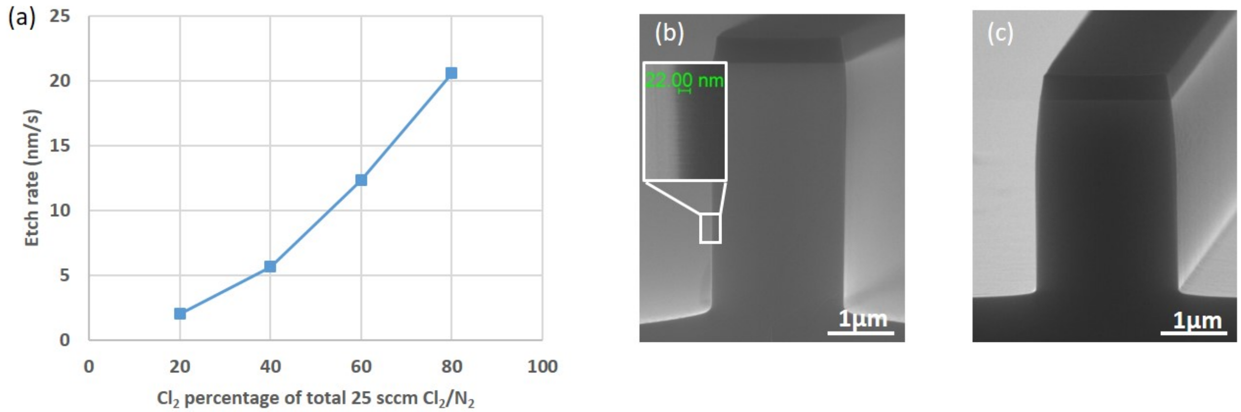

Figure 4.7 (a) Etch rate as a function of Cl_2 concentration at 5 mTorr, 50 W rf, 600 W ICP and 20°C. The total flow rate of (Cl_2+N_2) was kept constant at 25 sccm. (b) SEMs of samples etched using 80% Cl_2 concentration for 3 mins. The inset shows the 20 nm thick passivation layer. (c) SEMs of samples etched using 60% Cl_2 concentration for 4 mins. Figures are from [109].

Increasing the rf power increases the ion energy and therefore the sputter rate. In order to protect the passivation layer, the rf power needs to be reasonably low. Another reason is Cl_2 dissociates easily and the chemical reactivity of the gas composition can be too high to achieve anisotropic etching. We found a quadratic relationship between etch rate and chlorine concentration. A very similar relationship was reported in [112]. A thin passivation layer can be seen in Figure 4.7, the average thickness of which was about 20 nm. Increasing the N_2 concentration increased the passivation effect. Overcut sidewalls (roughly 87°) were observed when Cl_2 concentrations were 20% and 40%, indicating sidewall passivation proceeded too fast. In addition, the passivation layer on two closely positioned waveguides appeared thinner, which was due to sputter effect of gas molecules bounced off two facing sidewalls. The effect of varying the ICP power was examined at two different chlorine concentrations. The etch rate variation was more noticeable at 20% Cl_2 than at 80% Cl_2. At 80% Cl_2, the etch rate decreased monotonically, which could be attributed to sputter desorption of reactive Cl(I) from the surface prior to reaction. At 20% Cl_2, the increase in etch rate after 600 W could probably be ascribed to increased sputter desorption effect. Figure 4.8 also shows etch rates are relatively invariant at 600 W ICP power and indicates precise etch depths can be achieved under these conditions. Moreover, we recorded much lower

DC bias voltages, which is good for lowering etch-induced damage to the devices. Etch selectivity of photoresist generally remained above 20:1.

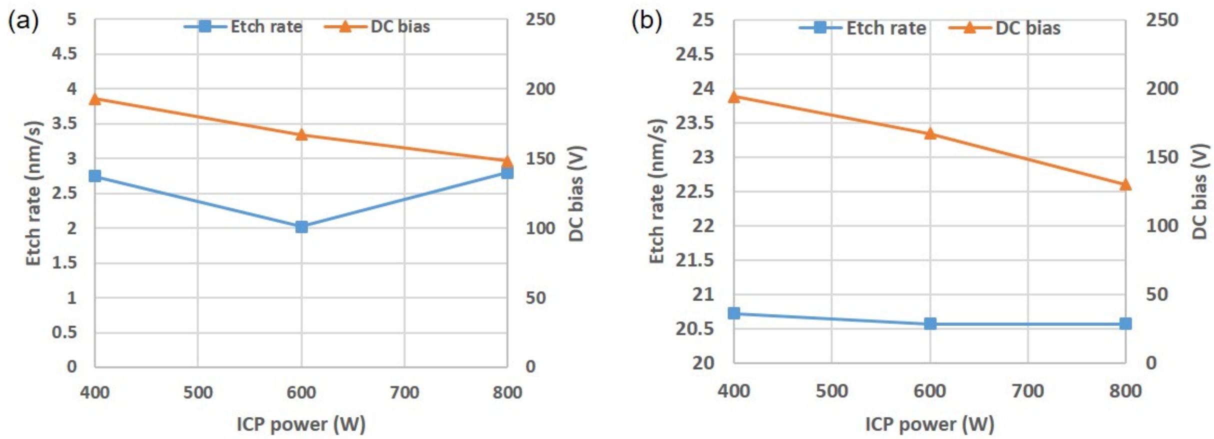

Figure 4.8 Etch rate and DC bias voltage as a function of ICP power at (a) 20% and (b) 80% Cl_2 of total 25 sccm (Cl_2+N_2) flow, 5 mTorr, 50 W rf and 20°C. Figures are from [109].

4.5 Summary of etch recipes

Highly anisotropic etching has been achieved using both slow and fast etch recipes. Slow etch recipe gives etch rates between 0.25 nm/s and 3.8 nm/s while fast etch recipe gives etch rates between 2.0 nm/s and 21 nm/s. These recipes give two orders of magnitude difference in etch rates and facilitate the fabrication of waveguides with different dimensions, located on different vertically separated guiding layers. The slow etch recipe can be used for the fabrication of shallow waveguides where the etch depth needs to be accurately controlled. The fast etch recipe can be used to etch deeper waveguides in the range of a couple of hundred nanometers to a few microns. This broad range is ideal for fabricating MGVI chips in the $Al_xGa_{1-x}As$ material system. In order to increase the flexibility of using reactive ion etching processes for the production of vertically integrated waveguides, we also include information on an etch recipe which has an intermediate etch rate. Final results are shown in Table 4.2. The fast etch recipe has also been used to fabricate suspended, 2D high-contrast $Al_xGa_{1-x}As$ waveguides for nonlinear applications in a different wafer structure [110], which has been discussed in Section 3.5. It has also been used to fabricate spot-size converters in the same wafer but with the first three epitaxial layers firstly removed [141]. In both cases, similar etch rates were reported, demonstrating the stability and reproducibility of these recipes.

Table 4.2 Fast, slow and intermediate etch recipes. Table is from [109].

	Pressure	rf power	ICP power	Gas flow (sccm)	Temperature	Etch rate
Slow recipe	5 mTorr	100 W	200 W	10 BCl_3	20 °C	0.25 nm/s
Intermediate recipe	5 mTorr	50 W	600 W	5 Cl_2/20 N_2	20 °C	2.0 nm/s
Fast recipe	5 mTorr	50 W	600 W	20 Cl_2/5 N_2	20 °C	21 nm/s

4.6 Propagation loss measurement of nanowaveguides

In order to verify the applicability of the recipes developed above, we fabricated high confinement waveguides with varying lengths. The high confinement waveguide has a width of 800 nm and a height of 3.175 μm, the waveguide schematic and TE mode profile of which are shown in Figure 4.1(a). Detailed fabrication procedures are as follows. Samples were spin-coated with HSQ and baked at 250 °C for 3 mins. The samples were then exposed using Vistec EBPG 5000+ EBL System and developed in 25% TMAH at 80 °C for 45 seconds. The samples were hard-baked at 250 °C for 60 mins before finally being etched using the fast etch recipe shown in Table 4.2. A cross-sectional view of the fabricated nanowaveguides can be seen in Figure 4.9(a). The sidewall and surface roughnesses are shown in Figure 4.9(b). We used a Ti:sapphire laser operating at a wavelength of 850 nm as the light source. A polarizing beam splitter was used to select the polarization of the input light in order to excite the TE modes of the waveguides. We used two Newport M-40x objective lenses for coupling light in and out of the waveguides. The optical power was kept constant at 1 mW before the input lens. The output power from waveguide was measured using Newport 883-SL optical detectors and plotted versus the waveguide lengths. The coupling efficiency between nanowaveguides and objective lenses was about 10% due to mode mismatch. An average propagation loss of 6.7 dB/cm was measured, which represented a worst-case scenario result. At such a narrow waveguide width, the mode field intensity at the waveguide/air interface was quite large. We want to point out that, smooth HSQ patterns were developed during the lithography. Sidewall roughness was due to the erosion of the resist during the etching process. Propagation loss largely resulted from narrow waveguide dimensions and sidewall roughness. Compared to some propagation loss characteristics found in the literature [94], results in this paper are quite competitive. Though some researchers used resist-reflow methods to improve sidewall roughness [142], whether it's applicable to MGVI

$Al_xGa_{1-x}As$ chips remains to be seen. While the resist-reflow methods are generally good for fabricating straight waveguides, it may not be applicable in MGVI $Al_xGa_{1-x}As$ chips where dense features exist and multiple etching steps are needed.

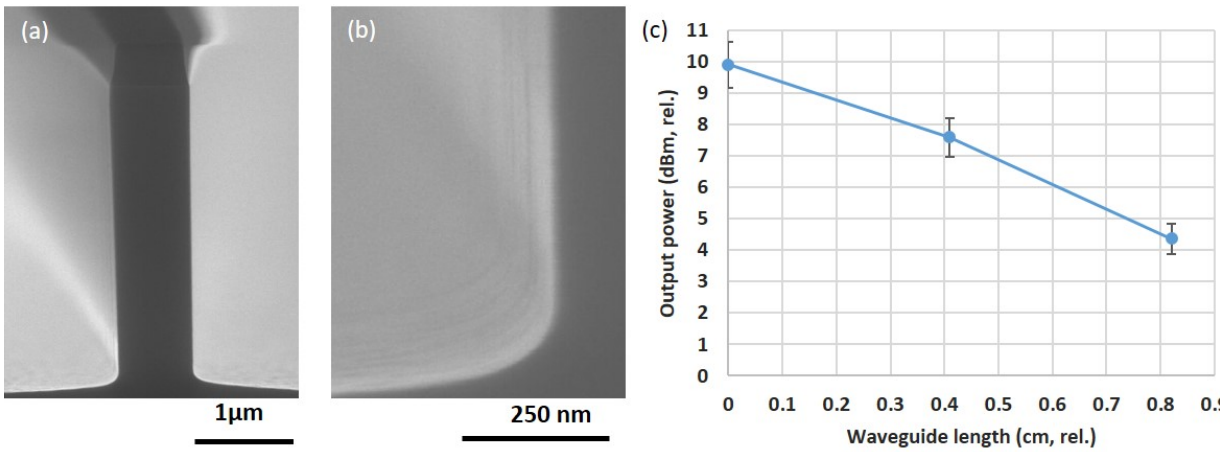

Figure 4.9 (a) Scanning electron micrograph of the high confinement waveguides with a width of 800 nm and a height of 3.175 μm. HSQ still remained on the sample. (b) Zoomed-in view of the bottom of the waveguides showing the sidewall and surface roughnesses. (c) Propagation loss of nanowaveguides. Figures are from [109].

4.7 Conclusion

We successfully developed two etch recipes that meet the stringent requirements of fabricating MGVI $Al_xGa_{1-x}As$ chips. The slow etch recipe used BCl_3 and achieved an etch rate of 0.25 nm/s while the fast etch recipe used Cl_2/N_2 gases and achieved an etch rate of more than 20 nm/s. We fabricated simple high aspect ratio $Al_xGa_{1-x}As$ nanowaveguides of 800 nm width using the fast etch recipe and measured a propagation loss of 6.7 dB/cm for the fundamental TE mode of the waveguide at the wavelength of 850 nm. Results are published in [141, 109]. We proved that highly precise and anisotropic etching can be achieved. As fabrication of state-of-the-art optoelectronic devices essentially relies on ICP-RIE techniques, our work is an important step forward in demonstrating the feasibility of making MGVI chips in the $Al_xGa_{1-x}As$ material system.

Chapter 5
Two-guide-layer AlGaAs chip

5 Two-guide-layer AlGaAs chip

This chapter reviews the techniques of designing spot-size converters and introduces the design and fabrication process of our spot-size converter on the two-guide-layer $Al_xGa_{1-x}As$ chip.

5.1 Introduction

For a long time, integrated optics was mostly devoted to new materials and concepts. It has now clearly entered into an era where it is mainly driven by applications. Optical fiber communications remains a strong driving force, resulting in photonic integrated circuits that are becoming increasingly complex. Up to now, optical circuits were achieved through existing passive and active guided wave components, assembled by using standard, or polarization maintaining fiber pigtails. In the longer term, monolithic integration is expected to drive down the costs and improve system robustness.

At the interface of optical waveguide structures and fibers, the issue of fiber-to-waveguide coupling is one of the key challenges to be solved. Planar optical waveguides in low refractive index contrast material systems whose dimensions are matched to those of optical fibers may show negligible coupling losses for end-fire coupling. However, the designs associated with low refractive index contrast come at a price. Low refractive index contrast waveguides lead to bend radii of curvature in the range of millimeters. This severely hinders the development of device miniaturization for a lot of applications, such as arrayed waveguide grating and ring resonators. Increasing the refractive index contrast allows for the design of high confinement waveguides with much smaller dimensions, which reduces the bend radii but at the expense of a reduced end-fire fiber-to-waveguide coupling efficiency. In order to simultaneously have efficient fiber-to-waveguide coupling and small bend radii, spot-size converters come into play. By properly designing spot-size or mode converters, we can integrate waveguides with large cross-sectional dimensions for efficient fiber-to-waveguide coupling with high-confinement waveguides for small bend radii. In particular, the conversion efficiencies of the spot-size converters should be high and lengths should be short, so that device miniaturization is not compromised by the integration of spot-size converters.

Spot-size converters have been implemented in a range of material systems. All are based on volume reduction in the waveguides along the propagation axis in order to reduce, or increase the confinement of the mode to match the geometries of waveguides and optical fibers. Current developments in silicon photonics make silicon an attractive candidate as a motherboard for photonic integrated circuits. The good thermal and mechanical properties also make it a good candidate for hybrid integration. Spot-size converters in silicon come in different structures. The Lipson group demonstrated a spot-size converter on SOI by tapering the silicon layer over a length of about 40 microns [143]. The width and height of the silicon waveguide were 470 nm and 270 nm, respectively. The width of the waveguide was tapered down to 100 nm. A lensed fiber with a beam waist of 5 microns at the wavelength of 1550 nm was used to couple light to the taper. A coupling efficiency of -3.3 dB was demonstrated and the 3-dB alignment tolerance was about 2 microns in the vertical and horizontal directions. This is one of the most compact spot-size converters achieved on SOI platform to date. However, there are some drawbacks about the design. Firstly, the light was not guided in the lower layer since no waveguides were formed in it. Light was coupled into the high-confinement waveguide at the cleaving facet. Secondly, it brings in a stringent cleaving requirement for the device. Moving away from the cleaving facet would greatly reduce the coupling efficiency. These drawbacks make the design less attractive for more sophisticated integration. In addition, silicon does not provide gain, which makes the integration of active devices problematic.

A different type of spot-size converters demonstrated on SOI platform is by creating a large waveguide on top of a standard SOI high-confinement waveguide. These designs unanimously deposited extra layers on SOI wafer to create large waveguides and used tapers to convert light from the top large waveguides to silicon waveguides. Maegami deposited silicon oxynitride on top of a 470 nm wide and 220 nm deep silicon waveguide. [144] The silicon waveguide width/height was firstly laterally/vertically tapered from 470/220 nm down to less than 150 nm. A 1.2-micron silicon oxynitride layer was then deposited. The width and depth of the large silicon oxynitride waveguide were both 1.2 microns. The large silicon oxynitride waveguide was not tapered. Light was coupled from a lensed fiber into the large waveguide and gradually converted to the high-confinement silicon waveguide over a length of about 1 cm. The author measured a coupling efficiency of 1.5 dB/facet at the wavelength of 1510 nm. In this design, the main disadvantage was, the conversion of light was achieved over an excessively long length. In a similar way, Sisto deposited a 10-micron thick silicon oxynitride on top of the 500 nm by 220 nm silicon waveguide [145]. Multiple silicon nitride rods were created in the SiON layer and arranged in a circular way to form a waveguide that had a mode shape that closely resembled that of a single mode fiber. The width of the SiN rod that was closest to the silicon waveguide was tapered from 500 nm to 2.1 microns, then met the silicon waveguide whose width was tapered from 150 nm up to 500 nm. Such schemes for integration requires extremely complicated fabrication processes. Similarly, the integration of active devices is problematic.

There is a lot of research in developing spot-size converters in III-V semiconductors. There are many advantages associated with III-V semiconductors. The remaining of this chapters gives the design and fabrication process of our spot-size converter on the two-guide-layer $Al_xGa_{1-x}As$ chip.

5.2 III-V semiconductor spot-size converters

Currently, PICs are based on many different integration schemes, including etch-and-regrowth [5, 6], quantum-well intermixing (QWI) [7, 8], selective-area growth [9] and hybrid material integration [10]. These methods have several drawbacks that either limit the integration complexity, or incur high fabrication costs, as discussed in Section 1.2. One alternative is regrowth-free vertical integration, in which functional waveguides composed of different yet compatible III-V semiconductor materials are vertically stacked in one epitaxial growth run and coupled to each other by means of lateral tapers defined in a process of fabrication. This integration scheme, is known by a number of different names: Single-Mode Vertical Integration [28], Asymmetric Twin-Waveguide (ATG) Technology [29], Multi-Guide Vertical-Integration (MGVI) [30], or Taper-Assisted Vertical Integration (TAVI) [35], has been proven a versatile PIC platform in indium phosphide (InP). Two-guide [31, 32], three-guide [33], and even four-guide [34] vertical integration PICs have been successfully developed and commercialized in InP. The major advantage of the vertical integration approach – an ability for independent optimization of the functional waveguides without additional growth steps or any other alteration of as-grown material – is not limited to InP and can be also extended to GaAs based PICs [45]. To do this, however, a fundamental problem of the TAVI of the different functional waveguides formed in the common AlGaAs - GaAs vertical stack should be solved first.

5.2.1 Wafer structure and waveguide modes

In this chapter, we report on the first, to our knowledge, TAVI of two AlGaAs – GaAs based waveguides operating in the 850 nm spectral range. The structure demonstrated is a two layer spot size converter, which allows for low loss and displacement tolerant coupling from an optical fiber to a semiconductor waveguide. Vertically integrated SSCs in InP PICs [42, 146] are known to be a robust solution to high-efficiency fiber to PIC coupling, commonly used in the vertically integrated PICs in InP [147], and so could be its AlGaAs – GaAs counterpart.

To demonstrate the TAVI SSC in AlGaAs – GaAs, we designed and fabricated a dual waveguide layer chip, the wafer structure of which was first introduced in Section 2.3.1. The design consists of a lower waveguide layer for an efficient and displacement-tolerant coupling to a single mode fiber (SMF), and an upper waveguide layer for on-chip routing, interconnecting, and other passive functions. The former is a relatively weakly vertically confined waveguide with the mode size suitable for a PIC to fiber coupling. The latter is a strongly vertically confined waveguide intended for a passive guiding in a limited footprint area of the PIC. Because of significant – and intentional – mode mismatch between the two waveguides, the lateral tapering system is devices to adiabatically connect them, by facilitating controllable low-loss transmission from one to another. We measured a SSC conversion efficiency of (91±0.2)% (or −0.4 dB) between the upper and lower waveguide layers for the TE mode at the wavelength of 850 nm.

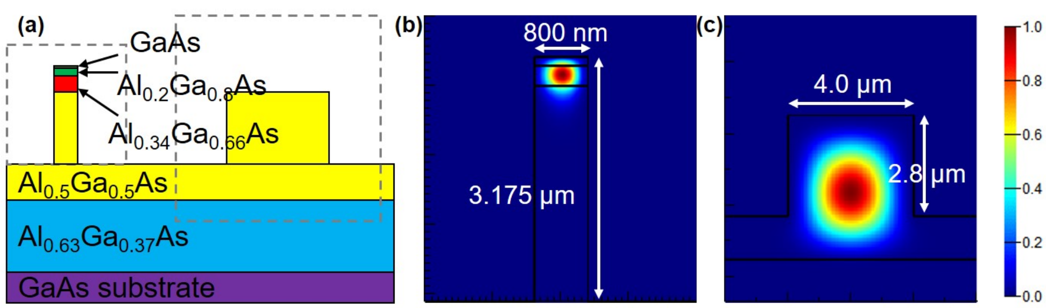

Figure 5.1 a) Wafer structure and schematics of Device WG and Coupling WG. b) TE_{00} mode profile for an 800 nm wide and 3.175 µm deep Device WG. c) TE_{00} mode profile for a 4 µm wide and 2.8 µm deep Coupling WG. Figures are from [153].

The wafer used in the experiment consists of five layers of AlGaAs with different aluminum concentrations. They are a 5 nm of GaAs, 120 nm of $Al_{0.2}Ga_{0.8}As$, 250 nm of $Al_{0.34}Ga_{0.66}As$, 4 μm of $Al_{0.5}Ga_{0.5}As$ and 3.5 μm of $Al_{0.63}Ga_{0.37}As$ from top to bottom, and are grown on an *n*-type (100) GaAs substrate. The first three layers on the top are suitable for implementing high refractive index contrast waveguides (termed Device WGs) for on-chip signal processing. The two bottom layers were designed as a large-dimension waveguide (or Coupling WGs) for efficient end-fire coupling to single mode fibers. A schematic of the wafer structure is shown in Figure 5.1(a). Modal fields were simulated using Lumerical® MODE Solutions. The Device WG has a width of 800 nm and a height of 3.175 μm whereas the Coupling WG has a width of 4 μm and a height of 2.8 μm. The electric field intensities of the TE_{00} modes of the Device WG and Coupling WG are shown in Figure 5.1(b) and (c), respectively.

5.2.2 Optimization of device parameters

Monolithically integrated SSCs on GaAs substrate can be sorted into two main categories [148]. In the first category, SSCs include vertical and lateral tapers to adiabatically transfer optical power between waveguides. This approach requires epitaxial regrowth and a more complicated fabrication process. In the second category, SSCs transfer optical power by means of lateral tapers and do not require epitaxial regrowth. We adopted a two-step lateral tapering scheme. The Device WG includes the 5 nm GaAs cap layer, the 120 nm $Al_{0.2}Ga_{0.8}As$ upper cladding and the 250 nm $Al_{0.34}Ga_{0.66}As$ core layer. The Coupling WG includes the 4 μm $Al_{0.5}Ga_{0.5}As$ as its core layer and the 3.5 μm $Al_{0.63}Ga_{0.37}As$ as its lower cladding layer. The dimensions of the Coupling WG were optimized for highest modal overlap with the fundamental mode of a lensed SMF (OZ optics, TSMJ-3U-840-5/125-0.25-23-2.9-13-1-AR) at the wavelength of 850 nm.

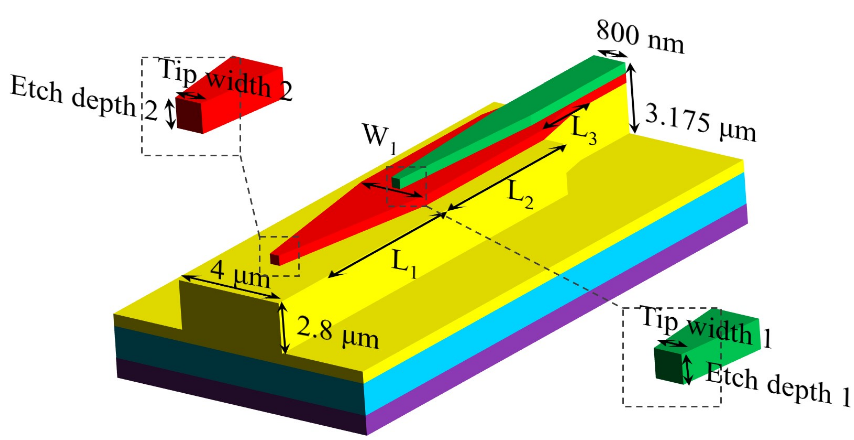

Figure 5.2 Perspective view of the proposed SSC. The Device WG is green, the Transition WG is red, and the Coupling WG is yellow. Figure is from [153].

Since the dimensions of the Device WG and Coupling WG have been set in the epitaxial wafer structure, the design focus is the tapers. The design parameters of the tapers are noted in Figure 5.2. The width of the Device WG is tapered down from 800 nm to 200 nm, a critical dimension that can be easily achieved using electron beam lithography (EBL), over a length of L_2. The width of the transition waveguide (Transition WG), which is shown in grey in Figure 5.2, is tapered down from W_1 to 200 nm over a length of L_1. A third taper section that connects the Device WG and the Transition WG is added, which mainly ensures smooth conversion and eliminates beating effects but does not influence overall conversion efficiency much. As such, its length, L_3, is set to a constant value, 100 µm.

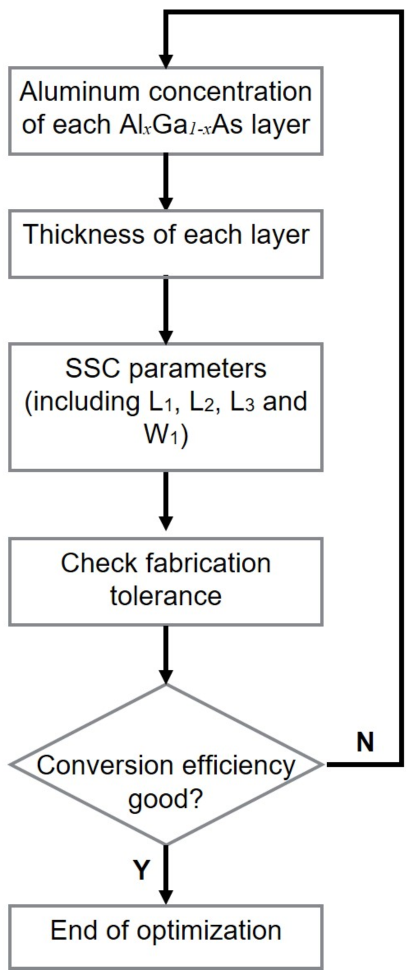

Figure 5.3 Iterative optimization process of the device parameters.

The initial values of L_1, L_2 and W_1 are 600 µm, 280 µm and 2.4 µm, respectively. These parameters were optimized iteratively, as shown in Figure 5.3. Firstly, we optimized L_2 and W_1

by monitoring the conversion efficiency of Device WG TE_{00} mode to Coupling WG TE_{00} mode with RSoft CAD® BPM. The results are shown in Figure 5.4(a). As can be seen, the optimum value for the Transition WG width W_1 is about 2.4 μm and that for L_2 is 280 μm. Secondly, we optimized L_2 and L_1. As shown in the Figure 5.4(b), the conversion efficiency is more sensitive to L_2 than L_1. The optimum values of L_2 and L_1 are about 600 μm and 280 μm, respectively. Thirdly, we confirmed that the set of values of L_2=600 μm and W_1=2.4 μm were optimized, as shown in Figure 5.4(c). Lastly, final taper simulation results are shown in Figure 5.5. A total length of about 1000 μm was necessary and a theoretical conversion efficiency of 97% (or –0.1 dB) was obtained.

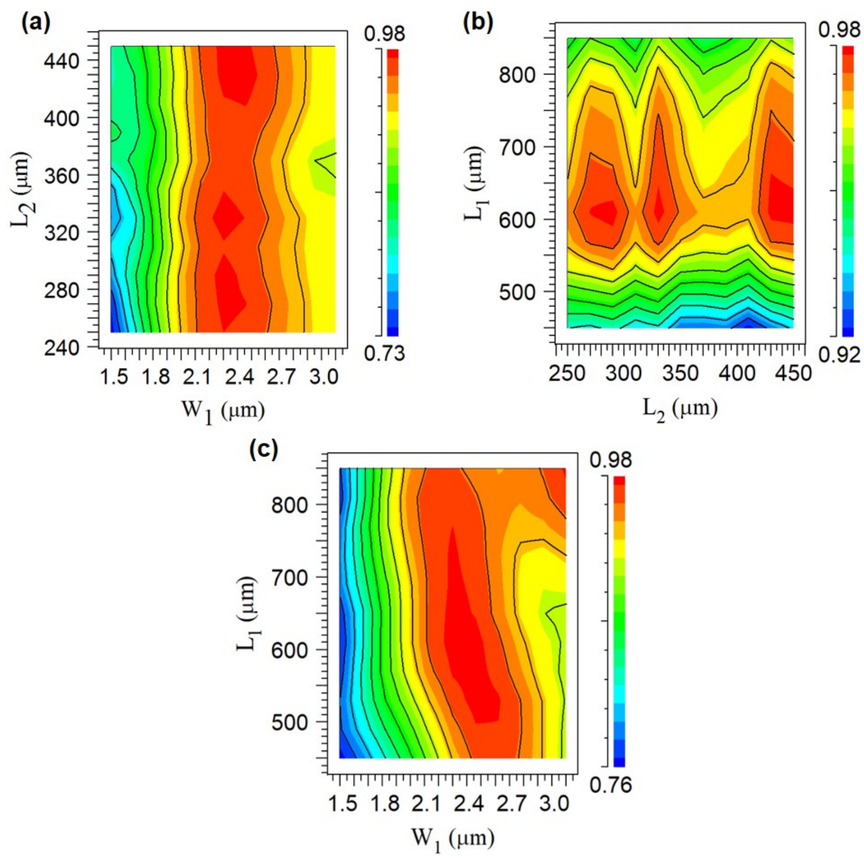

Figure 5.4 a) Conversion efficiency of SSCs dependence on L_2 and W_1, b) L_2 and L_1, c) L_1 and W_1. Figures are from [153].

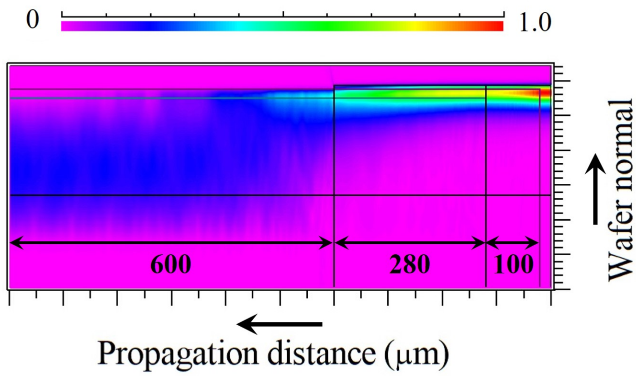

Figure 5.5 Finalized SSC dimensions and its simulation. Figure is from [153].

5.2.3 Fabrication tolerance study

We studied the fabrication tolerance of the critical design parameters of the SSC, especially the two shallow etch depths and two taper tip widths. It is found that etch depth 2 (which is required to create the Transition WG shown in red in Figure 5.2) is more tolerant compared to etch depth 1 (shown in green in Figure 5.2). While etch depth 2 can vary by 40 nm (16% of targeted 250 nm) with only a 5% reduction in conversion efficiency, the same amount of variation in etch depth 1 (20 nm, 16% of targeted 125 nm) would induce a 10% reduction in conversion efficiency. Overall, the conversion efficiency is higher than 88%, as shown in Figure 5.6(a). In fact, the target depths of 125 nm and 250 nm are easy to achieve with the 0.25 nm/s etch rate as discussed in Chapter 4.

Overall, the fabrication tolerance of taper tip widths is very high. As shown in Figure 5.6(b), a 100% variation (of 200 nm target width) in taper width 1 (shown in green in Figure 5.2), the conversion efficiency reduces by only 9%, while the same amount of variation in taper tip width 2 (shown in red in Figure 5.2) barely affects the conversion efficiency. In conclusion, etch depth 1 and taper tip width 1 are the most critical dimensions in achieving a high experimental conversion efficiency.

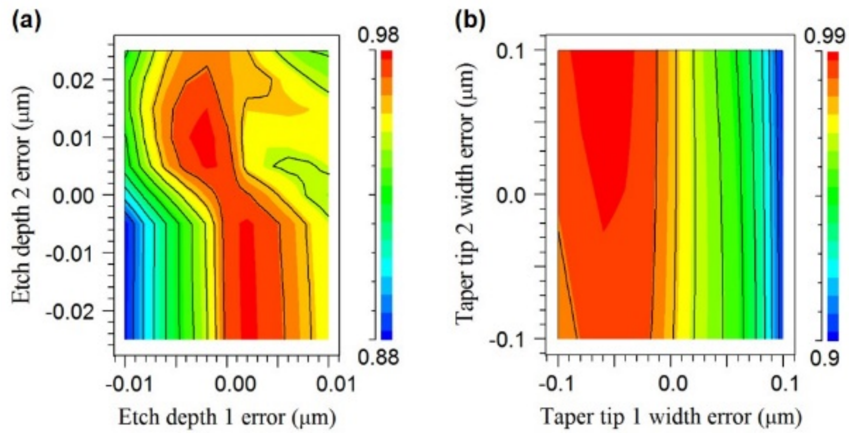

Figure 5.6 Fabrication tolerance of a) two shallow etch depths and b) two taper tip widths. Positive (negative) values on x and y axis means larger (smaller) than target depths or widths were achieved. Figures are from [153].

5.2.4 Device fabrication

Device fabrication involved electron beam lithography (EBL) followed by inductively-coupled plasma, reactive ion etching (ICP-RIE). In order to achieve precise and highly anisotropic etching, which was critical in fabricating the SSC, the two recipes developed in Chapter 4 were used [109]. The first recipe gives an etch rate of 0.25 nm/s while the second one gives an etch rate of 20 nm/s. Firstly, we masked the sample with HSQ using EBL, used the slow etch recipe to etch through the 5 nm GaAs and 120 nm $Al_{0.2}Ga_{0.8}As$, and achieved an accurate etch depth of 125 nm. We then removed the HSQ using buffered oxide etcher (BOE). Next, a second masking layer of HSQ was deposited and patterned using EBL. This layer was used to etch through the 250 nm $Al_{0.34}Ga_{0.66}As$ layer using the slow-etch recipe. After etching, the HSQ mask was again removed using BOE. Lastly, we masked the sample with HSQ and patterned the coupling waveguide structures using EBL. The fast etch recipe was used to etch 2.8 μm into the 4 μm $Al_{0.5}Ga_{0.5}As$ layer.

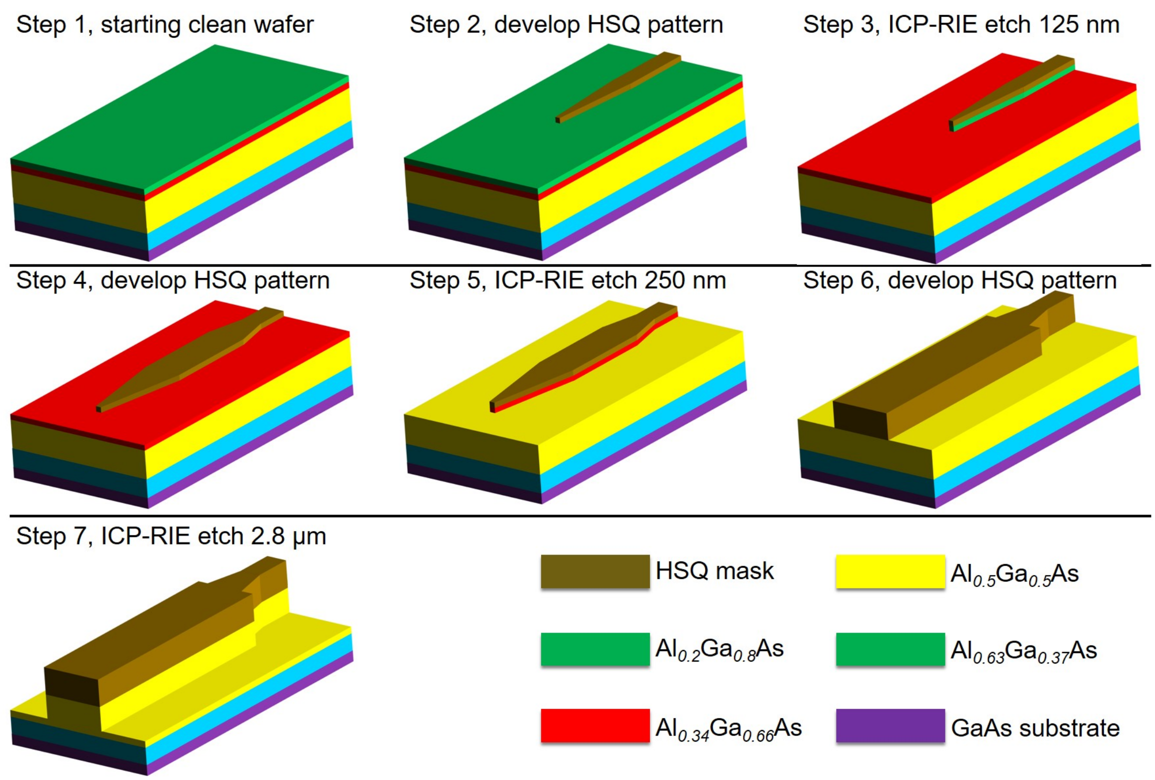

Figure 5.7 Main fabrication steps of the proposed SSC. Note, the 5 nm GaAs cap layer has been omitted to make the figures more concise.

The main fabrication steps are shown in Figure 5.7. Since the fabrication process requires multiple etching steps, alignment markers should be prepared. First, double-layer photoresist (PMMA on MMA) was deposited and patterned using EBL. Second, tungsten was sputtered on to the sample using a sputter system (AJA International ATC Orion 5 Sputter Deposition System). Finally, a lift-off process left the clean sample with tungsten squares with a 20×20 μm^2 area. The alignment markers were covered by the HSQ mask and protected in each etching step. The preparation of alignment markers is not reflected in Figure 5.7. As a result, there supposed to be square alignment markers close to the edges of the sample in Figure 5.7. However, in order to make the figures more concise, the alignment markers are not shown.

We used a Ti:sapphire laser as a light source at the wavelength of 850 nm to excite fundamental TE modes of the waveguides. The input and output objective lenses were Newport M-60x (0.85 NA and 2.9 mm focal length) and Newport M-40x (0.65 NA and 4.5 mm focal length), respectively, for the measurement of the waveguide output mode profiles, Device WG propagation loss and the conversion efficiency of the SSC. Some SEM images of fabricated

SSCs along with measured waveguide output mode profiles are shown in Figure 5.8. The propagation loss of Device WG was measured using samples with straight Device WGs of various lengths. The output power from the Device WG was measured as a function of waveguide length. An average propagation loss of 6.7 dB/cm was measured.

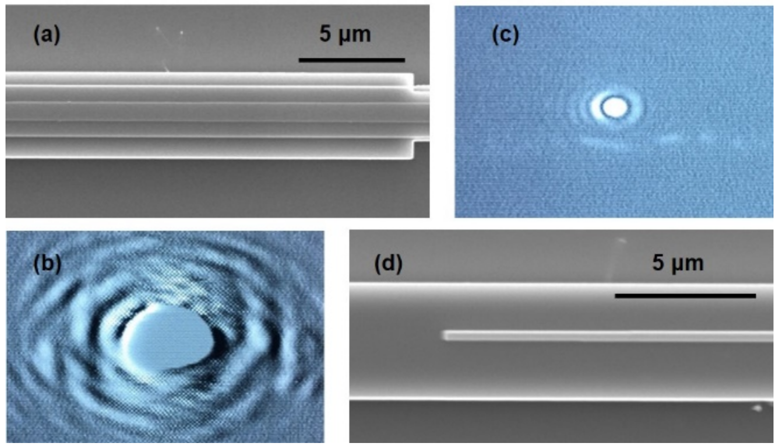

Figure 5.8 SEM images of (a) the starting section and (d) ending section of a spot-size converter. Measured output mode profiles of (b) Coupling WG and (c) Device WG. Figures are from [153].

5.2.5 Conversion efficiency measurement

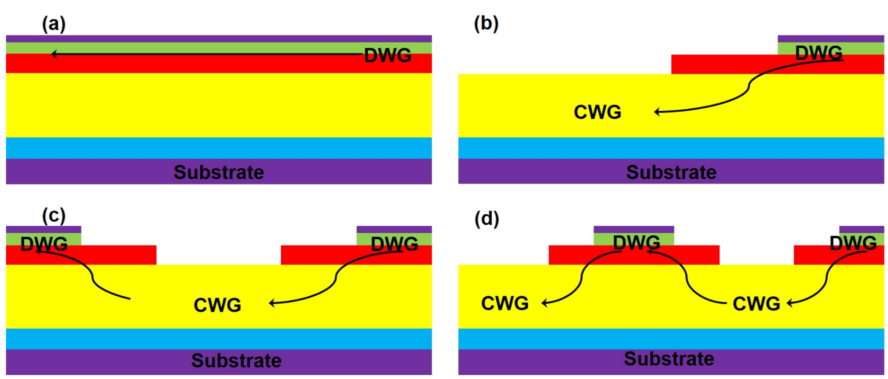

Figure 5.9 Schematics showing four groups of devices which integrated (a) zero, (b) one, (c) two, and (d) three SSCs.

In order to measure the conversion efficiency of SSCs, four groups of SSC devices were fabricated, as shown in Figure 5.9. The first group consisted of straight Device WGs which ran all the way from input facet to output facet, and served as a reference group. In other words, zero

SSC were integrated in this group. The second group included one SSC that coupled light from Device WG to Coupling WG. The third group included two SSCs which coupled light from Device WG to Coupling WG, then back to Device WG. The fourth group included three SSCs which coupled light from Device WG to Coupling WG, then to Device WG, and finally to Coupling WG. Lengths of all these devices were the same and about 5 mm. We kept the input optical power before the input lens constant at 1 mW for all the devices and measured the output power. The output power of all four groups was normalized to the first group, as shown in Figure 5.10. Each data point represents the average output power of one group of devices.

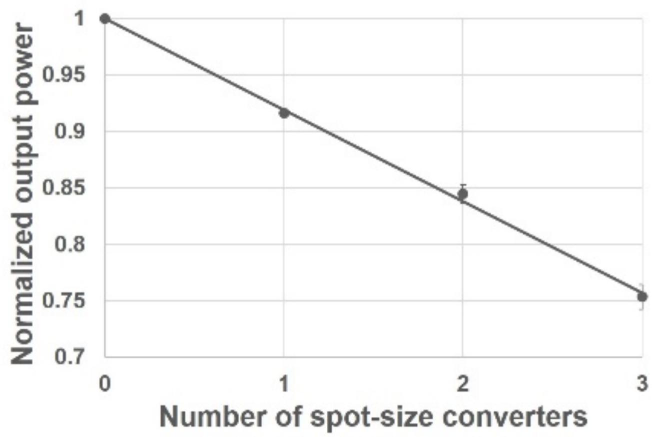

Figure 5.10 Normalized output power of the four groups of devices with different number of integrated SSCs. Figure is from [153].

Using the experimental data in Figure 5.10, we measured an average conversion efficiency of (91$\pm$0.2)% for the spot size converters that we designed and fabricated. The propagation loss of the Coupling WG was fitted using the experimental data and was found to be negligible over the device lengths used. In order to measure the coupling efficiency between the Coupling WG and a SMF, we used two lensed SMFs with a focused beam waist of 2.5 μm (OZ optics, TSMJ-3U-840-5/125-0.25-23-2.9-13-1-AR). A group of straight Coupling WGs, which ran all the way from the input facet to the output facet, were used. The input power from the SMF to the Coupling WGs was 1 mW. After the light propagated in the Coupling WG for about 5 mm, the output power collected using the second SMF was 304 μW. Assuming the propagation loss of the Coupling WG was negligible over the device lengths used, as we had previously demonstrated, and that light was only lost at the input and output facets, the above results translated into a coupling efficiency of 55% per facet between the Coupling WG and a SMF. The effective index of the fundamental TE/TM modes of the Coupling WG was 3.251, giving rise to a Fresnel reflection coefficient of 28% between air and the Coupling WG. After correcting for the Fresnel reflection, a 77% power overlap coefficient was obtained. The result agreed well with the theoretical power overlap coefficient between the fundamental TE/TM modes of the Coupling WG and those of the SMF by Lumerical® MODE Solutions, which was calculated to be about 80%. The same approach was used to measure the power overlap coefficient between the Device WG and the SMF, which was 15% after correcting the Fresnel reflection. The integration of SSCs increased the coupling efficiency by fivefold. We theoretically studied the displacement tolerance for two cases: with and without SSCs. The 1-dB horizontal and vertical displacement tolerances for the Coupling WG were both 1.4 μm. The 1-dB horizontal and vertical displacement tolerances for the Device WG were both 0.9 μm.

5.2.6 Comparison to literature results

A comparison of our results to the literature is listed in Table 5.1. As for SSCs in silicon as demonstrated in [143] and [144], they are not compatible with the idea of MGVI even though they are quite compact. For [149], vertical couplers were integrated. As discussed in Section 5.2.2, this approach requires epitaxial regrowth and a more complicated fabrication process, which makes it incompatible with MGVI. Even so, our experimental results show some improvement. Our experimental results are better than those in [150], which also utilized two-step lateral tapering scheme. Compared to [151] and [152], which utilized one-step lateral tapering scheme, our results are better as expected. Overall, our results are competitive compared to results based on a similar integration scheme found in the literature.

Table 5.1 Comparison of our experimental results to the literature.

Material system	Taper loss	Input loss	Total loss	SSC length	λ	Comments
	dB/cm			μm	nm	
Silicon	6.0	-	9.2	40	1550	A bottom waveguide is not formed [143]
Silicon	0.2	1.2	1.5	400	1550	Deposited 1.2×1.2 μm^2 SiON [144]
InP	0.6	1.1	1.7	400	1550	Vertical tapers were integrated [149]
InP	0.7	-	-	1100	1550	Two-step lateral tapering [150]
GaAs	1.4	0.9	2.3	1000	1310	One-step lateral tapering [151]
GaAs	1.8	0.8	2.6	800	1310	One-step lateral tapering [152]
GaAs	0.4	1.1	1.5	1000	850	This work, two-step lateral tapering [153]

5.3 Conclusion

In conclusion, we have designed and fabricated a vertically integrated SSC in $Al_xGa_{1-x}As$/GaAs, which allows for an efficient and displacement-tolerant coupling of the SMF to the Device Waveguide, via Coupling Waveguide. The measured insertion loss on a transmission from the Coupling to the Device Waveguide is only 0.4 dB, (91$\pm$0.2)% transmission, suggesting high efficiency of the adiabatic tapering system that connects two waveguides. SMF to the Device Waveguide insertion loss measured at -3 dB (-1.5 dB after correction for 28% Fresnel reflection at uncoated facet), still leaving a room for improvement, e.g. by optimization of the Coupling Waveguide layer structure and layout. Results are published in [153]. Demonstration of the vertically integrated SSC well-performing at 850 nm marks a major step towards building the TAVI platform in GaAs as a versatile and cost-efficient PIC technology for applications in data center interconnects, non-invasive biosensing, and quantum optics.

Chapter 6
Arrayed waveguide gratings

6 Arrayed waveguide gratings

One of the key applications of the vertical integration approach in $Al_xGa_{1-x}As$ is the realization of a compact wavelength division multiplexing (WDM) device which can combine multiple wavelength channels around 850 nm. This chapter discusses the working principle of arrayed-waveguide gratings (AWGs), including the multiplexing properties and performance characteristics such as free spectral range, crosstalk, insertion loss and uniformity. The design procedures are presented step by step in detail. A range of fabrication challenges are discussed. The proof-of-concept demonstration of AWGs as on-chip signal processing devices proves the applicability of multi-guide vertical-integration (MGVI) scheme in the $Al_xGa_{1-x}As$ semiconductors.

6.1 Introduction

Arrayed waveguide gratings (AWGs) were first reported by M. Smit in 1988 as novel focusing and dispersive devices which can be used as (de)multiplexers and wavelength filters [154, 155]. Since then, AWG devices have been widely used in systems that involve wavelength division multiplexing (WDM) in telecom applications. Various materials such as silica [156, 157], silicon [158], silicon nitride [159, 160], germanium [161], polymers [162, 163], III-V semiconductors (InP, GaAs and InGaAsP) [164-166] have been used. Besides their applications as wavelength multiplexers or demultiplexers, the use of AWG devices for optical sensing [167], quantum information technologies [168] and as micro-spectrometers [158] have also been reported in the literature.

Most of the current AWG devices operate in the near-infrared wavelength region because the low-loss windows at 1310 nm or at 1550 nm are used for fiber optics communication. However, near-infrared light is not recommended for biosensing in an aqueous environment because of the strong absorption of light by water, which may cause detrimental heat, or unwanted optical signal absorption [169]. The absorption will easily heat and even kill the biological cells. With the recent advances in big-data related business and cloud-computing services, intra-data-center traffic is growing at a rate of 22% a year [1]. The current intra-datacenter network is facing the problem of the power consumption increase driven by the ever-increasing traffic. As current data center communications use 850 nm vertical cavity surface emitting lasers (VCSELs), monolithic integration would enable efficient wavelength division multiplexing (WDM) devices for data communications. The work in this Chapter was aimed at designing an AWG working in the range of the near infrared (NIR) region around 850 nm.

To fully harness the power of photonic integrated circuits (PICs), the ability of monolithically integrating passive and active devices on a single chip is highly desired. As discussed in Section 1.4, $Al_xGa_{1-x}As$ materials can meet the challenges. Monolithic integration in $Al_xGa_{1-x}As/GaAs$ would enable efficient wavelength division multiplexing (WDM) devices. There is a potential to use $Al_xGa_{1-x}As/GaAs$ as a platform for PICs in the cost sensitive application. $Al_xGa_{1-x}As$ has also been identified as the promising semiconductor system for quantum optics.

6.2 AWG configuration and working principle

In this chapter, the AWGs consist of a single input waveguide, two symmetrical Rowland type star couplers [170], phased array waveguides, and between four and eight output waveguides. With reference to the AWG schematic in Figure 6.1(a) and the expanded view of a star coupler on the receiver side in Figure 6.1(b), the general operation is as follows [170].

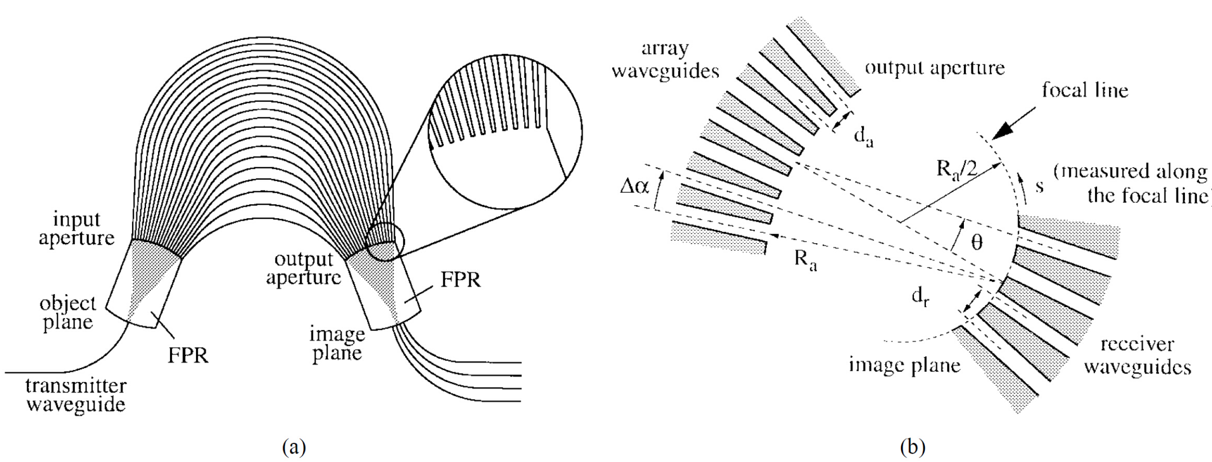

Figure 6.1 (a) Layout of the AWG demultiplexer. (b) Geometry on the receiver side. Figures are from [170].

The mode traveling in the input waveguide is incident on the object side of the first star coupler. Once inside the star coupler, the mode is no longer laterally confined by the waveguide and expands, or diffracts over the length of the star coupler. The surface shape of the image side of the first star coupler is circular and concave with the same radius as the expanding wavefront so that all of the light entering the phased array has the same phase. The phased array consists of multiple waveguides which have a constant path length difference ΔL between any two adjacent waveguides equal to an integer multiple of the central device wavelength in the material, λ_0. In other words, the phase of the wavefront incident on the phased array waveguides is mapped to the object side of the second star coupler. Since the object surface of the second star coupler has a convex shape, the diverging wavefront on the image side of the first star coupler has been mapped to a converging wavefront as the object in the second star coupler. The second star coupler is also a free-propagation region which allows the wavefront to continue to converge and focus on the image side of the second star coupler where the output waveguides are located. To provide a spectral filtering response, an output waveguide is positioned on the star coupler at the focal point where the wavelength of interest comes to a focus. For wavelengths other than the central wavelength, the constant path length difference ΔL produces a phase delay which causes a wavelength dependent wavefront tilt. As a result, wavelengths longer than the central wavelength produce a phase tilt which is counterclockwise (i.e., positive θ direction or positive s direction defined in Figure 6.1) and shorter wavelengths produce a clockwise phase tilt. The magnitude of the tilt is proportional to the difference between the channel wavelength and the central wavelength λ-λ_0. The wavefront tilt causes the focal position to shift in the direction of the tilt laterally on the image side of the second star coupler. As the wavelength increases, the focal position moves in the positive s direction. The position for each output waveguide coincides with the focal positions of the desired wavelengths for transmission.

6.2.1 Performance characteristics

Some of the most important AWGs performance characteristics include crosstalk, uniformity of transmission and insertion loss.

Crosstalk is defined as the unwanted signal in a wavelength channel caused by the coupling of energy from another channel and is of most concern in the phased array and the second star coupler output. The most probable causes of crosstalk in the AWGs are evanescent coupling between adjacent output and phased array waveguides, background radiation due to the shallow etch waveguide structure, field truncation at the star coupler and fabrication error. Evanescent coupling occurs if two waveguides are placed too close to each other. When this happens the tail of the electric field of one waveguide extends in to the second waveguide and coupling between the two waveguides can take place. Typically, there are only two places in an AWG geometry where this is of concern, the phased array waveguide spacing d_p (subscript p for phased array waveguide) and the input and/or output waveguides spacing d_o on the star couplers. Crosstalk can be reduced by enlarging the waveguide spacing. However, as the phased array waveguide spacing is increased, less of the mode incident on the phased array from the first star coupler will couple into the phased array, increasing the insertion loss. Therefore, waveguide separation is a trade-off between crosstalk and insertion loss.

Another source of crosstalk is the slab-mode at the input coupled to the output waveguides. Shallow ridge waveguides support slab modes which can propagate through the substrate and cause background noise in the output and increase crosstalk. The slab mode originates from light on the input. Since the mode emanating from a fiber is much larger than the semiconductor waveguide profile, light can also be coupled into the slab mode. If the output waveguides are directly across the wafer from the input waveguides and since semiconductor devices are generally very short in length, the slab mode can cause a large amount of background noise. A common solution to this is to offset the input waveguides to the output waveguides by 90 degrees. One of the advantages of using $Al_xGa_{1-x}As$ semiconductors is that the GaAs substrate is absorbing and the slab mode which scatters in the substrate will be absorbed.

A finite number of phased array waveguides captures a finite portion of the incident mode in the first star coupler. The captured field by the phased array is therefore truncated. The image on the output waveguides is the Fourier transform of the object field in the second star coupler. The Fourier transform of a truncated field produces side lobes in the output which contributes to crosstalk. Crosstalk due to this truncation is minimized in design by reducing the amount of truncation by increasing the number of phased array waveguides.

In practice, the crosstalk in AWGs are not limited by design, but by fabrication errors. For strong constructive interference and small crosstalk, the light from all paths through the AWG has to arrive with the correct relative phase generated in the phased array. Fabrication inhomogeneities, including varying waveguide width or height, imperfect etching of waveguide surfaces in the phased array, and the filling in of the gaps between the waveguides near the star coupler are the major sources of phase error in AWGs.

Uniformity is defined as the difference in the power levels of the central wavelength and outer most wavelength. If the wavelength is changed, it will move through the image plane and follow the envelope described by the far-field of the individual array waveguides. If we approximate the modal field of the array waveguides as a Gaussian beam and neglect the effects of coupling on the beam shape, we can derive some simple analytical equations for estimating insertion loss, channel nonuniformity and bandwidth.

6.2.2 Device variable declaration

Rowland type star couplers will be the couplers in this design [170]. The length of the coupler is R, which is also the radius of curvature at the surface adjacent to the phased array. The surface adjacent to the input and output waveguides has a radius of curvature of $R/2$. Separation of the phased array waveguides d_p adjacent to the star couplers are held constant. The sequencing of the phased array waveguides starts from the one with the shortest distances. We are designing a demultiplexer, therefore the second coupler has multiple output waveguides. d_o is the separation of output waveguides adjacent to the second star coupler. The modal refractive index in the phased array and in the star couplers are n_p and n_s, respectively. x, which is the focal point on the image side of the second coupler, is a rotational coordinate and increases in a clockwise fashion. The position of the input waveguide on the first star coupler is denoted as x_1. Lastly, m is an integer that represents the grating order. Note, d_o and d_p are center-to-center distance between waveguides. The variables are noted in Figure 6.2 and listed in Table 6.1.

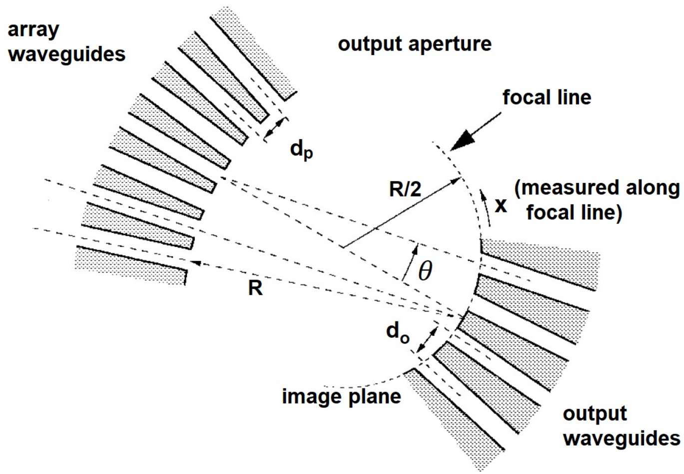

Figure 6.2 Geometry on the output star coupler with dimensional parameters.

Table 6.1 List of device design variables.

R	the radius of curvature at the surface adjacent to the phased array
$R/2$	radius of curvature at the surface adjacent to the input and output waveguides
d_p	separation of the phased array waveguides adjacent to the star couplers
d_o	separation of output waveguides adjacent to the second star coupler
n_p	modal refractive index in the phased array
n_s	modal refractive index in the star couplers
n_g	group index in the phased array
x	the focal point on the image side of the second coupler
x_1	position of the input waveguide on the first star coupler
m	an integer that represents the grating order

6.2.3 AWG theoretical model

The phase equation for an AWG is as follows [170]

$$\frac{n_s(\lambda)x_1 d_p}{R} + n_p(\lambda)\Delta L - \frac{n_s(\lambda)x d_p}{R} = m\lambda$$

…………………………… (Equation 6.1)

According to Equation (3.3) in reference [171],

$$\lambda_0 = \frac{n_p(\lambda_0)\Delta L}{m}$$

…………………………… (Equation 6.2)

is called the center wavelength.

The channel spacing is 415.2 GHz, which is 1 nm around 850 nm, as opposed to 0.2 nm that is usually defined for DWDM around 1550 nm. In the above equation, n_p and λ_0 are known variables, which can be found in Table 6.1, m and ΔL are to be determined. The AWGs in this thesis consist of a single input waveguide located in the center of the first star coupler. Therefore, the central wavelength focuses at position x equal to zero which is at the center of the output star coupler. At other wavelengths,

$$x(\lambda) = \frac{\left[m\lambda - n_p(\lambda)\Delta L\right]R}{n_s(\lambda)d_p}$$

…………………………… (Equation 6.3)

6.2.3.1 AWG dispersion

In an AWG, the path length difference ΔL causes the focal length position to shift laterally along x, which denotes the image position on the output side of the second star coupler. In designing AWGs, the dispersion of the focal position dx with respect to the wavelength $d\lambda$ is defined as $\Delta x/\Delta\lambda = dx/d\lambda$, which can be found by differentiating both sides of Equation 6.3. When the bandwidth of the device is small, which is usually the case for DWDM system, the differentiation will only depend on geometrical parameters.

The path length difference ΔL, required to satisfy the interference condition is found by setting differentials Δx and $\Delta\lambda$ equal to the output waveguide spacing d_o and wavelength channel spacing $\Delta\lambda$, respectively. The following important equation can be found:

$$\Delta L = \frac{n_s d_p d_0 \lambda_0}{n_g R \Delta\lambda}$$

…………………………… (Equation 6.4)

The definition of the parameters in the above equation can be found in Table 6.1. For waveguide with a strong confinement factor and little refractive index dispersion ($n_g \approx n_s$), the above can be rewritten as $\Delta L = d_p d_o \lambda_0 / R\Delta\lambda$. However, usually the original form has to be kept as n_s and n_g are different.

6.2.3.2 Free spatial range

The free *spatial* range of the *m*-th and *(m+1)*-th order for the central wavelength of the AWG is obtained by

$$X_{fsr} = x_m - x_{m-1} = \frac{\lambda_0 R}{n_s d_p}$$

…………………………… (Equation 6.5)

6.2.3.3 Number of channels

The number of available wavelength channels is found by dividing the free spatial range by the wavelength channel spacing.

$$N_{chan} = \frac{X_{fsr}}{d_o} = \frac{\lambda_0 R}{n_s d_p d_o}$$

…………………………… (Equation 6.6)

6.2.3.4 Free spectral range

The free spectral range of the *m*-th and *(m+1)*-th order is found by using the AWG dispersion

$$\lambda_{fsr} = \frac{X_{fsr}}{dx/d\lambda} = \frac{\lambda_0}{m'}$$

…………………………… (Equation 6.7)

The definition of free spectral range is consistent with the grating theory when the *modified* grating order is defined as

$$m' = n_g m / n_p$$

…………………………… (Equation 6.8)

6.2.4 Step-by-step AWG Design

6.2.4.1 Waveguide separation

To start designing an AWG, the first parameter to consider is the waveguide separations on the star couplers for the phase array and output waveguides: d, which can be d_p or d_o. They should be large enough to suppress evanescent coupling between adjacent waveguides, large enough to allow lithography and etching steps to take place, but small enough to avoid excess coupling loss. The dimensions of waveguide are given in Figure 4.1 and Figure 5.1.

Table 6.2 Overlap analysis based on the waveguide structure.

Gap	0.4 µm	0.6 µm	0.8 µm
Overlap	-9.2 dB	-23.4 dB	-49 dB

According to [171], -10 dB overlap has been suggested to be safe. Therefore, the gap can be as small as 0.4 µm. Waveguides gap increases quickly moving further away from star coupler, again, the gap should be large to allow lithography and etching. Recalculate the overlap when d = 1.2 µm (center-to-center distance of adjacent waveguides) using couple mode theory (two waveguides co-exist). The supermodes have almost identical effective indices n_{eff}, therefore, the beating length is long enough to suppress beating between two waveguides.

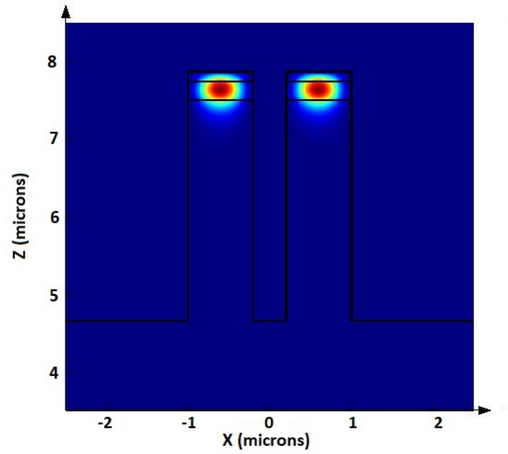

Figure 6.3 Electric field intensity of the symmetric supermode of the two coupled waveguides.

6.2.4.2 Star coupler length

The length of the star couplers affects the uniformity and crosstalk of the device. Uniformity of the device is defined as the power difference between outer channels and the center channels of the output waveguides. Using a Gaussian approximation, the far field intensity distribution can be expressed as follows [170]

$$I(\theta) = I_0 \exp\left(\frac{-2\theta^2}{\theta_0^2}\right)$$

…………………………… (Equation 6.9)

where θ equals the modal diffraction angle and θ_0 is the angular width of the Gaussian far field amplitude and equals

$$\theta_0 = \frac{\lambda_0}{n_s w \sqrt{2\pi}}$$

…………………………… (Equation 6.10)

where w, is the waveguide width, λ_0 is the center wavelength which is set to 850 nm, n_s (subscription s for 'slab') is the effective index of the waveguide mode in star couplers. Because the modes are no longer laterally confined due to the large dimension of the star couplers, we can calculate the effective index using a 1D model where only vertical confinement is considered. *w* should be the effective waveguide width, 445 nm, which can be obtained by inspecting the simulated mode [170].

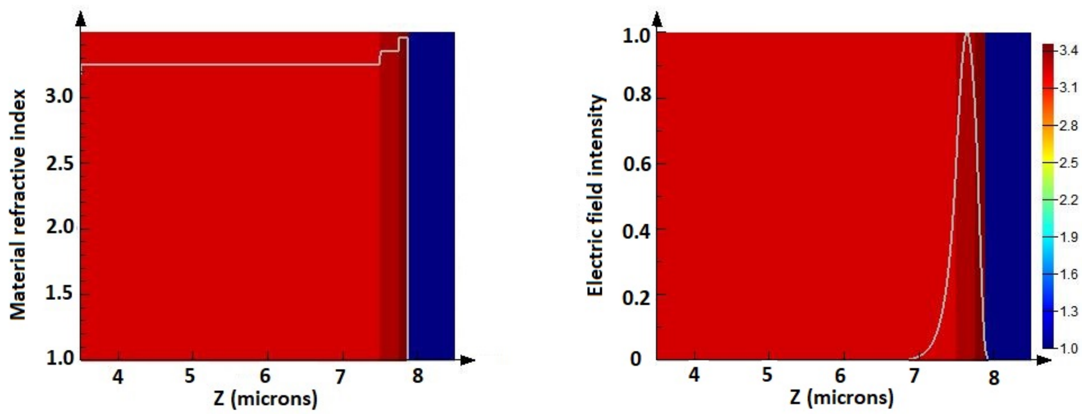

Figure 6.4 (a) Material refractive index of the wafer in the vertical (wafer growth) direction and (b) the slab mode profile in the star couplers.

According to the calculation, n_s = 3.2927. The modal effective index of the phased array, n_p = 3.2502. We can calculate

$$\theta_0 = \frac{\lambda}{n_s w\sqrt{2\pi}} = \frac{850\ nm}{3.2927 \times 445\ nm \times \sqrt{2\pi}} = 0.2317\ (radians)$$

…………………………… (Equation 6.11)

The uniformity L_u or power difference between the center channel and the outside channel is found by

$$L_u = -10 \times log\ \exp(\frac{-2{\theta_{max}}^2}{\theta_0^2})$$

…………………………… (Equation 6.12)

where θ_{max} equals the subtended angle of the outside phased array waveguide. To find θ_{max}, we need to set an acceptable uniformity, according to [170] [171], the L_u = -1.5 dB is reasonable. In this thesis, we pick a stricter value for L_u = -0.5 dB, as a result, θ_{max} = 0.0555 radians = 3.1825 degrees. Note, θ_0 and θ_{max} are half angles. Therefore, the minimal star coupler length is found using the following equation

$$R = \frac{N_{chan} d_p}{\theta_{max}} = \frac{2 \times (800\ nm + 400\ nm)}{\theta_{max}} = 43.204\ \mu m$$

…………………………… (Equation 6.13)

In the above equation, N_{chan} is the number of channels in the AWG. Since we are talking about half angles θ_0 and θ_{max}, $N_{chan} = 2$ corresponds to 5 total output waveguides. This R value should be compared to the one found in Section 6.2.3.3, where the equation is used

$$N_{chan} = \frac{X_{fsr}}{d_o} = \frac{\lambda_0 R}{n_s d_p d_o}$$

…………………………… (Equation 6.14)

Here, R should be large than 34 μm so that X_{fsr} is large enough to accommodate 6 channels (increased from 5 because we are considering X_{fsr} here). According to Section 6.2.3.4, the free spectral range should be larger than 5 nm. Let's put $\lambda_{fsr} = \frac{X_{fsr}}{dx/d\lambda} = \frac{\lambda_0}{m'} = 6\ nm$, therefore, (the modified) grating order should be smaller than 141.

6.2.4.3 Number of phased array waveguides

This parameter has been entirely omitted in reference [171]. The number of phased array waveguides affects the amount of field truncation at the first star coupler/phased array interface. More waveguides would increase sampling points of the first star coupler's field, suppress the side lobes and lower the crosstalk while increasing the transmission. More phased array waveguides require a longer star coupler to maintain good uniformity of the output and wider star coupler to allow room for the waveguides. However, longer star couplers increase the propagation loss. The output waveguide spacing d_o is the separation of output waveguides at the second star coupler d_o = 1.2 μm. Therefore, d_o/w = 2.7 according to [170], recalling that, w is the effective waveguide width w = 445 nm. According to equation (8) in [170], θ_0 is now different by a factor of $\sqrt{2\pi}$.

$$\theta_0 = \frac{\lambda}{n_s w\sqrt{2\pi}} = 0.2317\ (radian)$$

…………………………… (Equation 6.15)

Assuming a 0.5 dB non-uniformity L_u, gives a value of $\theta_{max} = 0.05555$. According to III-B in [170], s_{max} is equal to 2 times the output waveguide separation d_o, as we aim to design 5 wavelength channel waveguides. Therefore,

$$R = \frac{N_{chan} d_o}{\theta_{max}} = 43.204\ \mu m$$

…………………………… (Equation 6.16)

It has been suggested that the separation of the phased array waveguides should be small, d_p is the same as d_o. Using Equation (6.4) ,

$$\Delta L = \frac{n_s d_p d_0 \lambda_0}{n_g R \Delta\lambda} = 23.537\ \mu m$$

…………………………… (Equation 6.17)

There is an important parameter for calculating the number of arrayed waveguides, called aperture half angle. According to reference [170], $\theta_a = 2\theta_0 = 0.4634$. Therefore, number of phased array waveguides

$$N_a = \frac{2\theta_a R}{d_p} + 1 = 35$$

…………………………… (Equation 6.18)

Therefore, it is clear now that the number of phased array waveguides should be 35.

6.2.4.4 Path length difference

According to the equation below, ΔL can be calculated.

$$\Delta L = \frac{n_s d_p d_0 \lambda_0}{n_g R \Delta\lambda} = \frac{3.2927 \times 1.2\ \mu m \times 1.2\ \mu m \times 0.85 um}{3.963 \times 43.204\ \mu m \times 1\ nm} = 23.537 \mu m$$

.... (Equation 6.19)

To reduce the value, one can go back to redefine d_p and d_o and R. At this moment, let's keep ΔL as it is.

6.2.4.5 Phased array waveguide layout

A phase array geometry should consist of waveguides with large enough separation to restrict evanescent coupling and have minimum total path length to reduce propagation loss. The most common geometry is horseshoe or Ω shaped.

Table 6.3 AWG design results.

Number of channels	5
Channel spacing	1 nm
Center wavelength λ_0	850 nm
Number of phased array waveguide	35
Grating order m	90
Modified grating order m'	109 < 141
Path length difference ΔL	23.537 µm
Free propagation region length R	43.204 µm
Waveguide gap	400 nm
Non-uniformity	0.5 dB

6.3 Lumerical® MODE simulations

The design parameters from Table 6.3 are used to layout the various AWG components, i.e. input star coupler and output star coupler, and simulate the propagation of light through the complete device.

6.3.1 Input star coupler

The top view and perspective view of the input star coupler are shown in Figure 6.5. Light is input to the center of the five input waveguides in the fundamental TE mode of the waveguide, propagates in the input waveguide, disperses in the star coupler and gets sampled by the 35 arrayed waveguides. Using varFDTD of the Lumerical MODE, monitors are utilized to measure the propagation in the star coupler and power of light in the arrayed waveguides. The electric field profile showing the expansion of light in the star coupler is captured in Figure 6.6. The expansion results of the input electric field into the fundamental TE mode of the arrayed waveguides are shown in Figure 6.7. A total transmission of 0.881 (-0.6 dB) is simulated indicating a low insertion loss of the input star coupler.

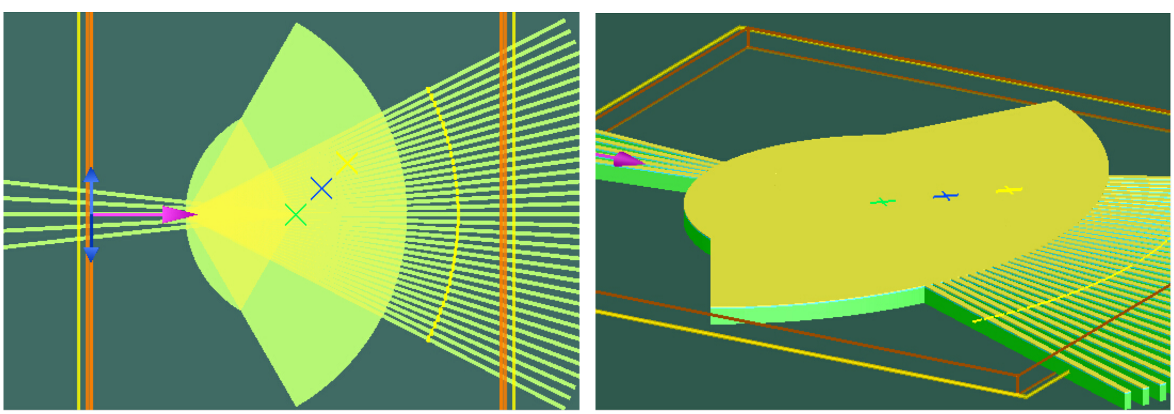

Figure 6.5 Top view (left) and perspective view (right) of the input star coupler.

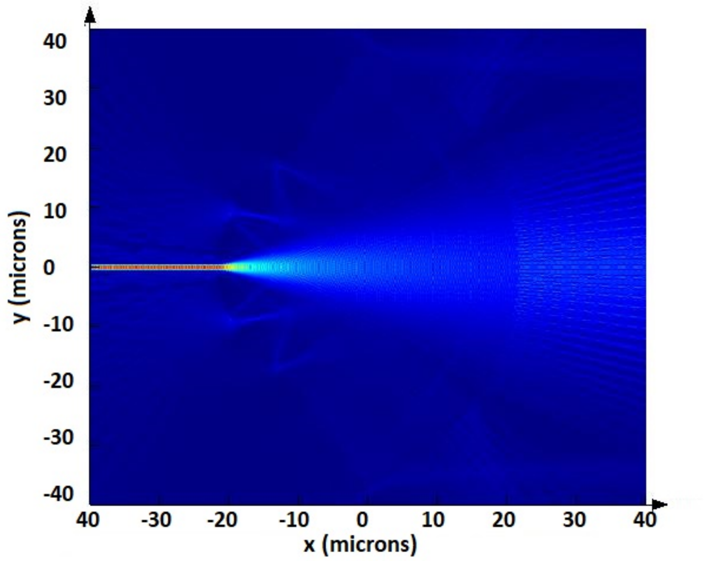

Figure 6.6 The electric field profile showing the expansion of light in the star coupler.

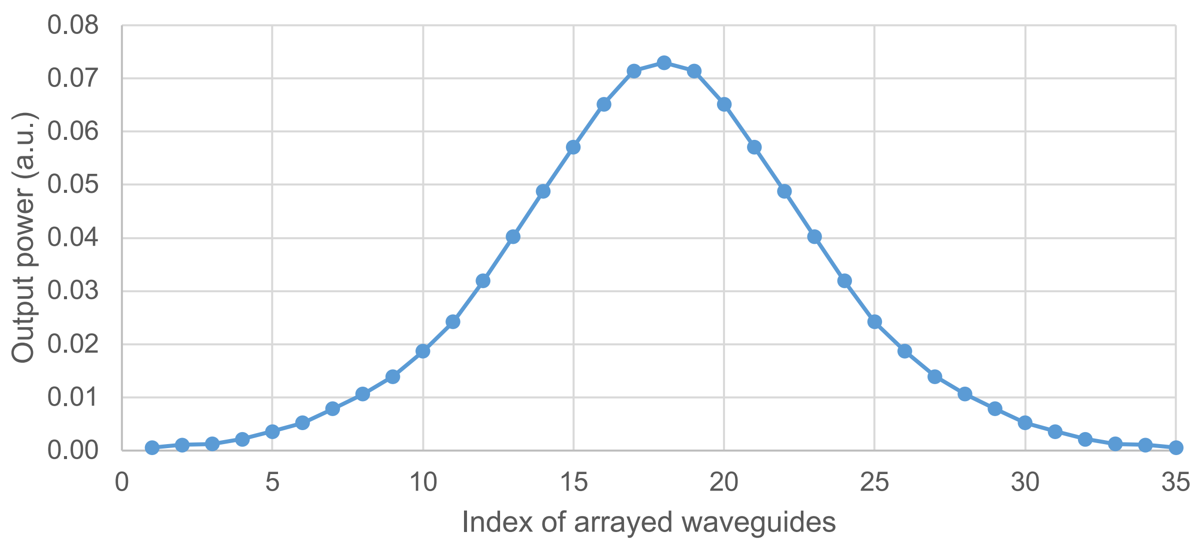

Figure 6.7 Expansion results of the input electric field into the arrayed waveguides.

6.3.2 Output star coupler

The top view and perspective view of the output star coupler are shown in Figure 6.8. The expansion results in the previous section are taken to be the power distribution in the arrayed waveguides before the star coupler. The design parameter ΔL in Table 6.3 is used to calculate phase delayed in the arrayed waveguides. Using varFDTD of the Lumerical MODE, monitors are utilized to measure the propagation in the output star coupler. The focusing features of light at a wavelength of 850 nm and 851 nm are shown in Figure 6.9 and Figure 6.10, respectively. The filtering results of the output coupler are shown in Figure 6.11. An average channel transmission of 0.390 (-4.1 dB) is obtained for the output coupler. The channel crosstalk is below -25 dB. The simulation results confirmed the design parameters in Table 6.3.

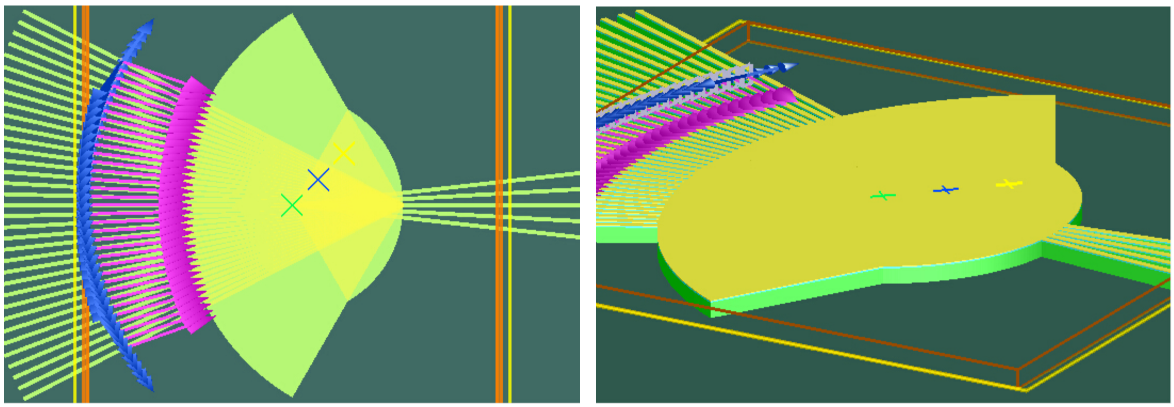

Figure 6.8 Top view (left) and perspective view (right) of the output star coupler.

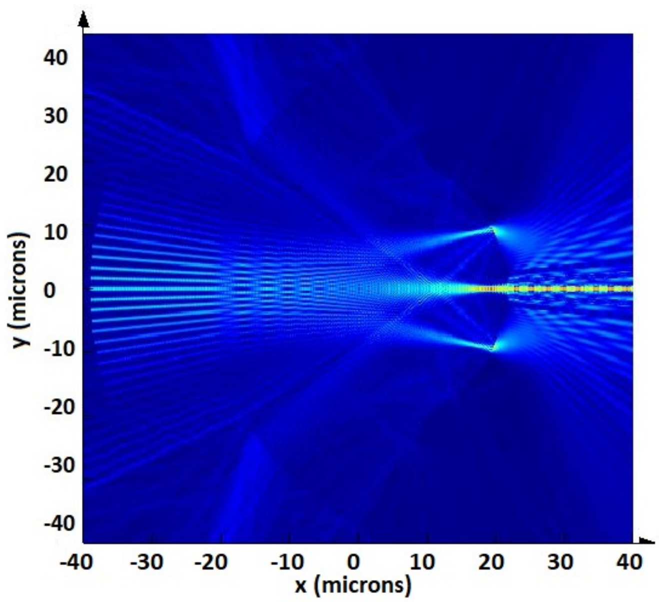

Figure 6.9 The electric field profile at the wavelength of 850 nm showing the focusing of light in the star coupler in to the center output waveguide.

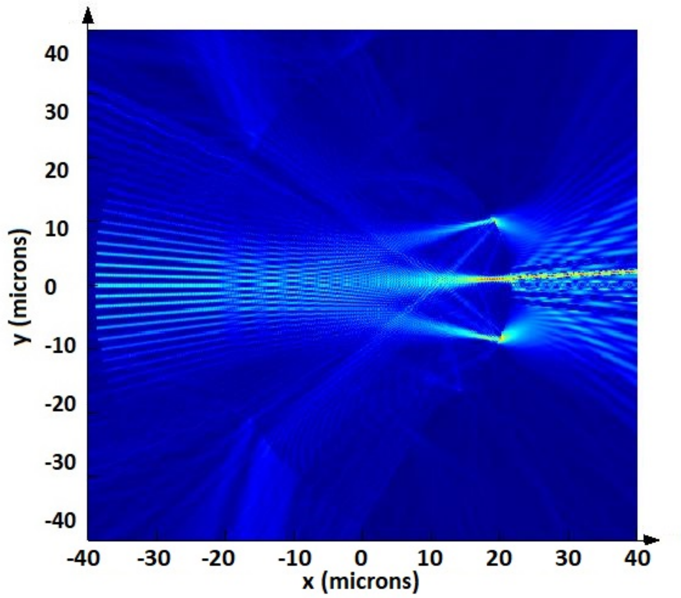

Figure 6.10 The electric field profile at the wavelength of 851 nm showing the focusing of light in the star coupler in to the next output waveguide.

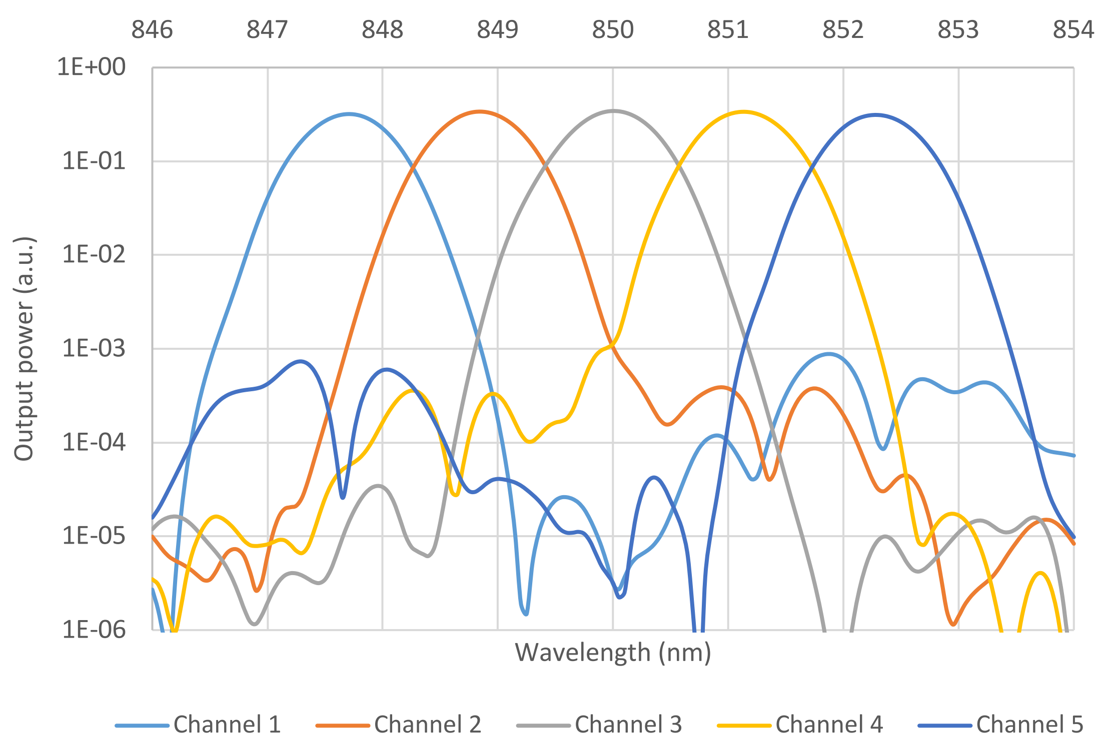

Figure 6.11 Wavelength filtering results in the output star coupler.

6.4 Preliminary fabrication results

Device fabrication involved electron beam lithography (EBL) followed by inductively-coupled plasma, reactive ion etching (ICP-RIE). In order to achieve precise and highly anisotropic etching, which was critical in fabricating the SSC, the two recipes developed in Chapter 4 were used [109]. In the region where the input waveguides, output waveguide, or arrayed waveguides join the star couplers, patterns are very dense. For instance, in order to etch deep waveguides, 600-nm thick HSQ is required. In addition, the gap between waveguides can be as small as 400 nm and these waveguides are densely positioned. In order to tackle the proximity issue during resist preparation and pattern development, a high aspect ratio HSQ development process is used. The procedures are shown in Table 6.4.

Table 6.4 High aspect ratio HSQ recipe.

Step 0	Use pure FOx15
Step 1	1500 RPM, 584 RPM^2 acceleration, 60 seconds, 600 nm thickness.
Step 2	250 °C hot plate bake, 3 mins
Step 3	Exposure dose 1000 - 1200 μC/cm^2 (aged HSQ dose tend to be lower.)
Step 4	Beamer fracture resolution 10 nm, current 5 nA, energy 100 kV.
Step 5	Developer (TMAH 25%) @ 80 °C, for 30 seconds – 1 min.
Step 6	DI water rinse 1.5 mins.
Step 7	Dip in IPA for 10 seconds.
Step 8	Nitrogen blow dry (be careful not to damage fine features.)
Step 9	Hard bake (post-exposure bake) 250 °C for 60 mins.

The optical microscope images of the developed HSQ resist are shown in Figure 6.12. The layout of the AWG is automated by WDM Phasar software. The AWG pattern was successfully developed on the HSQ mask using EBL. Next, the sample was etched using the fast etch recipe in one step to transfer the AWG pattern in to the wafer. Scanning electron microscope (SEM) images of the etched AWG structure with HSQ still remaining are shown in Figure 6.13. As can been seen from the figures, the HSQ mask looks almost intact in all areas after ICP-RIE plasma etching. However, using the fast etch recipe, we encountered undercut profile of the $Al_xGa_{1-x}As$ waveguides even though the HSQ mask was almost intact. More SEM images of the arrayed waveguides that are further away from the star couplers are shown in Figure 6.14. Undercut structures are also seen in the outer most waveguides.

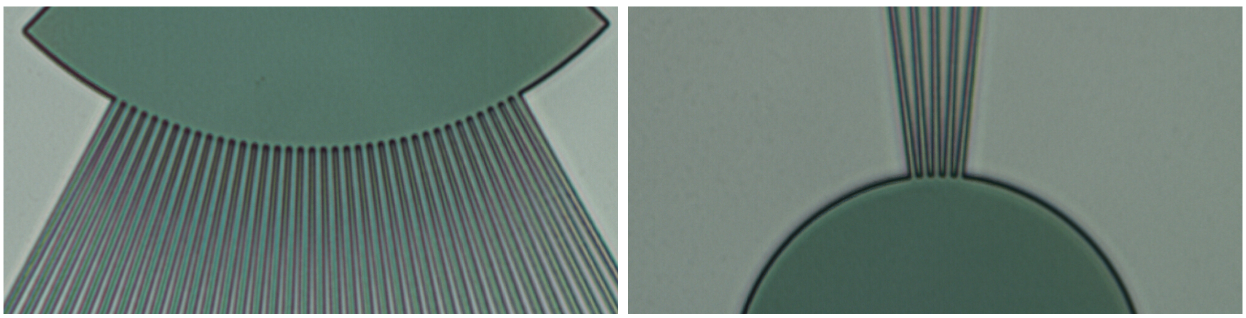

Figure 6.12 Optical microscope images of the HSQ (left) at the arrayed waveguides/star coupler section and (right) input or output waveguides/star coupler section.

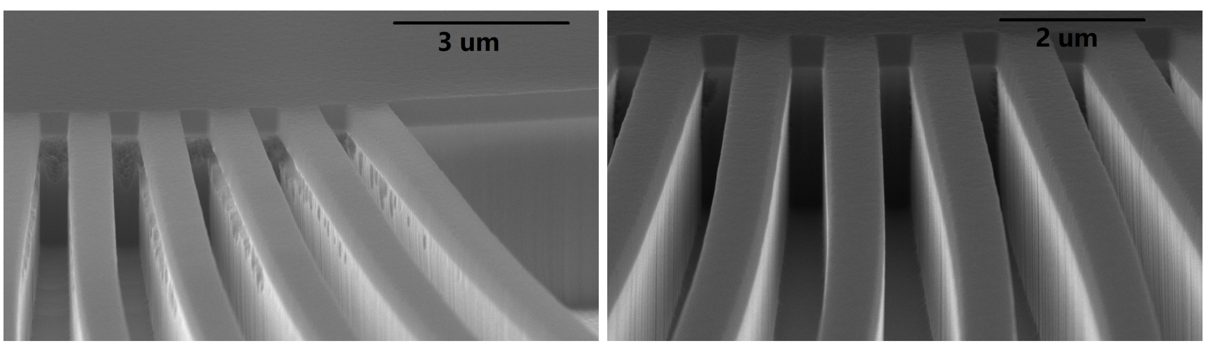

Figure 6.13 Scanning electron microscope (SEM) images at the arrayed waveguide/star coupler section of the etched AWG structure with HSQ still remaining.

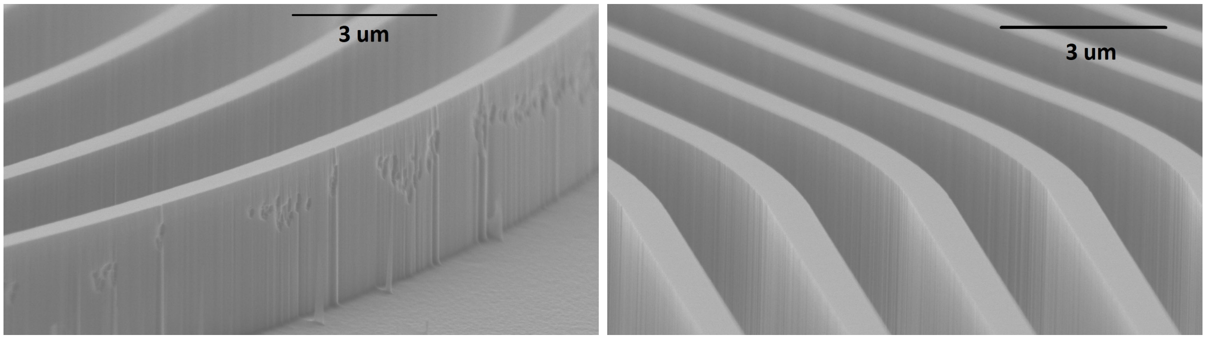

Figure 6.14 Scanning electron microscope (SEM) images of the arrayed waveguides away from star couplers section of the etched AWG structure without HSQ mask.

The current fabrication challenge is the undercut structures. As described in Chapter 4, the fast etch recipe relies on a thin passivation layer to fabricate highly anisotropic waveguides. Accordingly, we could attribute the undercut structures during the AWG fabrication process to two possible reasons. First, when waveguides are positioned closed to one another, reactive ions can bounce back and forth in the two facing sidewalls of the waveguides. The physical sputtering effect is increased. When the passivation layer is no longer present, the etching becomes isotropic, causing structures as shown in Figure 6.13. Similar isotropic etching effects have been measured when two simple straight waveguides are positioned about a few hundred nanometers apart. The appearance of the undercut structures indicates that chemical etching is the dominant mechanism, as described in Section 4.4. Second, it seems that outer most waveguides have a more undercut structure than the waveguides that are surrounded on both side, as can be seen in Figure 6.14. The reason for this is unclear at the moment. This could possibly be attributed to that the macro distribution of reactive ions could change when big and irregular microstructures like AWGs are present. It attacks the passivation layer and results in isotropic etching. A similar trend was observed by looking at more SEM images: same sides of the waveguides in a part of the AWG device tend to get undercut structure more frequently.

To address the above fabrication challenge, we could design AWGs differently so as to allow a bigger gap between waveguides. This would increase the size of the device and would probably make the fabrication more feasible. Another solution would be to develop new dry etch recipes that do not rely on passivation layers for anisotropic at all.

6.5 Conclusion

We presented the step-by-step design procedures of an AWG in the two-guide-layer wafer in detail. Theoretical design calculation was confirmed by the Lumerical® MODE simulations. We attempted using the fast etch recipe from Chapter 4 to fabricate AWGs in a single etch step, without integrating SSCs from Chapter 5. The current fabrication challenge is the undercut structures. The proof-of-concept design of AWGs in this Chapter demonstrates it is feasible to devise complicated signal processing devices on the top waveguide in the two-guide-layer wafer. With the results in previous chapters, it proves the applicability of multi-guide vertical-integration (MGVI) scheme in the $Al_xGa_{1-x}As$ semiconductors.

Chapter 7
Three-guide-layer AlGaAs chip

7 Three-guide-layer AlGaAs chip

First, this chapter discusses improved design approaches to the FCW, PWG and the SSC that connects the two waveguides. Second, this chapter details the design of waveguide photodiode integrated on a three-guide-layer chip.

7.1 Large-dimension, deep-etched, single-mode $Al_xGa_{1-x}As$ waveguides

The realization of single mode, III–V semiconductor optical waveguides with a large mode size is challenging. On one hand, it is desirable to increase the modal area of the fundamental mode TE_{00}. To do so, the most straightforward way is to increase waveguide dimensions. On the other hand, higher order modes emerge if waveguide dimensions go beyond the cutoff values. In order to design single mode, III–V semiconductor optical waveguides with a large mode size, there are two common ways. One of them is leakage control of higher order modes. This method involves carefully designing special lower waveguide cladding structures. In this scheme, a waveguide would support a low-loss fundamental TE_{00} mode. All higher order modes suffer extremely high losses due to the specially designed lower waveguide cladding structures. The differential leakage loss provides foundation of achieving single mode operation. By the terms 'low-loss' and 'extremely high loss', this section aims to design lower than 1×10^{-2} dB/cm for mode TE_{00} and higher than 100 dB/cm for all higher order modes, with special attention given to TE_{20} and TE_{10} modes. Note, we focus on TE modes throughout this section.

7.1.1 Introduction

The salient features of single mode waveguides are their subwavelength width, strong birefringence, relatively high propagation loss, high sensitivity to wavelength and waveguide width, all of which may provide new opportunities for novel device applications yet limit device performance. Although it is natural to use single mode waveguides for single mode devices, it is not essential and not always desirable in practice. First, the strong birefringence may make the devices polarization sensitive and unsuitable in a lot of applications where state of optical signal polarization is randomized, i.e. fiber-optic communications. Second, despite the strong confinement in these waveguides, there is a significant wave amplitude at the sidewall of the waveguide, which results in scattering, a major source of propagation loss [172]. The high propagation loss arising from subwavelength width and strong lateral confinement is highly undesirable for PICs. Third, waveguide losses are sensitive to wavelengths and waveguide widths, which brings about more challenges in the design and fabrication of devices. Fourth, if single mode operation is required, the waveguide cross section is usually small. One important practical consideration is the efficiency of coupling light into such waveguides from a standard single mode fiber, which has a much larger mode size.

Multi-mode waveguides not only have smaller propagation losses, but are also less polarization sensitive, easier to fabricate and easier to couple to single mode fibers. However, higher order modes have to be managed properly. When a multi-mode waveguide is coupled to single mode fiber, higher order modes can be excited. Higher order modes can also be excited where there are waveguides bends or waveguide irregularities such as sidewall roughness or geometric asymmetry.

When higher order modes get excited and propagate along with the fundamental modes, a mode filter can be integrated in to the waveguide to eliminate higher order modes [173]. Waveguides are squeezed in width and higher order modes get leaky and become unguided in the filter section. When the width is increased to the original value, only the fundamental mode exists and propagates.

Another approach to eliminate higher order modes is through differential leakage of different modes by controlling the etching depth of ridge waveguides. The most widely adopted method for making low-loss III–V semiconductor optical waveguides with a large mode size involves etching a shallow rib in the upper cladding layer or core to give very weak horizontal confinement of the fundamental mode. While shallow-etched waveguides are relatively straightforward to fabricate, they have a number of disadvantages [172]. The main drawbacks are: 1) the etch depth is very critical and difficult to achieve accurately over the entire wafer; 2) light is confined loosely in the lateral direction so bend losses are often high; 3) any light launched or scattered into higher order modes leaks out horizontally and can cause severe corner losses and background scatter at the output; 4) devices have to be spaced sufficiently to avoid coupling between waveguides; and 5) optical modes tend to be more elliptical in shape and result in low coupling efficiency to single mode fibers.

Many of the disadvantages of shallow-etched guides can be overcome by deeply etching through the upper cladding layer, the waveguide core and part of the lower cladding layer [174]. This gives a very strong horizontal confinement of light which greatly reduces the problems of bend losses, crosstalk and background scatter. This is because any light launched or scattered into higher order modes of deeply-etched waveguides leaks vertically into the substrate rather than horizontally. In the AlGaAs system, the GaAs substrate will absorb all photons in the 700 – 870 nm wavelength range, helping to reduce cross-talk. Deeply-etched waveguides are also ideal for making high performance multimode interference (MMI) splitters and recombiners which require strong horizontal confinement for accurate self-imaging. A further advantage of deep-etched guides is, because the number of modes supported depends mainly on the epitaxial structure, the etch depth is not very critical and the required accuracy can easily be achieved using conventional reactive ion etching (RIE), which considerably simplifies the fabrication process. The idea of using differential leakage loss to eliminate higher-order modes have been demonstrated for a number of $Al_xGa_{1-x}As$ waveguide devices [175-181].

All the aforementioned features are extremely valuable for the design of devices in this thesis: 1) light scatters vertically rather horizontally – reduces cross talk of devices on the upper layers; 2) tight horizontal confinement of deeply etched waveguides – facilitates the design of multi-mode interferometers (MMIs), bends etc.; 3) tight confinement would allow light to be sharply bent and routed in the circuits; 4) less stringent etch depth requirement – we can easily fabricate devices using ICP-RIE.

The main disadvantage, or challenge, of using deep-etched guides is that a more complex lower cladding design is needed for single-mode operation, especially for large guide dimensions. The number of modes that can propagate in a waveguide of this type is determined almost entirely by the refractive index and thickness of the *main* lower cladding layer. Single-mode operation is achieved when this index is lower than the effective index of the fundamental mode but higher than the effective indices of all other modes. This means that only the fundamental mode is evanescent in the lower cladding layer and all other modes leak into the GaAs substrate. The main goal when we design this type of waveguide is to maximize the higher order mode losses without allowing light in the fundamental mode to leak into the substrate.

7.1.2 Design

7.1.2.1 Laying out design parameters

The design principle of single mode $Al_xGa_{1-x}As$ optical waveguides with a large mode size follows the paper by Heaton [175]. The designs of high refractive index contrast passive waveguide (PWG) and fiber coupling waveguide (FCW) are independent of each other to a large extent in the perspective of modal properties. However, it is important to note that the thicknesses and refractive indices of the PWG core layer and the lower cladding layer do play a role in the design of spot-size converter that connects the FCW and PWG. They clearly will affect how light is coupled between the PWG and FCW. Overall, the design procedures pertaining to the FCW in this section have minimum effects on other device designs.

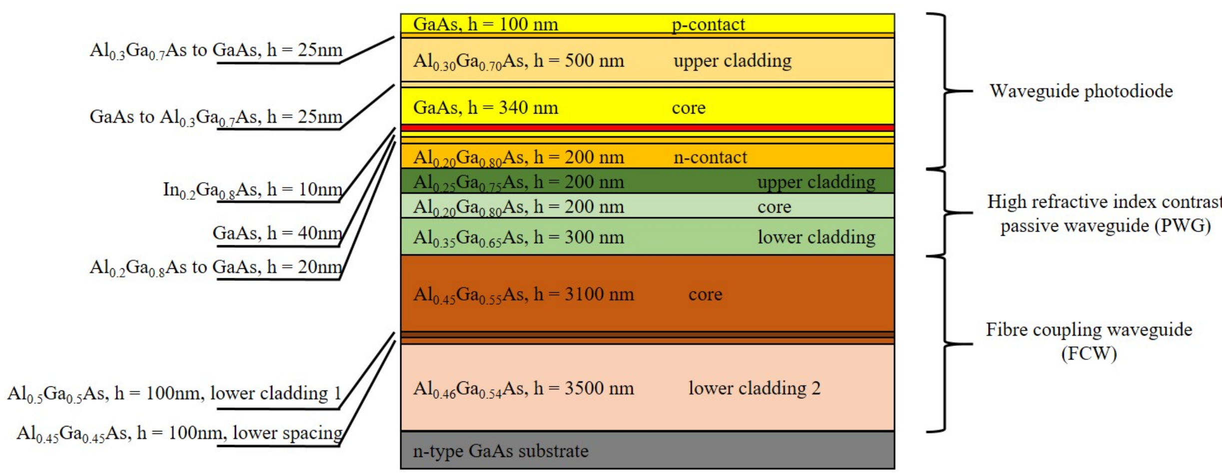

Figure 7.1 Wafer description of the three-guide-layer $Al_xGa_{1-x}As$ chip. The intended use and functionality is also shown along with the material composition and thickness of each layer.

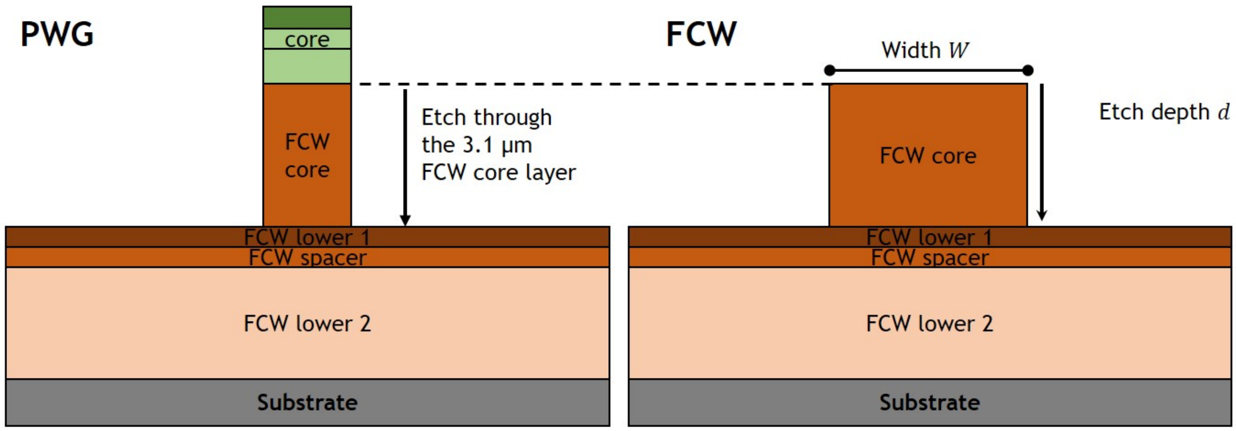

Figure 7.2 Passive waveguide (PWG) and fiber-coupling waveguide (FCW) structures side-by-side as a comparison.

The side-by-side comparison the PWG and FCW structures is shown in Figure 7.2. We can see two important issues to consider. First, the materials of FCW core and lower cladding layer 2 must be the same to provide room for achieving differential leakage. Second, because we etch 3.1 μm into the FCW core layer, making the PWG a deeply etched waveguide with a high confinement in the vertical direction, modifying the overall FCW core thickness would not affect the PWG characteristics. Of course, the FCW lower cladding layer 1, spacer layer, lower cladding layer 2, which are further away, are supposed to have even smaller effects on the PWG properties.

7.1.2.2 Design principle

The principle based on which we make single mode $Al_xGa_{1-x}As$ optical waveguides with a large mode size is that, only the fundamental mode has an effective index that is higher than the material refractive index of the lower cladding layer 2. This means that all modes except the fundamental mode leak strongly through the lower cladding structure into the substrate [182]. The first cladding index is lower so that this layer controls the overall rate at which the light leaks from all modes in the waveguide. The second cladding layer acts as a mode filter, and the first cladding layer controls how much light reaches the filter. Some alternate wafer designs described in the referenced papers also had a spacer layer between the two lower cladding layers. This layer had the same index as the core and was originally thought to improve the filtering process. In practice, however, spacer layers were not found to be very useful [175]. A high index substrate, which is the natural choice for $GaAs/Al_xGa_{1-x}As$ waveguides, is not strictly necessary for this type of mode filtering to work, but it is essential for calculating the losses of modes in this type of leaky waveguide.

7.1.2.3 FCW core width and thickness

The width of the waveguide affects the effective index of the guided modes. Take the fundamental TE_{00} and TE_{10}, TE_{20} as examples. When the width increases, the indices of these three modes increase and converge to the FCW core material refractive index, as shown in Figure 7.3. When this happens, to effectively filter higher order modes, i.e. TE_{10} and TE_{20}, the aluminum content of lower cladding 2 material must also converge to the value of the FCW core material such that n_{eff} of the higher order modes are below n_2. Assuming epitaxial growth can distinguishably grow 1% aluminum fraction in $Al_xGa_{1-x}As$, which is determined by our wafer provider, there will be an optimum value of the waveguide width, beyond which epitaxial growth reliability becomes an issue.

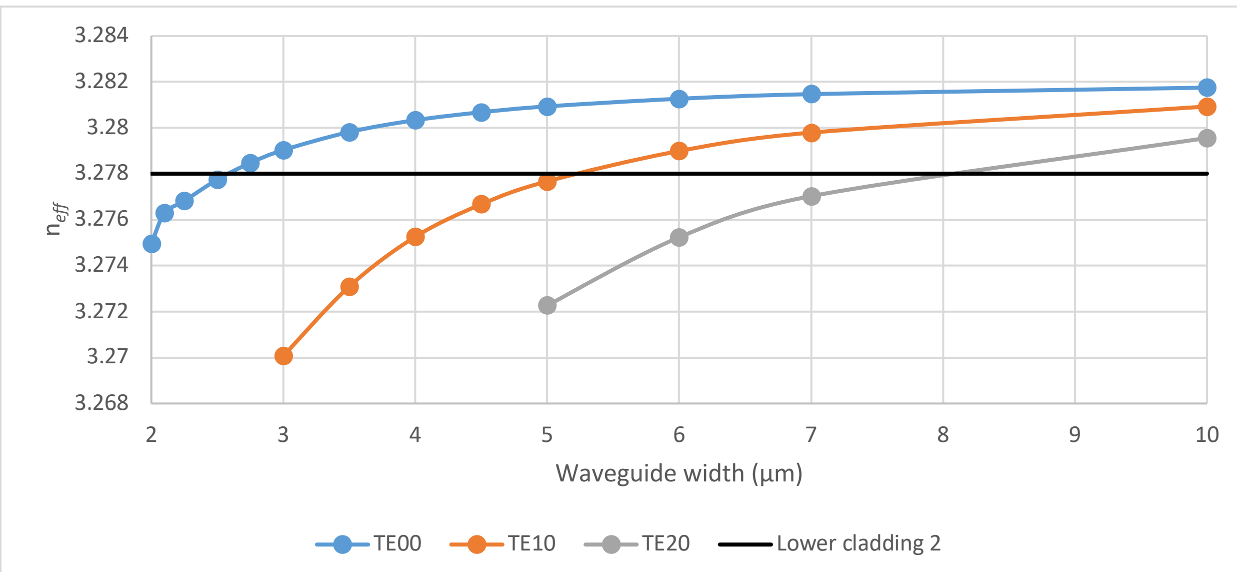

Figure 7.3 Effective indices of horizontal modes as a function of waveguide width. t_0 = 3.1 µm, t_1 = 0.1 µm, t = 0.1 µm, t_2 = 3.5 µm. The etch depth is $d = t_0$.

In order to improve the power coupling efficiency to a SMF at 850 nm, we choose 4 µm as the waveguide width. It was found that at this width, we can choose 46% aluminum fraction $Al_xGa_{1-x}As$ for FCW lower cladding 2 layer. Figure 7.3 shows horizontally polarized TE modes. Higher-order, vertically-polarized modes have similar features. However, it was found that once higher-order, vertically-polarized modes exist, it is hard to filter them by carefully designing the lower cladding structures [182]. That said, we need to choose a relatively smaller FCW core thickness compared to its width. After many design iterations, we picked $t_0 = 3.1$ µm. The fundamental mode area is not affected by modifying low cladding structures, even though its loss is significantly affected. Therefore, at this point where we have $w = 4.0$ µm and $t_0 = 3.1$ µm fixed, it makes sense to see how large the mode power overlap integral and power coupling coefficient are.

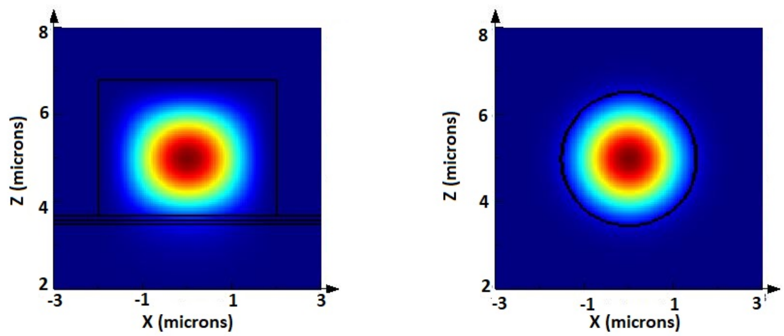

Figure 7.4 Mode profiles of the fundamental TE_{00} mode of the FCW waveguide (left) and a SMF with a focused beam waist of 3 µm (right). The circular curve surrounding the fiber mode is $1/e^2$ power level curve corresponding to the beam waist of 3 µm.

Shown in Figure 7.4 are mode profiles of the fundamental TE_{00} mode of the FCW waveguide and a SMF with a focused beam waist of 3 µm. The calculated power overlap integral for the two modes is 98%.

7.1.2.4 Lower cladding structures

The materials for lower cladding 1 layer, spacer layer and lower cladding 2 layer are fixed before optimizing the thickness. To design large-dimension-single-mode waveguides, we want to see how the leakage losses can be controllably optimized.

Table 7.1 Optimization iteration base point.

	Thickness	Material
FWC lower 1 layer	0.1 μm	$Al_{0.50}Ga_{0.50}As$
FCW spacer layer	0.1 μm	$Al_{0.45}Ga_{0.55}As$
FCW lower 2 layer	3.5 μm	$Al_{0.46}Ga_{0.54}As$

Because changing the thickness of each layer has similar effects as changing the material, we fix the materials first. In particular, material of FCW lower cladding 2 layer is $Al_{0.46}Ga_{0.54}As$, which is closest to FCW core material if we consider 1% aluminum epitaxial growth reliability. It was found that, indeed, *effective indices* of higher order modes are smaller than the refractive index of $Al_{0.46}Ga_{0.54}As$, making higher order modes leaky. This lays out the foundation of controlled leakage.

The main reason for using two lower cladding layers is to reduce the overall epitaxy thickness. The field solution in the first cladding layer is evanescent in the plane for all waveguide widths so that this layer provides a barrier to most of the light in the waveguide. It is the fraction of light from each mode which leaks through into the second cladding layer that determines the mode loss. The first cladding layer has to be thick enough and have a low enough refractive index to prevent too much light leaking from the fundamental mode but must also allow sufficient light to leak from the other modes.

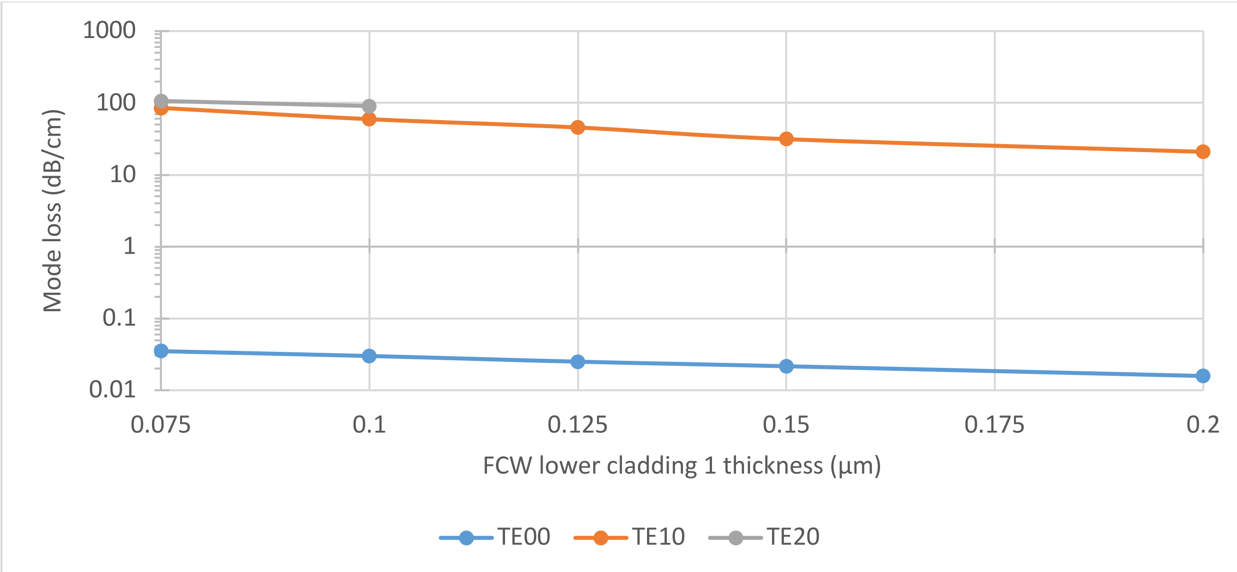

Figure 7.5 Mode losses of TE$_{00}$, TE$_{10}$ and TE$_{20}$, when they exist, as a function of FCW lower cladding 1 thickness. Note, all the other parameters are taken from Table 7.1.

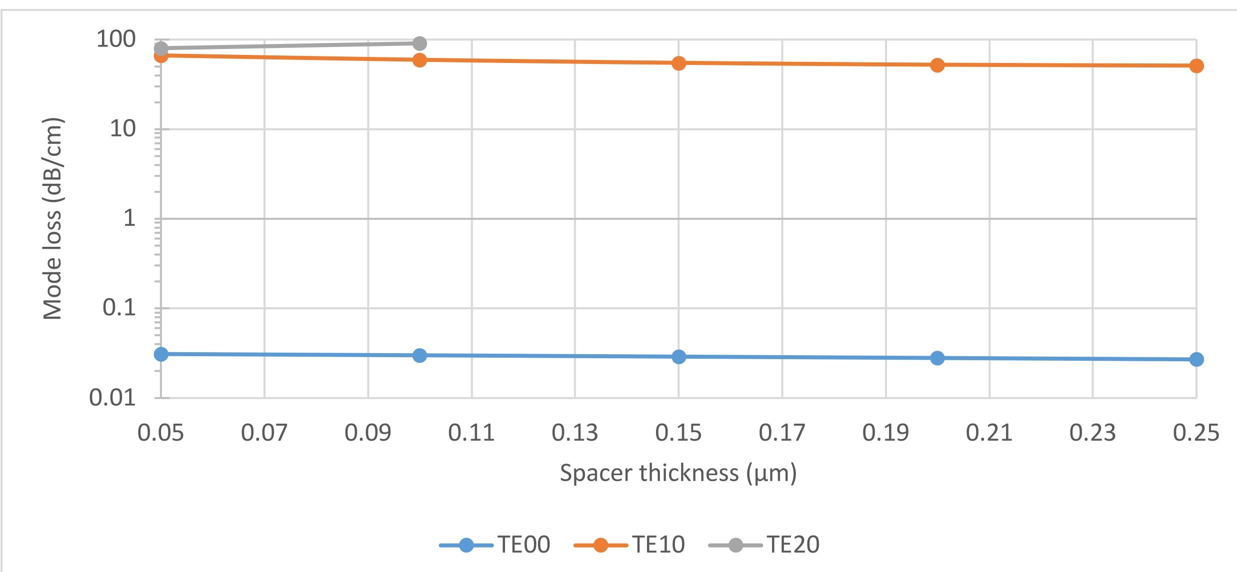

Figure 7.6 Mode losses of TE$_{00}$, TE$_{10}$ and TE$_{20}$, when they exist, as a function of FCW spacer layer thickness. Note, all the other parameters are taken from Table 7.1.

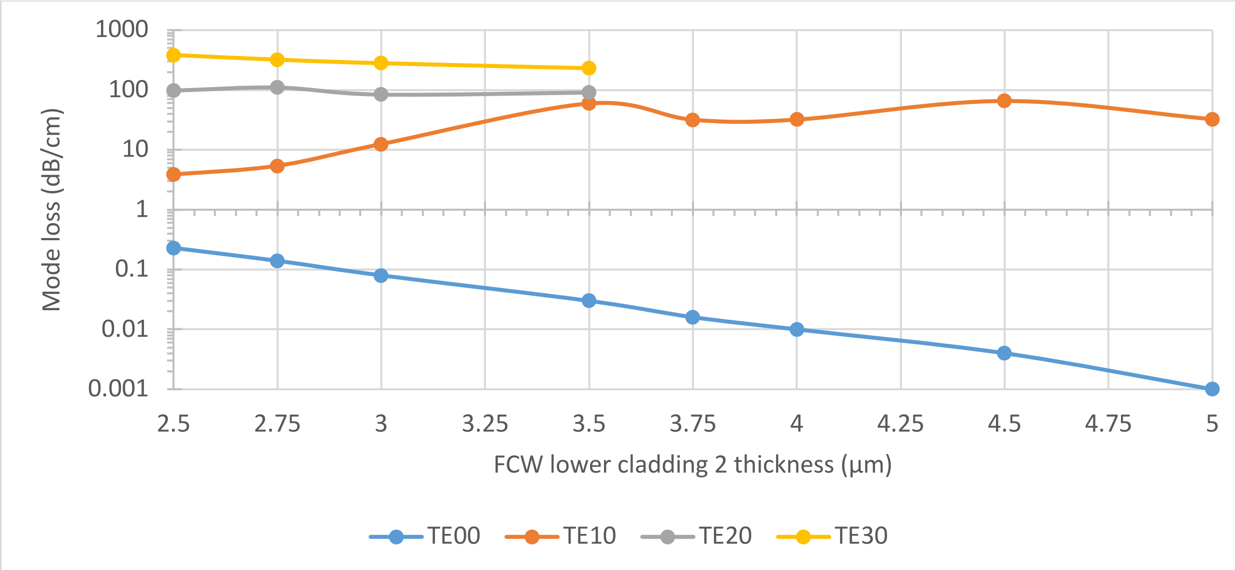

Figure 7.7 Mode losses of TE*00*, TE*10* and TE*20*, when they exist, as a function of FCW lower cladding 2 thickness. Note, all the other parameters are taken from Table 7.1.

Please note, shown in Figure 7.7 are only the TE_{00}, TE_{10}, TE_{20} and TE_{30} modes as it is their losses which need to be controlled. We want the TE_{00} loss to be as small as possible and the losses of all higher order modes to be as large as possible. What is not shown are the higher-order vertically-polarized modes, and some slab modes if they exist. The reasons are two-fold, which are important to point out. First, they have negligible mode power overlap integral and power coupling coefficients. These modes will not be efficiently excited and we ignore them here. For all slab modes, they reside in lower cladding 2 layer and are far away from the TE_{00} mode, which again makes them impossible to be excited when a SMF source is optimized for TE_{00}. For example, the power overlap integral coefficient is in the order of 1×10^{-5}. Some higher-order vertically-polarized modes seem to sit in the FCW core area but actually have negligible power overlap integral and power coupling coefficients with the SMF mode. Second, they have high losses. Higher-order vertically-polarized modes, in the cases considered in the above parameter scan, all have higher propagation losses than the fundamental mode considered. This is partially due to that the FCW already has been optimized as in Section 7.1.2.3. They seem to sit in the FCW core area but are very unlikely to be excited in the first place. Even if they are, they leak into the substrate very quickly and actually are not guided modes.

As can be seen from Figure 7.7, at the optimum values, all higher order modes TE_{10}, TE_{20} and TE_{30} have losses between 60 and 100 dB/cm, while the loss of TE_{00} is only between 0.01 and 0.05 dB/cm. If we assume a 5-mm propagation length, higher order modes that even initially have an equal power as TE_{00} would be attenuated be at least 30 dB compared to TE_{00}. This achieves large area single mode waveguide that couples efficiently to SMFs.

7.1.3 Etch errors and wavelength characteristics

So far, we have considered etch depth exactly the same as FCW core thickness, such that FCW core is fully etched and FCW lower cladding 1 is intact. We need to consider etch error effects because when etching about t_0 = 3.1 μm deep waveguide, errors are inevitable in practice.

As can be seen from Figure 7.8, the losses for TE_{00} remains small when the sample is over etched. Those of TE_{10} and higher-order horizontally-polarized modes remain high. Some higher-order vertically-polarized modes, if they exist, and slab modes follow the same pattern which has been discussed in the previous sections. The conclusion is that, an etch error as large as 600 nm is tolerable. Close observation tells us that, if errors is unavoidable, it is more favorable to under etch the FCW structure (left part of Figure 7.8). This way, TE_{10} losses will increases a little bit.

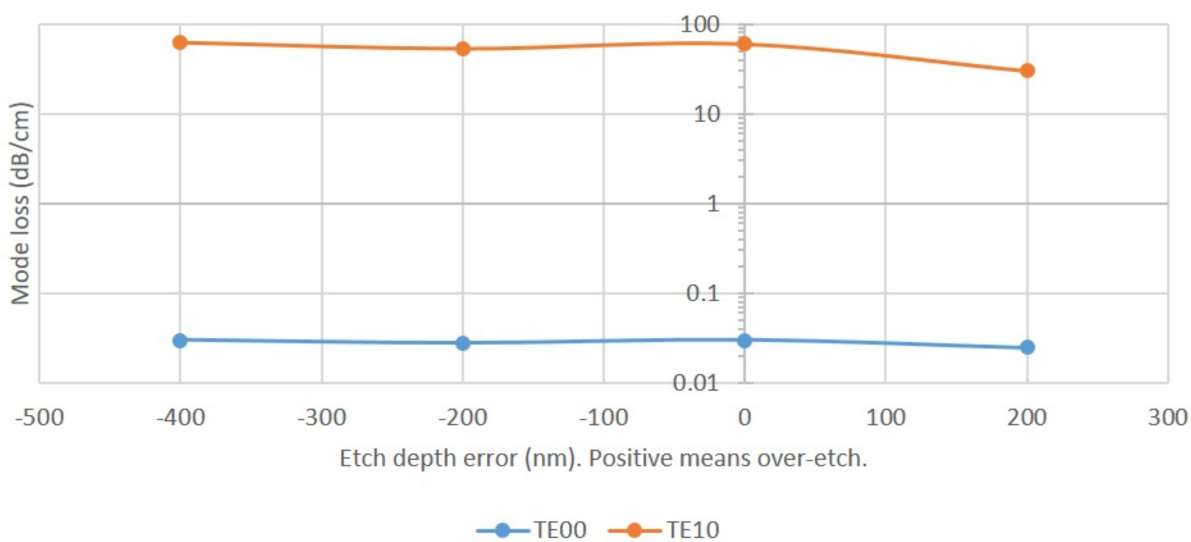

Figure 7.8 Etch error analysis. Positive values mean for over-etch. Negative values mean for less-than-desired etch depth.

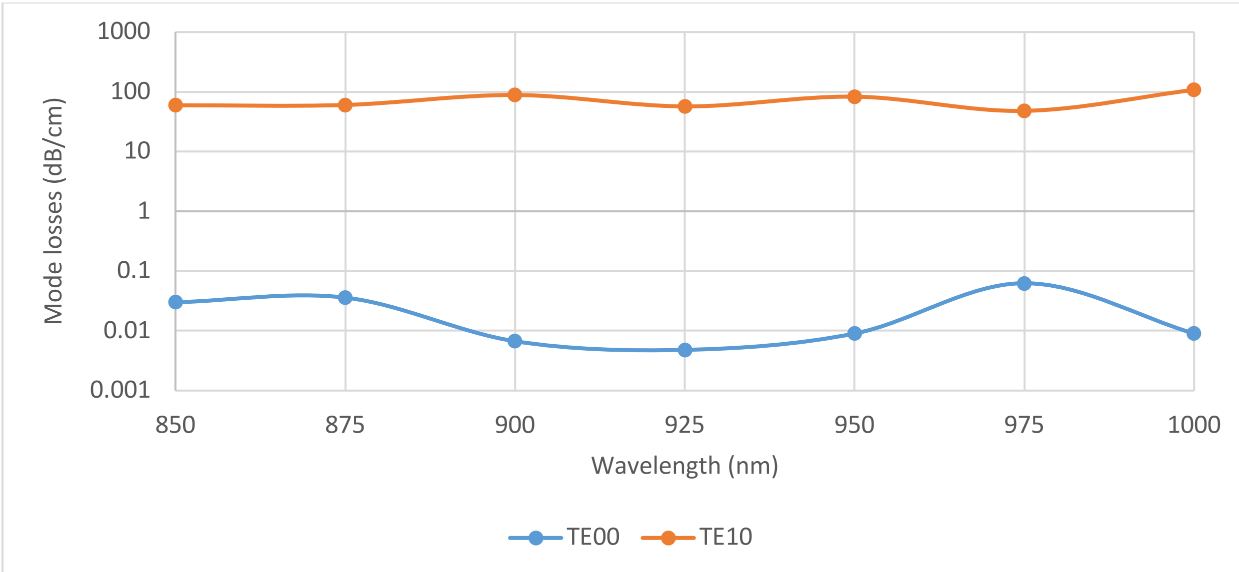

Figure 7.9 Wavelength characteristics of the large-dimension, deep-etched, single mode waveguides.

Lastly, we scan the wavelength between 850 nm and 1000 nm. Higher order modes of longer wavelength are supposed to have larger losses. Some higher order modes, i.e. TE_{20}, would vanish when wavelength increases, which is favorable. The most concerning issue is the losses of the TE_{00} and TE_{10} modes. As can be seen from Figure 7.9, all design features hold throughout the wavelength range of interest.

7.1.4 Conclusion

This section finishes the design of single mode $Al_xGa_{1-x}As$ optical waveguides with a large mode size. The final design dimensions are shown in the Figure 7.1. Compared to the paper [175], this is much improved in terms of differential leakage between TE_{00} and TE_{10}. In our case, we have (50 dB/cm)/(0.05 dB/cm) $\cong 1000$ while in [175] it is only about $(6\ dB/cm)/(0.25\ dB/cm) = 24$. This means our design of eliminating higher order modes through differential leakage of different modes by controlling the etching depth of ridge waveguides is successful.

7.2 Passive waveguide (PWG) characteristics

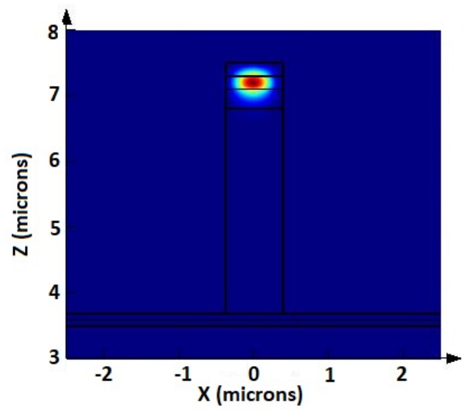

Figure 7.10 Mode profile of the fundamental TE_{00} mode of the PWG. The waveguide width is 760 nm and the waveguide depth is 3.8 µm. The FCW core layer is completely etched.

The design of PWG and FCW is independent of each other to a large extent. In order to demonstration the interdependence between the designs of the PWG and FCW, the bend losses of the PWG is used as a benchmark. When a waveguide is bent, the vertical leakage becomes more significant, and the effects of the FCW core layer, which acts as a lower cladding layer, are clearer. Figure 7.11 compares the change of PWG characteristics before and after FCW design, i.e. changing the FCW core layer thickness from 2.1 µm to 3.1 µm. As can be seen, there is no change at all.

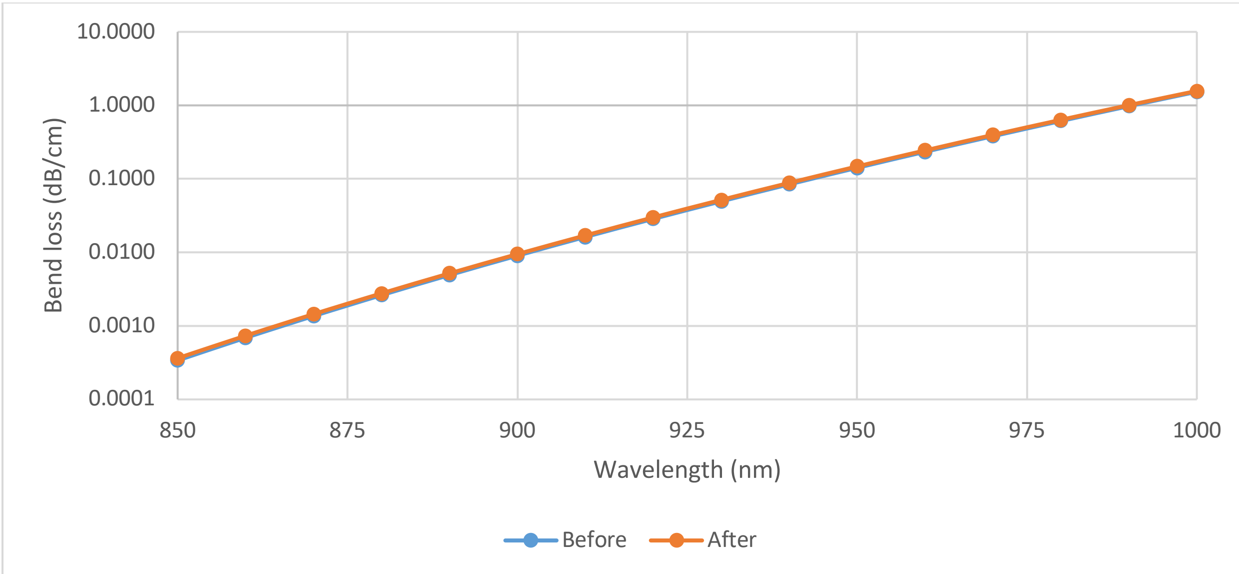

Figure 7.11 Bend loss of the PWG TE_{00} mode as a function of wavelength for 60 µm bend radius and 600 nm etch depth into the FCW core before and after FCW design, i.e. changing the FCW core layer thickness from 2.1 µm to 3.1 µm.

The FCW core is acting as a lower cladding for the PWG waveguide. The thickness of the FCW core is changed from 2.1 µm before FCW design to 3.1 µm after. Additional etching into the FCW core provides additional degree of freedom to control the bend loss for different radii over the wavelength range of interest. Therefore, increasing the thickness of the FCW core can further improve the design.

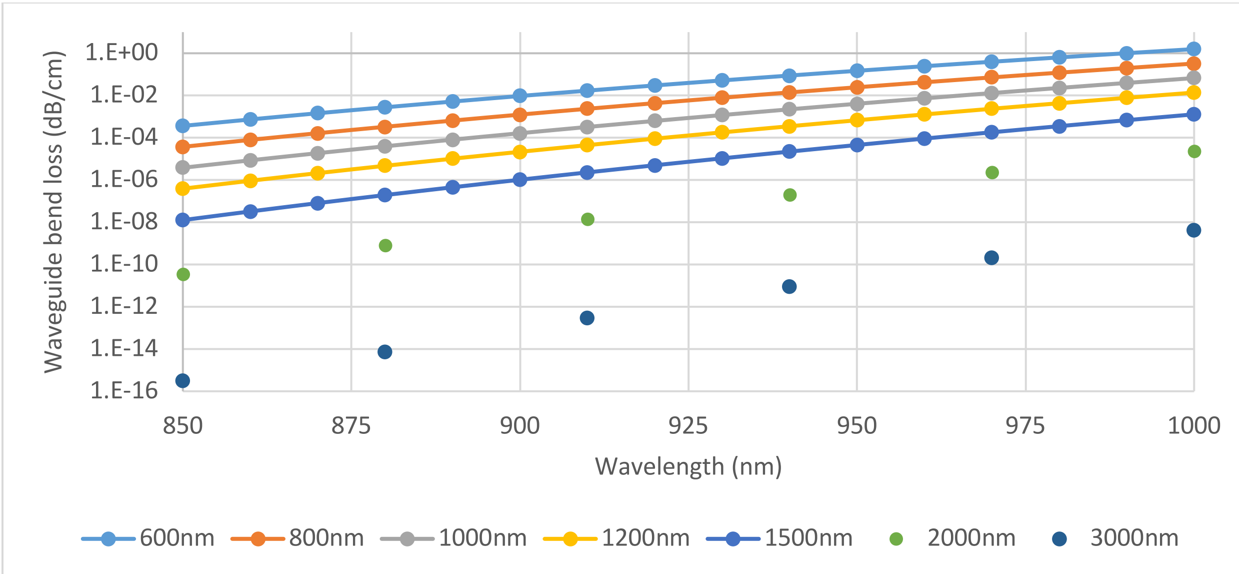

Figure 7.12 Bend loss of the PWG TE_{00} mode as a function of wavelength for 60 µm bend radius and different etch depth into FCW core (from 600 nm to 3000 nm).

Figure 7.12 shows the bend loss at 60 µm radius for different etch depths into FCW core layer. Increasing the etch depth, clearly decreases the bend loss due to a higher vertical confinement and lower leakage into the substrate.

7.2.1.1 Waveguide aspect ratio and bend loss

At an etch depth of 3000 nm the FCW core layer is completely etched away and the PWG has an aspect ratio of 5. The over etch depth into FCW core plays vital role in controlling the bend loss. Another paper reported bend radius around 10 µm [183]. In order to have a bend radius that is as small as 10 µm, we need to increase the aspect ratio of the waveguide. We look at the bend loss for aspect ratio between ≈ 2 and 5.

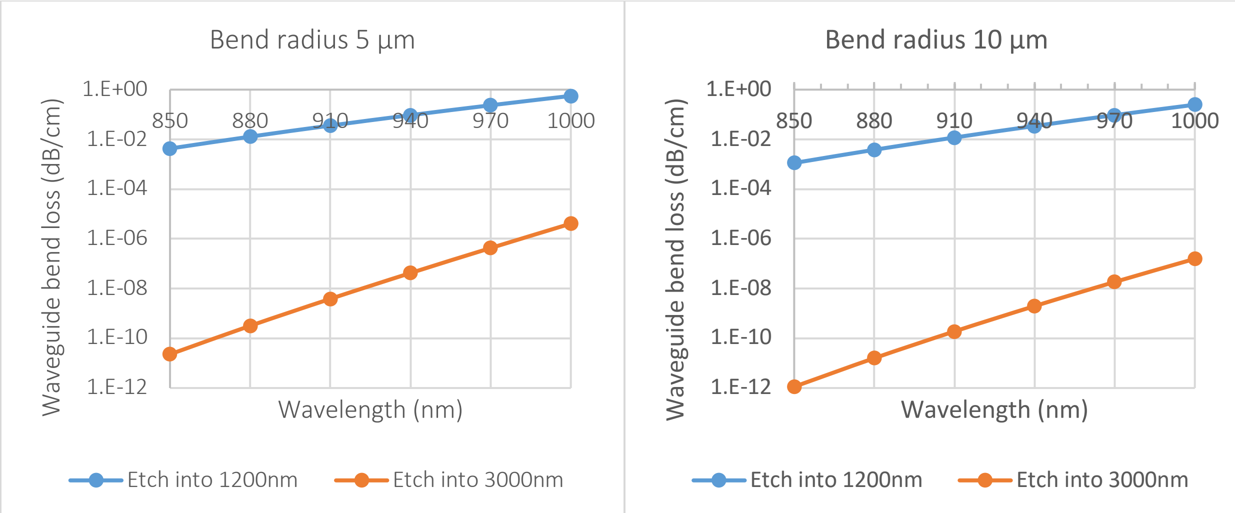

Figure 7.13 Calculated waveguide bend loss for different bend radii and etch depths.

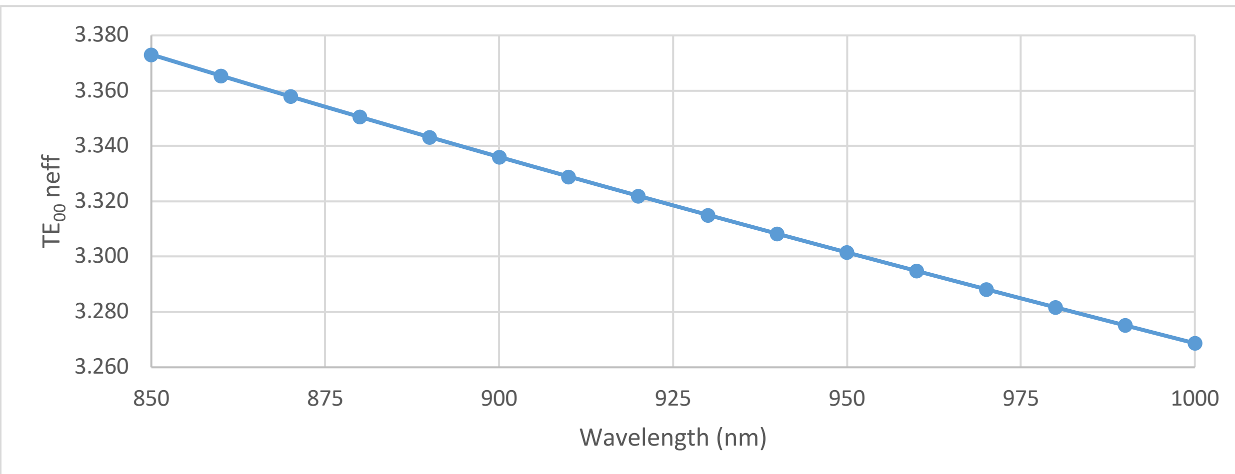

Figure 7.14 Effective index of the fundamental TE_{00} for a straight PWG waveguide with etch depth of 3000 nm in to the FCW core layer.

According to Figure 7.13, aspect ratio should be larger than 2 to have a 10 μm bend radius. In order to see how the integration of a SSC would improve the coupling efficiency, the power overlap integral is calculated for the PWG and a SMF with a focused beam waist of 3.0 μm. The SMF is the one used in Figure 7.4. The power overlap integral is 13%. Because the power overlap integral is as large as 98%, the integration of a spot size convert could theoretically improve the coupling efficiency from a SMF to the PWG by 7.5 times. The improvement of coupling efficiency has been demonstrated when we used our two-guide-layer wafer in Chapter 5, results of which are published in [141].

7.3 Improved spot-size converter design

Due to improved designs of the FCW and PWG, the new spot-size converter design is greatly improved. The total length of the SSC is greatly reduced. Figure 7.15 shows a simulated conversion efficiency of 96% with Rsoft® BMP method is achieved over a total length of 350 μm, making the SSC one of the shortest SSCs in $Al_xGa_{1-x}As$ semiconductors.

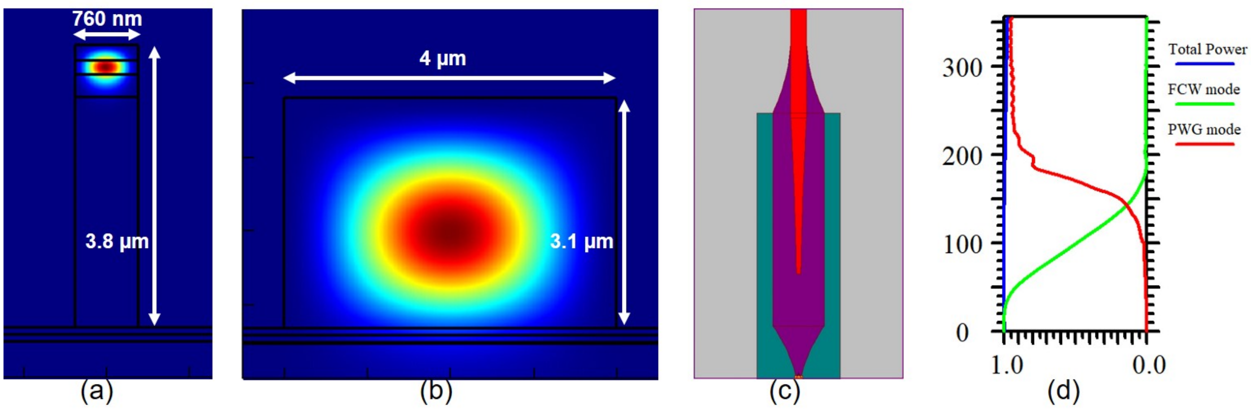

Figure 7.15 Field profiles of TE_{00} modes of (a) PWG and (b) FCW, respectively. (c) Top view of the spot-size converter. (d) Vertical coupling between the TE_{00} modes of the FCW and PWG.

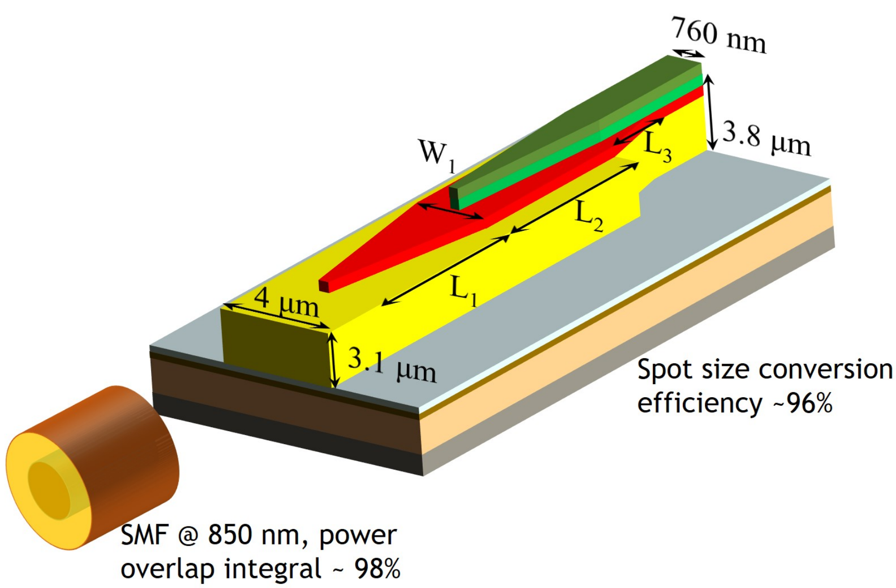

Figure 7.16 Schematic view of the SSC with the dimensions of the PWG and FCW.

The working principle and design procedures of the SSC is detailed in Chapter 5. The parameters labeled in Figure 7.16 are as follows: exponential taper length L_1 = 50 μm, transition waveguide length L_2 = 200 μm, quadratic taper length L_3 = 100 μm, transition waveguide width W_1 = 2.5 μm. There is a 50 μm gap between the end of the first taper (i.e. where L_1 ends) and the start of the second taper (i.e. where L_2 starts). This can be seen from the top view of the spot-size converter in Figure 7.15. Therefore, the actual length of second taper is 150 μm even though the length of the transition waveguide is 200 μm.

To summarize, the improved designs approaches to the FCW, PWG and the SSC that connects the two waveguides greatly improve the device performance. The overall devices length has been reduced from ≈1000 μm to 350 μm.

7.4 Single quantum well waveguide photodiode

7.4.1 Introduction

Photo detection in semiconductors works on the general principle of the production of electron-hole pairs under the illumination of light. When a semiconductor material is illuminated by photons of an energy greater than or equal to its bandgap, the absorbed photons promote electrons from the valence band into excited states in the conduction band, where they behave like free electrons that are able to travel long distances across the crystal structure under the influence of an intrinsic or externally-applied electric field. In addition, the positively-charged holes left in the valence band contribute to electrical conduction by moving from one atomic site to another under the effects of the electric field. In this way, the separation of electron-hole pairs generated by the absorption of light gives rise to a photocurrent, which refers by definition to the fraction of the photogenerated free charge-carriers collected at the edges of the material by the electrodes of the photodetecting structure, and whose intensity at a given wavelength is an increasing function of the incident light intensity.

Among the four main structures of photovoltaic photodetectors – PIN (or PN) diodes, APD (avalanche photodiodes), Schottky junctions, and MSM (metal-semiconductor-metal) photodiodes, PIN diodes and APD diodes are more amenable to waveguide structures and have attracted a lot of research in the context of telecommunications. Based on the above discussion, the design of the WGPD in this section will be based on a PIN photodiode.

7.4.2 Photodiode characteristics

7.4.3 $In_xGa_{1-x}As$ properties

The absorption functions of the main semiconductor materials or semiconductor families used to build photodiodes in the spectral range of 600 nm and 1.8 μm are shown in Figure 1. They can be chosen as a function of the wavelengths to be detected.

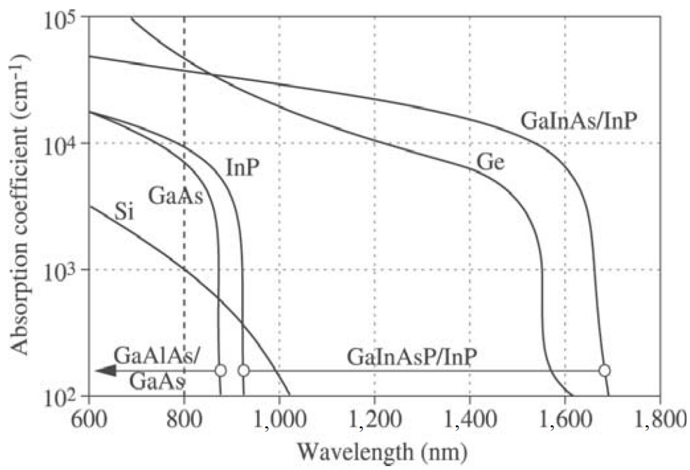

Figure 7.17 Absorption spectra for semiconductor materials used in the visible to near-infrared range. Figure is from [184].

From 400 to 900 nm, there are silicon and the $Al_xGa_{1-x}As$/GaAs families. Gallium arsenide (GaAs) has a direct bandgap; its absorption coefficient is approximately 10^4 cm^{-1} for $\lambda = 800$ nm and increases very rapidly below the corresponding wavelength λ_G ($\lambda_G = 870$ nm). Highly developed for the construction of microwave integrated circuits and diode lasers, it is available as a high-quality substrate for creating defect-free heterojunctions with $Al_xGa_{1-x}As$, $In_xGa_{1-x}As_{1-y}P_y$ and $Al_xGa_yIn_{1-x-y}As$ alloys. However, since we are aiming to design waveguide photodiodes in the spectral range of 850-1000 nm, which is relevant for Raman spectroscopy if the 830 nm is used as the excitation wavelength, bulk GaAs is not suitable. For the $In_xGa_{1-x}As_{1-y}P_y$ family, it can be grown lattice-strained to InP and $Al_xGa_{1-x}As$ [185, 186]. Unfortunately, $Al_xGa_{1-x}As$ lattice-matched components all have high energy bandgaps. We used $In_xGa_{1-x}As$ as the quantum well material.

The most important parameter is the band gap. Optical properties of $In_xGa_{1-x}As$ are based mainly on [66] and [187]. All components of $In_xGa_{1-x}As$ have direct bandgaps. Its bandgap energy varies from 0.8 eV to 1.42 eV (GaAs). The energy band structures of strained $In_xGa_{1-x}As/GaAs$ have been thoroughly studied in the references [188-190] and [191, 192]. For $In_xGa_{1-x}As$ with small x value grown on (001) GaAs substrate, the energy bandgap is

$$E_g(x) = 1.42 - 1.11x + 0.45x^2\ (eV)$$

……………………………………… (Equation 7.1)

Therefore, strained $In_{0.2}Ga_{0.8}As$ on GaAs has about E_g = 1.226 eV (λ_g = 1011 nm) and is good for absorbing light in the spectral range of 850 nm to 1011 nm. The band discontinuity and band offset have been studied in [193, 194]. Conduction band discontinuity ΔE_c= ($0.44\Delta E_{gg}$) eV, where $\Delta E_{gg}(eV) = [1.247y + 1.5(1-x) - 0.4(1-x)^2]$ (eV) is the difference between Γ-valleys in $Ga_xIn_{1-x}As$ and $Al_yGa_{1-y}As$.

The critical thickness of $In_xGa_{1-x}As$ grown on GaAs has been thoroughly studied. As detailed in [195], the critical thickness of $In_{0.2}Ga_{0.8}As$ is about 17 nm and that of $In_{0.25}Ga_{0.75}As$ is about 12 nm. Table 7.2 lists some examples of $In_xGa_{1-x}As$ (x = 0.25 or 0.30) on GaAs. As can be seen, a 10 nm thick high quality $In_{0.2}Ga_{0.8}As$ can be grown on GaAs. The critical thickness of $In_xGa_{1-x}As$ as a function of indium content is shown in Figure 7.18 [195].

Table 7.2 Critical thickness of strained $In_xGa_{1-x}As$ on GaAs in the literature. The temperature at which the experiment was carried out was also shown.

Indium content	InGaAs/GaAs	Temperature	Band offset	Comments
25%	120/1000Å	1.6K	Q_c=0.6	Ref [194]
25%	120/120Å	RT	Q_c=0.65	Ref [196]
25%	120/150 Å	77K	-	Ref [197]
30%	120/- Å	8K	Q_c=0.65	Ref [198]

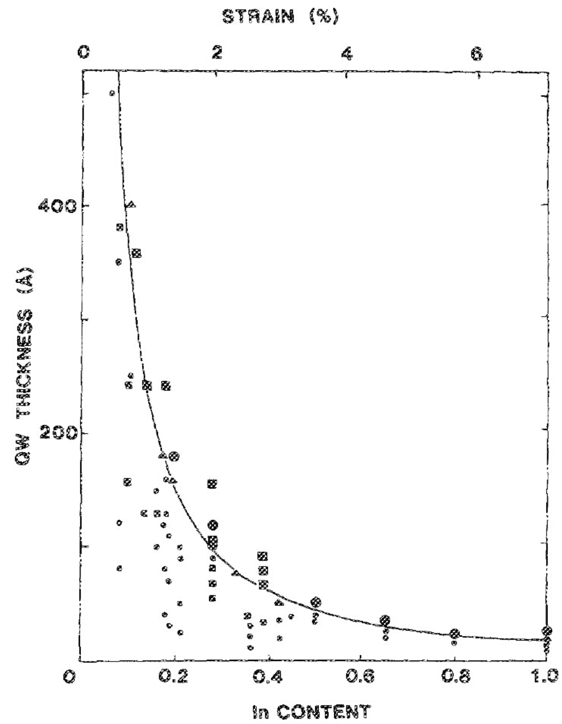

Figure 7.18 Experimental data and calculated dependence (solid line) of the critical thickness of $In_xGa_{1-x}As$ as a function of indium content. Figure is from [195].

The thickness of the barrier layer is also important. If the thickness of the barrier layer, i.e. GaAs, becomes too small, the barrier layer may not be strong enough to endure the strain introduced by $In_xGa_{1-x}As$. It's been shown that the GaAs barrier has to be no thinner than 40 nm so that strain relaxation does not occur for a 12-nm-thick $In_{0.25}Ga_{0.75}As$ [199]. To be safe, the GaAs barrier for a 10-nm-thick $In_{0.2}Ga_{0.8}As$ layer in our waveguide photodiode design has a minimum thickness of 40 nm.

7.4.4 Optical absorption of the SQW structure

The optical absorption properties of the single quantum well structure (SQW) were simulated using a free software, nextnano®. The simulated results were compared to literature results and agreed very well with published experimental results. According to nextnano®, 1.4% strain is included in the model. Calculated bandgap of $In_{0.2}Ga_{0.8}As$ is 1.198 eV and GaAs 1.423 eV. Lattice temperature is 300 K.

The calculated absorption coefficient between 1.1 eV and 1.5 eV is shown Figure 7.19. TE mode is considered. From the simulation, the 1hh-1e transition occurs around 1.266 eV (979 nm).

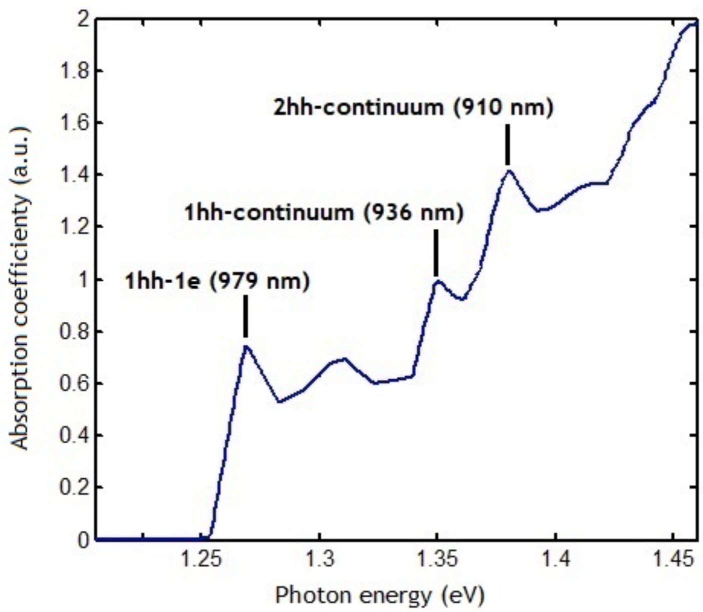

Figure 7.19 Optical absorption of the 10/40 nm $In_{0.2}Ga_{0.8}As$/GaAs single quantum well (SQW) structure using nextnano®.

Too see if the model is correct, below (left) is the results from showing 10 nm $In_{0.2}Ga_{0.8}As$ well surrounded by 50 nm GaAs barriers, compared to the nextnano® simulation using exactly the same parameter in the paper. Simulation give 1hh-1e transition at 1.266 eV (979 nm) for 300K lattice temperature. Because of errors in $In_{0.2}Ga_{0.8}As$ bandgap, this exact 1hh-1e transition can be anywhere between 1.269 eV (977 nm) and 1.212eV (1022 nm). From the paper, it is around 1000 nm, which falls right in the middle.

7.4.5 Mode propagation and absorption properties

The complete wafer structure of the three-guide-layer wafer is shown in Figure 7.1. The epitaxial layers for the waveguide photodiode (WGPD) are shown in Table 7.3. There are nine layers in total. The layer characteristics are as follows in the wafer growth direction. A 200 nm thick, 5×10^{17} cm^{-3} silicon doped n-type $Al_{0.2}Ga_{0.8}As$ is used as the n-contact layer. According to Section 2.2.2.1 and Figure 2.6, the change of refractive index $|\Delta n|$ is smaller than 1×10^{-3}.

Next, a 20 nm thick $Al_{0.2}Ga_{0.8}As$/GaAs grading layer is inserted before a 40 nm thick GaAs barrier layer is grown. A 10 nm $In_{0.2}Ga_{0.8}As$ layer is used as the well material for the QW structure. A 340 nm GaAs layer is used as the second barrier for the QW well structure. The 20 nm thick $Al_{0.2}Ga_{0.8}As$/GaAs grading layer, 40 nm thick GaAs barrier layer, 10 nm $In_{0.2}Ga_{0.8}As$ layer and 340 nm GaAs layer form the intrinsic region of the WGPD. According to Section 2.2.2.2 and Figure 2.7, the change of refractive index $|\Delta n|$ of the GaAs barriers is smaller than 0.02. According to Section 2.2.2.3 and Figure 2.9, the change of refractive index $|\Delta n|$ of the $In_{0.2}Ga_{0.8}As$ is smaller than 0.01.

Next, a 25 nm thick, 1×10^{18} cm^{-3} carbon doped *p*-type GaAs/$Al_{0.3}Ga_{0.7}As$ grading layer is inserted before a 500 nm thick, 1×10^{18} cm^{-3} carbon doped *p*-type $Al_{0.3}Ga_{0.7}As$ layer is grown. The 500 nm thick, 1×10^{18} cm^{-3} carbon doped *p*-type $Al_{0.3}Ga_{0.7}As$ layer plays the role of the upper cladding layer of the WGPD. Finally, a 25 nm thick, 1×10^{18} cm^{-3} carbon doped *p*-type $Al_{0.3}Ga_{0.7}As$/GaAs grading layer is inserted before a 100 nm thick, 5×10^{18} cm^{-3} carbon doped *p*-type GaAs layer is grown as the *p*-contact layer. According to Section 2.2.2.4 and Figure 2.11, the change of refractive index $|\Delta n|$ of the 500 nm thick, 1×10^{18} cm^{-3} carbon doped *p*-type $Al_{0.3}Ga_{0.7}As$ layer is smaller than 1.4×10^{-3}.

Table 7.3 The composition, thickness, doping characteristics of the epitaxial layers in the WGPD structure.

Material	Thickness (nm)	Doping level (cm^{-3})	Dopant species	Dopant type
GaAs	100	5×10^{18}	Carbon	p
$Al_{0.3}Ga_{0.7}As$ to GaAs	25	1×10^{18}	Carbon	p
$Al_{0.3}Ga_{0.7}As$	500	1×10^{18}	Carbon	p
GaAs to $Al_{0.3}Ga_{0.7}As$	25	1×10^{18}	Carbon	p
GaAs	340	-	-	-
$In_{0.2}Ga_{0.8}As$	10	-	-	-
GaAs	40	-	-	-
$Al_{0.2}Ga_{0.8}As$ to GaAs	20	-	-	-
$Al_{0.2}Ga_{0.8}As$	200	5×10^{17}	Silicon	n

A schematic of the WGPD wafer structure is shown in Figure 7.20. Simulation is carried out with RSoft® BPM method. Light is launched in from the PWG, which has been discussed in Section 7.2. A vertical coupler is used to transfer light into the WGPD [200]. An optimization process, which is similar to Figure 5.3, is used. Basically, the material composition and thickness of each layer, and geometrical design parameters, i.e. the width of the WGPD ridge, width of the mesa and length of the taper, are varied. Power monitors and contour monitor are positioned after the taper where the remaining total power in the PWG mode is about ($1/e^2$). The goal of the optimization process is to achieve smooth transfer and efficient absorption of the light.

The final WGPD geometry is shown in Figure 7.21(a) and has a mesa width of 6 μm and a ridge width of 3 μm. As the light propagates in the PWG mode along Z direction, it is evanescently coupled in to the WGPD structure and gets absorbed. The WGPD length corresponding to ($1/e^2$) residual power is about 60 μm. With 200 μm WGPD length, about 99% of the PWG mode power is absorbed, as shown in Figure 7.21(b) and (c).

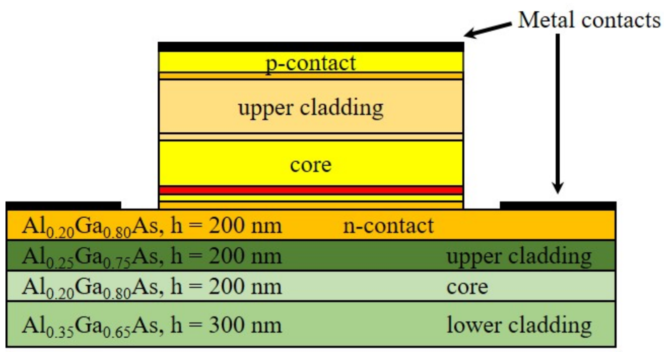

Figure 7.20 Schematic of the WGPD wafer structure. The layer descriptions for the thick layers, i.e. the 200 nm $Al_{0.2}Ga_{0.8}As$ *n*-contact, 340 nm GaAs intrinsic layer, 500 nm $Al_{0.3}Ga_{0.7}As$ upper cladding layer and 100 nm GaAs *p*-contact layer, are shown. The three layers for passive waveguide (PWG) are also included and shown in green.

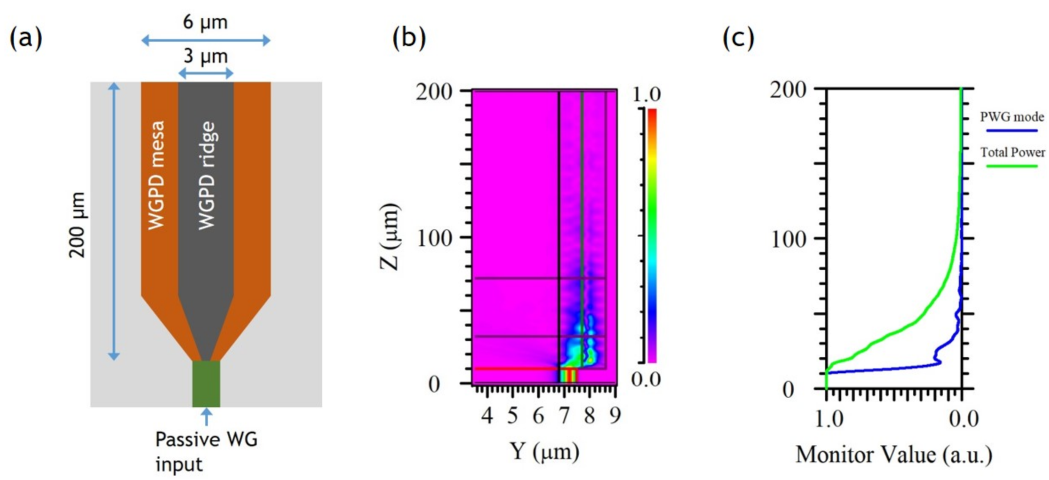

Figure 7.21 (a) Schematic of the WGPD. (b) Propagation and absorption profiles at the wavelength of 850 nm. (c) Power monitors for the PWG mode and total power.

The effects of the refractive index change due to doping are simulated. The effects of changing material refractive indices in the RSoft® BPM tools, as well as absorption coefficients where applicable. The findings are as follows. The changes in the refractive index of the *n*-contact and *p*-contact layers were very small, no effects were present. The effects in all the grading layers and the 10 nm $In_{0.2}Ga_{0.8}As$ QW layer are insignificant because these layers are very thin. The change in the 340 nm GaAs layer in the intrinsic region have a very minor effect on the vertical coupling and absorption profile. In summary, the changes in the refractive indices or absorption coefficients have negligible effects.

7.4.6 Responsivity

Using Crosslight® SimuPICS3D tools, we obtained a simulated photo responsivity of 0.66 A/W at the wavelength of 850 nm. The simulated WPGD structure is shown in Figure 7.22. The *p*-contact and *n*-contact are positioned on the 100 nm thick, 5×10^{18} cm^{-3} carbon doped *p*-type GaAs layer and 200 nm thick, 5×10^{17} cm^{-3} silicon doped *n*-type $Al_{0.2}Ga_{0.8}As$ layer, respectively. These contacts are assumed to be perfect in the model. The vertical mode profile of the WGPD is shown in Figure 7.23. For the simulation, 1 mW optical power is launched in the fundamental mode. The propagation distance of the WGPD is 350 µm. The simulated output current of the WPGD is 0.66 mA. The output light power when the WGPD is bias at -2 V is scanned when the input power is varied from zero to 1 mW and shown in Figure 7.24. The wave intensity profile of the input light is meshed out in the direction of propagation and shown in Figure 7.25. According to the simulations, a theoretical responsivity of 0.66 A/W is obtained for the WGPD.

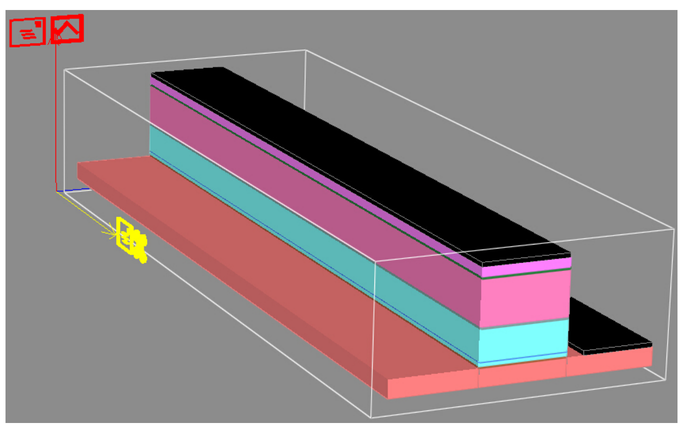

Figure 7.22 Perspective view of the simulated WGPD structure in the Crosslight® SimuPICS3D.

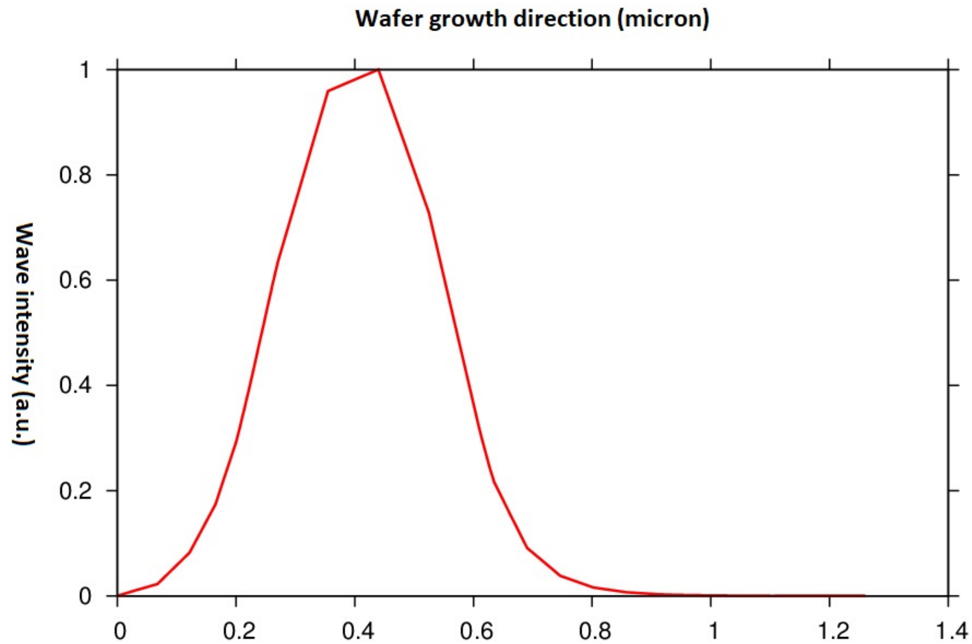

Figure 7.23 Fundamental mode profile of the WGPD structure in the wafer growth directions. The origin is the bottom of the n-contact. The total thickness of teh WGPD is 1.26 μm.

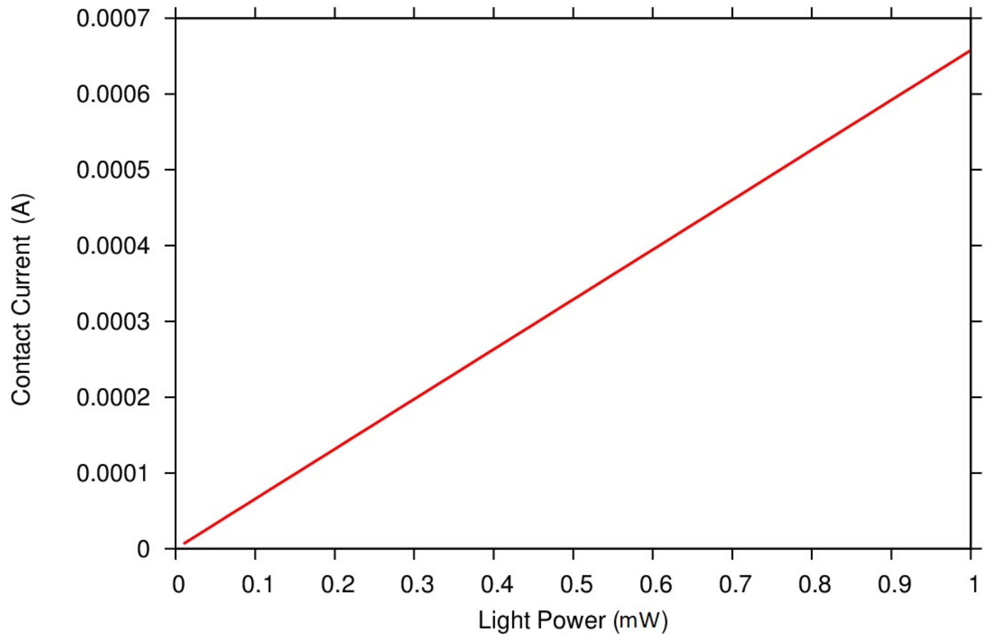

Figure 7.24 Simulated output current of the WGPD as a function of the input power at a bias of -2V.

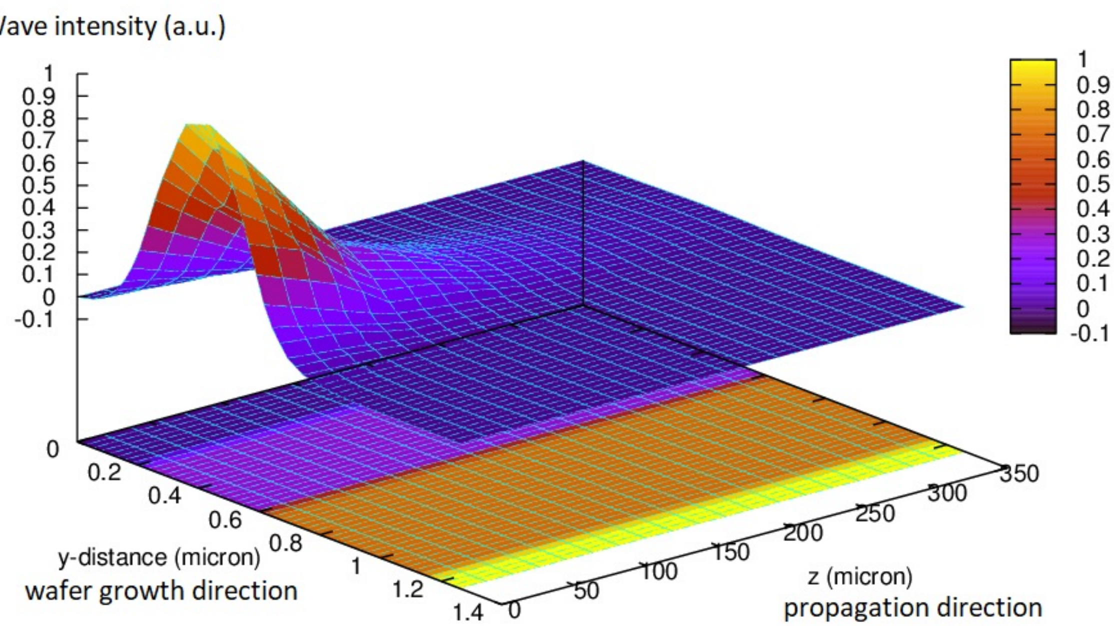

Figure 7.25 Wave intensity profile (in y direction) of the input light meshed in the direction of propagation (in z direction).

7.5 Conclusion

This chapter discussed the theoretical design of a three-guide-layer AlGaAs chip, results of which are published in [201]. First, we presented the design of single mode $Al_xGa_{1-x}As$ optical waveguides with a large mode size. The differential leakage loss between TE_{00} and TE_{10} is 30 dB. The calculated power overlap integral for the two modes is 98% between the FCW waveguide and a SMF with a focused beam waist of 3 μm. Second, we designed a new SSC and achieved a conversion efficiency of 96% for a total SSC length of 350 μm, making it one of the shortest SSCs in the $Al_xGa_{1-x}As$ semiconductors. The two waveguides, PWG and FCW, are polarization insensitive. The single mode operation of the FCW holds for straight and bent waveguides. Third, we designed a WGPD using a 10 nm thick $In_{0.2}Ga_{0.8}As$ as the QW. We simulated the light propagation using RSoft® BPM tools and obtained a theoretical coupling efficient of 99% between the PWG and the WGPD. We simulated the photo responsivity of the WGPD using Crosslight® SimuPICS3D tools and obtained a theoretical responsivity of 0.66 A/W.

Chapter 8
Summary of the thesis

8 Summary of the thesis

The rapidly growing Internet services put a higher bandwidth requirement on datacenters. A low-power and low-cost photonic integrated circuit (PIC), using wavelength division multiplexing (WDM), holds the promise to further scale the density, reach, and bandwidth needed for next-generation datacenter networks. Photonic integrated circuits (PICs) have the potential to produce miniaturized devices, reduce costs and lower the power requirements of optical devices. Monolithically integrated optical components are defined by lithography and thus aligned with high precision, which improves device lifetime and reliability. However, it remains a challenge to monolithically integrate different active and passive components into the same chip, such as those requiring lasers, detectors, or semiconductor-optical-amplifiers (SOAs). One of the biggest challenges facing monolithic photonic integration is the requirement of different bandgap energies for different functional components. Current integration schemes, such as etch-and-regrowth, quantum well intermixing, selective-area-growth and hybrid material integration, suffer from drawbacks that either limit the integration complexity of incur high fabrication costs. The intention of this thesis is to show that multi-guide vertical-integration (MGVI) is a practical approach for integrating multiple optical components with different band gap energies in the $Al_xGa_{1-x}As$ semiconductor system.

8.1 Discussion of results

To design and fabricate optical devices, the index of refraction, n, has to be precisely known. We first analyzed the index of refraction, n, described as a function of the aluminum content, x, and the wavelength, λ, in a semi-empirical model. The carrier induced change of refractive index, Δn, of the $Al_xGa_{1-x}As$ and $In_xGa_{1-x}As$ semiconductors was modeled following literature papers [63-65, 69]. The results were used in the design and simulation of the different wafer structures proposed in this thesis. The carrier induced change of refractive index, Δn, was found to be practically negligible in the design of the three-guide-layer wafer in Chapter 7.

For the realization of vertically integrated circuits operating at 850 nm in AlGaAs, it is critically important to be able to accurately control etch depth. In this thesis, we have explored the use of both wet etching and reactive ion etching processes in the fabrication of such circuits. In Chapter 3, we analyzed wet etching techniques using our first wafer, a two-guide-layer wafer, and demonstrate successful sacrificial etching of $Al_xGa_{1-x}As$ layers with a low aluminum content on $Al_xGa_{1-x}As$ layers with a high aluminum content. Selectivity of 15:1 and 40:1 for citric acid, or succinic acid wet etchants have been obtained. Wet chemical etching recipes provided precise etching depth control. Due to the fact that wet chemical etching was isotropic and lateral etching proceeded at a speed equal to that of vertical etching, slanted waveguide sidewalls were created. The use of wet chemical etching recipes in the fabrication of deep-etched high-aspect-ratio waveguides could be a challenge. However, wet chemical etching recipes induce low damage and can be used in the fabrication of waveguide photodiodes. In addition, we demonstrated sacrificial etching of $Al_{0.7}Ga_{0.3}As$ layers against $Al_xGa_{1-x}As$ layers with $x < 0.5$ on a different wafer structure in HF solutions. The isotropic etching characteristics were utilized in the fabrication of suspended waveguides, where we measured a propagation loss of 25±1 dB/cm and 34±1 dB/cm for the TE and TM modes, respectively, at the wavelength of 1550 nm [110, 202]. The measured propagation losses were still high and could be attributed to an increased electric field at the waveguide sidewalls and thus increased scattering.

In Chapter 4, we developed plasma etching techniques using a combination of EBL and inductively-coupled plasma reactive ion etching (ICP-RIE). We successfully developed two dry etch recipes which allowed for highly precise and anisotropic etching. A slow etch recipe with BCl_3 achieved an etch rate of 0.25 nm/s while a fast etch recipe with Cl_2/N_2 achieved an etch rate of more than 20 nm/s. We fabricated 800-nm wide and 3.2-μm deep straight waveguides using the fast etch recipe and measured a propagation loss of 6.7 dB/cm for the fundamental TE mode at the wavelength of 850 nm [109, 110]. We proved that highly precise and anisotropic etching could be achieved. To the best knowledge of the author, this was the largest difference in etch rates of ICP-RIE recipes that were used in the monolithic integration of optical waveguides. As fabrication of state-of-the-art optoelectronic devices essentially relies on ICP-RIE techniques, the work in this Chapter demonstrated the feasibility of making MGVI chips in the $Al_xGa_{1-x}As$ material system in a University-based fabrication-center environment.

In Chapter 5, we fabricated and tested a vertically integrated spot-size converter (SSC) in the two-guide-layer wafer, which allowed for an efficient coupling from a single mode fiber (SMF) to the high-confinement Device Waveguide (DWG, top waveguide of the wafer), via the large-dimension Coupling Waveguide (CWG, bottom waveguide of the wafer). We measured an insertion loss of 0.4 dB (91±0.2% transmission) on a transmission from the CWG to the DWG at the wavelength of 850 nm. SMF-CWG-DWG insertion loss measures at -3 dB (-1.5 dB after correction for 28% Fresnel reflection at uncoated facet), still leaving a room for improvement, e.g. by optimization of the Coupling Waveguide layer structure and layout [141, 153]. In addition, we designed an arrayed waveguide grating (AWG) in the two-guide-wafer. The proof-of-concept design of AWGs in Chapter 6 demonstrated it is feasible to devise complicated signal processing devices on the top waveguide in the two-guide-layer wafer. We discussed challenges faced in realizing circuits with closely spaced features, based on our preliminary fabrication experiments. The current fabrication challenge was the undercut structures of the devices, which can be circumvented by changing waveguide gaps.

In Chapter 7, we discussed the theoretical design of a three-guide-layer $Al_xGa_{1-x}As$ chip. We presented the design of single mode $Al_xGa_{1-x}As$ optical waveguides with a large mode size based on differential leakage loss between TE_{00} and TE_{10}, which was more than 30 dB. The calculated power overlap integral for the two modes was 98% between the FCW waveguide and a SMF with a focused beam waist of 3 µm. We designed a new SSC and achieved a conversion efficiency of 96% for a total SSC length of 350 µm, making it one of the shortest SSCs in the $Al_xGa_{1-x}As$ semiconductors. We designed a WGPD using a 10 nm thick $In_{0.2}Ga_{0.8}As$ as the QW. We simulated the light propagation using RSoft® BPM tools and obtained a theoretical coupling efficient of 99% between the PWG and the WGPD. We simulated the photo responsivity of the WGPD using Crosslight® SimuPICS3D tools and obtained a theoretical responsivity of 0.66 A/W. Compared to the Chapter 5, the design results in this Chapter showed much improvement.

8.2 Future work

In this thesis, the potential for monolithically integrating different functional components in $Al_xGa_{1-x}As$ using the multi-guide vertical integration approach has been investigated. This approach opens up the opportunity of realizing functional optical circuits, operating at 850 nm which have applications in data center communications, quantum optics and biosensing. The $Al_xGa_{1-x}As$ material system was the first to be used for telecommunications back in the 1980s and continues to have new applications.

8.2.1 WDM devices for data center interconnects

Currently, data center interconnects are dominated by 10 Gbps optical links based on vertical cavity surface emitting lasers (VCSELs) emitting at 850 nm and multi-mode fibers (MMFs). The ever-growing internet traffic calls for upgrading the links to 40 Gbps and then 100 Gbps and the physical size of the data center interconnects require links up to 2 km [44]. The upgrade path to 100 Gbps using VCSELs is to use multiple lanes over parallel optics. While VCSELs are relatively inexpensive, the reach distance of such links is limited to less than 150 meters due to the modal dispersion in MMFs. The use of MMFs in parallel optics drives up the cost. The other option for 100 Gbps links is to use wavelength division multiplexing (WDM) over single mode fibers (SMFs) in the 1.31/1.55 μm windows. However, this requires lasers built in InP/InGaAsP material systems, which is more expensive. This high capacity optical interconnects (OIs) can be built by using wavelength division multiplexing (WDM) transmission over single mode fiber (SMF), which also allows for a step-by-step upgrade by adding more wavelengths per fiber (e.g. by reducing channel spacing) or / and more symbols per bit (e.g. by using coherent receivers). Whereas OIs built in $Al_xGa_{1-x}As$ at the wavelength of 850 are limited to a short reach, this should not be an issue with data centers, which, in most cases, do not require OIs longer than 1 km [30]. The multi-guide vertical integration (MGVI) approach has been proven to be cost-effective [28, 34, 35, 43]. The 1-km WDM point-to-point link loss budget based in $Al_xGa_{1-x}As$ has been estimated [45]. In addition, $Al_xGa_{1-x}As$ semiconductors are more robust and offer cost advantage. Finally, PIC footprint size scales down with a reduction of operating wavelength and increase of index contrast between materials it is made from, both factors playing to the advantage of $Al_xGa_{1-x}As$. The vertical integration approach demonstrated in this thesis provides a new avenue to WDM devices for data center communications.

8.2.2 PICs for quantum optics technology

Research on chip quantum information technology is growing fast and $Al_xGa_{1-x}As$ has also been identified as the promising semiconductor system [92]. Key components including waveguide integrated single-photon detectors [203], waveguide integrated single photon sources [204-206, 98] and quantum state manipulating waveguides [92, 207-209] have been successfully demonstrated. PICs offer a promising approach for future practical and large-scale quantum information processing technologies, with the prospect of on-chip generation, manipulation and measurement of complex quantum states of light. Our group also worked on correlated photon generation using four-wave mixing [93, 99]. The vertical integration approach in this thesis provides a novel avenue to monolithic integration of optical components. The integration of pump lasers, nonlinear optical elements, and signal processing waveguides opens the possibility of a true quantum optics technology in $Al_xGa_{1-x}As$ semiconductors.

8.2.3 Optical biosensing in the 785–850 nm spectral window

The 850 nm spectral window could also find potential use in non-invasive biosensing [210-215]. Hemoglobin has the lowest absorption coefficient in the 785–850 nm spectral window. 1.31/1.55-μm light is not recommended for biosensing in an aqueous environment because of the strong absorption of light by water, which may cause detrimental heat, or unwanted optical signal absorption [169]. There has been a trend of miniaturizing bulking optical systems for diagnostic systems, i.e. optical coherence tomography (OCT) [216-218], NIR absorption spectroscopy [219] and Raman spectroscopy [220]. Therefore, PICs in $Al_xGa_{1-x}As$ semiconductors naturally provide a suitable platform for biosensing applications in the spectral range of 785–850 nm. The miniaturization of optical detection systems for biosensing applications calls for light collection [221, 222], signal processing and detection on a chip. The MGVI scheme in $Al_xGa_{1-x}As$ semiconductors allows for monolithic integration of large-dimension waveguides, which could improve light collection efficiency from scattering media. The efficient and misalignment-tolerant end-fire coupling between optical fibers and large-dimension waveguides on the chip, as demonstrated in Chapter 5, also provides a means of efficient coupling from optical fibers if they are used as an endoscopy collection method. Spectral filtering components, such as those based on arrayed waveguide gratings (AWGs), have been proven essential to biosensing applications [218, 220, 223]. The vertical integration approach in this thesis offers the prospect of producing a fully integrated optical biosensor at a low cost.

References

[1] Cisco Systems. Inc., "Cisco Global Cloud Index: Forecast and Methodology, 2016-2021," White paper, 2018.

[2] C. F. Lam, H. Liu, B. Koley, X. Zhao, V. Kamalov and V. Gill, "Fiber optic communication technologies: What's needed for datacenter network operations," *IEEE Communications Magazine,* vol. 48, no. 7, pp. 32-39, 2010.

[3] H. Liu, C. F. Lam and C. Johnson, "Scaling Optical Interconnects in Datacenter Networks Opportunities and Challenges for WDM," in *2010 18th IEEE Symposium on High Performance Interconnects*, Mountain View, CA, 2010.

[4] D. F. Welch, F. A. Kish, S. Melle, R. Nagarajan, M. Kato, C. H. Joyner, L. J. Pleumeekers, P. R. Schneider, J. Back, A. G. Dentai, V. G. Dominic, P. W. Evans, M. Kauffman, D. J. H. Lambert, S. K. Hurtt, A. Mathur, M. L. Mitchell, M. Missey, S. Murthy, A. C. Nilsson, R. A. Salvatore, F. M. Van Leeuwen, J. Webjorn, M. Ziari, S. G. Grubb, D. Perkins, R. Michael and D. G. Mehuys, "Large-Scale InP Photonic Integrated Circuits: Enabling Efficient Scaling of Optical Transport Networks," *IEEE Journal of Selected Topics in Quantum Electronics,* vol. 13, no. 1, pp. 22-31, 2007.

[5] K. D. Choquette, M. Hong, R. S. Freund, J. P. Mannaerts, R. C. Wetzel and R. E. Leibenguth, "Vertical-Cavity Surface-Emitting Laser Diodes Fabricated by In Situ Dry Etching and Molecular Beam Epitaxial Regrowth," *IEEE Photonics Technology Letters,* vol. 5, no. 3, pp. 284-287, 1993.

[6] X. Duan, Y. Huang, H. Huang, X. Ren, Q. Wang, Y. Shang, X. Ye and S. Cai, "Monolithically Integrated Photodetector Array With a Multistep Cavity for Multiwavelength Receiving Applications," *Journal of Lightwave Technology,* vol. 27, no. 21, pp. 4697-4702, 2009.

[7] J. H. Marsh, "Quantum well intermixing," *Semiconductor Science and Technology,* vol. 8, no. 6, pp. 1136-1155, 1993.

[8] B.-C. Qiu, X.-F. Liu, M.-L. Ke, H.-K. Lee, A. C. Bryce, J. S. Aitchison, J. H. Marsh and C. B. Button, "Monolithic fabrication of 2 x 2 crosspoint switches in InGaAs/InAlGaAs multiple quantum wells using quantum well intermixing," *IEEE Photonics Technology Letters,* vol. 13, no. 12, pp. 1292-1294, 2001.

[9] M. Aoki, H. Sano, M. Suzuki, M. Takahashi, K. Uomi and A. Takei, "Novel structure MQW electroabsorption modulator/DFB-laser integrated device fabricated by selective area MOCVD growth," *Electronics Letters,* vol. 27, no. 23, pp. 2138-2140, 1991.

[10] G. Roelkens, A. Abassi, P. Cardile, U. Dave , A. de Groote, Y. de Koninck, S. Dhoore, X. Fu, A. Gassenq , N. Hattasan, Q. Huang, S. Kumari , S. Keyvaninia , B. Kuyken , L. Li, P. Mechet , M. Muneeb , D. Sanchez , H. Shao , T. Spuesens , A. Z. Subramanian , S. Uvin , M. Tassaert , K. van Gasse , J. Verbist , R. Wang , Z. Wang , J. Zhang , J. van Campenhout , X. Yin , J. Bauwelinck , G. Morthier , R. Baets and D. van Thourhout , "III-V-on-Silicon Photonic Devices for Optical Communication and Sensing," *Photonics,* vol. 2, no. 3, pp. 969-1004, 2015.

[11] I. V. Kulkova, S. Kadkhodazadeh, N. Kuznetsova, A. Huck, E. S. Semenova and K. Yvind, "High-quality MOVPE butt-joint integration of InP/AlGaInAs/InGaAsP-based all-active optical components," *Journal of Crystal Growth,* vol. 402, pp. 243-248, 2014.

[12] K. Shimoyama, Y. Inoue, M. Katoh, H. Gotoh, Y. Suzuki and H. Yajima, "A new selective MOVPE regrowth process utilizing in-situ vapor phase etching for optoelectronic integrated circuits," *Journal of Crystal Growth,* vol. 107, pp. 767-771, 1991.

[13] F. Bugge, A. Mogilatenko, U. Zeimer, O. Brox, W. Neumann, G. Erbert and M. Weyers, "Characterization and optimization of 2-step MOVPE growth for single-mode DFB or DBR laser diodes," *Journal of Crystal Growth,* vol. 315, no. 1, pp. 74-77, 2011.

[14] J. E. Haysom and R. Clayton, "Quantum well intermixing for opto-electronics manufacturing," in *Proc. SPIE 10313, Opto-Canada: SPIE Regional Meeting on Optoelectronics, Photonics, and Imaging*, 29 August 2017.

[15] D. G. Deppe, L. J. Guido, N. Holonyak Jr. and K. C. Hsieh, "Stripe-geometry quantum well heterostructure $Al_xGa_{1-x}As$-GaAs lasers defined by defect diffusion," *Appl. Phys. Lett.,* vol. 49, no. 9, pp. 510-512, 1986.

[16] B. S. Ooi, K. McIlvaney, M. W. Street, A. S. Helmy, S. G. Ayling, A. C. Bryce, J. H. Marsh and J. S. Roberts, "Selective quantum-well intermixing in GaAs-AlGaAs structures using impurity-free vacancy diffusion," *IEEE Journal of Quantum Electronics,* vol. 33, no. 10, pp. 1784-1793, 1997.

[17] O. P. Kowalski, C. J. Hamilton, S. D. McDougall, J. H. Marsh, A. C. Bryce, R. M. De La Rui, B. Vögele, C. R. Stanley, C. C. Button and J. S. Roberts, "A universal damage induced technique for quantum well intermixing," *Appl. Phys. Lett.,* vol. 72, no. 5, pp. 581-583, 1998.

[18] S. Charbonneau, P. J. Poole, P. G. Piva, G. C. Aers, E. S. Koteles, M. Fallahi, J.-J. He, J. P. McCaffrey, M. Buchanan, M. Dion, I. C. Mitchell and I. V. Mitchell, "Quantum-well intermixing for optoelectronic integration using high energy ion implantation," *Journal of Applied Physics,* vol. 78, no. 6, pp. 3697-3705, 1995.

[19] H. Leier, A. Forchel, G. Horcher, J. Hommel, S. Bayer, H. Rothfritz, G. Weimann and W. Schlapp, "Mass and dose dependence of ion-implantation-induced intermixing of GaAs/GaAlAs quantum-well structures," *Journal of Applied Physics,* vol. 67, no. 4, pp. 1805-1813, 1990.

[20] U. Younis, B. M. Holmes and D. C. Hutchings, "Characterization and optimization of ion implantation for high spatial resolution quantum well intermixing in GaAs/AlGaAs superlattices," *The European Physical Journal - Applied Physics,* vol. 66, no. 1, p. 10101, 2014.

[21] C. J. McLean, A. McKee, G. Lullo, A. C. Bryce, R. M. De La Rue and J. H. Marsh, "Quantum well intermixing with high spatial selectivity using a pulsed laser technique," *Electronics Letters,* vol. 31, no. 5, pp. 1285-1286, 1995.

[22] T. Wong, V. M. Menon, F. Xia and S. R. Forrest, "An asymmetric twin waveguide eight-channel polarization-independent arrayed waveguide grating with an integrated photodiode array," *IEEE Photonics Technology Letters,* vol. 16, no. 4, pp. 1170-1172, 2004.

[23] F. Xia, J. K. Thomson, M. R. Gokhale, P. V. Studenkov, J. Wei, W. Lin and S. R. Forrest, "An asymmetric twin-waveguide high-bandwidth photodiode using a lateral taper coupler," *IEEE Photonics Technology Letters,* vol. 13, no. 8, pp. 845-847, 2001.

[24] C. Zhang, S. Liang, H. Zhu and W. Wang, "Widely tunable dual-mode distributed feedback laser fabricated by selective area growth technology integrated with Ti heaters," *Optics Letters,* vol. 38, no. 6, pp. 3050-3053, 2013.

[25] T. Komljenovic, S. Srinivasan, E. Norberg, M. Davenport, G. Fish and J. E. Bowers, "Widely Tunable Narrow-Linewidth Monolithically Integrated External-Cavity Semiconductor Lasers," *IEEE Journal of Selected Topics in Quantum Electronics,* vol. 21, no. 6, pp. 214-222, 2015.

[26] Y.-H. Jhang, K. Tanabe, S. Iwamoto and Y. Arakawa, "InAs/GaAs quantum dot lasers on silicon-on-insulator substrated by metal-stripe wafer bonding," *IEEE Photon. Technol. Lett.,* vol. 27, no. 8, p. 875–878, 2015.

[27] S. Keyvaninia, M. Muneeb, S. Stanković, P. J. Van Veldhoven, D. Van Thourhout and G. Roelkens, "Ultra-thin DVS-BCB adhesive bonding of III-V wafers, dies and multiple dies to a patterned silicon-on-insulator substrate," *Opt. Mater. Express,* vol. 3, no. 1, pp. 35-46, 2013.

[28] V. Tolstikhin, "Single-mode vertical integration of active devices within passive waveguides of InP-based planar WDM components," in *Integrated Photonics Conference*, Vancouver, BC, 2002.

[29] F. Xia, V. M. Menon and S. R. Forrest, "Photonic integration using asymmetric twin-waveguide (ATG) technology: part I-concepts and theory," *IEEE Journal of Selected Topics in Quantum Electronics,* vol. 11, no. 1, pp. 17-29, 2005.

[30] V. Tolstikhin, "Regrowth-free multi-guide vertical integration in InP for optical communications," in *IPRM 2011 - 23rd International Conference on Indium Phosphide and Related Materials*, Berlin, 2011.

[31] P. V. Studenkov, F. Xia, M. R. Gokhale and S. R. Forrest, "Asymmetric twin-waveguide 1.55-μm wavelength laser with a distributed Bragg reflector," *IEEE Photonics Technology Letters,* vol. 12, no. 5, pp. 468-470, 2000.

[32] V. I. Tolstikhin, C. D. Watson, K. Pimenov, R. Moore, Y. Logvin and F. Wu, "Laterally Coupled DFB Lasers for One-Step Growth Photonic Integrated Circuits in InP," *IEEE Photonics Technology Letters,* vol. 21, no. 10, pp. 621-623, 2009.

[33] S. Kuntze, V. Tolstikhin, F. Wu, Y. Logvin, C. Watson, K. Pimenov, R. Moore, A. Moore, H. Wang and T. Oogarah, "Transmitter and Receiver Solutions ror Regrowth-Free Multi-Guide Vertical Integration in InP," in *Integrated Photonics Research, Silicon and Nanophotonics and Photonics in Switching*, Monterey, CA, 2010.

[34] V. Tolstikhin, R. Moore, K. Pimenov, Y. Logvin, F. Wu and C. D. Watson, "One-step growth optical transceiver PIC in InP," in *2009 35th European Conference on Optical Communication*, Vienna, 2009.

[35] V. Tolstikhin, S. Saeidi and K. Dolgaleva, "Design optimization and tolerance analysis of a spot-size converter for the taper-assisted vertical integration platform in InP," *Applied Optics,* vol. 57, no. 13, pp. 3586-3591, 2018.

[36] P. V. Studenkov, M. R. Gokhale and S. R. Forrest, "Efficient coupling in integrated twin-waveguide lasers using waveguide tapers," *IEEE Photonics Technology Letters,* vol. 11, no. 9, pp. 1096-1098, 1999.

[37] R. K. Watts, "Evanescent field coupling of thin-film laser and passive waveguide," *Journal of Applied Physics,* vol. 44, no. 20, p. 5635–5636, 1973.

[38] Y. Suematsu, M. Yamada and K. Hayashi, "Integrated twin-guide AlGaAs laser with multiheterostructure," *IEEE Journal of Quantum Electronics,* vol. 11, no. 7, pp. 457-460, 1975.

[39] K. Iga, T. Kambayashi and K. Wakao, "GaInAsP/InP DH lasers and related fabricating techniques for integration," *Journal of Quantum Electronics,* vol. 15, no. 8, pp. 707-710, 1979.

[40] H. Wang, C. Li and S. R. Forrest, "A fully integratable 1.55-µm wavelength continuously tunable asymmetric twin-waveguide distributed Bragg reflector laser," *IEEE Photonics Technology Letters,* vol. 15, no. 9, pp. 1189-1191, 2003.

[41] P. V. Studenkov, M. R. Gokhale, W. Lin, I. Glesk, P. R. Prucnal and S. R. Forrest, "Monolithic integration of an all optical Mach-Zehnder demultiplexer using an asymmetric twin waveguide structure," *IEEE Photonics Technology Letters,* vol. 13, no. 6, pp. 600-602, 2001.

[42] V. Tolstikhin, A. Densmore and K. Pimenov, "InP-Based Single-Mode Vertically Integrated Waveguide Photodetectors: Characterization and Performance analysis," in *Integrated Photonics Research Conference*, Washington D.C., 2003.

[43] V. Tolstikhin, A. Densmore, K. Pimenov and S. Laframboise, "Single-mode vertical integration of p-i-n photodetectors with optical waveguides for monitoring in WDM transmission systems," *IEEE Photonics Technology Letters,* vol. 15, no. 6, pp. 843-845, 2003.

[44] B. Koley and V. Vusirikala, "100GbE and beyond for warehouse scale computing interconnects," *Optical Fiber Technology,* vol. 17, no. 5, pp. 363-367, 2011.

[45] V. Tolstikhin, S. Wagner and J. S. Aitchison, "High-capacity optical interconnects using WDM photonic integrated circuits in GaAs," in *2012 Optical Interconnects Conference*, Santa Fe, NM, 2012.

[46] D. T. Marple, "Refractive Index of GaAs," *Journal of Applied Physics,* vol. 35, no. 4, pp. 1241-1242, 1964.

[47] H. C. Casey Jr., D. D. Sell and M. B. Panish, "Refractive index of $Al_xGa_{1-x}As$ between 1.2 and 1.8 eV," *Applied Physics Letters,* vol. 24, no. 2, pp. 63-65, 1974.

[48] D. E. Aspnes, S. M. Kelso, R. A. Logan and R. Bhat, "Optical properties of $Al_xGa_{1-x}As$," *Journal of Applied Physics,* vol. 60, no. 2, pp. 754-767, 1986.

[49] R. E. Fern and A. Onton, "Refractive Index of AlAs," *Journal of Applied Physics,* vol. 42, no. 9, pp. 3499-3500, 1971.

[50] F. Stern, "Dispersion of the index of refraction near the absorption edge of semiconductors," *Physical Review,* vol. 133, no. 6A, pp. A1653-1664, 1964.

[51] M. A. Afromowitz, "Refractive index of $Ga_{1-x}Al_xAs$," *Solid State Communications,* vol. 15, no. 1, pp. 59-63, 1974.

[52] S. Adachi, "GaAs, AlAs, and $Al_xGa_{1-x}As$: Material parameters for use in research and device applications," *Journal of Applied Physics,* vol. 58, no. 3, pp. R1-R29, 1985.

[53] S. Adachi, "Optical properties of $Al_xGa_{1-x}As$ alloys," *Physical Review B,* vol. 38, no. 17, pp. 12345-12352, 1988.

[54] S. Adachi, "Optical dispersion relations for GaP, GaAs, GaSb, InP, InAs, InSb, $Al_xGa_{1-x}As$ and $In_xGa_{1-x}As_yP_{1-y}$," *Journal of Applied Physics,* vol. 66, no. 12, pp. 6030-6040, 1989.

[55] D. W. Jenkins, "Optical constants of $Al_xGa_{1-x}As$," *Journal of Applied Physics,* vol. 68, no. 4, pp. 1848-1853, 1990.

[56] C.-H. Lin and J. M. Meese, "Optical properties of bulk $Al_xGa_{1-x}As$," *Journal of Applied Physics,* vol. 74, no. 10, pp. 6341-6348, 1993.

[57] J. Zheng, C.-H. Lin and C. H. Kuo, "Optical properties of bulk AlGaAs," *Journal of Applied Physics,* vol. 82, no. 2, pp. 792-797, 1997.

[58] Y. Kokubo and I. Ohta, "Refractive index as a function of photon energy for AlGaAs between 1.2 and 1.8 eV," *Journal of Applied Physics,* vol. 81, no. 4, pp. 2042-2043, 1997.

[59] R. J. Deri and M. A. Emanuel, "Consistent formula for the refractive index of $Al_xGa_{1-x}As$ below the band edge," *Journal of Applied Physics,* vol. 77, no. 9, pp. 4667-4672, 1995.

[60] S. Gehrsitz, F. K. Reinhart, C. Gourgon, N. Herres, A. Vonlanthen and H. Sigg, "The refractive index of $Al_xGa_{1-x}As$ below the band gap: Accurate determination and empirical modeling," *Journal of Applied Physics,* vol. 87, no. 11, pp. 7825-7837, 2000.

[61] B. H. Kolner and D. M. Bloom, "Electrooptic Sampling in GaAs Integrated Circuits," *IEEE Journal of Quantum Electronics,* vol. 22, no. 1, pp. 79-93, 1986.

[62] H. C. Huang, S. Yee and M. Soma, "The carrier effects on the change of refractive index for n-type GaAs at λ = 1.06, 1.3, and 1.55 µm," *Journal of Applied Physics,* vol. 67, no. 3, pp. 1497-1503, 1990.

[63] B. R. Bennett, A. R. Soref and J. A. Del Alamo, "Carrier induced change in refractive index of InP GaAs and InGaAsP," *IEEE Journal of Quantum Electronics,* vol. 26, no. 1, pp. 113 - 122, 1990.

[64] E. Burstein, "Anomalous optical absorption in InSb," *Phys. Rev.,* vol. 93, p. 632, 1954.

[65] T. S. Moss, G. J. Burrell and B. Ellis, Semiconductor Opto-Electronics, New york: Willey, 1973, pp. 48-94.

[66] "NSM Archive," [Online]. Available: http://www.ioffe.ru/SVA/NSM/Semicond/index.html. [Accessed 2016].

[67] K.-F. Berggren and B. E. Sernelius, "Band-gap narrowing in heavily doped many-valley semiconductors," *Physical Review B,* vol. 24, no. 4, pp. 1971-1986, 1981.

[68] H. S. Bennett and J. R. Lowney, "Models for heavy doping effects in gallium arsenide," *Journal of Applied Physics,* vol. 62, no. 2, pp. 521-527, 1987.

[69] C. H. Henry, R. A. Logan and K. A. Bertness, "Spectral dependence of the change in refractive index due to carrier injection in GaAs lasers," *Journal of Applied Physics,* vol. 52, no. 7, pp. 4457-4461, 1981.

[70] M. Tong, D. G. Ballegeer, A. Ketterson, E. J. Roan, K. Y. Cheng and I. Adesida, "A Comparative Study of Wet and Dry Selective Etching Processes for GaAs/AIGaAs/InGaAs Pseudomorphic MODFETs," *Journal of Electronic Materials,* vol. 21, no. 1, pp. 9-15, 1992.

[71] J.-M. Lee, K.-S. Lee and S.-J. Park, "Removal of dry etch damage in p-type GaN by wet etching of sacrificial oxide layer," *Journal of Vacuum Science & Technology B,* vol. 22, no. 2, pp. 479-482, 2004.

[72] A. G. Baca and C. I. Ashby, Fabrication of GaAs Devices, London: The lnstitution of Engineering and Technology, 2005.

[73] T. Takebe, T. Yamamoto, M. Fujii and K. Kobayashi, "Fundamental Selective Etching Characteristics of $HF + H_2O_2 + H_2O$ Mixtures for GaAs," *Journal of the Electrochemical Society,* vol. 140, no. 4, pp. 1169-1180, 1993.

[74] C. Juang, K. Kuhn and R. B. Darling, "Selective etching of GaAs and $Al_{0.30}Ga_{0.70}As$ with citric acid/hydrogen peroxide solutions," *Journal of Vacuum Science & Technology B: Microelectronics Processing and Phenomena,* vol. 8, no. 5, pp. 1122-1124, 1990.

[75] G. C. DeSalvo, . W. F. Tseng and J. Comas, "Etch Rates and Selectivities of Citric Acid/Hydrogen Peroxide on GaAs, $Al_{0.3}Ga_{0.7}As$, In0.2Ga0.8As, $In_{0.53}Ga_{0.47}As$, $In_{0.52}Al_{0.48}As$, and InP," *Journal of the Electrochemical Society,* vol. 139, no. 3, pp. 831-835, 1992.

[76] B. Mao, J. A. Nielsen, R. A. Friedman and G. Lee, "The Applications of Citric Acid/Hydrogen Peroxide Etching Solutions in the Processing of Pseudomorphic MODFETs," *Journal of the Electrochemical Society,* vol. 141, no. 4, pp. 1082-1085, 1994.

[77] M. Otsubo, T. Oda, H. Kumabe and H. Miki, "Preferential Etching of GaAs Through Photoresist Masks," *Journal of the Electrochemical Society,* vol. 123, no. 5, pp. 676-680, 1976.

[78] A. Tang, K. Sadra and B. G. Streetman, "Selective Etching of $Al_xGa_{1-x}As$ and $In(Al_xGa_{1-x})As$ Alloys in Succinic Acid-Hydrogen Peroxide Solutions," *Journal of Electrochemical Society,* vol. 140, no. 5, pp. L82-L83, 1993.

[79] S. A. Merritt and M. Dagenais, "Etch Characteristics of Succinic Acid/Ammonia/Hydrogen Peroxide versus Aluminum Mole Fraction in AlGaAs," *Journal of the Electrochemical Society,* vol. 140, no. 9, pp. L138-L139, 1993.

[80] D. W. Shaw, "Localized GaAs Etching with Acidic Hydrogen Peroxide Solutions," *Journal of the Electrochemical Society,* vol. 128, no. 4, pp. 874-880, 1981.

[81] X. Wu, L. A. Coldren and J. L. Merz, "Selective etching characteristics of HF for $Al_xGa_{1-x}As$/GaAs," *Electronics Letters (UK),* vol. 21, no. 30, pp. 558-559, 1985.

[82] T. Kitano, S. Izumi, H. Minami, T. Ishikawa, K. Sato, T. Sonoda and M. Otsubo, "Selective wet etching for highly uniform GaAs/$Al_{0.15}Ga_{0.85}As$ heterostructure field effect transistors," *Journal of Vacuum Science & Technology B,* vol. 15, no. 1, pp. 167-170, 1997.

[83] M. Konagai, M. Sugimoto and K. Takahashi, "High efficiency GaAs thin film solar cells by peeled film technology," *Journal of Crystal Growth,* vol. 45, pp. 277-280, 1978.

[84] E. Yablonovitch, T. Gmitter, J. P. Harbison and R. Bhat, "Extreme selectivity in the lift-off of epitaxial GaAs films," *Applied Physics Letters,* vol. 51, no. 28, pp. 2222-2224, 1987.

[85] J. Yoon, S. Jo, I. S. Chun, I. Jung, H.-S. Kim, M. Meitl, E. Etienne, X. Li, J. J. Coleman, U. Paik and J. A. Rogers, "GaAs photovoltaics and optoelectronics using releasable multilayer epitaxial assemblies," *Natutre,* vol. 465, pp. 329-333, 2010.

[86] O. Moutanabbir and U. Gösele, "Heterogeneous Integration of Compound Semiconductors," *Annual Review of Materials Research,* vol. 40, pp. 469-500, 2010.

[87] R. T. Chen, L. Lin, C. Choi, Y. J. Liu, B. Bihari, L. Wu, S. Tang, R. Wickman, B. Picor, M. K. Hibbs-Brenner, J. Bristow and Y. Liu, "Fully Embedded Board-Level Guided-Wave Optoelectronic Interconnects," *Proceedings of the IEEE,* vol. 88, no. 6, pp. 780-793, 2010.

[88] P. Kumar, S. Kanakaraju and D. L. Devoe, "Sacrificial etching of $Al_xGa_{1-x}As$ for III–VMEMS surface micromachining," *Applied Physics A,* vol. 88, no. 4, p. 711–714, 2007.

[89] M. M. A. J. Voncken, J. J. Schermer, G. J. Bauhuis, P. Mulder and P. K. Larsen, "Multiple release layer study of the intrinsic lateral etch rate of the epitaxial lift-off process," *Applied Physics A,* vol. 79, no. 7, pp. 1801-1807, 2004.

[90] W. Chang, C. P. Kao, G. A. Pike and E. Yablonovitch, "Vapor phase epitaxial lift-off of GaAs and silicon single crystal films," *Solar Energy Materials and Solar Cells,* vol. 58, no. 2, pp. 141-146, 1999.

[91] L. Li, P. Kumar, L. Calhoun and D. L. DeVoe, "Piezoelectric $Al_{0.3}Ga_{0.7}As$ longitudinal mode bar resonators," *Journal of Microelectromechanical systems,* vol. 15, no. 3, pp. 465-470, 2006.

[92] J. Wang, A. Santamato, P. Jiang, D. Bonneau, E. Engin, J. W. Silverstone, M. Lermer, J. Beetz, M. Kamp, S. Höfling, M. G. Tanner, C. M. Natarajan, R. H. Hadfield, S. N. Dorenbos, V. Zwiller, J. L. O'Brien and M. G. Thompson, "Gallium arsenide (GaAs) quantum photonic waveguide circuits," *Optics Communications,* vol. 327, pp. 49-55, 2014.

[93] K. Dolgaleva, P. Sarrafi, P. Kultavewuti, K. M. Awan, N. Feher, J. S. Aitchison, L. Qian, M. Volatier, R. Arès and V. Aimez, "Tuneable four-wave mixing in AlGaAs nanowires," *Optics Express,* vol. 23, no. 17, pp. 22477-22493, 2015.

[94] C. Lacava, V. Pusino, P. Minzioni, M. Sorel and I. Cristiani, "Nonlinear properties of AlGaAs waveguides in continuous wave operation regime," *Optics Express,* vol. 22, no. 5, pp. 5291-5298, 2014.

[95] A. S. Helmy, P. Abolghasem, J. S. Aitchison, B. J. Bijlani, J. Han, B. M. Holmes, D. C. Hutchings, U. Younis and S. J. Wagner, "Recent advances in phase matching of second-order nonlinearities in monolithic semiconductor waveguides," *Laser Photonics Rev.,* vol. 5, no. 2, pp. 272-286, 2011.

[96] F. Leo, J. Safioui, B. Kuyken, G. Roelkens and S.-P. Gorza, "Generation of coherent supercontinuum in a-Si:H waveguides: experiment and modeling based on measured dispersion profile," *Optics Express,* vol. 22, no. 23, pp. 28997-29007, 2014.

[97] D. Duchesne, M. Peccianti, M. R. E. Lamont, M. Ferrera, L. Razzari, F. Légaré, R. Morandotti, S. Chu, B. E. Little and D. J. Moss, "Supercontinuum generation in a high index doped silica glass spiral waveguide," *Optics Express,* vol. 18, no. 2, pp. 923-930, 2010.

[98] R. Horn, P. Abolghasem, B. J. Bijlani, D. Kang, A. S. Helmy and G. Weihs, "Monolithic Source of Photon Pairs," *Phys. Rev. Lett.,* vol. 108, p. 153605, 2012.

[99] P. Kultavewuti, E. Y. Zhu, L. Qian, V. Pusino, M. Sorel and J. S. Aitchison, "Correlated photon pair generation in AlGaAs nanowaveguides via spontaneous four-wave mixing," *Optics Express,* vol. 24, no. 4, pp. 3365-3376, 2016.

[100] C. Autebert, N. Bruno, A. Martin, A. Lemaitre, C. G. Carbonell, I. Favero, G. Leo, H. Zbinden and S. Ducci, "Integrated AlGaAs source of highly indistinguishable and energy-time entangled photons," *Optica,* vol. 3, no. 2, pp. 143-146, 2016.

[101] A. Orieux, M. A. M. Versteegh, K. D. Jöns and S. Ducci, "Semiconductor devices for entangled photon pair generation: a review," *Rep. Prog. Phys.,* vol. 80, no. 7, p. 076001, 2017.

[102] R. W. Boyd, Nonlinear optics, 3rd ed., Academic Press, 2008.

[103] M. A. Foster, A. C. Turner, J. E. Sharping, B. S. Schmidt, M. Lipson and A. L. Gaeta, "Broad-band optical parametric gain on a silicon photonic chip," *Nature,* vol. 441, pp. 960-963, 2006.

[104] P. Apiratikul, J. J. Wathen, G. A. Porkolab, B. Wang, L. He, T. E. Murphy and C. J. K. Richardson, "Enhanced continuous-wave four-wave mixing efficiency in nonlinear AlGaAs waveguides," *Optics Express,* vol. 22, no. 22, pp. 26814-26824, 2014.

[105] P. P. Absil, J. V. Hryniewicz, B. E. Little, P. S. Cho, R. A. Wilson, L. G. Joneckis and P.-T. Ho, "Wavelength conversion in GaAs micro-ring resonators," *Optics Letters,* vol. 25, no. 8, pp. 554-556, 2000.

[106] J. Meier, W. S. Mohammed, A. Jugessur, L. Qian, M. Mojahedi and J. S. Aitchison, "Group velocity inversion in AlGaAs nanowires," *Optics Express,* vol. 15, no. 20, pp. 12755-12762, 2007.

[107] P. Kultavewuti, E. Y. Zhu, X. Xing, L. Qian, V. Pusino, M. Sorel and J. S. Aitchison, "Polarization-entangled photon pair sources based on spontaneous four wave mixing assisted by polarization mode dispersion," *Scientific Reports,* vol. 7, p. 5785, 2017.

[108] M. Pu, L. Ottaviano, E. Semenova and K. Yvind, "Efficient frequency comb generation in AlGaAs-on-insulator," *Optica,* vol. 3, no. 8, pp. 823-826, 2016.

[109] Z. Liao and J. S. Aitchison, "Precision etching for multi-level AlGaAs," *Optical Material Express,* vol. 7, no. 3, pp. 895-903, 2017.

[110] P. Kultavewuti, Z. Liao and J. S. Aitchison, "2D high-contrast AlGaAs waveguides for nonlinear applications," in *2016 IEEE Photonics Conference (IPC)*, Waikoloa, HI, 2016.

[111] J. Robinson and Y. Rahmat-Samii, "Particle Swarm Optimization in Electromagnetics," *IEEE Transactions on Antennas and Propagation,* vol. 52, no. 2, pp. 397-407, 2004.

[112] R. Shul, G. McClellan, R. Briggs, D. Rieger, S. Pearton, C. Abernathy, J. Lee, C. Constantine and C. Barratt, "High-density plasma etching of compound semiconductors," *Journal of Vacuum Science & Technology A,* vol. 15, no. 3, pp. 663-637, 1997.

[113] M. Volatier, D. Duchesne, R. Morandotti, R. Arès and V. Aimez, "Extremely high aspect ratio GaAs and GaAs/AlGaAs nanowaveguides fabricated using chlorine ICP etching with N_2-promoted passivation," *Nanotechnology,* vol. 21, no. 13, p. 134014, 2010.

[114] Y. Peng, X. Ye, B. Xu, P. Jin, J. Niu, R. Jia and Z. Wang, "Optimization of inductively coupled plasma etching for low nanometer scale air-hole arrays in two-dimensional GaAs-based photonic crystals," *Journal of Semiconductors,* vol. 31, no. 1, p. 012003, 2010.

[115] D. S. Rawal, A. Kapoor, H. Sharma, B. Sehgal and H. K. Malik, "A Highly Selective Low Pressure Inductively Coupled Plasma Etching Process for GaAs Using Photoresist Mask," *The Open Plasma Physics Journal,* vol. 4, pp. 34-39, 2011.

[116] D. S. Rawal, B. K. Sehgal, R. Muralidharan and H. K. Malik, "Experimental Study of the Influence of Process Pressure and Gas Composition on GaAs Etching Characteristics in Cl_2/BCl_3-Based Inductively Coupled Plasma," *Plasma Science and Technology,* vol. 13, no. 2, pp. 223-229, 2011.

[117] T. Brückl and H. Zull, "Actinometry of inductively coupled Cl_2/N_2 plasmas for dry etching of GaAs," *Journal of Applied Physics,* vol. 98, p. 023307, 2005.

[118] L. Jalabert, P. Dubreuil, F. Carcenac, S. Pinaud, L. Salvagnac, H. Granier and C. Fontaine, "High aspect ratio GaAs nanowires made by ICP-RIE etching using Cl_2/N_2 chemistry," *Microelectronic Engineering,* vol. 85, no. 5, pp. 1173-1178, 2008.

[119] R. Braive, L. L. Gratiet, S. Guilet, G. Patriarche, A. Lemaître, A. Beveratos, I. Robert-Philip and I. Sagnes, "Inductively coupled plasma etching of GaAs suspended photonic crystal cavities," *Journal of Vacuum Science & Technology B,* vol. 27, no. 4, pp. 1909-1914, 2009.

[120] Y. H. Park, J. K. Kim, J. H. Lee, Y. W. Joo, H. S. Noh, J. W. Lee and S. J. Pearton, "N_2 effect on GaAs etching at 150 mTorr capacitively-coupled Cl_2/N_2 plasma," *Microelectronic Engineering,* vol. 87, no. 4, pp. 548-552, 2010.

[121] K. Liu, X. Ren, Y. Huang, S. Cai, X. Duan, Q. Wang, C. Kang, J. Li, Q. Chen and J. Fei, "Inductively coupled plasma etching of GaAs in Cl_2/Ar, Cl_2/Ar/O_2 chemistries with photoresist mask," *Applied Surface Science,* vol. 356, pp. 776-779, 2015.

[122] J. Lu, X. Meng, A. J. SpringThorpe, F. R. Shepherd and M. Poirier, "Inductively coupled plasma etching of GaAs low loss waveguides for a traveling waveguide polarization converter, using chlorine chemistry," *Journal of Vacuum Science & Technology A,* vol. 22, no. 3, pp. 1058-1061, 2004.

[123] K. A. Atlasov, P. Gallo, A. Rudra, B. Dwir and E. Kapon, "Effect of sidewall passivation in BCl_3/N_2 inductively coupled plasma etching of two-dimensional GaAs photonic crystals," *Journal of Vacuum Science & Technology B,* vol. 27, no. 5, pp. L21-L24, 2009.

[124] I. González, L. Muñoz Camuñez, A. González Taboada, C. Robles Urdiale, . J. M. Ripalda Cobián and P. A. Postigo Resa, "Fabrication of high quality factor GaAs/InAsSb photonic crystal microcavities by inductively coupled plasma etching and fast wet etching," *Journal of Vacuum Science & Technology B,* vol. 32, no. 1, p. 011204 , 2013.

[125] J. Lee, M. Jeon, M. Devre, K. Mackenzie, D. Johnson, J. Sasserath, S. Pearton, F. Ren and R. Shul, "Understanding of etch mechanism and etch depth distribution in inductively coupled plasma etching of GaAs," *Solid-State Electronics,* vol. 45, no. 9, pp. 1683-1686, 2001.

[126] J. Lee, M. Jeon, G. Cho, H. Yim, S. Chang, K. K. Kim, M. Devre, Y. S. Lee, R. Westerman, D. Johnson, J. N. Sasserath and S. J. Pearton, "Utilization of Optical Emission Spectroscopy for End-Point Detection during AlGaAs/GaAs and InGaP/GaAs Etching in BCl_3/N_2 Inductively Coupled Plasmas," *J. Electrochem. Soc.,* vol. 148, no. 9, pp. G472-G474, 2001.

[127] J. W. Lee, Y. T. Lim, I. K. Baek, S. Y. Yoo, G. S. Cho, M. H. Jeoin, J. Y. Leem and S. J. Pearton, "Comparison of planar inductively coupled plasma etching of GaAs in BCl_3, BCl_3/Ar, and BCl_3/Ne," *Applied Surface Science,* vol. 233, no. 1, pp. 402-410, 2004.

[128] D. S. Wuu, C. R. Chung, Y. H. Liu, R. H. Horng and S. H. Huang, "Deep etch of GaP using high-density plasma for light-emitting diode applications," *Journal of Vacuum Science & Technology B,* vol. 20, no. 3, pp. 902-908, 2002.

[129] M. K. Connors, J. J. Plant, K. G. Ray and G. W. Turner, "Chamber conditioning process development for improved inductively coupled plasma reactive ion etching of GaAs/AlGaAs materials," *Journal of Vacuum Science & Technology B,* vol. 31, no. 2, p. 021207 , 2013.

[130] M. K. Connors, L. J. Missaggia, W. S. Spencer and G. W. Turner, "Inductively coupled plasma reactive ion etching of GaAs wafer pieces with enhanced device yield," *Journal of Vacuum Science & Technology B,* vol. 32, no. 2, p. 021207 , 2014.

[131] S. Golka, M. Arens, M. Reetz and T. Kwapien, "Time-multiplexed, inductively coupled plasma process with separate $SiCl_4$ and O_2 steps for etching of GaAs with high selectivity," *Journal of Vacuum Science & Technology B,* vol. 27, no. 5, p. 2270 , 2009.

[132] J. W. Lee, M. W. Devre, D. Johnson and J. N. Sasserath, "Advanced selective dry etching of GaAs/AlGaAs in high density inductively coupled plasmas," *Journal of Vacuum Science & Technology A,* vol. 18, no. 4, p. 1220, 2000.

[133] Y. Cheng, J. Zou, M. Wan, W. Wang, X. Peng, L. Feng, W. Deng and Z. Zhu, "Factors Affecting the Top Stripping of GaAs Microwire Array Fabricated by Inductively Coupled Plasma Etching," *Chin. Phys. Lett.,* vol. 32, no. 5, p. 058102, 2015.

[134] P. S. Nam, L. M. Ferreira, T. Y. Lee and K. N. Tu, "Study of grass formation in GaAs backside via etching using inductively coupled plasma system," *Journal of Vacuum Science & Technology B,* vol. 18, no. 6, pp. 2780-2784, 2000.

[135] D. C. Hays, H. Cho, J. W. Lee, M. W. Devre, B. H. Reelfs, D. Johnson, J. N. Sasserath, L. C. Meyer, E. Toussaint, F. Ren, C. R. Abernathy and S. J. Pearton, "High selectivity Inductively Coupled Plasma etching of GaAs over InGaP," *Applied Surface Science,* vol. 156, no. 1, pp. 76-84, 2000.

[136] Y. Matsukura, H. Tanaka and J. Wada, "Selectivity enhancement of GaAs/AlGaAs dry etching by a pulse-excited inductively coupled plasma source," *Journal of Vacuum Science & Technology B,* vol. 18, no. 2, pp. 864-867, 2000.

[137] C. B. Cooper, S. Salimian and H. F. Macmillan, "Reactive ion etch characteristics of thin InGaAs and AlGaAs stop-etch layers," *Journal of Electronic Materials,* vol. 18, no. 5, p. 619–622, 1989.

[138] H. Tamura and H. Kurihara, "GaAs and GaAlAs Reactive Ion Etching in BCl_3-Cl_2 Mixture," *Japanese Journal of Applied Physics,* vol. 23, no. 9, pp. L731-L733, 1984.

[139] C. Constantine, R. J. Shul, C. T. Sullivan, M. B. Snipes, G. B. McClellan, M. Hafich, C. T. Fuller, J. R. Mileham and S. J. Pearton, "Etching of GaAs/AlGaAs rib waveguide structures using $BCl_3/Cl_2/N_2/Ar$ electron cyclotron resonance," *Journal of Vacuum Science & Technology B,* vol. 13, no. 5, pp. 2025-2030, 1995.

[140] W. Lim, I. Baek, P. Jung, J. Lee, G. Cho, J. Lee, K. Cho and S. Pearton, "Investigation of GaAs Dry Etching in a Planar Inductively Coupled BCl_3 Plasma," *Journal of The Electrochemical Society,* vol. 151, no. 3, pp. G163-G166, 2004.

[141] Z. Liao, M. Alam and J. S. Aitchison, "Experimental demonstration of vertically integrated AlGaAs/GaAs waveguides," in *2016 IEEE Photonics Conference (IPC)*, Waikoloa, HI, 2016.

[142] G. A. Porkolab, P. Apiratikul, B. Wang, S. H. Guo and C. . J. K. Richardson, "Low propagation loss AlGaAs waveguides fabricated with plasma-assisted photoresist reflow," *Optics Express,* vol. 22, no. 7, pp. 7733-7743, 2014.

[143] V. R. Almeida, R. R. Panepucci and M. Lipson, "Nanotaper for compact mode conversion," *Optics Letters,* vol. 28, no. 15, pp. 1302-1304, 2003.

[144] Y. Maegami, R. Takei, E. Omoda, T. Amano, M. Okano, M. Mori, T. Kamei and Y. Sakakibara, "Spot-size converter with a SiO_2 spacer layer between tapered Si and SiON waveguides for fiber-to-chip coupling," *Optics Express,* vol. 23, no. 16, pp. 21287-21295, 2015.

[145] M. M. Sisto, B. Fisette, J. E. Paultre, A. Paquet and Y. Desroches, "Novel spot size converter for coupling standard single mode fibers to SOI waveguides," in *Proc. SPIE 9752, Silicon Photonics XI*, San Francisco, California, United States, 2016.

[146] F. Wu, V. Tolstikhin, Y. Logvin and C. Brooks, "Spot-Size Converter: A Generic Building Block for Regrowth-Free Multi-Guide Vertical Integration in InP," in *Integrated Photonics Research, Silicon and Nanophotonics Conference*, Toronto, ON, 2011.

[147] V. Tolstikhin, "Multi-Guide Vertical Integration in InP - A Regrowth-Free PIC Technology for Optical Communications," in *Compound Semiconductor Manufacturing Technology Conference*, New Orleans, LA, 2013.

[148] I. Moerman, P. P. Van Daele and P. M. Demeester, "A Review on Fabrication Technologies for the Monolithic Integration of Tapers with III–V Semiconductor Devices," *IEEE Journal of Selected Topics in Quantum Electronics,* vol. 3, no. 6, pp. 1308-1320, 1997.

[149] D. D’Agostino, E. Kleijn, R. Santos, H. P. M. M. Ambrosius and M. K. Smit, "A dense Spot Size Converter Array fabricated in a generic process on InP," in *Proc. of SPIE*, 2013.

[150] F. Wu, V. Tolstikhin, A. Densmore and S. Grabtchak, "On-chip spot-size converter using a two-step lateral taper for efficient coupling to InP-based photonic integrated circuits," in *Optical Amplifiers and Their Applications, Technical Digest (CD) (OSA, 2004)*, 2004.

[151] B. Mersali, A. Ramdane and A. Carenco, "Optical-Mode Transformer: A III–V Circuit Integration Enabler," *IEEE Journal of Selected Topics in Quantum Electronics,* vol. 3, no. 6, pp. 1321-1331, 1997.

[152] R. E. Smith, C. T. Sullivan, G. A. Vawter, G. R. Hadley, J. R. Wendt, M. B. Snipes and J. F. Klem, "Reduced Coupling Loss Using a Tapered-Rib Adiabatic-Following Fiber Coupler," *IEEE Photonics Technology Letters,* vol. 8, no. 8, pp. 1052-1054, 1996.

[153] Z. Liao, S. J. Wagner, M. Z. Alam, V. Tolstikhin and J. S. Aitchison, "Vertically integrated spot-size converter in AlGaAs-GaAs," *Optics Letters,* vol. 42, no. 20, pp. 4167-4170, 2017.

[154] M. K. Smit, "New focusing and dispersive planar component based on an optical phased array," *Electronics Letters,* vol. 24, no. 7, pp. 385-386, 1988.

[155] A. R. Vellekoop and M. K. Smit, "Low-loss planar optical polarisation splitter with small dimensions," *Electronics Letters,* vol. 25, no. 15, pp. 946-947, 1989.

[156] K. Okamoto, K. Takiguchi and Y. Ohmori, "16-channel optical add/drop multiplexer using silica-based arrayed-waveguide gratings," *Electronics Letters,* vol. 31, no. 9, pp. 723-724, 1995.

[157] T. Saida, A. Kaneko, T. Goh, M. Okuno, A. Himeno, K. Takiguchi and K. Okamoto, "Athermal silica-based optical add/drop multiplexer consisting of arrayed waveguide gratings and double gate thermo-optical switches," *Electronics Letters,* vol. 36, no. 6, pp. 528To-529, 2000.

[158] P. Cheben, J. H. Schmid, A. Delâge, A. Densmore, S. Janz, B. Lamontagne, J. Lapointe, E. Post, P. Waldron and D.-X. Xu, "A high-resolution silicon-on-insulator arrayed waveguide grating microspectrometer with submicrometer aperture waveguides," *Optics Express,* vol. 15, no. 5, p. 2299, 2007.

[159] D. Dai, Z. Wang, J. F. Bauters, M.-C. Tien, M. J. R. Heck, D. J. Blumenthal and J. E. Bowers, "Low-loss Si3N4 arrayed-waveguide grating (de)multiplexer using nano-core optical waveguides," *Optics Express,* vol. 19, no. 15, pp. 14130-14136, 2011.

[160] D. Martens, A. Z. Subramanian, S. Pathak, M. Vanslembrouck, P. Bienstman, W. Bogaerts and R. G. Baets, "Compact Silicon Nitride Arrayed Waveguide Gratings for Very Near-Infrared Wavelengths," *IEEE Photonics Technology Letters,* vol. 27, no. 2, pp. 137To-140, 2015.

[161] A. Malik, M. Muneeb, S. Pathak, Y. Shimura, J. V. Campenhout, R. Loo and G. Roelkens, "Germanium-on-Silicon Mid-Infrared Arrayed Waveguide Grating Multiplexers," *IEEE Photonics Technology Letters,* vol. 25, no. 18, p. 2013, 1805-1808.

[162] N. Keil, H.-H. Yao, C. Zawadzki, J. Bauer, M. Bauer, C. Dreyer and J. Schneider, "Athermal all-polymer arrayed-waveguide grating multiplexer," *Electronics Letters,* vol. 37, no. 9, pp. 579-580, 2001.

[163] B. Yang, Y. Zhu, Y. Jiao, L. Yang, Z. Sheng, S. He and D. Dai, "Compact Arrayed Waveguide Grating Devices Based on Small SU-8 Strip Waveguides," *J. Lightwave Technol.,* vol. 29, no. 13, pp. 2009-2014, 2011.

[164] M. Zirngibl, C. Dragone and C. H. Joyner, "Demonstration of a 15x15 arrayed waveguide multiplexer on InP," *IEEE Photonics Technology Letters,* vol. 4, no. 11, pp. 1250-1253, 1992.

[165] M. Kohtoku, H. Sanjoh, S. Oku, Y. Kadota, Y. Yoshikuni and Y. Shibata, "InP-based 64-channel arrayed waveguide grating with 50 GHz channel spacing and up to -20 dB crosstalk," *Electronics Letters,* vol. 33, no. 21, pp. 1786 - 1787, 1997.

[166] Y. Yoshikuni, "Semiconductor arrayed waveguide gratings for photonic integrated devices," *IEEE Journal of Selected Topics in Quantum Electronics,* vol. 8, no. 6, pp. 1102 - 1114, 2002.

[167] K. Kodate and Y. Komai, "Compact spectroscopic sensor using an arrayed waveguide grating," *Journal of Optics A: Pure and Applied Optics,* vol. 10, no. 4, p. 044011, 2008.

[168] N. Matsuda, H. Nishi, P. Karkus, T. Tsuchizawa, K. Yamada, W. J. Munro, K. Shimizu and H. Takesue, "Generation of entangled photons using an arrayed waveguide grating," *Journal of Optics,* vol. 19, no. 12, p. 124005, 2017.

[169] M. G. Hale and M. R. Querry, "Optical Constants of Water in the 200-nm to 200-μm Wavelength Region," *Applied Optics,* vol. 12, no. 3, pp. 555-563, 1973.

[170] M. K. Smit and C. V. Dam, "PHASAR-Based WDM-Devices: Principles, Design and Applications," *IEEE Journal of Selected Topics in Quantum Electronics,* vol. 2, no. 2, pp. 236-250, 1996.

[171] K. Rausch, Broadband Arrayed Waveguide Grating Multiplexers on InP, THE UNIVERSITY OF ARIZONA, 2005.

[172] R. J. Deri and E. Kapon, "Low-loss III-V semiconductor optical waveguides," *IEEE Journal of Quantum Electronics,* vol. 27, no. 3, pp. 626-640, 1991.

[173] S. Darmawan, S.-Y. Lee, C.-W. Lee and M.-K. Chin, "A rigorous comparative analysis of directional couplers and multimode Interferometers based on ridge waveguides," *IEEE Journal of Selected Topics in Quantum Electronics,* vol. 11, no. 2, pp. 466-475, 2005.

[174] M.-K. Chin, C.-w. Lee, S.-Y. Lee and S. Darmawan, "High-index-contrast waveguides and devices," *Applied Optics,* vol. 44, no. 15, pp. 3077-3086, 2005.

[175] J. M. Heaton, M. M. Bourke, S. B. Jones, B. H. Smith, K. P. Hilton, G. W. Smith, J. C. H. Birbeck, G. Berry, S. V. Dewar and D. R. Wight, "Optimization of deep-etched, single-mode GaAs-AlGaAs optical waveguides using controlled leakage into the substrate," *Journal of Lightwave Technology,* vol. 17, no. 2, pp. 267-281, 1999.

[176] M.-K. Chin, C. Xu and W. Huang, "Theoretical approach to a polarization-insensitive single-mode microring resonator," *Optics Express ,* vol. 12, no. 14, pp. 3245-3250, 2004.

[177] B. M. A. Rahman, W. Boonthittanont, S. S. A. Obayya, T. Wongcharoen, E. O. Ladele and K. T. V. Grattan, "Rigorous Beam Propagation Analysis of Tapered Spot-Size Converters in Deep-Etched Semiconductor Waveguides," *Journal of Lightwave Technology,* vol. 21, no. 12, pp. 3392-3398, 2003.

[178] V. Van, P. P. Absil, J. V. Hryniewicz and P.-T. Ho, "Propagation Loss in Single-Mode GaAs-AlGaAs Microring Resonators: Measurement and Model," *Journal of Lightwave Technology,* vol. 19, no. 11, pp. 1734-1739, 2001.

[179] E. D. Finlayson, J. M. Heaton, A. B. M. Rahman and S. S. A. Obayya, "Polarization Conversion in Passive Deep-Etched GaAs/AlGaAs Waveguides," *Journal of Lightwave Technology,* vol. 24, no. 3, pp. 1425-1432, 2006.

[180] S. S. A. Obayya, S. Haxha, B. M. A. Rahman, C. Themistos and K. T. V. Grattan, "Optimization of the optical properties of a deeply etched semiconductor electrooptic modulator," *Journal of Lightwave Technology,* vol. 21, no. 8, pp. 1813-1819, 2003.

[181] A. D. Ferguson, A. Kuver, J. M. Heaton, Y. Zhou, C. M. Snowden and S. Iezekiel, "Low-loss, single-mode GaAs/AlGaAs waveguides with large core thickness," *IEE Proceedings - Optoelectronics,* vol. 153, no. 2, pp. 51-56, 2006.

[182] R. J. Deri, A. Shahar, E. Colas, R. N. Thurston, W. J. Tomlinson, A. Yi-Yan and M. Seto, "Single-mode semiconductor optical waveguides with large dimensions suitable for compact bend applications," *Applied Physics Letters,* vol. 57, no. 23, p. 2396 , 1990.

[183] D. Liang, J. Wang and D. C. Hall, "Single-Facet Folded-Cavity Diode Laser With Ultrasmall Bend Radius High-Index-Contrast Oxidized AlGaAs Ridge Waveguide," *IEEE Photonics Technology Letters,* vol. 19, no. 8, pp. 598-600, 2007.

[184] D. Decoster and J. Harari, "Semiconductor materials used in PIN photodiodes for the visible and near-infrared," in *Optoelectronic Sensors*, Hoboken, USA, John Wiley & Sons, Inc., 2009, pp. 42-49.

[185] S. Adachi, Properties of Semiconductor Alloys: Group-IV, III–V and II–VI Semiconductors, John Wiley & Sons Ltd, 2009.

[186] S. Adachi, "Refractive indices of III–V compounds: Key properties of InGaAsP relevant to device design," *Japanese Journal of Applied Physics,* vol. 53, no. 8, pp. 8775-8792, 1982.

[187] P. Bhattacharya, Properties of Lattice-Matched and Strained InGaAs, London: INSPEC, the Institution of Electrical Engineers, 1993.

[188] H. Kato, N. Iguchi, S. Chika, M. Nakayama and N. Sano, "Effective Mass Reversal on $In_xAl_{1-x}As$/GaAs Strained-Layer Superlattices," *Japanese Journal of Applied Physics,* vol. 25, no. 9, pp. 1327-1331, 1986.

[189] E. P. O'Reilly, "Valence band engineering in strained-layer structures," *Semiconductor Science and Technology,* vol. 4, pp. 121-137, 1989.

[190] G. Ji, D. Huang, U. K. Reddy, T. S. Henderson, R. Houdré and H. Morkoç, "Optical investigation of highly strained InGaAs-GaAs multiple quantum wells," *Journal of Applied Physics,* vol. 62, no. 8, pp. 3366-3373, 1987.

[191] J. Singh, Physics of Semiconductors and Their Heterostructures, New York: McGraw Hill, 1993.

[192] K. Huang, K. Tai, S. N. Chu and A. Cho, "Optical studies of $In_xGa_{1-x}As$/GaAs strained-layer quantum wells," *Applied Physics Letters,* vol. 54, no. 20, pp. 2026-2028, 1989.

[193] M. Shur, Physics of Semiconductor Devices, Pearson, 1990.

[194] J. Reithmaier, R. Höger, H. Riechert, A. Heberle, G. Abstreiter and G. Weimann, "Band offset in elastically strained InGaAs-GaAs multiple quantum wells determined by optical absorption and electronic Raman scattering," *Applied Physics Letters,* vol. 56, no. 6, pp. 536-538, 1990.

[195] T. G. Andersson, Z. Chen, V. D. Kulakovskii, A. Uddin and J. T. Vallin, "Variation of the critical layer thickness with In content in strained $In_xGa_{1-x}As$-GaAs quantum wells grown by molecular beam epitaxy," *Applied Physics Letters,* vol. 51, no. 10, pp. 752-754, 1987.

[196] S. Niki, C.-L. Lin, W. S. Chang and H. H. Wieder, "Band-edge discontinuities of strained-layer $In_xGa_{1-x}As$ - GaAs heterojunctions and quantum wells," *Applied Physics Letters,* vol. 55, no. 13, pp. 1339-1341, 1989.

[197] H. Hou, L. Wang, R. Tang and J. Zhou, "Pressure dependence of photoluminescence in $In_xGa_{1-x}As$-GaAs strained quantum wells," *Physical Review B,* vol. 42, no. 5, pp. 2926-2931, 1990.

[198] J. Pamulapati, P. Bhattacharya, R. L. Tober, J. P. Loehr and J. Singh, "Characterization of high-quality pseudomorphic InGaAs - GaAs quantum wells by luminescence and reflectance techniques," *Journal of Applied Physics,* vol. 71, no. 9, pp. 4487-4491, 1992.

[199] R. Grey, J. P. R. David, P. A. Claxton, F. Gonzalez Sanz and J. Woodhead, "Relaxation of strain within multilayer InGaAs/GaAs pseudomorphic structures," *Journal of Applied Physics,* vol. 66, no. 2, pp. 975-977, 1989.

[200] J.-S. Choe, W.-S. Han, D. J. Kim, J.-H. Kim, C. J. Youn, D.-Y. Kim, Y.-H. Kwon and E.-S. Nam, "Optimization of spot-size converter for low polarization dependent loss of waveguide photodetector," *Optics Express,* vol. 21, no. 25, pp. 30175-30182, 2013.

[201] Z. Liao and J. S. Aitchison, "Monolithic integration of waveguide photodiodes (WGPD) with vertically integrated AlGaAs waveguides," in *Photonics Conference (IPC), 2017 IEEE*, Orlando, FL, 2017.

[202] P. Kultavewuti, Z. Liao and J. S. Aitchison, "High-index-contrast suspended waveguides in AlGaAs," *draft paper,* 2018.

[203] J. P. Sprengers, A. Gaggero, D. Sahin, . S. Jahanmirinejad, G. Frucci, F. Mattioli, R. Leoni, J. Beetz, M. Lermer, M. Kamp, S. Höfling, R. Sanjines and A. Fiore, "Waveguide superconducting single-photon detectors for integrated quantum photonic circuits," *Applied Physics Letters,* vol. 99, no. 18, p. 181110, 2011.

[204] A. J. Shields, "Semiconductor quantum light sources," *Nature Photonics,* vol. 1, p. 215–223, 2007.

[205] C. Santori, D. Fattal, J. Vučković, G. S. Solomon and Y. Yamamoto, "Indistinguishable photons from a single-photon device," *Nature,* vol. 419, p. 594–597, 2002.

[206] Y. He, Y. He, Y. Wei, D. Wu, M. Atatüre, C. Schneider, S. Höfling, M. Kamp, C.-Y. Lu and J.-W. Pan, "On-demand semiconductor single-photon source with near-unity indistinguishability," *Nature Nanotechnology,* vol. 8, pp. 213-217, 2013.

[207] R. J. Horn, P. Kolenderski, D. Kang, P. Abolghasem, C. Scarcella, A. D. Frera, A. Tosi, L. G. Helt, S. V. Zhukovsky, J. E. Sipe, G. Weihs, A. S. Helmy and T. Jennewein, "Inherent polarization entanglement generated from a monolithic semiconductor chip," *Scientific Reports,* vol. 3, p. 2314, 2013.

[208] R. Marchildon and A. S. Helmy, "Quantum interference in monolithic nanophotonics," in *Proc. SPIE Quantum Sensing and Nano Electronics and Photonics XIV*, San Francisco, California, United States, 2017.

[209] R. P. Marchildon and A. S. Helmy, "Dispersion-enabled quantum state control in integrated photonics," *Optica,* vol. 3, no. 3, pp. 243-251, 2016.

[210] D. D. Cunningham, In Vivo Glucose Sensing, Hoboken, N.J.: Wiley, 2010.

[211] C.-R. Kong, I. Barman, N. C. Dingari, J.-W. Kang, L. Galindo, R. R. Dasari and M. S. Feld, "A novel non-imaging optics based Raman spectroscopy," *AIP Advances,* vol. 1, p. 032175, 2011.

[212] C. Conti, M. Realini, C. Colombo, K. Sowoidnich, N. K. Afseth, M. Bertasa, A. Botteon and P. Matousek, "Noninvasive Analysis of Thin Turbid Layers Using Microscale Spatially Offset Raman Spectroscopy," *Analytical chemistry,* vol. 87, no. 11, p. 5810–5815, 2015.

[213] K. Ma, J. M. Yuen, N. C. Shah, J. T. Walsh, M. R. Glucksberg and R. P. Van Duyne, "In Vivo, Transcutaneous Glucose Sensing Using Surface-Enhanced Spatially Offset Raman Spectroscopy: Multiple Rats, Improved Hypoglycemic Accuracy, Low Incident Power, and Continuous Monitoring for Greater than 17 Days," *Analytical Chemistry,* vol. 83, pp. 9146-9152, 2011.

[214] J. M. Yuen, N. C. Shah, J. T. Walsh Jr, M. R. Glucksberg and R. P. Van Duyne, "Transcutaneous Glucose Sensing by Surface-Enhanced Spatially Offset Raman Spectroscopy in a Rat Model," *Analytical chemistry,* vol. 82, no. 20, p. 8382–8385, 2010.

[215] J. Shao, M. Lin, Y. Li, X. Li, J. Liu, J. Liang and H. Yao, "In Vivo Blood Glucose Quantification Using Raman Spectroscopy," *PLoS ONE,* vol. 7, no. 10, pp. 1-6, 2012.

[216] W. Drexler, M. Liu, A. Kumar, T. Kamali, A. Unterhuber and R. A. Leitgeb, "Optical coherence tomography today: speed, contrast, and multimodality," *Journal of Biomedical Optics,* vol. 19, no. 7, p. 071412, 2014.

[217] N. Ismail, B. I. Akca, L. Chang, F. Sun, G. Sengo, K. Wörhoff, M. Pollnau and R. M. De Ridder, "Raman Spectroscopy and Optical Coherence Tomography on a Chip," 2016.

[218] A. Nitkowski, K. Preston, N. Sherwood-Droz, B. S. Schmidt and A. R. Hajian, "On-chip spectrometer for low-cost optical coherence tomography," in *Proc. of SPIE Optical Coherence Tomography and Coherence Domain Optical Methods in Biomedicine XVIII*, 2014.

[219] E. Ryckeboer, R. Bockstaele, M. Vanslembrouck and R. Baets, "Glucose sensing by waveguide-based absorption spectroscopy on a silicon chip," *Biomedical Optics Express,* vol. 5, no. 5, pp. 1636-1648, 2014.

[220] N. Ismail, L.-P. Choo-Smith, K. Wörhoff, A. Driessen, A. C. Baclig, P. J. Caspers, G. J. Puppels, R. M. de Ridder and M. Pollnau, "Raman spectroscopy with an integrated arrayed-waveguide grating," *Optics Letters,* vol. 36, no. 23, pp. 4629-2631, 2011.

[221] N. Ismail, K. Wörhoff, A. Driessen, R. M. de Ridder and M. Pollnau, "Excitation and Light Collection From Highly Scattering Media With Integrated Waveguides," *IEEE Photonics Technology Letters,* vol. 23, no. 5, pp. 278-280, 2011.

[222] A. Dhakal, A. Raza, F. Peyskens, A. Z. Subramanian, S. Clemmen, N. L. Thomas and R. Baets, "Efficiency of evanescent excitation and collection of spontaneous Raman scattering near high index contrast channel waveguides," *Optics Express,* vol. 23, no. 21, pp. 27391-27404, 2015.

[223] B. I. Akca, B. Považay, A. Alex, K. Wörhoff, R. M. de Ridder, W. Drexler and M. Pollnau, "Miniature spectrometer and beam splitter for an optical coherence tomography on a silicon chip," *Optics Express,* vol. 21, no. 14, pp. 16648-16656, 2013.